



The University of
Nottingham

UNITED KINGDOM • CHINA • MALAYSIA

INVESTIGATION OF SWIRL PIPE FOR IMPROVING CLEANING EFFICIENCY IN CLOSED PROCESSING SYSTEM

Guozhen Li, BEng, MSc

Thesis submitted to the University of Nottingham
for the degree of Doctor of Philosophy

December 2015

ABSTRACT

This thesis provides unique insights into the fundamentals of improving the efficiency of 'Clean-In-Place' procedures in closed processing systems by locally introducing intensified hydrodynamic force from swirl flows induced by an optimised four-lobed swirl pipe without increasing the overall flow velocities.

The studies, carried out employing Computational Fluid Dynamics (CFD) techniques, pressure transmitters and a fast response Constant Temperature Anemometer (CTA) system, covered further optimisation of the four-lobed swirl pipe, RANS-based modelling and Large Eddy Simulation of the swirl flows, and experimental validation of the CFD models through the measurements of pressure drop and wall shear stress in swirl flows with various Reynolds Number.

The computational and experimental work showed that the swirl pipe gives rise to a clear increase of mean wall shear stress to the downstream with its value and variation trend being dependent on swirl intensity. Moreover, it promotes a stronger fluctuation rate of wall shear stress to the downstream especially further downstream where swirl effect is less dominant.

As the increase of either the mean or the fluctuation rates of wall shear stress contributes to the improvement of CIP procedures in the closed processing systems. This thesis demonstrates that, with the ability to exert strengthened hydrodynamic force to the internal surface of the pipe downstream of it without increasing the overall flow velocity, the introduction of swirl pipe to the CIP procedures should improve the cleaning efficiency in the closed processing systems, consequently shortening the downtime for cleaning, and reducing the costs for chemicals and power energy.

ACKNOWLEDGEMENTS

I would like to thank the graduate school of the University of Nottingham for the scholarship granted to me to make this PhD possible.

I owe a great debt of gratitude to my supervisors, Dr. Philip Hall and Prof. Nick Miles for their precious support, advice, guidance, encouragement, inspiration and invaluable input to this research.

I extend my gratitude to:

Zheng Wang for his help and valuable input to the establishment of the rig.

Phillip Windsor, Jie Dong, Chi Zheng and Julian Zhu for their support and help with the installation of rig.

Prof. Xiaogang Yang for his advice on Large Eddy Simulations.

Prof. Tao Wu for his valued input and critical evaluation of my work.

My friends Kaiqi Shi, Kam Hoe Yin and Weiguang Su for their useful experiences and helpful discussions.

My friends Jie Dong and Lele Zhang who make hard times easier and dull moments funnier.

Finally, I am especially grateful to my parents, my sisters Suping and Suzheng, my brother GuoPing and my aunt for their love, support and understanding which are precious to me.

TABLE OF CONTENTS

ABSTRACT	I
ACKNOWLEDGEMENTS	II
TABLE OF CONTENTS	III
LIST OF FIGURES.....	VIII
LIST OF TABLES.....	XVI
NOMENCLATURE	XVII
CHAPTER 1: INTRODUCTION.....	1
1.1 General Introduction	1
1.2 Aims and Objectives	4
1.3 Thesis Outline	5
CHAPTER 2: LITERATURE REVIEW	8
2.1 Cleaning of Closed Processing Pipe System.....	8
2.1.1 Fouling of Pipe Surface.....	8
2.1.2 Clean In Place.....	9
2.1.3 Cleaning Efficiency.....	10
2.2 Hydrodynamic Effects of Cleaning Liquid	15
2.2.1 Hydrodynamic Factors.....	15
2.2.2 Mechanism of Particle Detachment in Flow	20
2.3 Swirl Flow.....	21
2.3.1 Swirl Induction Pipes.....	21
2.3.2 Modelling Swirling Flow	28
2.3.3 Definition of Terms and Equations for Swirl Flow	37
2.4 Measuring Swirl Flow.....	41
2.4.1 Measuring Flowfield	41
2.4.2 Measuring Wall Shear Stress	45
2.4.3 Measuring Cleanability	50

2.5 Conclusion	52
CHAPTER 3: TRANSITION AND SWIRL PIPE CREATION	53
3.1 Introduction	53
3.2 Geometry Calculation	53
3.2.1 Four-lobed Transition Pipe Calculation	54
3.2.2 Different Types of Transition	60
3.2.3 Spreadsheet for 4-lobed Transition Pipe	65
3.2.4 Spreadsheet for 4-lobed Swirl Inducing Pipe	66
3.3 Geometry Creation	66
3.3.1 Transition Pipe Creation	66
3.3.2 Swirl Inducing Pipe Creation	68
3.3.3 Optimized Swirl Pipe Creation	70
3.4 Conclusions.....	73
CHAPTER 4: COMPUTATIONAL FLUID DYNAMICS METHODOLOGY	74
4.1 Introduction	74
4.2 Modelling Turbulence	76
4.2.1 RANS Approach	79
4.2.2 Near Wall Treatment for Wall-Bounded Turbulence Flows	86
4.3 Numerical Schemes	96
4.3.1 Solver	97
4.3.2 Numerical Discretization	101
4.4 CFD Model Formulation	109
4.4.1 CFD Software Package.....	109
4.4.2 Enabling Assumptions	109
4.4.3 Flow Domain	110
4.4.4 Meshing	112
4.4.5 Boundary Conditions	133
4.4.6 Solution Methodology	135
4.4.7 Judging Convergence	142

4.5 Conclusions	146
CHAPTER 5: FURTHER OPTIMISATION OF THE 4-LOBED SWIRL PIPE	147
5.1 Introduction.....	147
5.2 Numerical Method and Models	150
5.3 Results and Discussions.....	152
5.3.1 Pressure Drop	152
5.3.2 Swirl Development within Swirl Pipes	154
5.3.3 Swirl Effectiveness.....	157
5.3.4 Swirl Decay	159
5.3.5 Wall shear stress	161
5.4 Conclusions	165
CHAPTER 6: RANS-BASED SIMULATION OF SWIRL FLOW DOWNSTREAM OF THE OPTIMISED SWIRL PIPE	167
6.1 Introduction.....	167
6.2 Simulation Setup	168
6.3 Results and Discussions.....	169
6.3.1 Pressure Drop	169
6.3.2 Tangential Velocity.....	171
6.3.3 Swirl Decay	177
6.3.4 Wall Shear Stress	180
6.4 Conclusions	192
CHAPTER 7: LARGE EDDY SIMULATION OF SWIRL FLOW DOWNSTREAM OF THE OPTIMISED SWIRL PIPE	194
7.1 Introduction.....	194
7.2 Large Eddy Simulation.....	195
7.2.1 Filtering Operation.....	196
7.2.2 Sub-Grid-Scale Models	197

7.3 Simulation Setup	202
7.3.1 Meshing	202
7.3.2 Initial Conditions for LES.....	204
7.3.3 Discretization for LES	204
7.3.4 Choice of SGS Model	205
7.4 Results and Discussions	208
7.4.1 Unsteady Swirl Flow	208
7.4.2 Pressure Drop	214
7.4.3 Tangential Velocity	216
7.4.4 Swirl Decay.....	218
7.4.5 Wall Shear Stress	222
7.5 Conclusions.....	235

CHAPTER 8: VALIDATION OF THE COMPUTATIONAL FLUID DYNAMICS

RESULTS 237

8.1 Introduction	237
8.2 Dealing with Errors and Uncertainties in CFD	237
8.3 Hydraulic Rig Layout.....	240
8.4 Producing Swirl Pipe by Investment Casting	243
8.5 Pressure Drop Validation	246
8.5.1 Pressure Drop Measurement.....	246
8.5.2 Pressure Drop in Swirl Flow (1m cylindrical+0.4m swirl pipe+4m cylindrical).....	248
8.5.3 Pressure Drop in Non-Swirl Flow (1m cylindrical+0.4m control pipe+4m cylindrical)	253
8.5.4 Pressure Drop across Swirl Pipe Only	257
8.6 Wall Shear Stress Validation	261
8.6.1 Constant Temperature Anemometry (CTA).....	261
8.6.2 Calibration of the Hot-Film Probe.....	264
8.6.3 Measurements of Mean Wall Shear Stress in Swirl Flows.....	270

8.6.4 Fluctuation of Wall Shear Stress in Swirl Flows.....	279
8.7 Conclusions	286
CHAPTER 9: CONCLUSIONS AND FUTURE WORK	288
9.1 Conclusions	288
9.1.1 Further Optimisation of the 4-Lobed Swirl Pipe	288
9.1.2 RANS-Based Simulation of Swirl Flows.....	288
9.1.3 Large Eddy Simulation of Swirl Flows	289
9.1.4 Experimental Validation.....	290
9.2 Contribution to Knowledge.....	290
9.3 Further Work	291
9.3.1 CFD Modelling.....	291
9.3.2 Experimental Work	293
REFERENCE.....	295
APPENDICES.....	308
Appendix 2.1 Mechanism of Particle Detachment in Flow.....	308
Appendix 3.1 Spreadsheet for 4-Lobed Transition Pipe.....	317
Appendix 3.2 Spreadsheet for 4-Lobed Swirl Inducing Pipe	319
Appendix 3.3 Cross-section Development of the 4-Lobed Transition Pipe	320
Appendix 5.1 Optimization of a Four-Lobed Swirl Pipe for Clean-In-Place Procedures.....	322
Appendix 8.1 Drawing of the Optimised Swirl Pipe for Investment Casting	331
Appendix 8.2 Experimental and Calculated data for Calibrating the Tot-film Sensor	333

LIST OF FIGURES

Figure 2.1.1 Sinner circles for three different cleaning situations (after PathogenCombat, 2011)	11
Figure 2.1.2 Microscope pictures of biofilm grown under three conditions (after PathogenCombat, 2011)	14
Figure 2.2.1 Geometries used for showing the influence of flow patterns on the cleanability of equipment (after Friis and Jensen, 2002)	17
Figure 2.3.1 Three types of swirl generators (after Najafi et al., 2011).....	22
Figure 2.3.2 Classification of Swirl Types (After Steenbergen and Voskamp, 1998), corresponding to the three types of swirl generators.....	22
Figure 2.3.3 <i>Swirly-Flo</i> pipe used by Raylor and Ganeshliangam (after Ganeshalingham, 2002).....	24
Figure 2.3.4 Optimal Swirl inducing pipe, 400mm length, P:D=8	25
Figure 2.3.5 Transition pipes prior/after swirl inducing pipe	27
Figure 2.4.1 Schematic Diagram of PIV Setup and Camera Angle with the Laser at an Angle (after Ariyaratne, 2005)	44
Figure 3.2.1 Fully developed swirl pipe cross-section.....	54
Figure 3.2.2 Transition Pipe at Intermediate Stage as Lobes Develop ($\gamma = 65^\circ$)	56
Figure 3.2.3 Indication of total area of 4 segmental lobes (a), total area of inner segments (b) and total lobe area (c) at intermediate stage	59
Figure 3.2.4 Axial and tangential velocity contours at fully developed and intermediate stage of transition pipe (2m/s inlet velocity).....	62
Figure 3.2.5 Lobe area developments with pipe length for α , β and linear transitions	63
Figure 3.3.1 Demonstration of 18 sections used to sweep and blend into transition pipe	67
Figure 3.3.2 Graph of γ versus length for transition pipe	68

Figure 3.3.3 Demonstration of 21 sections used to sweep and blend into half of the full swirl inducing pipe	69
Figure 3.3.4 Graph of twist versus length for swirl inducing pipe	70
Figure 3.3.5 Entry transition pipe prior to (a) and exit transition pipe after (b) swirl inducing pipe (after Ariyaratne, 2005)	71
Figure 3.3.6 The optimized 600mm length 4-lobed swirl pipe	72
Figure 3.3.7 The further optimized 400mm length 4-lobed swirl pipe	73
Figure 4.2.1 Near-Wall Region in Turbulent Flows (after ANSYS 2011a)	87
Figure 4.3.1 Overview of the Pressure-Based Segregated (a) and Coupled (b) Solution Methods	100
Figure 4.4.1 Configuration of simulation geometry	110
Figure 4.4.2 Velocity profiles downstream of circular pipe inlet	112
Figure 4.4.3 Circular Pipe face Mesh and Distribution of Highly Skewed Cells	116
Figure 4.4.4 A detail view of the interface at the swirl/circular pipe intersection	118
Figure 4.4.5 Discontinuity in contour of wall shear stress at the circular/swirl and swirl/circular interfaces	119
Figure 4.4.6 Face meshes of swirl inducing pipe, transition pipe, and circular pipe	120
Figure 4.4.7 Face meshes of swirl inducing pipe, transition pipe, and circular pipe	122
Figure 4.4.8 Swirl pipe meshes with unstructured grid by Ariyaratne (2005) and structured hexahedral grid with O-block	123
Figure 4.4.9 y^+ contours for computational domain geometry (2m/s inlet velocity)	125
Figure 4.4.10 Histogram of Q_{EAS} quality distribution	131
Figure 4.4.11 Histogram of Aspect Ratio quality distribution	132
Figure 4.4.12 Pressure downstream of swirl pipe for various turbulence models and wall functions (3m/s inlet velocity)	136

Figure 4.4.13 Tangential velocity downstream of swirl pipe for various turbulence models and wall functions (3m/s inlet velocity)	137
Figure 4.4.14 Pressure downstream of swirl pipe for various advection schemes (3m/s inlet velocity)	138
Figure 4.4.15 Tangential velocity downstream of swirl pipe for various advection schemes (3m/s inlet velocity)	139
Figure 4.4.16 Pressure downstream of swirl pipe for various pressure interpolation schemes (3m/s inlet velocity)	140
Figure 4.4.17 Tangential velocity downstream of swirl pipe for various pressure interpolation schemes (3m/s inlet velocity)	141
Figure 4.4.18 Pressure and tangential velocity after swirl pipe for various Pressure-velocity coupling schemes (3m/s inlet velocity)	142
Figure 4.4.19 Scaled residuals for a final simulation model	143
Figure 4.4.20 Variation of static pressure at inlet as solution proceeding (last 100 iterations)	144
Figure 4.4.21 Variation of wall shear stress 0.5m downstream of swirl pipe with iteration number (last 100 iterations)	144
Figure 4.4.22 Histogram of mass imbalance	145
Figure 4.4.23 Variation of mass imbalance (inlet-outlet) as solution was proceeding (last 100 iterations)	145
Figure 5.1.1 Optimal Swirl inducing pipe and transition pipes	147
Figure 5.1.2 Two configurations of swirl pipes	150
Figure 5.2.1 Configuration of simulation geometries	151
Figure 5.3.1 Pressure drop across the two swirl pipes in flows with various inlet velocities	153
Figure 5.3.2 Tangential velocity distribution within the two swirl pipes for various inlet velocities	155
Figure 5.3.3 Swirl intensity distribution within the two swirl pipes for various inlet velocities	156
Figure 5.3.4 Swirl effectiveness variation within the two swirl pipes for various	

inlet velocities.....	157
Figure 5.3.5 Tangential velocity distribution downstream of the two swirl pipes for various inlet velocities	160
Figure 5.3.6 Swirl intensity variation downstream of the two swirl pipes for various inlet velocities.....	161
Figure 5.3.7 Tangential wall shear stress distribution downstream of the two swirl pipes for various inlet velocities.....	162
Figure 5.3.8 Non-dimensional tangential WSS distribution downstream of the two swirl pipes for various inlet velocities.....	163
Figure 5.3.9 Axial wall shear stress distribution downstream of the two swirl pipes for various inlet velocities	164
Figure 5.3.10 Total wall shear stress distribution downstream of the two swirl pipes for various inlet velocities	165
Figure 6.2.1 Configuration of simulation geometry	168
Figure 6.3.1 Static pressure variation in the horizontal pipe system for various inlet velocities.....	170
Figure 6.3.2 Tangential velocity (m/s) distribution within and downstream swirl pipe for various velocities	173
Figure 6.3.3 Classification of swirl types (After Steenbergen and Voskamp, 1998)	174
Figure 6.3.4 Tangential velocity profiles in radial direction (2m/s inlet velocity)	174
Figure 6.3.5 Tangential velocity variation downstream of swirl pipe exit....	175
Figure 6.3.6 Correlation of initial tangential velocity with inlet velocity	176
Figure 6.3.7 Correlation of swirl pipe effect distance with inlet velocities...	177
Figure 6.3.8 Swirl intensity variation downstream of swirl pipe exit.....	179
Figure 6.3.9 Correlation of swirl decay rate with Reynolds number.....	179
Figure 6.3.10 Tangential WSS variation downstream of swirl pipe exit	182
Figure 6.3.11 Non-dimensional tangential WSS variation downstream of swirl pipe exit.....	183

Figure 6.3.12 Axial wall shear stress variation downstream of swirl pipe exit	184
Figure 6.3.13 Axial velocity profiles in radial direction (2m/s velocity)	185
Figure 6.3.14 Correlation of average axial WSS with Reynolds number	185
Figure 6.3.15 Contours of WSS at interior wall of swirl pipe and downstream for inlet velocities of 1m/s, 1.5m/s, 2m/s, 2.5m/s, 3m/s respectively from top to bottom	188
Figure 6.3.16 Circular distribution of WSS at 0.5m, 1m, and 1.5m downstream of swirl pipe exit (2m/s inlet velocity)	189
Figure 6.3.17 Contours of axial and tangential velocity at cross-flow planes 0.5m, 1m, and 1.5m downstream of swirl pipe exit (2m /s inlet velocity) ..	189
Figure 6.3.18 Wall shear stress variation downstream of swirl pipe exit for various inlet velocities	191
Figure 7.3.1 Fine grid in the near wall region of cylindrical pipe and swirl pipe for LES.....	202
Figure 7.3.2 y^+ contours of computational domain geometry for LES (2m/s inlet velocity)	203
Figure 7.3.3 Comparison of wall shear stress distribution for various SGS models and RANS (2m/s inlet velocity)	206
Figure 7.3.4 Comparison of tangential velocity distribution for various SGS models and RANS (2m/s inlet velocity)	208
Figure 7.4.1 Comparison of axial and tangential velocity contours obtained by RANS and LES (2m/s inlet velocity)	210
Figure 7.4.2 Velocity vectors in cross-flow planes 0.2m, 0.5m and 1m downstream of the swirl pipe (2m/s inlet velocity)	211
Figure 7.4.3 Pathline of swirl flow downstream of swirl pipe showing vortices (2m/s inlet velocity)	212
Figure 7.4.4 The four curved axes about which the four vortices rotate	213
Figure 7.4.5 Static pressure variation in the flow system for various inlet velocities predicted by LES and RANS	215

Figure 7.4.6 Tangential velocity variation downstream of swirl pipe exit for LES and RANS.....	217
Figure 7.4.7 Swirl intensity variation downstream of swirl pipe exit for LES and RANS (1m/s inlet velocity).....	218
Figure 7.4.8 Swirl intensity variation downstream of swirl pipe exit for LES and RANS (1.5m/s inlet velocity)	219
Figure 7.4.9 Swirl intensity variation downstream of swirl pipe exit for LES and RANS (2m/s inlet velocity).....	219
Figure 7.4.10 Swirl intensity variation downstream of swirl pipe exit for LES and RANS (2.5m/s inlet velocity)	220
Figure 7.4.11 Swirl intensity variation downstream of swirl pipe exit for LES and RANS (3m/s inlet velocity).....	220
Figure 7.4.12 Swirl intensity decay trend downstream of swirl pipe exit obtained by LES for various inlet velocities.....	222
Figure 7.4.13 Contours of instantaneous wall shear stress in swirl pipe and circular pipes obtained by LES for inlet velocities of 1m/s, 1.5m/s, 2m/s, 2.5m/s, 3m/s respectively from top to bottom.....	224
Figure 7.4.14 Contours of time averaged wall shear stress in swirl pipe and circular pipes obtained by LES for inlet velocities of 1m/s, 1.5m/s, 2m/s, 2.5m/s, 3m/s respectively from top to bottom.....	225
Figure 7.4.15 The four vortex core regions within swirl pipe and downstream circular pipe for inlet velocities of 1m/s, 2m/s and 3m/s respectively from top to bottom.....	227
Figure 7.4.16 Wall shear stress variation downstream of swirl pipe exit obtained by LES and RANS for various inlet velocities	228
Figure 7.4.17 wall shear stress variation over time at circumferences of the swirl pipe exit and its downstream (3m/s inlet velocity).....	229
Figure 7.4.18 Variation of normalized wall shear stress fluctuation rate in swirl and circular pipes (1m/s inlet velocity)	231
Figure 7.4.19 Variation of normalized wall shear stress fluctuation rate in swirl	

and circular pipes (1.5m/s inlet velocity)	231
Figure 7.4.20 Variation of normalized wall shear stress fluctuation rate in swirl and circular pipes (2m/s inlet velocity).....	232
Figure 7.4.21 Variation of normalized wall shear stress fluctuation rate in swirl and circular pipes (2.5m/s inlet velocity)	232
Figure 7.4.22 Variation of normalized wall shear stress fluctuation rate in swirl and circular pipes (3m/s inlet velocity).....	233
Figure 8.3.1 Schematic diagram and layout of the experimental rig.....	242
Figure 8.4.1 Demonstration of the investment casting process for optimised swirl pipe.....	245
Figure 8.5.1 Swirl pipe, pressure transmitter, magnetic flow meter and squirrel data logger	247
Figure 8.5.2 Pressure drop versus flow velocity for 1m cylindrical+0.4m swirl pipe+4m cylindrical pipe	250
Figure 8.5.3 Comparison of the pressure drop in swirl flow obtained by experimentation and CFD.....	251
Figure 8.5.4 Crevices in the cylindrical/cylindrical and swirl/cylindrical connections; internal surface roughness of swirl pipe	253
Figure 8.5.5 Pressure drop versus flow velocity for 1m cylindrical+0.4m control pipe+4m cylindrical pipe	255
Figure 8.5.6 Comparison of the pressure drop in cylindrical pipe flow obtained by experimentation and the Darcy–Weisbach equation	256
Figure 8.5.7 Demonstration of the calculation of pressure drop across the swirl pipe only by subtraction.....	257
Figure 8.5.8 Pressure drop across swirl pipe only obtained by experimentation and CFD for various flow velocities	259
Figure 8.5.9 Comparison of Pressure Loss across optimised swirl pipe with previously used swirl pipes.....	260
Figure 8.6.1 Glue-on hot-film probe and MiniCTA 54T42	263
Figure 8.6.2 Allocation of the hot-film sensor at the five points on the	

circumference	265
Figure 8.6.3 Measurement flow chart for sensor calibration.....	267
Figure 8.6.4 Calibration of hot-film sensor (sensor at top)	268
Figure 8.6.5 Calibration of hot-film sensor (sensor at +45°)	269
Figure 8.6.6 Calibration of hot-film sensor (sensor at middle)	269
Figure 8.6.7 Calibration of hot-film sensor (sensor at -45°)	270
Figure 8.6.8 Calibration of hot-film sensor (sensor at bottom).....	270
Figure 8.6.9 Measurement procedure for wall shear stress.....	271
Figure 8.6.10 Mean wall shear stress downstream of swirl pipe for various flow velocities.....	273
Figure 8.6.11 Mean wall shear stress downstream of control pipe for various flow velocities	273
Figure 8.6.12 Comparison of mean wall shear stress downstream of swirl pipe obtained by experimentation and CFD models	276
Figure 8.6.13 Flow direction in the near wall region of swirl flow.....	278
Figure 8.6.14 Examples of wall shear stress fluctuation downstream of swirl pipe measured by hot-film probe	280
Figure 8.6.15 Normalized voltage fluctuation rates downstream of swirl pipe for various flow velocities	282
Figure 8.6.16 Normalized voltage fluctuation rates downstream of control pipe for various flow velocities	282
Figure 8.6.17 Comparison of the normalized fluctuation rate of voltage signals under swirl flow and non-swirl flow conditions	283

LIST OF TABLES

Table 2.1.1 Effects of chemical and hydraulic (or physical) processes on soil removal (after Graßhoff 1997)	13
Table 4.4.1 Y^+ value for different sections of the geometry at different inlet velocities	126
Table 4.4.2 A summary of the mesh independence test results	128
Table 4.4.3 Skewness ranges and cell quality	129
Table 4.4.4 Skewness ranges and cell quality	130
Table 4.4.5 Simulation conditions at inlet	134
Table 5.2.1 Models and parameters used for the simulations	151
Table 5.3.1 Comparison of the two swirl pipe in swirl induction	153
Table 6.2.1 Simulation conditions at inlet	169
Table 6.3.1 The unit length pressure losses for swirl and circular pipes	170
Table 6.3.2 Swirl decay rate calculated in terms of friction factor	179
Table 8.5.1 Flow velocities at which pressure drop measurements were performed	247
Table 8.5.2 Pressure drop across 1m cylindrical+0.4m swirl pipe+4m cylindrical pipe for various velocities	249
Table 8.5.3 Mean experimental pressure drop in swirl flow and comparison to CFD	249
Table 8.5.4 Pressure drop across 1m cylindrical+0.4m control pipe+4m cylindrical pipe for various velocities	254
Table 8.5.5 Mean experimental pressure drop in cylindrical pipe flow and comparison to Darcy–Weisbach equation	254
Table 8.5.6 Comparison of the experimental pressure drop across the swirl pipe only with the RANS and LES results	258
Table 8.6.1 Mean wall shear stress downstream of swirl pipe and control pipe for various flow velocities	274
Table 8.6.2 Comparison of mean wall shear stress in swirl flows obtained by experimentation and CFD models	275

NOMENCLATURE

A	Area	m^2
A_H	Material dependent Hamaker constant	
C_D	Drag coefficient	
C_μ	Dimensionless constant	
C_w	Empirical constant (0.15)	
C_s	Smagorinsky constant	
d	particle diameter	m
D	Pipe diameter	m
d_h	Hydraulic diameter	m
E	Wall functions empirical constant (= 9.793)	
E_a	Acquired voltage output from Constant Temperature Anemometry	v
E_{corr}	Corrected voltage	v
f	Fanning friction factor of the pipe	
f'	Moody friction factor ($f' = 4f$)	
g	the gravitational acceleration	m/s^2
I	Turbulence intensity	%
k	Turbulent kinetic energy	m^2/s^2
K_s	Wall roughness height	m
L	Length of pipe corresponding to pressure loss	m
l	length scale of the large-scale turbulence	
m	Particle mass	kg
M_D	Moment of the surface stresses	N·m
p	Wetted perimeter	m
p	Static pressure	pa
Q_{EAS}	Equi-Angle Skew, a normalised measure of mesh skewness	

R	Pipe radius	m
r	Radius at point where tangential velocity is calculated	m
Re	Reynolds number	
Re_p	Particle Reynolds number	
S	Swirl number or swirl intensity	
S_0	Initial swirl intensity	
T_w	Sensor hot temperature (60°C)	°C
T_0	Ambient reference temperature related to the last acquisition	°C
T_a	Ambient temperature during acquisition	°C
u	Flow velocity	m/s
u	Axial velocity	m/s
u'	Root-mean-squared of velocity fluctuation	m/s
U	Mean flow velocity	m/s
U^*	Dimensionless velocity	
u_τ	Friction velocity, defined as $\sqrt{\frac{\tau_w}{\rho}}$	
V	Average velocity of the fluid flow	m/s
V	Particle volume	m ³
v	Velocity scale of large-scale turbulence	
w	Tangential velocity	m/s
x	Distance downstream of swirl pipe	m
y	Normal distance to the wall	m
y^+	Non-dimensional distance of a point from the wall $= \frac{\rho y u_\tau}{\mu}$	
z_0	Particle-to-surface distance	m
α	Empirical coefficient	
β	Swirl decay rate parameter = $\alpha \cdot f'$	
Δ	Filter cutoff width	m
ΔP	Pressure loss due to friction in pipe	pa

ε	Turbulence dissipation rate	
λ	Friction factor for fully developed flow	
κ	Von Kármán constant (= 0.4187)	
μ_t	Turbulent viscosity	kg/ms
μ	Dynamic viscosity	kg/ms
ρ	Fluid density	kg/m ³
τ_w	Wall shear stress	pa
$\tau_{w\theta}$	Tangential wall shear stress	pa
$\tau'_{w\theta}$	Non-dimensional tangential wall shear stress	
Ω_{ij}	Vorticity	s ⁻¹

Abbreviations

CFD	Computational Fluid Dynamics
CIP	Clean-In-Place
CTA	Constant Temperature Anemometer
CMC	Carboxymethyl cellulose
CCD	Charge Coupled Device
DNS	Direct numerical simulation
EHEDG	European Hygienic Equipment Design Group
ERT	Electrical Resistance Tomography
FDM	Finite-Difference Method
FVM	Finite-Volume Method
FEM	Finite-Element Method
ICEM CFD	The Integrated Computer Engineering and Manufacturing code for Computational Fluid Dynamics
LES	Large Eddy Simulation
LDV	Laser Doppler Velocimetry
LDA	Laser Doppler Anemometry
PRESTO!	PREssure STaggering Option

PISO	Pressure-Implicit with Splitting of Operators
PIV	Particle Image Velocimetry
PDA	Phase Doppler Anemometry
PVC	Precessing vortex core
QUICK	Quadratic Upstream Interpolation for Convection Kinetics
RSM	Reynolds Stress model
RNG	Renormalization group
WMLES	Algebraic Wall-Modeled LES Model

CHAPTER 1: INTRODUCTION

1.1 General Introduction

At the University of Nottingham (UK), research into design and optimisation of swirl induction pipes has been taking since 1993. Early emphasis concentrated on the physical effects of swirl section, later research was directed toward optimizing the swirl pipe configuration, number of lobes, pitch to diameter ratio and transition pipes. Currently, a number of potential applications have been identified for swirl pipes and the advantages of applying swirl pipes have been investigated through experimental work and Computational Fluid Dynamics (CFD) modelling.

Previous researchers have shown that a *Swirly-Flo* pipe before a bend can reduce wear and produce better particle distribution through the bend (Raylor, 1998, Wood et al., 2001). A three-lobed helix pipe applied in pneumatic transport locally increased the conveying velocity and produced an improved particle distribution across the downstream section of the horizontal pipe (Fokeer, 2006). Ariyaratne (2005) further optimized a four-lobed near-optimal swirl pipe recommended by Ganeshalingam (2002) by adding a transition pipe either prior to or after the near-optimal swirl pipe providing a gradual transition from circular to lobed cross-section and vice versa . The swirl pipe was applied to hydraulic transport and the induced swirl flow was found to provide better particle distribution and prevent solids dragging along the bottom of the pipe.

Another potential application identified for swirl pipe was the cleaning of pipes. It is well documented and proven by previous research on swirl pipes that the tangential velocity component imparted upon swirl flows effectively sweeps and lifts deposited particles in the bottom of the pipe into the main stream (Heywood

and Alderman, 2003, Fokeer, 2006, Ariyaratne, 2005). It is expected that the swirl flow induced by the swirl pipe can potentially intensify hydrodynamic impact on pipe surface and consequently increase cleaning efficiency downstream of it. Though the beneficial effects of swirl pipes have been proven in wear prevention, in pneumatic and hydraulic transport, the relation of geometrically induced swirl flow and the cleaning of pipe surface in a closed processing system is not clear, and it is not entirely understood how the swirl pipe and the system it is applied to operate.

Therefore, this research aims to investigate the hydrodynamic potential of an optimized 4-lobed swirl pipe on improving cleaning efficiency in a closed processing system.

Rapid and effective cleaning of closed processing systems is very important in many industries, especially in the beverage and food industries where production lines are cleaned daily to maintain both high heat transfer rates and low pressure drops in heat treatment units and more importantly, to ensure the appropriate level of microbial quality and thus the safety of the products (Lelièvre et al., 2002, Jensen et al., 2005). In many cases, the only practical way to clean closed processing systems is by using Clean-In-Place (CIP) procedures which is a method of cleaning the interior surfaces of pipes, vessels, process equipment and associated fittings, without disassembling them (Friis and Jensen, 2002). Efficient CIP processes will result not only in reduced downtime and costs for cleaning but also decreased environmental impact (in the disposal of spent chemicals) (Gillham et al., 1999).

Researchers have shown that in some areas some bacteria may remain on equipment surfaces after standard CIP procedures (Elevens et al., 1999, Lelièvre et al., 2002). Traditional methods of improving CIP efficiency include increasing the overall cleaning fluid velocity, the concentration and temperature

of the cleaning chemical and longer running time. For a company these methods increase costs and downtime, reducing production efficiency, and for the environment it is an additional load due to the extra chemical consumption.

Due to the fact that CIP cleaning is typically performed at constant flow rates throughout the system, and the cleaning time is decided based on the criteria that the area most difficult to clean must be cleaned at the end of the process. One of the concerns related to improvement of cleaning efficiency is finding a way to locally increase the hydrodynamic force of cleaning fluid acting at the fluid/equipment interfaces without increasing the overall cleaning fluid velocity. Swirl pipe may serve as an alternative approach to achieve this condition without consuming considerably more energy.

The advantage of swirl pipe, especially after transition pipe is added, over other swirl generation devices is that it has minimal intrusion to the flow. The swirl motion is geometrically induced to the downstream by the spiral lobed cross-section of the swirl pipe which avoids the insertion of any objects which would otherwise be mounted inside the pipe, such as blades, helical ribs and honeycomb structures that might contribute to problems regarding the fouling and cleaning of the pipes. Moreover, with the introduction of transition pipes, the swirl pipe is easier to connect to a circular pipe than other devices. However, swirl pipes cause a higher pressure loss than circular pipes and the acquired swirl pattern decays downstream along the pipe. Therefore, excessive use of swirl pipes to increase hydrodynamic effects indiscriminately for the whole pipeline may be too costly. Localized intervention of the swirl pipe should prove to be more cost effective.

Despite the large body of literature on the swirl flows and their applications, there is still a lack of understanding of geometrically induced swirl flow involved in pipe cleaning. In the studies of CIP, most published work utilizes flows

parallel to a test surface and experiments have been mainly performed in the laminar flow regime (Friis and Jensen, 2002). The use of geometrically induced turbulent swirl flow in the pipe cleaning industry is still lacking attention. The unique contribution of this thesis to the literature is the application of geometrically induced swirl flow induced by an optimized four-lobed swirl pipe to CIP procedures in order to increase cleaning efficiency in closed processing systems without increasing the overall flow velocity. In doing so, this study provides better understanding of the fluid dynamics of the geometrically induced swirl flow, especially in the boundary layer where cleaning takes place.

1.2 Aims and Objectives

The primary focus of this study is to investigate the potential of a swirl flow induced by an optimized 4-lobed swirl pipe on improving cleaning efficiency of closed processing systems by locally increasing hydrodynamic effects downstream of it without increasing the overall velocity.

The intention of the research is to:

- Complete a comprehensive literature survey on factors influencing cleaning efficiency in closed processing system especially the hydrodynamic effects of cleaning fluid, the hydrodynamic properties of swirl flows and its applications, the experimental and modelling techniques used by current and previous researchers to gain knowledge of methodology.
- Create and optimize the 3D geometry of a 4-lobed swirl pipe and produce a stainless steel casting prototype for experimental work.
- Establish a steady state CFD model through RANS approach to obtain averaged value of the geometrically induced swirl flows in terms of its tangential velocity, swirl intensity, swirl decay rate and the wall shear stress exerted on the pipe surface.

- Carry out Large Eddy Simulations and provide insight into the unsteadiness of wall shear stress of the swirl flows.
- Build a hydraulic rig and validate the CFD results using experimentally measured pressure loss and wall shear stress.

1.3 Thesis Outline

This thesis consists of 9 chapters. The following gives a brief description of each chapter contained.

The current chapter, Chapter 1 gives a general background context and motivation against which this study was carried out, the aims and objectives of this work and the outline structure of the thesis.

Chapter 2 is a literature review concerning the required knowledge of two topics, namely the cleaning of closed processing system and studies on swirl flows. In this chapter, the definition of Clean-In-Place and the factors influencing its efficiency especially the hydrodynamic factors of the cleaning fluid are conveyed. Previous research on swirl pipes is summarized. The important terms and equations for swirl flow are explained. The techniques in terms of swirl flow modelling and measurement are reviewed.

Chapter 3 details the calculation and geometry creation process of a transition pipe and a swirl inducing pipe. Based on the calculation, the spreadsheets that include necessary data for the sketch of cross-sections of transition and swirl inducing pipe are generated. The cross-sections are swept and blended into transition and swirl inducing pipe respectively using the software Pro/Engineer. The optimised 4-lobed swirl pipe, which was not tested previously, is defined.

Chapter 4 covers the computational fluid dynamics methodology involved in

modelling turbulent flow. The discussion focuses mainly on the Reynolds-averaged Navier–Stokes (RANS) approach. The turbulence models for RANS, discretization schemes and meshing of the pipe geometries are presented. The general set up of the simulation models used for RANS modelling are summarized.

Chapter 5 focuses on further optimisation of the 600mm length 4-lobed swirl pipe by shortening the length of its swirl inducing pipe section (resulting in a 400mm length swirl pipe). A numerical comparison of the horizontally mounted four-lobed 600mm length swirl pipe and the further optimised 400mm length swirl pipe in terms of swirl induction effectiveness into flows passing through them is presented.

Chapter 6 presents a computational fluid dynamics model (RANS approach) of the swirl flows that is induced in a fluid flow passing through the horizontally mounted optimized 400mm length swirl pipe. Pressure loss, tangential velocity, swirl type, swirl intensity and its decay rate of the swirl flow are investigated in flows with various inlet velocities. Special attention is paid to the potential of the swirl flow on improving 'Clean-In-Place' efficiency by locally increasing the mean wall shear stress downstream of the swirl pipe without increasing inlet velocity.

In Chapter 7, Large Eddy Simulations (LES) are carried out in order to see the unsteadiness of the geometrically induced swirl flow downstream of the optimised 400mm swirl pipe. The fluctuation rate of wall shear stress in the sections along the pipe are calculated and compared. In order to avoid intensive literature review on CFD method in Chapter 4, definitions and models regarding LES approach are presented in this Chapter.

Chapter 8 concerns the establishment of the experimental hydraulic rig and the

validation of the simulation results, mainly the pressure loss and the wall shear stress variation downstream of the swirl pipe. The measured pressure loss for a series of flow velocities are compared to the predicted results. A glue-on hot film is calibrated and used to measure the mean value and the fluctuation rate of the wall shear stress downstream of the swirl pipe. The experimental results are compared to the RANS and LES results. The sources associated with experimental errors are discussed.

Finally, Chapter 9 draws together the conclusions from computational and experimental research in this thesis and discusses the implications of the present findings for research and practice. Possible future work to advance the present research are suggested and discussed.

CHAPTER 2: LITERATURE REVIEW

2.1 Cleaning of Closed Processing Pipe System

2.1.1 Fouling of Pipe Surface

Fouling problems of the pipe surface in closed processing systems are common in many industries. For instance, in oil transportation industry, wax deposition on the inner walls of crude oil pipelines presents a costly problem in the production and transportation of oil. The timely removal of deposited wax is required to address the reduction in flow rate that it causes, as well as to avoid the eventual loss of a pipeline in the event that it becomes completely clogged (Aiyejina et al., 2011).

Rapid and effective cleaning of closed processing pipe systems is especially important in food industries. Protein in milk processing systems (Changani et al., 1997), yeast, bacteria and beer stone on the inside of beer tubing systems (MATIC, 2010) can decrease the heat transfer rate, increase the pressure in heat treatment unit, and more over affect the quality and flavour of the product.

Another common problem in closed processing pipe system is the formation of biofilms, as biofilms grow wherever there is water (SpiroFlo, 2010). Biofilms are a collection of microorganisms surrounded by the slime they secrete, attached to the pipe surface (Dreesen, 2003). For closed systems, biofilm geometry is mainly a two dimensional structure which is often composed of patches (cells, exopolymers, and food residues) and/or isolated cells (PathogenCombat, 2011). Within the protective slime, the bacteria build communities to take apart and consume nutrients that no single bacteria could break down alone. In addition, the biofilms concentrate nutrients with polymer webs in order to survive despite

water purification tactics. This highly efficient combination makes the bacteria in the biofilm a near self-sufficient community. (Dreesen, 2003, SpiroFlo, 2010, Coghlan, 1996).

More than 99% of all bacteria live in biofilm communities but some can be beneficial. For instance, sewage treatment plants rely on biofilms to remove contaminants from water. However, biofilms can also cause problems by corroding pipes, clogging water filters, causing rejection of medical implants, and harbouring bacteria that contaminate food in processing systems. This in turn can create a hazard to food quality and human health (Dreesen, 2003). Efficient cleaning of fouling in processing systems is vital in food industries.

2.1.2 Clean In Place

In the food and beverage industries, production lines are often cleaned daily to maintain both high heat transfer rates and low pressure drops in heat treatment units and more importantly, to ensure the appropriate level of microbial quality and thus the safety of the products (Lelièvre et al., 2002, Jensen et al., 2005). In many cases, the only practical way to clean closed processing systems is by using Clean-In-Place (CIP) procedures. CIP is a method of cleaning the interior surfaces of pipes, vessels, process equipment and associated fittings, without disassembling them (Friis and Jensen, 2002). A closed food processing system is defined as one which is built of pipe works, pumps, valves, heat exchanger, etc. and tanks for the purpose of processing food products (PathogenCombat, 2011). The common ground for closed processing systems is that the primary cleaning method applied is CIP (PathogenCombat, 2011, Changani et al., 1997).

CIP is usually performed through the circulation of formulated detergents. This typically involves a warm water rinse, washing with alkaline and/or acidic solution, and a clear rinse with warm water to flush out residual cleaning agents

(Dev et al., 2014). Efficient CIP processes will result not only in reduced downtime and costs for cleaning but also reduced environmental impact (in the disposal of spent chemicals) (Gillham et al., 1999). Industries that rely heavily on CIP are those requiring frequent internal cleaning of their processes to meet the high levels of hygiene. These include: dairy, beverage, brewing, processed foods, pharmaceutical, and cosmetics industries. The benefit to industries by using CIP is that the cleaning is faster, less labour intensive, more repeatable and reproducible, and poses less chemical exposure risks to people.

2.1.3 Cleaning Efficiency

Cleaning is a complex operation with its efficiency depending on many factors, e.g. the soil to be removed, cleaning time, temperature of the cleaning agent and the hydrodynamic force of the moving liquid (Lelieveld et al., 2003, Jensen et al., 2005).

Lelièvre et al. (2002a) reported that soil removal is obviously affected by cleaning conditions such as the nature of cleaning agent, its concentration, its temperature, its contact time with surfaces, and lastly, the favourable effect of hydrodynamics. These factors mentioned are also reported in the studies of Changani et al. (1997) and Sharma et al. (1991).

According to PathogenCombat (2011), a large European research project looking at safe food production, cleaning efficiency depends on four energy factors as presented using Sinners Circle (Figure 2.1.1). The factors are:

- Mechanical energy (or hydrodynamic effect) to physically remove soil
- Chemical action from detergents to dissolve soil in order to facilitate removal
- Thermal energy - the cleaning temperature
- Cleaning time

An efficient combination of those factors varies depending on the type of soil and the severity of the fouling. The idea is that a restriction in one factor may be compensated by increasing the effect of one or more of others.

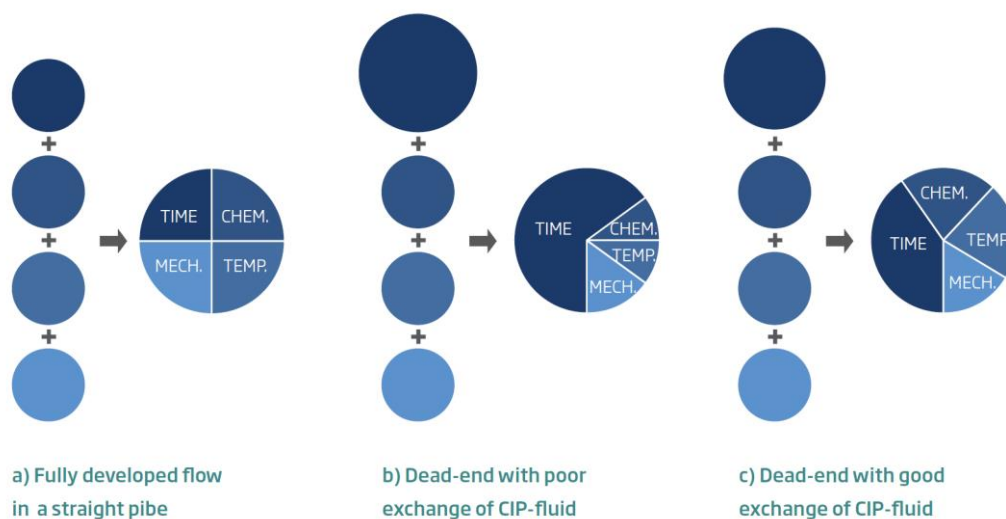


Figure 2.1.1 Sinner circles for three different cleaning situations (after PathogenCombat, 2011)

Figure 2.1.1 displays three different cleaning situations using Sinner's Circle to describe the relative importance of the four factors: the time, hydrodynamics, chemistry and temperature. The Sinner's circle does not explain the actual "amount" of each factor; it only indicates relative correlation between them.

Research established that the time taken to clean is a function of temperature, flow dynamics, and the cleaning chemical concentration. Other factors affect cleaning include the finish on the closed processing equipment surface, the geometry of the equipment, and the overall process design (Changani et al., 1997).

2.1.3.1 Cleaning Agent

Detergent and its operating temperature play an important role in CIP procedure. Lelièvre et al. (2002a) investigated the respective contribution of both cleaning agent (sodium hydroxide 0.5%) and mechanical action of the fluid

flow on the cleaning efficiency. The trial was carried out in stainless steel pipes soiled by *B. cereus* spores under static conditions. They concluded that the sodium hydroxide and the wall shear stress have a combined action on the spore removal. The cleaning agent induced a decrease in the adhesion strength of *B. cereus* spores, ensuring their removal when a wall shear stress is applied since the hydrodynamic forces become greater than the adhesion force (Bergman and Trägårdh, 1990, YIANTSIOS and KARABELAS, 1995).

This conclusion was also supported by other researchers. Visser (1995) stated the removal of colloid particles is controlled by the wall shear stress, but the presence of a cleaning detergent ensures a decrease in the adhesion force and, consequently, improves the removal of these particles. Sharma et al. (1991) also found that high concentration of sodium hydroxide (high pH values as with sodium hydroxide) was found to induce a decrease in the adhesion force of colloids to surface. According to Hall (1998), mechanical action and cleaning agent were fully linked to ensure a complete removal of a biofilm of *Pseudomonas fragi*.

Graßhoff (1997) summarizes the contributions of chemical and hydraulic factors to soil removal as shown in Table 2.1.1. Table 2.1.1 was based on the consideration that cleaning of protein with NaOH-based solutions involved three stages, namely deposit swelling, uniform erosion and a final decay phase. In the swelling stage, the deposit swells on contact with alkali to form an open protein matrix of high void fraction; this 'uniform' swollen layer is removed by a combination of surface shear and diffusion in the erosion phase. The final 'decay' phase occurs when the swollen layer is thin and no longer uniform, and involves removal of isolated 'islands' by shear/mass transport. The process is complex and the interaction of NaOH with the protein matrix is concentration dependent (Gillham et al., 1999, Graßhoff, 1997, Bird and Fryer, 1991). The rate of cleaning in the breakdown stage is more sensitive to wall shear stress than

other stages, while the uniform stage is more sensitive to the temperature. The three stages of the cleaning process have been shown to be sensitive to different combinations of operating parameters and solution chemistry (Bird and Fryer, 1991).

Table 2.1.1 Effects of chemical and hydraulic (or physical) processes on soil removal (after Graßhoff 1997)

Factor	Effect
Chemical reaction /modification	Swelling of deposit matrix-change of voidage
	Dissolution-erosion
	Ageing-change in deposit composition and structure over time
Hydraulic action of reagent flow	Mass transfer of reagent and reaction products from deposit interface to bulk solution
	Lift-removal of particulate soil from surface
	Scouring-entrained particulates
	Surface shear stress-mechanical erosion

2.1.3.2 Adhesion Strength of Soil

According to Sharma et al. (1991), the adhesion strength of soil to pipe surface varies according to the material of soil, the contact area, particle diameter etc. Sharma et al. studied the effect of particle material on the release of particles from a glass surface. The two kinds of particles are ten-micrometre glass and polystyrene microspheres. It was observed that it is more difficult to displace polystyrene particles than glass microspheres. One explanation is that the polystyrene particles are much more deformable, giving rise to larger contact areas. The results suggested that particles with a smaller Young's modulus are more difficult to removal.

Sharma et al. calculated the values of contact radius for different particle

diameters for polystyrene and glass. The contact radii for polystyrene particles were found to be substantially larger than those for glass. It was also found that adhesive force increases with the particle diameter for both polystyrene and glass particles. However the adhesive force for polystyrene is significantly more than that of glass for all particle diameters.

The adhesion strength of soil to pipe surface is also affected by the flow condition under which it is formed. PathogenCombat (2011) found that biofilm resistance to flow during cleaning depends on the flow conditions during the build-up process. Figure 2.1.2 shows the difference between biofilm grown in three different conditions: static conditions, laminar flow and turbulent flow. The difference between the biofilm appearances is the direct result of different action of flow on bacterial growth. Dreesen (2003) also stated that how the biofilm layer reaches certain equilibrium thickness depends on the flow condition and nutrient level.

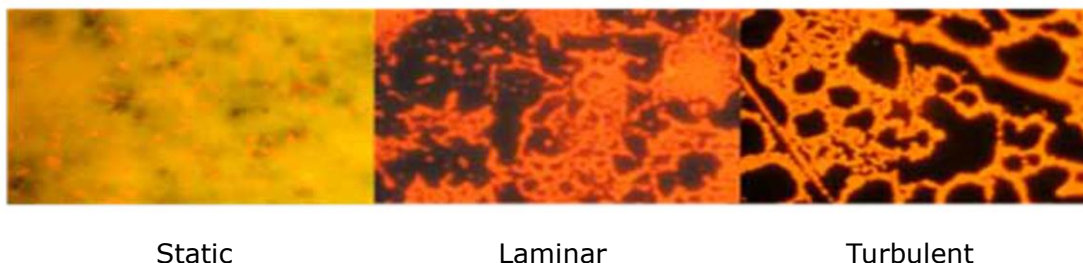


Figure 2.1.2 Microscope pictures of biofilm grown under three conditions (after PathogenCombat, 2011)

Other factors influence the adhesion strength of soil to pipe surface may include surface roughness of the equipment, and deposition time, which is the length of time for particles to settle at the equipment surface. (Sharma et al., 1991).

Since the adhesion strength between soil and pipe surface is determined by many factors, it is difficult to find a universal value for a certain category of soil. The adhesion strength value has to be related to a specific condition.

2.2 Hydrodynamic Effects of Cleaning Liquid

2.2.1 Hydrodynamic Factors

Investigations concerning the influence of the hydrodynamics of the flow on cleaning of surfaces in the food industry exposed to real-life flow conditions are still limited (Friis and Jensen, 2002).

Published work stated that cleaning efficiency depends, besides other criteria, on the hydrodynamic effect. The flow of detergent is an important factor in the cleaning of closed processing equipment. The cleaning liquid generates local tangential force acting on the soil on the surface and acts as a carrier for the chemicals and heat (Jensen et al., 2007). The shear force of the cleaning fluid at fluid/equipment interfaces are of importance in the cleaning mechanism. The removal kinetics is functions of fluid detergent velocity and of the wall shear stress (Gallot-Lavallée et al., 1984, Graßhoff, 1992, Visser, 1970, Sharma, 1991). In addition, the wall shear stress was proposed as a more local removal control parameter than the velocity (Paz et al., 2013, Paz et al., 2012).

Experimental studies have been performed in laminar regime and most of the studies conclude that the wall shear stress is the controlling factor for the rate and amount of microbial adhesion and removal (Duddridge et al., 1982, Powell and Slater, 1982, Fowler and McKay, 1980, Hall, 1998).

Lelièvre et al. (2002a) investigated the removal of *Bacillus cereus* spores on 304L stainless steel pipes. A simple model assuming a process combining removal and deposition during cleaning was established. The simple model was experimentally confirmed that the flow condition applied during soiling procedures has a significant effect on removal rate constant. In addition, the effective removal rate constant is significantly influenced by the wall shear

stress applied during cleaning.

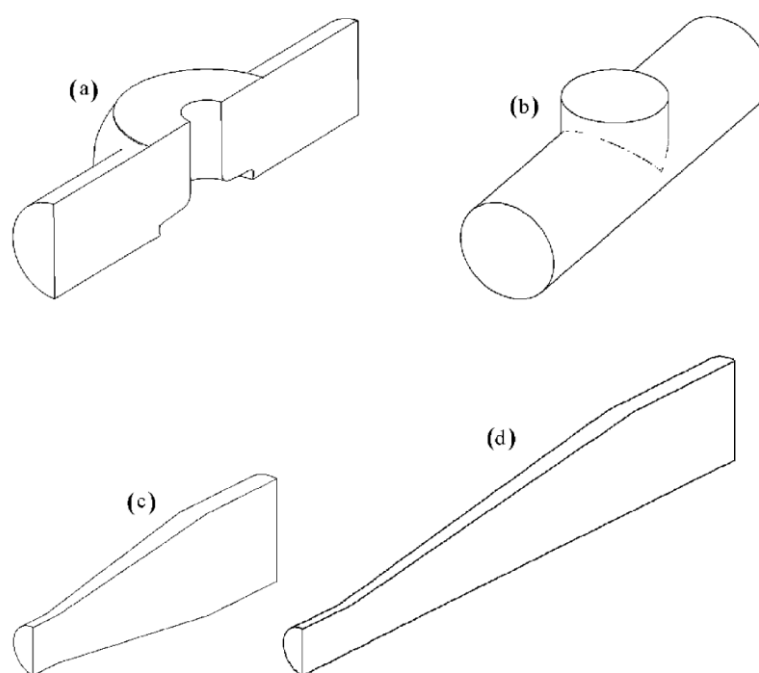
Lélievre et al. (2002) performed local wall shears stress analysis and cleanability experiments on different pieces of equipment made of stainless steel that represent production lines. In their study, the influence of the mean wall shear stress on bacterial removal was confirmed. The influence of loop arrangement was shown, particularly with the upstream effect of the gradual expansion pipe. Moreover, this work demonstrated the effect of the fluctuation rate on bacterial removal. It indicated that some low wall shear stress zones could be considered as cleanable because in these areas a high level of turbulence was observed, therefore, a high fluctuation rate. They therefore suggested that to predict cleaning, it is necessary to take into account not only the mean local wall shear stress, but also its fluctuation rate (Lelièvre et al., 2002). The presence of large wall shear stress fluctuation is because of flow pattern and hence, the geometry (Jensen et al., 2005).

Fluctuation rate of the wall shear stress was also studied by other researchers. Paulsson and Bergman's work (Paulsson and Trägårdh, 1989, Bergman and Trägårdh, 1990) showed that the mean wall shear stress has an influence on the removal of clay deposit but no influence of the fluctuation rate of the wall shear stress was demonstrated. Bénézech et al. (1998) compared experimental removal results (*Bacillus* spores in complex medium) with local measurements of wall shear stress made by Focke et al. (1985) in a corrugated plate heat exchanger. They concluded that the relevant parameter for cleaning efficiency was the fluctuation rate of wall shear stress.

Jensen et al. (2005) numerically investigated the test set-up of Lelièvre et al. (2002) in terms of wall shear stress and its fluctuation (in the form of turbulence intensity of the flow) using steady-state computational fluid dynamics (CFD) simulation adopting STAR-CD. A good correlation has been demonstrated

between CFD predictions and measured values of wall shear stress in discrete points by Lelièvre et al. (2002). The author suggested that a combination of the mean wall shear stress and the fluctuating part of the wall shear stress can be used for evaluating cleaning properties.

Friis and Jensen (2002) investigated the design of closed process equipment with respect to cleanability. Computational fluid dynamics was applied. The study of hydrodynamic cleanability of closed processing equipment was discussed based on modelling the flow pass through a valve house, an up-stand and various expansions in tubes as shown in Figure 2.2.1. The CFD simulations were validated using the standardized cleaning test proposed by the European Hygienic Engineering and Design Group.



(a) Upper mix-proof valve housing; (b) up-stand geometry with $h/D \approx 0.2$;
(c) 8.6° concentric expansion; (d) 8.6° eccentric expansion

Figure 2.2.1 Geometries used for showing the influence of flow patterns on the cleanability of equipment (after Friis and Jensen, 2002)

Their study showed that the wall shear stress was one of but not the sole parameter involved in the cleaning process of closed process equipment. The

nature of the fluid flow was also an important factor determining the cleaning efficiencies. It was found that the fluid exchange downstream of the up-stand was three times slower than in the main stream, which was caused by a recirculation zone in this area. Recirculation zones are known to be a problem. In the up-stand and tube expansion where the fluid exchanges in a steady recirculation is much slower than that in the main stream. The EHEDG test (Richardson et al., 2000) showed that tubes with recirculation were more difficult to clean. Friis and Jensen concluded that the wall shear stress plays a major role in cleaning of closed process systems. Another significant factor is the nature of recirculation zone presented. Steady recirculation zones such as the one found in the up-stand and concentric expansion can reduce cleaning efficiency. They further concluded that, since turbulent flow is often fully three-dimensional, this must be included in the CFD model. Therefore, three-dimensional modelling is recommended for complex geometries in order to predict the entire flow behaviour.

Jensen and Friis (2005) reported that the most difficult to clean areas are dead-ends and crevices in the geometry (resulting in recirculation zones) and shadow zones (resulting in stagnation points). In and around these features are low wall shear stress and fluid exchange (mass transfer), both of which reduce the cleaning efficiency. Fluid exchange in the cleaning area was also reported by PathogenCombat (2011), their study indicates that a combination of mean wall shear stress and fluid exchange is responsible for proper cleaning in complex geometries. Flow pattern, flow turbulence were also found to influence cleaning especially for complex geometries.

Hwang and Woo (2007) concluded that wall shear stress is of great importance in the fluid mechanics, as it represents the local tangential force by the fluid on a surface in contact with it. A laminar flow regime induces lower velocity gradients than a turbulent flow thus lower shear stress.

PathogenCombat (2011) stated that to improve cleaning efficiency, it is beneficial to promote turbulent flow or to introduce flow disturbance. These flow phenomena are advantageous during both production and cleaning. Turbulent flow is achieved at high flow rate (i.e. Reynolds number above 10,000). The alternative solution is to induce flow disturbances which locally may introduce flow patterns similar to turbulence and this way reduce residual contamination downstream.

Disturbances can be induced by geometry e.g. contractions, expansions or asymmetrical features as seen in a curvature or bend. PathogenCombat summarized methods to improve Cleaning-In-Place efficiency as following:

- Local enhancement of turbulence intensity and wall shear stress of flow
- Introduction of high mean wall shear stress
- Applying pulsating turbulent flow as a mean to break static flow patterns

Of the three methods proposed, swirl pipe may have the potential to locally enhance turbulence intensity and wall shear stress of cleaning flow.

Among the factors mentioned, the wall shear stress, which is a measure of the mechanical action of fluid flow on a process surface, is considered the dominating factor for cleaning. The effective removal rate is significantly influenced by the wall shear stress applied during cleaning (Lelièvre et al., 2002). The mean wall shear stress is especially relevant as a measure of cleaning efficiency in straight pipes, large parts of pumps, valves etc. In general, there is a threshold value of wall shear stress above which cleaning is considered efficient. The threshold is defined as the lowest mean wall shear stress sufficient to remove the specific type of soil or biofilm on the pipe surface (PathogenCombat, 2011). This so-called critical wall shear stress for removal of

specific microorganisms on various surfaces was also reported by Duddridge et al. (1982), Powell and Slater (1982), Fowler and McKay (1980), Jensen and Friis (2004) and, Bari and Veale (2012). For instance, Jensen and Friis (2012) suggested a critical wall shear stress of 3 Pa as a basis for their specific study. While Bari and Veale (2012) claimed that a wall shear stress as low as 0.15 Pa can be cleanable given a high fluctuation level.

The fluctuation rate of the wall shear stress was also reported to be important in the CIP efficiency. Some authors therefore suggested that to predict cleaning, it is necessary to take into account not only the mean local wall shear stress, but also its fluctuation rate (Friis and Jensen, 2002, Jensen et al., 2005, Bari and Veale, 2012, Lelièvre et al., 2002).

According to the literature, it is reported that, for straight circular pipes, the mean wall shear stress and its fluctuation are the dominating factors controlling cleaning. While for cleaning of more complex geometries and difficult to clean areas, the influencing factor may also include the flow pattern, flow exchange, flow turbulence, and the property of the recirculation zone.

Based on the understanding of swirl induction pipes which can locally change the flow pattern of the pipe flow, introduce greater turbulence into flow, enhance heat exchange at the wall, and induce higher velocity gradient at the wall, it is therefore positive that swirl pipe has the potential of enhancing cleaning efficiency.

2.2.2 Mechanism of Particle Detachment in Flow

Though investigations based on experiments and CFD simulation has shown the correlation of wall shear stress and soil cleaning. A theoretical basis of how the particle is detached from the surface is necessary to understand the cleaning

process and mechanism. A model proposed by Lorthois et al. (2001) and later was adopted by several other researchers was summarized in Appendix 2.1. This model demonstrates a positive correlation between the adhesion force that binds particles to the pipe surface and the wall shear stress of flow to remove particles.

2.3 Swirl Flow

2.3.1 Swirl Induction Pipes

Swirl flow in a pipe can be defined as a combination of vortex and axial motions, with helical streamlines (Baker and Sayre, 1974). Swirl flow, which contains a tangential velocity component, is always accompanied by an increase in velocity fluctuations (Fokeer, 2006, Algifri et al., 1988).

Swirl flows are usually used in gas turbine engines, furnaces, burners and cyclones with the purpose of heat transfer enhancement, mixing, separation etc. Generally three methods can be employed in order to generate swirl flows (Gupta et al., 1984):

- In method one as shown in Figure 2.3.1a, passing through a rotational section, fluid flow acquires tangential momentum and enters the pipe in the form of a swirling flow.
- In method two as shown in Figure 2.3.1b, fluid flow is introduced to the pipe through fixed blades (vanes), which are mounted inside of the pipe with a specified angle. In this case, the blades' angle appears as an effective parameter on flow field swirl intensity.
- In method three as shown in Figure 2.3.1c, fluid flow is introduced to the pipe by means of tangential inlet so that it can acquire rotational momentum and enters the pipe in the form of a swirling flow.

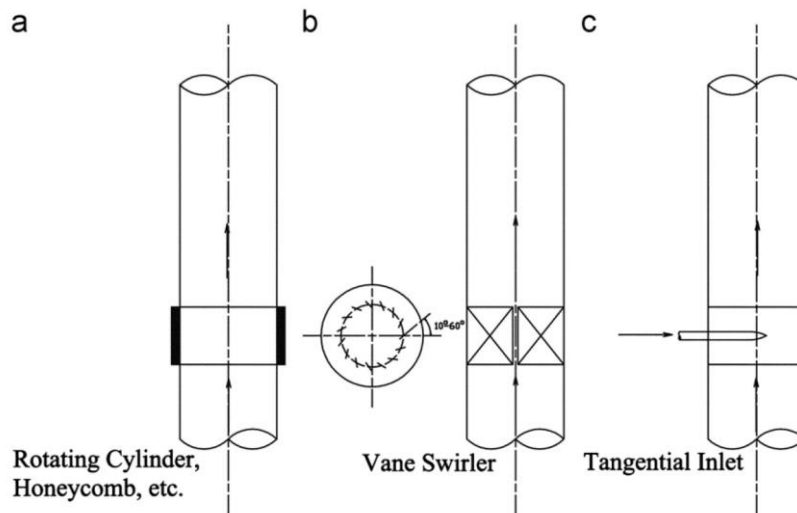


Figure 2.3.1 Three types of swirl generators (after Najafi et al., 2011)

Downstream of the swirl generator, the previously non-swirling flow is imparted a swirl velocity component known as tangential velocity component.

It is suggested that the radial distribution of tangential velocities is associated with the swirl generation methods (Kitoh, 1991). Steenbergen and Voskamp (1998) defined three different swirl types according to the radial distribution of tangential velocities as:

- Concentrated Vortex (CV)- rotation concentrated near the pipe centre
- Solid Body (SB)- almost uniform rotation
- Wall Jet (WJ)- angular momentum concentrated near the wall

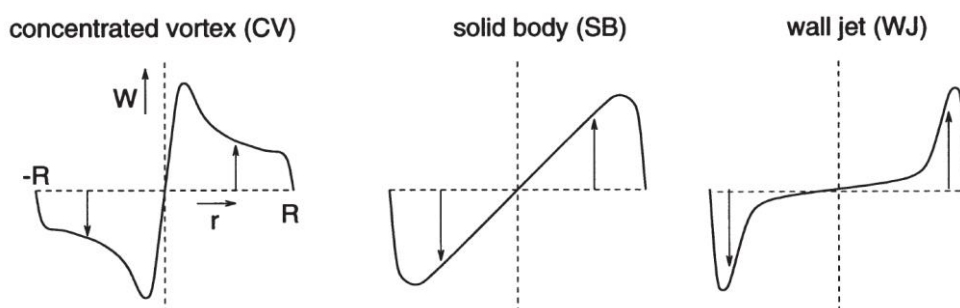


Figure 2.3.2 Classification of Swirl Types (After Steenbergen and Voskamp, 1998), corresponding to the three types of swirl generators

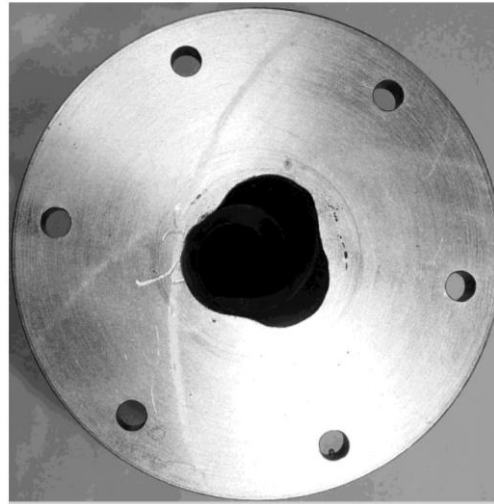
In addition to the three methods, swirl induction pipes with non-circular cross-sections have been investigated in order to induce swirl into flow passing through them. These included pipes with spiral ribs or fins located within the pipe (Robinson, 1921, Yuille, 1927, Wolfe, 1967, Charles et al., 1971, Schriek et al., 1974), pipes with rifles installed inside (Howard, 1939), and tubes with spiral grooves (Spanner, 1940). Those swirl induction pipes were applied respectively to mitigate the problem of subsiding and the deposit of particles in the pipe, improve tubular heat exchangers, reduce pipe wear, increase particle conveying efficiency, and save power. It should be noted that the insertions of ribs or fins mounted inside the pipe will be subject to direct impact from the particles in the flow giving rise to damage and wear of the pipe. Moreover, when applied in food or beverage industries, the insertions may contribute to problems regarding fouling and cleaning of the pipes.

At the University of Nottingham, research into helically formed swirl induction pipes can be traced back to 1993, when Jones suggested a new idea to the problem of settling particles in which a pipe section could be given a helical profile to promote suspension of particles at relatively low velocities (Jones, 1997). The idea was investigated later by Raylor (1998), Ganeshalingham (2002), Tonkin (2004), Ariyaratne (2005) and Fokeer (2006). It should be mentioned that the swirl induction pipes investigated avoid the use of insertions of ribs, fins or vanes inside the pipes. Rather it is the helically shaped geometry of the swirl pipe that force the fluid passing through it to rotate within itself and direct to downstream. A chronological review of their work is given below.

1998 (Raylor, 1998): Raylor's experimental investigation was based upon a swirl pipe found in marine boilers which are used to improve heat exchanger efficiency. The pipe, as shown in Figure 2.3.3, has the trade name '*Swirly-Flo* pipe'. Raylor's investigation aimed at pipe induced swirling flow to reduce wear and produce better distribution throughout a bend.



Longitudinal view



Cross-sectional view

Figure 2.3.3 *Swirly-Flo* pipe used by Raylor and Ganeshliangam (after Ganeshalingham, 2002)

Raylor used commercial CFD software Fluent to examine various pipe shapes and flow fields in swirl inducing pipe. He suggested that when the pitch to diameter ratio in a geodesic pipe decreased, the swirl produced increased with increasing pressure loss. Raylor designed an experimental rig and used water and plastic beads mixture to test the simulation results. He concluded that *Swirly-Flo* pipe produces an increase in pressure drop across its length compared to a standard pipe. *Swirly-Flo* pipe induced swirling flow before a bend produced less pressure drop across the bend than non-swirling flow for water and water/plastic beads mixture. Swirling particles before the bend ensured a more even distribution of particles throughout the bend which has the potential to remove the characteristic wear zone.

The pitch to diameter ratio ($P:D$) is an important parameter defining the character of the twisted swirl induction pipe. Pitch is defined as the axial distance travelled by the rib as it rotates through 360 degrees (Singh and Charles, 1976). This was the basis Raylor used for definition of the pitch of the swirl induction pipe.

2002 (Ganeshalingam, 2002): Ganeshalingam continued Raylor's investigation on the '*Swirly-Flo* pipe' and validated the CFD code used with results from Particle Image Velocimetry (PIV), Electrical Resistance Tomography (ERT) and pressure measurements. Ganeshalingam simulated the radial distribution of tangential velocities downstream of the *Swirly-Flo* pipe and it was shown to fit with 'Wall Jet' swirl type classified by Steenbergen and Voskamp (1998) according to radial distribution of tangential velocity field. An exponential decay of the swirl downstream of a swirl pipe was implied from CFD and the decay was reported to be faster at higher Reynolds number.

Ganeshalingam also carried out further optimisation of the swirl-inducing pipe using CFD and continued experimental work on solid-liquid mixture flows. Ganeshalingam tested various cross-sections (triangular, square, pentagonal, hexagonal and 2,3,4,5 and 6 lobed cross-sections) of pipe and concluded that the 4-lobed cross-section was most effective at swirl generation over the others. Ganeshalingam recommended a P:D ratio of 8 and 400mm of length as optimal for the 4-lobed pipe. This optimal swirl inducing pipe is shown in Figure 2.3.4 with its configuration being as follows:

- The swirl pipe has a 4-lobed cross-section.
- The 4-lobed cross-section extends helically around and along the pipe.
- Axial distance travelled by each lobe as it rotates through 360° is 400mm.
- The equivalent diameter of the swirl pipe is 50mm.
- Its pitch to diameter ratio is 8.

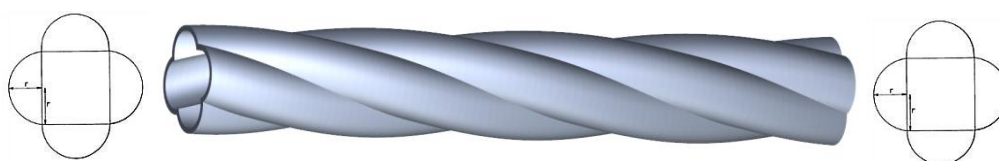


Figure 2.3.4 Optimal Swirl inducing pipe, 400mm length, P:D=8

This 4-lobed near-optimal design was further optimized and tested experimentally later by Ariyaratne (2005).

2004 (Tonkin, 2004): Tonkin investigated the application of the 4-lobed near-optimal swirl inducing pipe to various pipe configurations, when pumping a range of fluid and fluid/particle mixtures. Tonkin studied experimentally the effect of the 4-lobed near-optimal swirl inducing pipe on coal-water, sand-water and magnetite-water slurries of various particle sizes. The results showed that swirl induction produced greater benefit for denser slurries and higher concentrations. In addition, the swirl induced into slurries containing larger and denser particles was found to decay more rapidly.

Tonkin also investigated application of swirl inducing pipe to non-Newtonian (shear thinning) carrier liquids. A time independent fluid, CMC (carboxymethyl cellulose) was chosen to avoid changes in rheology as pumping time increased. PIV was used to measure the axial and tangential velocity of swirling flows downstream of the 4-lobed near-optimal swirl pipe with water and CMC. It was concluded that a significant tangential velocity was generated when pumping water in the turbulent regime, however, when the fluid viscosity was increased, leading to laminar flow, no significant tangential velocity was detected.

2005 (Ariyaratne, 2005): Ariyaratne further optimized the 4-lobed near-optimal swirl inducing pipe by designing a transition pipe for use as an entry and exit duct with the swirl inducing pipe, providing a gradual transition from circular to lobed cross-section and vice versa. The optimisation was carried out by using single-phase simulation employing Computational Fluid Dynamics. The CFD model was validated by experimental measurements of pressure loss. Transition pipes either before or after the swirl inducing pipe were found to reduce entry and exit pressure losses by providing a gradual transition from

circular to lobed cross-section. They also increased induced swirl and reduced swirl decay. Ariyaratne concluded that a β type transition with transition multiplier $n=0.5$ was optimum for both the entry and exit transition from several geometries tested. The configuration of transition pipe, as shown in Figure 2.3.5, is:

- The transition pipe's cross-section changes from a circular to a 4-lobed shape gradually.
- The areas of the cross-sections are constant and equal to that of the swirl pipe.
- The length of the transition pipe is 100mm, and each lobe rotates by 90° .
- Its pitch to diameter ratio is 8.

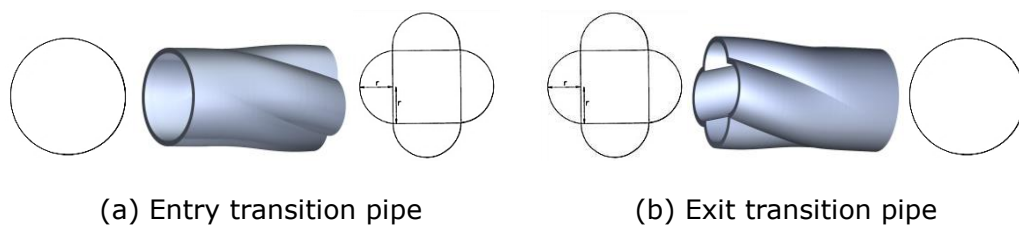


Figure 2.3.5 Transition pipes prior/after swirl inducing pipe

Ariyaratne suggested that the entry and exit transition should be an integral part of the swirl inducing pipe as it results in an efficient swirl induction which reduces energy costs from high pressure losses that otherwise occur due to sudden changes in flow geometry. Ariyaratne carried out settling slurry experiments, which showed that swirl induction resulted in better particle distribution and prevented solids dragging along the bottom of the pipe. This implies reduction in localised erosion and provides an opportunity to operate at lower flow velocities without blockage.

2006 (Fokeer, 2006): Fokeer investigated the application of geometrically induced swirl by a three lobed helix pipe on a lean phase of particulate

suspension in air along a horizontal pipe section. The research employed high speed photography, Particle Image Velocity (PIV), Laser Doppler Anemometry, and Computational Fluid Dynamics to obtain the characteristic of the air flow behaviour. It was concluded that the swirl pipe imparts a wall jet type swirl to both an air-only flow and a lean pneumatic flow with velocity and momentum shifts from axial to tangential closer to the wall. The swirl was found to decay proportionally with the distance downstream of the swirl pipe and inversely to the flow's Reynolds number. Additional pressure loss caused by the swirl pipe was found to be proportional to the Reynolds number of the flow and increased further with an addition of particles to the swirling flow.

Based on the suggestion of Ariyaratne (2005), a 400mm length swirl inducing pipe together with 100mm length entry and exit transition pipes at both ends as an integral pipe should be optimized in swirl induction. This optimised swirl pipe has a total length of 600mm (100mm+400mm+100mm). In this study, a further optimised swirl pipe that is comprised of a 100mm length entry transition pipe, half of the 400mm length swirl inducing pipe, and a 100mm length exit transition pipe is proposed. This further optimised swirl pipe has a total length of 400mm (100mm+200mm+100mm) which is 200mm shorter than Ariyaratne suggested. This further optimized 4-lobed swirl pipe is found numerically in Chapter 5 to be more cost-effective in swirl induction and is therefore used in this study.

2.3.2 Modelling Swirling Flow

2.3.2.1 Modelling turbulence

Swirl flow is turbulent and caused considerable degree of anisotropy in stress and dissipation tensor leading to a highly anisotropic eddy viscosity (Kitoh, 1991). Turbulent flows are characterized by fluctuations in velocity and pressure

in both space and time (Bhaskaran and Collins, 2003). In modelling swirling flow, turbulence is an important factor.

Many researchers have tried to numerically investigate swirl flow through Reynolds-averaged Navier–Stokes (RANS) approach adopting standard k - ϵ turbulence model and its variations (Renormalization Group (RNG) k - ϵ model and realizable k - ϵ model). In RANS approach, the Navier–Stokes equations are time averaged which gives rise to the Reynolds stresses to the time-averaged flow equations. These Reynolds stresses are modelled with classical turbulence models such as k - ϵ models (H.K.Versteeg and W.Malalasekera, 2010). The standard k - ϵ model solves two transport equations, one for the turbulent kinetic energy k , and one for the rate of its dissipation ϵ . These are then used to calculate the turbulent viscosity, μ_t , to close the Reynolds averaged Navier-Stokes equations (ANSYS, 2011a).

Launder and Spalding (1974) investigated the applicability of the k - ϵ model for simulating swirling flow along a twisted tape that was used to impart a swirling motion to a fluid to increase the surface transfer coefficient. The agreement was not very good. The main reason might be that the turbulent viscosity became strongly anisotropic in the complex strain field of the flow. Kobayashi and Yoda (1987) also argued that both k - ϵ model and its modifications with higher order terms in the Reynolds stress equation are not capable of predicting the axial and tangential velocity profiles in swirl flow because its eddy viscosity components are anisotropic. Similar conclusion was also reported by Nejad et al. (1989) that k - ϵ model is not successful in solving the velocity field in swirling flows.

Speziale et al. (2000) partially agreed with the above conclusion that traditional two-equation models such as the standard k - ϵ model with conventional near-wall treatments could not predict two critical effects (the rotationally dependent axial mean velocity and the presence of mean swirl velocity relative

to the rotating pipe) associated with turbulent flow in an axially rotating pipe. However, the author argued that at high Reynolds numbers, the traditional two-equation models could be used to predict this only with the implementation of a more sophisticated near-wall treatment that predicts a non-zero Reynolds shear stress $\tau_{r\theta}$. But this was not applicable to cases with low Reynolds number.

Bali (1998) proved that the k- ϵ turbulent model can successfully predict the weak swirl flow. In his study, the pneumatic swirling flow investigated has a small tangential velocity imparted to the air flow in the pipe using a propeller type swirl generator. The experimental and numerical axial and tangential velocity distributions along the pipe were found to be in good agreement. The standard k- ϵ model was also used by Ganeshalingham (2002) to investigate swirling flow induced by *Swirly-Flo* pipes which is a weakly swirling flow. Ganeshalingham stated that RNG k- ϵ model, Realizable k- ϵ model and Reynolds Stress Model (RSM) should show substantial improvements in results compared to standard k- ϵ where the flow features include streamline curvature and rotation, but the accuracy gained is not considerable when the extra time consumed is taken into account. Similar conclusion was drawn by Ariyaratne (2005) and Fokeer (2006). Ariyaratne (2005) decided to use standard k- ϵ model for initial work due to the large number of cases to be studied in optimizing the swirl pipe. Fokeer (2006) also decided to first use the k- ϵ model to obtain a baseline solution, which can then be improved by employing the Reynolds Stress Model.

The shortcomings of the standard k- ϵ model are summarized as follows (ANSYS, 2011a):

- It is valid when all Reynolds stresses are of the same order (isotropic eddy viscosity). If the eddy viscosity is not isotropic, the standard k- ϵ model is inadequate.
- Applicability is limited to high Reynolds number flows.
- The model is semi-empirical; transport equations for k and ϵ involve constants that are taken from measurements.
- Near wall treatment is accomplished via a wall function.

The advantage of standard k- ϵ model is its robustness, economy and reasonable accuracy for a wide range of turbulent flows in industrial flow simulations.

Najafi et al. (2011) investigated the trend of swirl intensity decay rate and its affecting factors through a turbulent swirl decay pipe flow. The swirling flow is created by means of a rotating honeycomb which produces solid body rotation at the inlet of a fixed pipe. In some of the cases, swirling flow being discussed had a swirl number as large as 0.6. In such turbulent flows viscosity is typically anisotropic (Kitoh, 1991), so the Najafi et al. adopted the Reynolds Stress model (RSM) formulation, which was considered to be the most reliable turbulence model (Najafi et al., 2005, Spall and Ashby, 2010). The numerical results were validated and compared with existing experimental data and mathematical relations, showing satisfactory coincide.

The RSM closes the Reynolds-averaged Navier-Stokes equations by solving transport equations for the Reynolds stresses, together with an equation for the dissipation rate. This means that seven additional transport equations are required in a 3D flow (ANSYS, 2011a). The advantages and disadvantages of Reynolds Stress model are as follow (H.K.Versteeg and W.Malalasekera, 2010) :

Advantages:

- Potentially the most general of all classical turbulence models.
- Only initial and/or boundary conditions need to be supplied.
- Very accurate calculation of mean flow properties and all Reynolds stress for many simple and more complex flows including wall jets, asymmetric channel and non-circular duct and curved flows.

Disadvantages:

- Very large computing costs (seven extra partial differential equations).
- Not as widely validated as the k - ε models.
- Performs just as poorly as the k - ε model in some flows due to identical problems with the ε -equation modelling (e.g. axisymmetric jets and unconfined recirculating flows).

According to ANSYS FLUENT User's Guide (ANSYS, 2011b), for modelling turbulent flow with a significant amount of swirl, ANSYS FLUENT suggests the consideration of using one of the advanced turbulence models: the RNG k - ε model, realizable k - ε model, or Reynolds stress model. The appropriate choice depends on the strength of the swirl, which can be gauged by the swirl number. For flows with weak to moderate swirl ($S < 0.5$), both the RNG k - ε model and realizable k - ε model yield appreciable improvement over the standard k - ε model. For highly swirling flows ($S > 0.5$), the RSM is strongly recommended. The effects of strong turbulence anisotropy can be modelled rigorously only by the second-moment closure adopted in the Reynolds stress model. This recommendation was followed in this study in the steady state RANS simulation of the swirl flows induced by the optimized swirl pipe.

With the rising of computing power, large eddy simulation (LES) methods are gaining popularity in industrial flow investigations over recent years though the mainstay for industrial flow simulation is still the Reynolds averaged

Navier-Stokes (RANS) method. The LES is superior to RANS method in that it resolves directly the large turbulent structures and models only the influence of the sub-grid scales on the resolved ones (H.K.Versteeg and W.Malalasekera, 2010). The LES has the potential for improved accuracy when the resolution of the largest eddies is important or when turbulent fluctuations of flow variables are needed.

Conway et al. (2000) applied the LES technique to the subsonic turbulent flow between the blades of a swirl generator. The large time-dependent streamwise vortices due to the blade surface curvature, the large scale time-dependent structures associated with the wake of the blades were captured by the LES.

Wegner et al. (2004) evaluated the performance of the unsteady RANS method employing a Reynolds stress model in predicting the precessing vortex core (PVC) phenomenon. Good agreement of mean velocities was achieved when comparing the unsteady RANS results to available experimental data and LES computations. However the energy contained in the coherent motion of the PVC was significantly under-predicted by the unsteady RANS. It is concluded that unsteady RANS is able to capture the precessing vortex core phenomenon both qualitatively and in parts also quantitatively. Wegner et al. stated that for 3D time-dependent simulation, the computational cost for LES is significantly increased when compared to steady state RANS. LES is very good for flow systems where flow is governed by large, turbulent structures, which can be captured by fairly coarse mesh. However, if the resolving of boundary layers is important, LES may give partially dissatisfying predictions in these regions, unless fine mesh is used. Many researchers have suggested hybrid LES-RANS methods to get around this bottleneck of LES near walls, where RANS is used near the wall while LES is utilized in the remaining part of the domain (Durbin, 2002).

Mikulčić et al. (2014) studied the highly swirled gas-solid flow inside a cement cyclone using LES with the Smagorinsky Subgrid-Scale model being employed for sub-grid scale modelling. A three dimensional geometry of a real industrial scroll type cyclone was used for the LES simulation employing a commercial finite volume CFD code FIRE. The turbulent fluctuations of the gas phase, the pressure drop, and concentration of particles associated with the complex swirled two-phase flow inside the cement cyclone were obtained. The numerically obtained results were compared with available measurement data, and showed good correlation with it.

Yang and Kær (2012) studied the flow structure of a isothermal swirling in the Sydney swirl flame database using both a RANS-based RNG $k-\epsilon$ turbulence model and a large eddy simulation with dynamic Smagorinsky-Lilly model. The streamlines indicated that the formation mechanisms of vortex breakdown detected from the two methods were different. The LES and RANS showed very different vorticity fields. Moreover the RANS fails to predict the precessing vortex core. The author concluded that the LES shows better agreement with the measurements in the statistical results and also better predict the flow pattern of the recirculation zones.

So far, the simulation investigations of the swirl flow induced by the swirl induction pipes are confined in the RANS method. The fluctuation property of the flow variables and the swirl flow instability has not been revealed yet. In Chapter 7 of this thesis, LES was attempted in order to provide insight into the unsteady property of the geometrically induced swirl flow.

2.3.2.2 Wall Shear Stress Modelling in swirl flows

Jensen et al. (2005) suggested that the technique used for measuring the mean and the fluctuating parts of wall shear stress has its shortcomings with respect

to hygiene. Because measurements can only be performed in a predefined number of discrete points, and the equipment tested has to be specially designed to mount the measuring probes. An alternative approach of applying computational fluid dynamics (CFD) was proposed. CFD is widely used with great success within other industries for prediction of flow patterns, quantitative hydrodynamic parameters, chemical processes, etc.

It used to be difficult for CFD simulation to predict wall shear stress quantitatively (Wilcox, 1998, Bouainouche et al., 1997). However, with the development of computer technology, models for simulating near-wall flow have been implemented in commercially available CFD codes. Prediction of wall shear stress was proven to be very good in some cases (Wilcox, 1998, Jensen et al., 2005).

Even though, investigations on wall shear stress in swirl flows are few. The study carried out by Zhu et al. (2012), PathogenCombat (2011), and Jensen et al. (2005) mentioned above, were performed either in circular pipes or complex geometries like sudden/gradual expansion or contraction, and up-stand etc. with non-swirling flows. So their studies cannot entirely reflect the wall shear stress variation and distribution pattern of swirl flows within the circular pipes or complex geometries.

The case involving simulation of wall shear stress in swirl flow is found in the study of Najafi et al. (2011) whose purpose was to investigate the swirl intensity decay rate of internal swirl flow downstream a rotating cylinder honeycomb (a swirl generator). Their simulation found that an increase in the inlet swirl intensity causes a rise in tangential wall shear stress and directing to the downstream. In addition, the variation of the swirl intensity of the swirl flow field was found similar to that of the tangential wall shear stress indicating that the value of tangential wall shear stress is proportional to the swirl intensity. The

definitions of swirl intensity and tangential wall shear stress are seen in section 2.3.3.

It should be mentioned that the swirl flows generated by the rotating cylinder honeycomb and the swirl flows induced by the swirl induction pipes are not entirely the same in that:

- The swirl induction mechanism is different that the former one was produced by flow passing through a rotational section, while the latter was induced by stationary spiral walls of the pipe.
- The circumferential distribution of wall shear stress downstream of the rotating cylinder honeycomb is even because of its circular cross-section shape. While the circumferential distribution of wall shear stress downstream of the swirl pipe may be uneven due to the lobed cross-section of the swirl pipe.
- The swirl flow Najafi et al. studied can be very strong (swirl number reaches 0.6). While swirl flow induced by the swirl pipe is a kind of weakly swirl flow (swirl number less than 0.15).

Despite the above difference, the positive correlation of swirl intensity and tangential wall shear stress indicated by Najafi et al. has provided a good expectation that the swirl flow induced by the swirl pipe should give rise to the tangential wall shear stress, consequently an increase of overall wall shear stress at the internal pipe surface downstream of the swirl pipe.

2.3.3 Definition of Terms and Equations for Swirl Flow

This section introduces a number of terms and equations that will be used in studying swirl flows.

Swirl number S (swirl intensity)

Although there is no standard for quantifying the strength of the swirl inside a pipe, the swirl number S , also termed swirl intensity, is commonly used. It defined as the ratio of the angular momentum flux to the axial momentum flux, multiplied by the hydraulic radius (Li and Tomita, 1994, Steenbergen and Voskamp, 1998, Rocklage-Marliani G., 2003):

$$S = \frac{\int_0^R uwr^2 \cdot dr}{R \int_0^R u^2 r \cdot dr} \quad (2.3.1)$$

S = swirl intensity

w = tangential velocity, m/s

r = radius at point where tangential velocity is calculated, m

R = pipe radius, m

u = axial velocity, m/s

Swirl decay

Swirl will decay downstream of the swirl pipe which is caused by transport of angular momentum to the pipe wall. To determine the distance over which swirl will prevail in the pipe several researchers had studied the swirl decay law (Steenbergen and Voskamp, 1998, Li and Tomita, 1994, Halsey, 1987, Reader-Harris, 1994). There was no unanimous agreement on the decay rates in swirling flow, in most reference, the observed swirl intensity fit with exponential decay functions:

$$S = S_0 e^{-\beta \frac{x}{D}} \quad (2.3.2)$$

S_0 = initial swirl intensity

β = swirl decay rate parameter = $\alpha * f'$

x = distance along pipe, m

D = pipe diameter, m

f' = Moody friction factor

α = empirical coefficient

Hydraulic diameter

The hydraulic diameter of a pipe is defined as (Nesbitt, 2000):

$$d_h = \frac{4A}{P} \quad (2.3.3)$$

d_h = hydraulic diameter, m

P = wetted perimeter, m

A = area, m²

Wall shear stress

Any real fluids (liquids and gases included) moving along solid boundary will incur a shear stress on that boundary. The no-slip condition dictates that the speed of the fluid at the boundary is zero, but at some height from the boundary the flow speed must equal that of the fluid. The region between these two points is aptly named the boundary layer. For all Newtonian fluids in laminar flow the shear stress is proportional to the strain rate in the fluid where the viscosity is the constant of proportionality. The shear stress is imparted onto the boundary as a result of this loss of velocity (Day, 2004, Timoshenko and Stephen, 1983).

The shear stress, for a Newtonian fluid, at a surface element parallel to a flat

plate, at the point y , is given by:

$$\tau_w(y) = \mu \frac{\partial u}{\partial y} \quad (2.3.4)$$

Where:

μ = dynamic viscosity of the fluid

u = velocity of the fluid along the boundary

y = height above the boundary

The wall shear stress can be related to the pressure loss in cylindrical pipe flow by (Sleigh and Goodwill, 2008):

$$\Delta P = \frac{\tau_w 4L}{d} \quad (2.3.5)$$

So,

$$\tau_w = \frac{\Delta P d}{4L} \quad (2.3.6)$$

ΔP = pressure loss due to friction in pipe

d = pipe diameter

L = length of pipe corresponding to pressure loss

In laminar flow, the pressure loss has a positive relation with flow velocity that $\Delta P \propto u$, in turbulent flow, $\Delta P \propto u^{1.7 \text{ to } 2.0}$ (Sleigh and Goodwill, 2008). For fluid flow in cylindrical pipe in closed processing system, the wall shear stress can be determined on a mean value basis where it is proportional to the flow rate (PathogenCombat, 2011).

The shear stress at the wall relates to the Fanning friction factor, a dimensionless number named after John Thomas Fanning (1837–1911), in that:

$$\tau_w = \frac{f\rho u^2}{2} \quad (2.3.7)$$

where:

τ_w = shear stress at the wall

f = Fanning friction factor of the pipe

u = fluid velocity in the pipe

ρ = density of the fluid

The friction factor is a function of flow Reynolds number and the ratio of wall roughness to pipe diameter, more information are covered in the book of Douglas et al. (2006).

Tangential wall shear stress

It is concluded that the existence of tangential wall shear stress in the swirl flow causes reduction of fluid flow swirl intensity (Steenbergen and Voskamp, 1998, Kitoh, 1991).

Kitoh (1991) derived an expression for the tangential wall shear stress by treatment of the Reynolds averaged angular momentum equation for incompressible, stationary and axially symmetric flow. The equation later used by Steenbergen and Voskamp (1998) and Najafi et al. (2011) reads:

$$\tau_{w\theta}(x) = \frac{\rho}{R^2} \int_0^R r^2 \frac{\partial}{\partial x} (\bar{U}\bar{W} + \overline{uw} - \mu \frac{\partial \bar{W}}{\partial x}) dr \quad (2.3.8)$$

where \bar{U} and \bar{W} are the time averaged value of the axial and tangential velocity components respectively; u and w are the instantaneous fluctuation of the axial and tangential velocity components respectively; ρ is the density; R is the radius of the pipe; μ is the kinematic viscosity; x and r are the axial and radial position; $r^2\bar{U}\bar{W}$ is the flux density of angular momentum per unit mass at

radial position r . Turbulent shear stress $\overline{u'w'}$ and viscous shear stress $\mu \partial \overline{W} / \partial x$ acting in the cross-flow plane can be neglected in turbulent flow having a slow axial development. Equation 2.3.8 actually illustrates that the change in the integrated flux of angular momentum on a cross section of flow is balanced by the moments exerted on the flow by the tangential wall shear stress. By interchanging integration and differentiation the following equation is obtained:

$$\tau_{w\theta}(x) = \frac{\rho}{R^2} \frac{\partial}{\partial x} \int_0^R r^2 (\overline{U}\overline{W}) dr \quad (2.3.9)$$

Equation 2.3.9 is made non-dimensional by the transformations of $x \rightarrow x/D$, $r \rightarrow r/R$, $\overline{U} \rightarrow \overline{U}/U_m$ and $\overline{W} \rightarrow \overline{W}/U_m$, with U_m being bulk velocity and D pipe diameter. The non-dimensional tangential wall shear stress is rearranged as:

$$\tau'_{w\theta}(x) = \frac{\tau_{w\theta}(x)}{0.5\rho U_m^2} = \frac{1}{2} \frac{dS}{d\left(\frac{x}{D}\right)} \quad (2.3.10)$$

with S being the swirl intensity as defined in equation 2.3.1. Equation 2.3.10 indicates that at the downstream region of the swirl pipe exit, the non-dimensional tangential wall shear stress is a linear function of the axial gradient of swirl intensity.

2.4 Measuring Swirl Flow

2.4.1 Measuring Flowfield

Invasive and non-invasive techniques can be employed in order to measure flowfield. Invasive techniques used probes present within the flow for data capture. A number of researchers have used invasive method to measure swirl flows. For instance, Ito et al. (1980) used an electrolytic solution that has the kinematic viscosity nearly equal to that of water to measure swirling flow electrochemically. A spherical multi-electrode probe was used to measure the three dimensional velocity components. Kitoh (1991) used a hot wire probe to

measure the flow angle and the mean velocity of a swirling water flow. Li and Tomita (1994) also used an invasive method to measure the radial velocity and pressure profiles at 15 different pipe sections in swirling pneumatic flow using a 3-holed spherical head probe. Measurements were carried out at 20 radial locations at each section and the swirl intensity was calculated.

The pressure and pressure drop within the flow system is normally measured using invasive pressure sensors. For instance, Senoo and Nagata (1972) used a cobra probe and a sphere static probe to measure the direction and static pressure of swirling air flow. Tonkin (2004) and Su et al. (2010) chose differential pressure transducers for pressure measurement in swirl and non-swirl flow respectively. To select a pressure transducer, the line pressure and pressure drop range should be estimated in advance. Ariyaratne (2005) initially used piezo-resistive pressure sensors to measure pressure drop. However, it was found the calibration of these sensors changed rapidly and it needed to be re-calibrated regularly. Therefore she used an inverted manometer in the subsequent tests which provided more accurate pressure drop results. Fokeer (2006) used U-tube water manometers and inclined manometers filled with a liquid of specific gravity 0.8 to measure the gauge pressure of pneumatic swirling flow. George (2007) used two types of pressure measuring devices, simple manometer tube and liquid pressure gauge for the measurement of pressure drop of the swirl pipe.

The disadvantage of the invasive methods is that the local disturbances and changes of flow in the probe area may result in poor measurements. On the other hand, non-invasive techniques have no physical parts within the flow and therefore do not cause any flow disturbance. These techniques include LDV (Laser Doppler Velocimetry), PDA (Phase Doppler Anemometry), PIV (Particle Image Velocimetry) and all tomography techniques.

Particle image velocimetry (PIV) is an optical method of flow visualization used in education and research. It is used to obtain instantaneous velocity measurements and related properties in fluids. The fluid is seeded with tracer particles which, for sufficiently small particles, are assumed to faithfully follow the flow dynamics. The flow in the target area is then illuminated with a laser light sheet and the motion of the particles is recorded using a CCD (Charge Coupled Device) camera. A sequence of two light pulses is recorded and the images are divided into subsections called interrogation areas. The interrogation areas are next correlated pixel by pixel. The correlation produces a signal peak identifying the common particle displacement. This displacement can then be used to construct a 2D vector map (Smits and Lim, 2000).

Ganeshalingam (Ganeshalingam, 2002) used Dantec FlowMap PIV system (with one CCD camera) to measure axial velocity of the flow downstream of the swirl inducing pipe and showed a good agreement with CFD predicted values. However, his attempt at measuring tangential velocity was not successful. To measure tangential velocity, Tonkin (2004) attempted a different setup of the PIV by placing the camera perpendicular to the cross-section and focusing through an optical window. Initially only a part of the cross-section was visible with the tangential viewer. It was adapted by adding a viewing box filled with water to prevent total internal reflection, and the whole pipe cross-section could be viewed. The disadvantage of Tonkin's method is that, with the use of tangential viewer, measurements at distance further downstream than $L/D=5$ (5 pipe diameters) may not be possible since the camera cannot focus that far through the viewer. This will prevent analysis of swirl decay downstream of the swirl pipe. Therefore, Ariyaratne (2005) decided to attempt PIV measurement of tangential velocity with the laser and camera at an angle of 90° as shown in Figure 2.4.1. However, this attempt was unsuccessful.

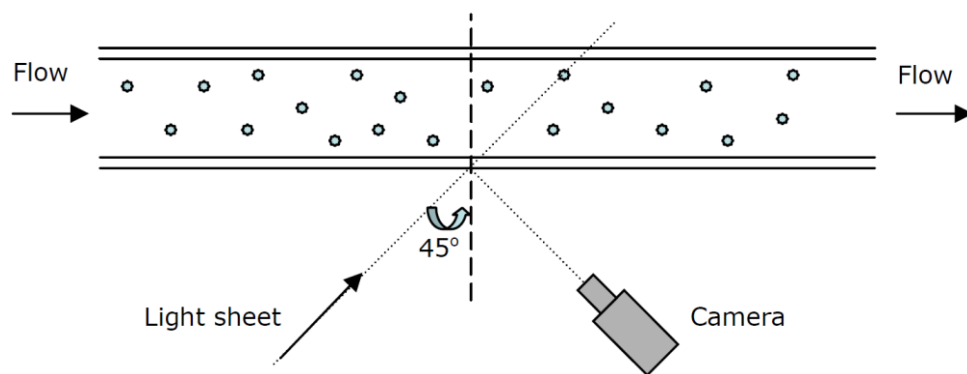


Figure 2.4.1 Schematic Diagram of PIV Setup and Camera Angle with the Laser at an Angle (after Ariyaratne, 2005)

Fokeer (2006) initially attempted PIV technique to understand the pneumatic swirl flow field downstream of the three lobed swirl pipe. A DANTEC FlowMap 2100 Particle Image Velocimetry (PIV) system was used. It was found that a lack of good seeding implied poor quality of the results and it was not possible to obtain a seeding material which would produce seeding particles in the three microns range without dirtying the endoscope. It was therefore decided to perform a series of Laser Doppler Anemometry (LDA) experiments.

LDA is a single point optical measuring technique which enables the velocity of the seeded particles conveyed by a fluid flow to be measured in a non-intrusive manner. The area of interest within the flow field is sampled by a crossed-beam point by point. The local velocity of the fluid can be determined by analysing the Doppler-equivalent frequency of the laser light scattered by the seeded particles within the flow. This technique was employed by Fokeer to measure the flowfield for three different Reynolds number air flows seeded with oil droplets of an average diameter of 3 microns. The instantaneous local fluid velocities components in the three directions were measured at four planes perpendicular to the pipe axis (130 measurement points per plane) downstream of both the control and swirl pipe sections. The measured u , v and w velocity components were converted into cylindrical polar velocity components u_x , u_r and u_θ .

Successful use of LDA in swirl flows has also been reported by Nejad et al. (1989), Parchen and Steenbergen (1998) and Rocklage-Marliani et al. (2003).

2.4.2 Measuring Wall Shear Stress

The measurement of mean and time resolved wall shear stress in a turbulent boundary layer is of vital importance to the fluid mechanics community. Wall shear stress sensors are traditionally classified by measurement method into two distinct groups, direct or indirect techniques.

The direct techniques directly measure the shear force acting on the model surface. Direct sensors measure the integrated force produced by the wall shear stress on a flush-mounted movable "floating" element. The floating element is attached to either a displacement transducer or is part of a feedback force-rebalance configuration. The performance of these devices has been limited by the following issues (Sheplak et al., 2004, Winter, 1977):

- The tradeoff between sensor spatial resolution and the ability to measure small forces.
- Measurement errors associated with sensor misalignment and required gaps.
- Measurement errors associated with pressure gradients.
- Cross-axis sensitivity to acceleration, vibration, and thermal expansion effects.
- Sensitivity drifts due to thermal-expansion effects.

Methods of this kind have stronger intrusion to the local flow field. Its measurement errors caused by stronger pressure gradient in swirl flow can be significant. More importantly, it only gives an integrated value of wall shear stress and cannot give a time-resolved wall shear stress fluctuation. Therefore

this method is not applicable for swirling flow.

Indirect sensors are generally simpler to fabricate and are more robust than floating-element sensors. Indirect techniques require an empirical or theoretical correlation, typically valid for very specific conditions, to relate the measured property to the wall shear stress. The MEMS (Microelectromechanical systems) community has produced a variety of different indirect transduction schemes such as hot-film sensors, micro-optical systems to measure near-wall velocity gradients, and mechanical micro-fences (Sheplak et al., 2004).

Of the indirect sensors, the thermal-based stress sensors were widely used. The operating principle of thermal shear stress sensor is the transduction of heat-transfer rate to voltage. Su et al. (2010) measured the mean and time varying fluctuation property of local wall shear stress of horizontal air-water bubbly flows in a circular pipe of 35mm inner diameter using a TSI-1268W hot film probe. The hot film sensor was made of a thin platinum film with dimensions of 1.0×0.127 mm and coated with a thin layer of quartz. The TSI-1268W probe is cast into the mounting block and is flush-mounted on the internal surface of the section. A pair of pressure taps was used to measure the pressure gradient in the region where the hot film probe is located. The pressure taps are connected to a 1151 capacitive differential pressure transducer with a measuring range of 0-5 kPa and accuracy of 12.5 Pa. The wall shear stress is calculated from the measured pressure gradient of single-phase water flow and is used for calibration. Vaze and Banerjee (2012), also used a Hot Film Anemometry to measure the wall shear stress in an air-water two phase flow.

Berca (2007) measured the wall friction in the cone of an industrial turbine model using a flush mounted hot-film probe. Berca designed a rotating supporter to adjust the angle made by the longitudinal direction of the hot file and the flow direction at the measuring point to obtain the maximal heat

dissipation and hence the largest wall shear stress.

The main limitations of the thermal-based stress sensors technique when being used for quantitative wall shear stress measurements are (Winter, 1977, Haritonidis, 1989, Sheplak et al., 2004):

- Difficulty in obtaining a unique calibration or relationship between heat transfer and wall shear stress.
- Reduction in sensitivity and problems in the dynamic response due to the frequency-dependent conductive heat transfer into the substrate.
- Measurement errors associated with mean temperature drift of the fluid.
- Flow perturbations due to heat transfer to the flow.

Methods other than Microelectromechanical systems have been used by researchers for wall shear stress measurements. For instance, Lelièvre et al. (2002) carried out local measurements of wall shear stress by analogy with mass transfer using an electrochemical technique. Platinum microelectrodes were placed close to the surface of stainless steel production lines. Each microelectrode consisted of cross-sectioned platinum wire of 1 mm in diameter. The local electrochemical measurements were carried out using a polarographic method involving the reduction of ferricyanide ions on the microcathodes. The reverse reaction occurred on the anode (nickel pipes inserted in the circuit). The measured electrochemical current increased with the applied voltage until the potential between the two electrodes was such that the current flowing through the circuit was controlled by the rate of diffusion of the reacting species to the surface of the working electrode. It then stabilised at a value named "limiting diffusional current". The average limiting current could be related to the average shear rate at the surface of the electrode. Same method was adopted later by Jensen et al. (2005), Hanratty and Campbell (1983). Rode et al. (1994) pointed out that this electrochemical method could be used for the investigation of

extremely non-homogeneous turbulent flow conditions with high amplitude fluctuations of the instantaneous local shear rate.

Gijssen et al. (1997) proposed an alternative method to determine the wall shear stress for flow in a rectangular duct. A highly deformable gel layer is used as the sensing element. The gel layer is attached to the inner wall of a flow model. The wall shear stress, exerted by the fluid, deforms the gel layer slightly. The small deformation of the gel layer can be measured accurately by means of speckle pattern interferometry. Through the known properties of the gel, the wall shear stress can be inferred from the deformation of the gel layer. The author stated that the measured wall shear stress far enough from the sidewall showed a good agreement with the computed wall shear stress for both the Newtonian and the non-Newtonian fluid.

Rudolph et al. (2009) presented a new wall shear stress measurement technique using the thermal tuft technique. The experimental investigations were carried out for turbulent flow conditions in an open wind tunnel facility. The thermal tuft is created through Joule heating and the resulting temperature is detected with an infrared camera. The surface temperature distribution around a small heated spot was used to visualise and quantify the near wall flow.

Große and Schröder (2008) introduced a method of using the micro-pillar wall-shear stress sensor MPS³ to measure the dynamic wall shear stress in turbulent pipe flow. The sensor device consisted of a flexible micro-pillar which extends from the wall into the viscous sublayer. The pillar-tip deflection caused by the exerting fluid forces serves as a measure for the local wall-shear stress. The pillar is statically calibrated in linear shear flow. A second-order estimate of the pillar dynamic response based on experimentally determined sensor characteristics shows the potential of the sensor configuration to also measure the dynamic wall-shear stress. Große and Schröder stated that the results

demonstrate a convincing agreement of the mean and dynamic wall-shear stress obtained with the MPS³ sensor technique with analytical, experimental, and numerical results from the literature.

Berthe et al. (2009) developed a new method for the spatial and temporal assessment of the wall shear stress. This wall-PIV technique can be regarded as a special development of the classical PIV. It permitted to look selectively at the flow closed to the wall. The selection was made by using a fluid, which does not permit the light to penetrate deeply into the flow. The fluid contained a molecular dye and seeded with buoyant particles illuminated by a monochromatic, diffuse light. Due to the dye, the depth of view is limited to the near wall layer. Due to the limited penetration depth of the light only the particles moving close to the wall are lighted. Within the illuminated layer, the particles appear more or less bright, depending of their distance to the wall. A grey value analysis with a special image processing program permitted to determine this distance, which was necessary for the calculation of the wall shear stress.

In experimental fluid mechanics, particle image velocimetry (PIV) is now the most common way to measure velocity. However, conventional PIV is usually difficult to apply to near-wall regions because of the low tracer density, high velocity gradient and strong wall reflection. Such problems are compounded when performing standard PIV next to inclined or curved boundaries. Nguyen et al. (2010) proposed a near-wall technique named interfacial PIV (IPIV) for wall shear stress measurement of near-wall flow over inclined and curved boundaries. The method handles curved boundaries by means of conformal transformation, directly measures the wall gradient, and yields the near-wall tangential velocity profile. The obtained results showed that stereo-IPIV wall gradient measurement yields good accuracy if the condition on apparent wall-normal tracer displacement on each camera image is satisfied.

2.4.3 Measuring Cleanability

Cleanability of the equipment surfaces is a very important issue in closed processing system. Equipment that is difficult to clean will need more severe CIP procedures that require more aggressive chemicals and longer cleaning and decontamination cycles. This will typically result in higher cost, longer downtime, reduced lifetime of the equipment and more effluent (EHEDG, 2004). Therefore, evaluation of the relative cleanability of the equipment is important in facilitating the design and testing of the closed processing equipment (K-patents, 2013). Researchers have developed a number of methods to examine the hygienic status of equipment surface after cleaning. These methods can also be adopted to evaluate the cleaning efficiency of the CIP procedures.

For instance, Bénézech et al. (2002) proposed a practical and quantitative method for assessing complex food equipment cleanability. After soiling a positive displacement pump by a composite model food made of custard and *Bacillus cereus* spores isolated from a food processing line, a mild cleaning-in-place procedure was carried out using basic detergents of sodium hydroxide and nitric acid. After cleaning, surfaces potentially in contact with the contaminated food were overlaid with nutrient agar containing a tetrazolium salt. Residual contaminants appeared as small red colonies and contamination levels could be defined. A non-parametric statistical analysis was performed to compare the different areas in the pump and three cleanability levels were defined.

Lelièvre et al. (2002) carried out cleanability experiments in stainless steel equipment. *Bacillus cereus* CUETM 98/4 isolated from an industrial dairy processing line was used as spore-forming strain. The spores were produced and harvested as described by Faille et al. (1997). They were suspended at 105

CFU ml⁻¹ in saline (0.145 M NaCl). The tested items were soiled in static conditions in the laboratory to allow a homogeneous adhesion to be obtained. They were vertically filled with the soiling suspension for 1 h at room temperature and turned over each 10 minutes. Finally, the items were drained. After the insertion of soiled items, the rig was rinsed for 2 min at 300 l h⁻¹. Cleaning was then performed with sodium hydroxide (0.5% w=w) at 60 °C for 10 minutes. Following the method of Husmarka et al. (1999), the adhering bacteria remaining after the CIP procedure were counted by the agar overlay technique using agar supplemented by tetrazolium chloride (TTC).

In another experiment performed by Lelièvre et al. (2002a), contaminated milk was used to soil the pipes. Two flow conditions were used: static or turbulent. Under static conditions, pipes were vertically filled with soiling suspension for an hour at 20 °C. Under turbulent conditions, the contaminated milk was circulated at 1.8m/s for an hour at 20 °C. The spore detection method remained the same.

Friis and Jensen (2002) performed hygiene test of mix-proof valve using EHEDG (European Hygienic Equipment Design Group) test (EHEDG, 1992). Prior to soiling the test pieces were autoclaved for 30 minutes at 120 °C. Soiling was conducted using a mixture of *Bacillus stearothermophilus*, *Calidolactis* and sour milk, followed by 4 hours of drying with air. The component was rinsed with water for 1 minute followed by washing for 10 minutes with a 63 °C 1% detergent solution and then rinsed again with cold water for 1 minute. Finally, the component was dismantled and filled with Shapton and Hindes agar and incubated for 20 hours at 58 °C. Remaining spores on the surfaces appeared as yellowish colouration on the purple agar.

Guillemot et al. (2007) used the strain of *S. cerevisiae* for soiling. After cleaning, the number of yeast cells remaining adherent to polystyrene was counted by means of optical microscopy and an image acquisition software.

From the above methods, a cleanability test is typically comprised of fouling of the equipment using contaminants such as spores (Bénézech et al., 2002, Lelièvre et al., 2002), contaminated milk (Lelièvre et al., 2002a, Friis and Jensen, 2002), or strain of *S. cerevisiae* (Guillemot et al., 2007), cleaning of the equipment using CIP procedures, and quantification of the residual contaminants.

2.5 Conclusion

- The fouling of internal pipe surfaces in the closed processing systems and their cleaning employing Clean-In-Place (CIP) procedures were introduced.
- The factor influencing cleaning efficiency of CIP procedures especially the hydrodynamic factors were summarized. A combination of the mean wall shear stress and the fluctuation of wall shear stress can be used for assessing the efficiency of CIP.
- The previous researches on swirl induction pipes were reviewed. The terms and equations will be used in this study were defined.
- The simulation of swirl flows using RANS and LES methods were discussed and compared. The works concerning wall shear stress modelling were reviewed.
- The techniques with respect to measurements of flowfield of swirl flow, pressure drop, wall shear stress and cleanability of the CIP procedures have been reviewed.

CHAPTER 3: TRANSITION AND SWIRL PIPE CREATION

3.1 Introduction

Ganeshalingam (2002) tested various cross-sections of pipe (3, 4, 5 and 6 lobed) and concluded, based on the evaluation criteria of Swirl Effectiveness (the ratio of the swirl intensity produced to the pressure loss), that the 4-lobed cross-section was most effective at swirl generation. He recommended a P:D ratio of 8 and 400mm of length as optimal for the 4-lobed pipe, namely the swirl inducing pipe. Later, Ariyaratne (2005) designed transition pipe which provides a gradual transition from circular to lobed cross-section and vice versa and connected it either prior to the 400mm length swirl inducing pipe as the entry transition or after it as the exit transition. The transition pipe was found to increase swirl induction at the exit of the swirl pipe and reduce pressure losses.

This chapter details the calculation and geometry creation process of the transition pipe and swirl inducing pipe. Based on the calculation, the spreadsheets that include necessary data for the sketch of cross-sections of transition and swirl inducing pipe are generated. The cross-sections are later swept and blended into transition and swirl inducing pipe respectively using Pro/Engineer. An optimised 4-lobed swirl pipe is defined which was not tested previously.

3.2 Geometry Calculation

This section presents the calculation process used to create spreadsheets that define the geometry of the 4-lobed transitions. These spreadsheets include the transition pipe cross-sections at any given length along the z co-ordinate axis as

it gradually develops from a circular to a 4 lobed cross-section. This information will be used later on by Pro/Engineer to create solid, 3 dimensional models for CFD modelling and experimental work.

The swirl pipe calculation is less complex and is partially included in the transition pipe calculation, thus only a brief calculation process is presented.

3.2.1 Four-lobed Transition Pipe Calculation

The calculation procedures for the four-lobed transition pipe are summarized as below (Ariyaratne, 2005):

1. Calculate r_f (lobe radius for fully developed swirl pipe) by equating swirl pipe cross-sectional area to circular pipe area of radius R_1 to give equal flow area.

Cross-sectional area of swirl pipe = area of square (BDEF) + area of 4 lobes = circular pipe.

$$2r_f \times 2r_f + \frac{\pi r_f^2}{2} \times 4 = 4r_f^2 + 2\pi r_f^2 = (4 + 2\pi)r_f^2 = \pi R_1^2$$

therefore

$$r_f = \sqrt{\frac{R_1^2}{2 + \frac{4}{\pi}}}$$

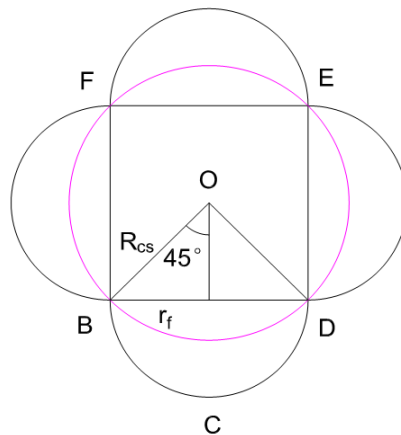


Figure 3.2.1 Fully developed swirl pipe cross-section

- 2.** Calculate the pipe length through which one lobe twists 90° using P: D ratio such that the lobe pattern repeats in the length of the transition.

$$Twist(deg/m) = \frac{360^\circ}{(P:D \text{ Ratio}) \times d_e}$$

$$Twist = \frac{360^\circ}{8 \times 0.05} = 900deg/m$$

where

P:D ratio = pitch-to-diameter ratio of pipe (=8)

d_e = equivalent diameter of pipe (=50mm)

Twist direction=-1 (negative for clockwise rotation)

Length of transition based on one lobe twisted 90° :

$$L = \frac{1000mm}{900^\circ} \times 90^\circ = 100mm$$

- 3.** Calculate minimum core radius R_{cs} (see Figure 3.2.1), which is the radius of circular section of fully developed swirl pipe, using r_f .

$$R_{cs} = \frac{r_f}{\sin 45^\circ} = \sqrt{2}r_f$$

- 4.** Introduce γ , which increases from 45° to 90° in a given number of increments (N_{inc}) as lobes develop.

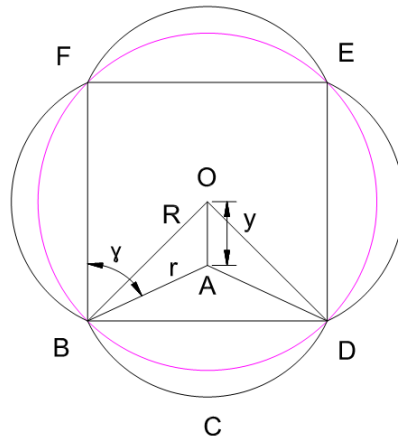


**Figure 3.2.2 Transition Pipe at Intermediate Stage as Lobes Develop
($\gamma = 65^\circ$)**

In Figure 3.2.2

r = lobe radius at intermediate stage of transition.

R = circular core radius for intermediate stage of transition pipe.

y = distance of lobe centre from origin O .

γ = angle made between the line perpendicular to the lobe origin (point B) and the lobe radius r .

$\gamma/\text{deg} = 45^\circ \rightarrow 90^\circ$, from no lobes (stage 1) to fully developed lobes in given number of incremental steps.

It can be seen from Figure 3.2.2 that:

$$\text{Area of segment } BCD = \text{area of sector } ABCD - \text{area of triangle } ABD$$

$$\text{Area of sector } ABCD = \frac{1}{2}r^2\theta = \frac{1}{2}r^2 \times 2\gamma = r^2\gamma$$

$$\text{Area of triangle } ABD = r\sin\gamma \times r\cos\gamma = r^2\sin\gamma\cos\gamma = r^2 \times \frac{1}{2}\sin 2\gamma$$

$$\text{Area of segment } BCD = r^2\gamma - \frac{1}{2}r^2\sin 2\gamma = r^2\left(\gamma - \frac{1}{2}\sin 2\gamma\right)$$

5. Introduce variables f and f_1 to facilitate calculation of area of segments and y .

Introduce variable f and allow:

$$f = (\gamma - \frac{1}{2}\sin 2\gamma)$$
(3.1)

Therefore

$$\text{Area of segment BCD} = fr^2$$

In triangle ABO, apply Sine Rule,

$$\frac{R}{\sin(180^\circ - \gamma)} = \frac{y}{\sin(\gamma - 45^\circ)}$$

$$\frac{R}{\sin \gamma} = \frac{y}{\sin \gamma \cos 45^\circ - \cos \gamma \sin 45^\circ}$$

Divided by $\cos 60^\circ$ and multiply $\sin 60^\circ$,

$$y = \frac{1}{\sqrt{2}}R \left[\frac{\sin \gamma - \cos \gamma}{\sin \gamma} \right] = \frac{1}{\sqrt{2}}R \left[1 - \frac{1}{\tan \gamma} \right]$$

Introduce another variable f_1 and allow:

$$f_1 = \frac{1}{\sqrt{2}} \left[1 - \frac{1}{\tan \gamma} \right]$$
(3.2)

Therefore

$$y = f_1 R$$
(3.3)

Up to now, variable f facilitates the calculation of segmental area and f_1 facilitates the calculation of y .

6. At each increment of γ , calculate R (intermediate core radius), r (intermediate lobe radius) and y keeping the cross-section area equal for all stages.

Calculate R for intermediate stage with equal cross-sectional area at all stages:

$$\pi R_1^2 = \text{area of pipe with no lobes (stage1, circular pipe)}$$

$$\text{Pipe area at intermedia stage} = \pi R_1^2$$

$$= \text{Area of 4 segmental lobes } (BCD \times 4) + \text{Area of square BDEF}$$

In triangle ABO, apply Cosine Rule and get,

$$r^2 = R^2 + y^2 - 2R \cdot y \cos 45^\circ = R^2 + y^2 - \sqrt{2}R \cdot y \quad (3.4)$$

Therefore,

$$\text{Area of 4 segmental lobes} = 4 \times f r^2 = 4f(R^2 + y^2 - \sqrt{2}R \cdot y)$$

Replace y using Equation (3.3)

$$\text{Area of 4 segmental lobes} = 4f(R^2 + f_1^2 R^2 - \sqrt{2}R^2 \cdot f_1)$$

$$\text{Area of 4 square BDEF} = (2R \cos 45^\circ)^2 = (2R \times \frac{1}{\sqrt{2}})^2 = 2R^2$$

Add area of the square and segmental lobes,

$$\text{Pipe area at intermediate stage} = 4fR^2(1 + f_1^2 - \sqrt{2}f_1) + 2R^2$$

Equate area of circular pipe,

$$\begin{aligned} \pi R_1^2 &= R^2(4f + 4ff_1^2 - 4\sqrt{2}ff_1 + 2) \\ R^2 &= R_1^2 \left[\frac{\pi}{4f + 4ff_1^2 - 4\sqrt{2}ff_1 + 2} \right] \\ R &= R_1 \sqrt{\frac{\pi}{4f + 4ff_1^2 - 4\sqrt{2}ff_1 + 2}} \end{aligned} \quad (3.5)$$

7. Calculate lobe area for each intermediate stage (LA_i) as a function of f, R and r.

We know that, as shown in Figure 3.2.3a,

$$\text{Total area of 4 segmental lobes} = 4fr^2$$

As shown in Figure 3.2.3b,

$$\text{Total area of INNER segments} = \text{Area of circle} - \text{Area of square BDEF} = \pi R^2 - 2R^2$$

Therefore, as shown in Figure 3.2.3c,

$$\text{Total lobe area at intermediate stage } (LA_i) = 4fr^2 - R^2(\pi - 2) \quad (3.6)$$

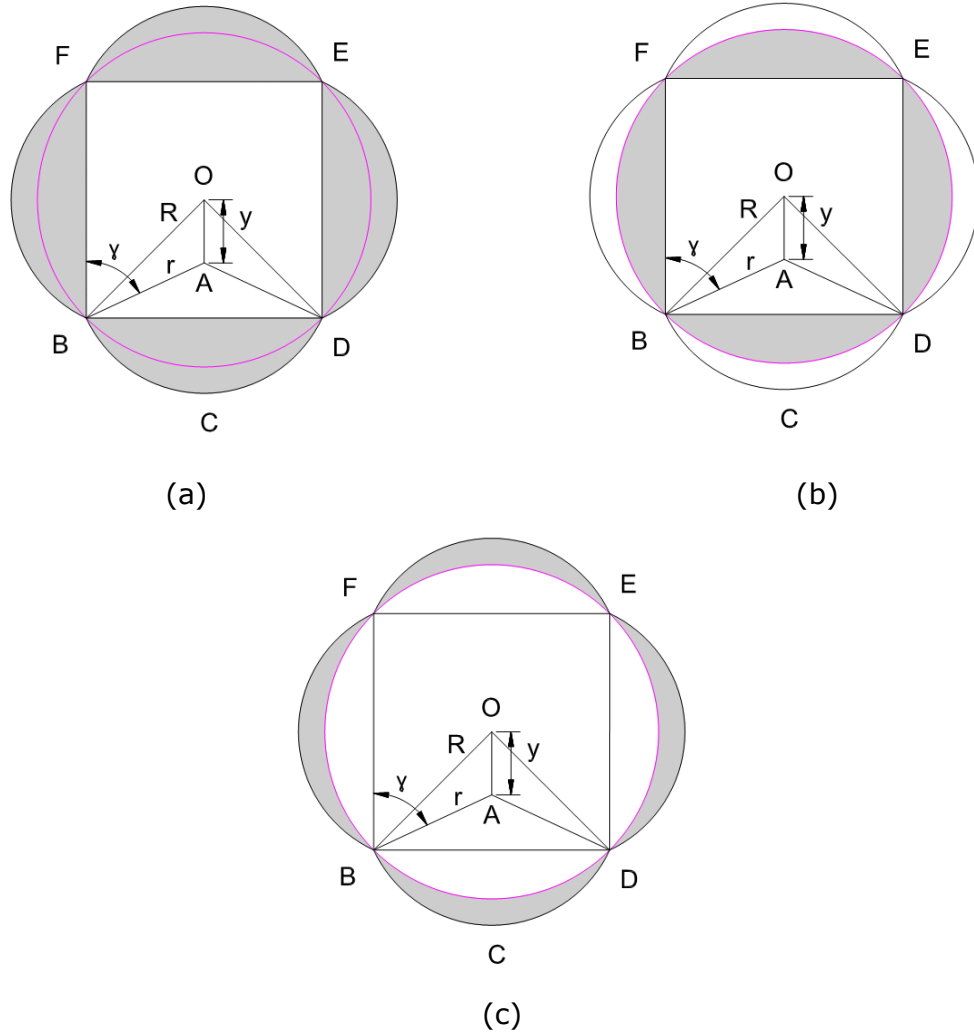


Figure 3.2.3 Indication of total area of 4 segmental lobes (a), total area of inner segments (b) and total lobe area (c) at intermediate stage

8. Introduce a function alpha:

$$\alpha = \frac{LA_i}{LA_{FD}} \quad (3.7)$$

Where,

LA_i = lobe area at intermediate stage

LA_{FD} = lobe area of fully developed swirl pipe

Here $LA_{FD} = (\text{Swirl pipe area} - \text{Area of circular only for } R_{cs}) = (4 + 2\pi)r_f^2 - \pi R_{cs}^2$,

where R_{cs} is the minimum core radius of circular section of fully developed swirl pipe as shown in Figure 3.1.

9. To avoid discontinuity in the case of a linear relationship, vary lobe area along length as a cosine relationship. Function α can now be defined as desired to determine lobe development in transition.

Define x/L (length ratio) as a cosine function of α ,

$$\frac{x}{L} = \frac{\cos^{-1}(1 - 2\alpha)}{\pi} \quad (3.8)$$

Where

x = intermediate length

L = total length

The above function can be varied to give different types of transition development based on lobe area growth.

Intermediate twist is calculated using:

$$Twist[0,90^\circ] = \frac{x}{L} \times 90^\circ \times Twist\ direction \quad (3.9)$$

Where twist direction is -1 (negative for clockwise rotation)

γ increases from 45° to 90° in given number of increments (N_{inc}) as lobes develop. For each increment of γ , function f and f_1 are calculated using Equation (3.1) and (3.2) respectively. These in turn are used to calculate R from equation (3.5), y from Equation (3.3) and r from Equation (3.4) at each increment stage. Lobe area is calculated using Equation (3.6), α using Equation (3.7), x/L using Equation (3.8) and the respective twist using Equation (3.9).

10. Tabulate calculated data at each stage of γ as it increases 45° to 90° .

3.2.2 Different Types of Transition

The transition pipe consists of gradual change of cross-section from circular to 4

lobed cross-sections. Other than the α transition discussed in section 3.2.1 bullet 8, there is also a β type of transition which is based on the relationship of the lobe area growth with length. In addition, applying a different transition multiplier, n , to α or β would generate a set of different transition curves. Moreover, a variable helix factor could also be introduced.

3.2.2.1 α transition

As defined in Equation (3.7), variable α is the ratio of lobe area at any intermediate stage to the total lobe area for fully developed lobes. In order to avoid discontinuity that would result from the use of a linear relationship, α was equated to a cosine relation of pipe length as defined in Equation (3.8). This cosine function of α , as shown below, gives a smooth transition.

$$\alpha = \left[\frac{1 - \cos \left[\pi \frac{x}{L} \right]}{2} \right] \quad (3.10)$$

3.2.2.2 β transition

Ganeshalingam (2002) indicated that there were two distinctive types of flow within the 4-lobed swirl pipe, namely the core flow and the lobe flow. It is clear from Figure 3.2.4 that, within the fully developed 4-lobed swirl pipe and the intermediate stage of the transition pipe, the core flow inside the inner circle consisted mainly of axial velocity, while the lobe flow in the lobe zones consisted mainly of tangential velocity.

It was therefore expected that defining the transition in terms of lobe area growth to the core area (circular area only) would give better results for 4-lobed transition. This was achieved by intruding a variable β , which is defined as a ratio of lobe area to the core area.

$$\beta = \frac{\frac{LA_i}{\pi R^2 - LA_i}}{\frac{LA_{FD}}{\pi R^2 - LA_{FD}}} \quad (3.11)$$

For the calculation of β type transition pipe, variable β then replaced α in Equation (3.7) and (3.8). Figure 3.2.5 depicts the lobe area development with the pipe length for α , β and linear transitions. It can be seen that the β transition provides a faster lobe development than α transition. Since the lobes, where tangential velocity is mainly concentrated, prevail for a longer length, it is expected that the β transition would result in greater swirl induction.

Ariyaratne (2005) carried out CFD modelling and confirmed that, as expected, β transition was more effective at swirl induction than α . Its value of swirl effectiveness was 5% greater than that of α . Therefore variable β will later be used in the calculation and creation of a transition pipe.

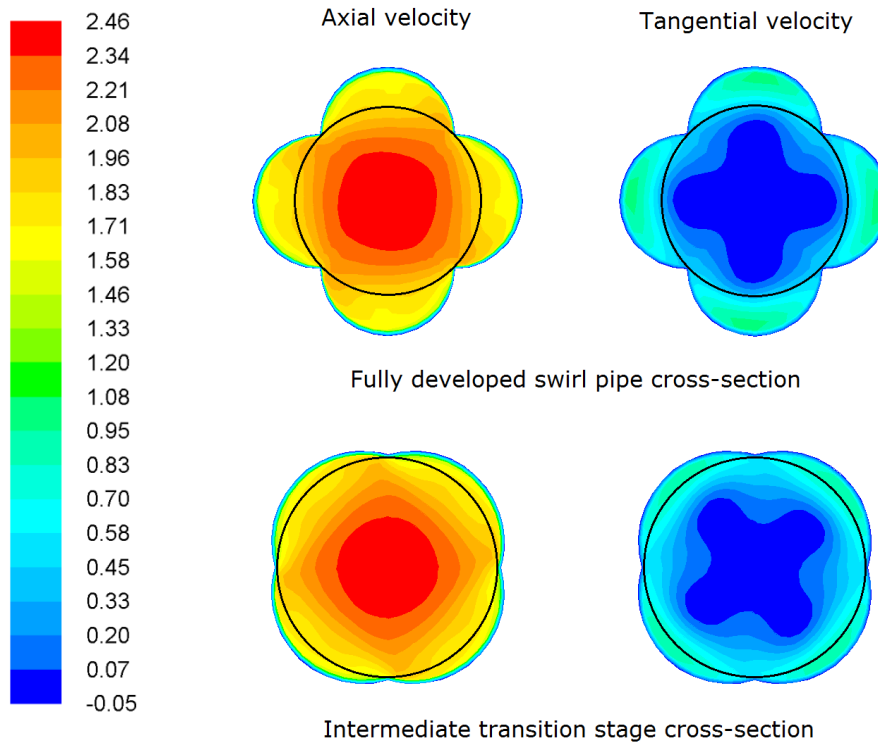


Figure 3.2.4 Axial and tangential velocity contours at fully developed and intermediate stage of transition pipe (2m/s inlet velocity).

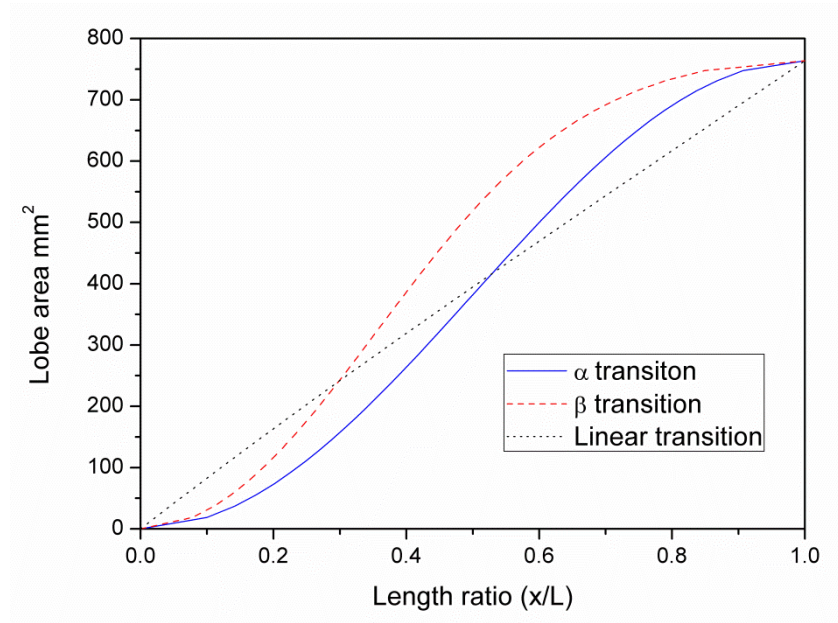


Figure 3.2.5 Lobe area developments with pipe length for α , β and linear transitions

3.2.2.3 Transition Multiplier

Applying a transition multiplier to variable α and β and Equation (3.10) and (3.11) change to:

$$\alpha = \left[\frac{1 - \cos \left[\pi \frac{x}{L} \right]}{2} \right]^n \quad (3.12)$$

and

$$\beta = \left[\frac{\frac{LA_i}{\pi R^2 - LA_i}}{\frac{LA_{FD}}{\pi R^2 - LA_{FD}}} \right]^n \quad (3.13)$$

Thus Equation (3.10) and (3.11) are instances of the transition multiplier being $n=1$. A series of transition curves can be created by varying the value of n . Generally, an n value smaller than 1 gives greater lobe area growth near the

start, while an n value larger than 1 decreases the lobe development near the start compared with n being 1. Besides, for the same value of transition multiplier n , the lobe development for β transition is nearer the start than for the α transition therefore a quicker lobe development for β transition.

Ariyaratne (2005) numerically compared the effect of different n values and found that the smaller the value of the transition multiplier n , the greater the tangential velocity generated, however the greater the pressure loss. She used the swirl effectiveness parameter as a balance of tangential velocity and pressure loss, and found that the swirl effectiveness was optimum at a value of $n=0.5$ where the lobes developed faster in the transition than with the original β transition case of $n=1$. This transition multiplier $n=0.5$ for β transition will therefore be used for the transition pipe creation.

3.2.2.4 Variable Helix

The types of transitions discussed above all have a constant change in twist with respect to the length, namely geodesic helices. Raylor (1998) proposed a brachistochrone helix for a swirl pipe, where the twist has a power law relationship with respect to length ratio.

$$Twist = \left(\frac{x}{L}\right)^t \times TwistAngle$$

t = power law variable for twist which can be changed to apply an increasing or decreasing helix as desired.

When

$t < 1$: the helix is faster nearer the start of the transition

$t = 1$: constant or geodesic helix where twist is linear with length

$t > 1$: the helix is faster nearer the end of the transition

It was found that, as the t value, and thereby the helix increases, the tangential velocity generated increases together with the pressure drop (Ariyaratne, 2005). However, the study of Ariyaratne (2005) showed that no advantage was gained from the use of the variable helix studied over the geodesic helix for entry transition. She argued that although the variable helix gives 'optimum swirl' it is not the 'minimal cost' design. She concluded that, based on the swirl effectiveness criterion, geodesic proves to be better than the variable helix designs for an entry transition. Therefore, the geodesic helix $t=1$ will be adopted later on in the geometry creation process.

3.2.3 Spreadsheet for 4-lobed Transition Pipe

Based on the transition pipe calculation and the optimisation results from Ariyaratne (2005), the spreadsheet for 4-lobed transition pipe was generated as shown in Appendix 3.1 Spreadsheet for 4-Lobed Transition Pipe. This spreadsheet only includes necessary data for geometry creation using Pro/Engineer, data such as x and y co-ordinates, lobe areas are not exhibited explicitly. The basic information of the transition pipe defined by the spreadsheet is summarized as below:

Lobe number	4	
Total length	100mm	Length of transition based on one lobe twisted 90 degrees
Equivalent diameter	50mm	
Pitch: Diameter ratio	8:1	
Type of transition	β	
Transition multiplier	$n=0.5$	
Variable helix	$t=1$	Geodesic helix
Twist degrees	90°	Degrees of twist per metre
Twist direction	-1	-1=clockwise
r_f	13.8182mm	Lobe radius (fully developed)
R_{cs}	19.5418mm	Minimum core radius (fully developed)
LA(total)	763.7834mm^2	Lobe area for fully developed swirl pipe
Total cross-section area	1963.4954mm^2	

3.2.4 Spreadsheet for 4-lobed Swirl Inducing Pipe

The swirl inducing pipe forms as the fully developed 4-lobed swirl pipe cross-section (as shown in Figure 3.2.1) extends helically along the pipe axis. The core radius R_{cs} and lobe radius r_f for the fully developed swirl pipe section can be calculated from section 3.2.1 bullets 1~3. The swirl inducing pipe has a pitch to diameter ratio of 8 indicating that the length for the 4-lobed cross-section rotates by 360 degrees is equivalent to 8 diameters that is 400mm. From Equation (3.9), the twist degree is 900 degrees per metre. Therefore, if we create one cross-section in the interval of every 10mm along the pipe, the twist angle between the adjacent two cross-sections is 9 degrees.

Based on above discussion, the spreadsheet was created which includes 21 sections along the pipe axis. The 21 sections will form a 200mm length swirl pipe that is half of the 400mm length swirl inducing pipe. A detailed spreadsheet for the swirl inducing pipe is presented in Appendix 3.2 Spreadsheet for 4-Lobed Swirl Inducing Pipe.

3.3 Geometry Creation

3.3.1 Transition Pipe Creation

The transition pipe was created in a Pro/Engineer software using an advanced swept blend feature. The swept blend is a combination between a general blend and a sweep feature in the Pro/Engineer. It allows for blending together several varying cross-sections following a specific trajectory.

Originally 10 cross-sections including the circle and the fully developed swirl pipe section were sketched in the X-Y plane based on a constant γ interval of 5 degrees. The use of constant γ interval cross-sections was because γ directly signifies the lobe changes and provides better accuracy in sweeping one

cross-section onto the following one when the swept blend is used in the Pro/Engineer. In the swept blend process:

- Selected Z-axis as trajectory so the cross-sections were normal to the trajectory.
- All the sketched sections in the X-Y plane were made to have the same number of 4 curves and consequently 4 intersection points (Figure 3.3.1a).
- Specified a start point from the four points for each sections making sure that the points were traceable and following a clockwise twist.
- Specified the depths between the two adjacent two cross-sections according to the spreadsheet.
- Confirmed the above operations and the cross-sections were swept and blended along Z-axis transforming them into the transition pipe as shown in Figure 3.3.1c.

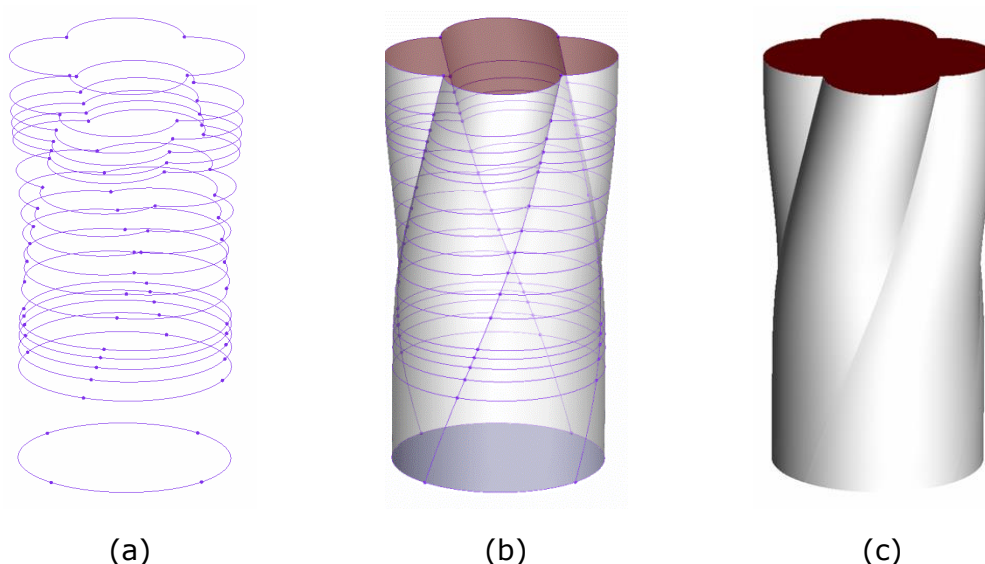


Figure 3.3.1 Demonstration of 18 sections used to sweep and blend into transition pipe

It was noticed that, due to the application of a transition multiplier $n=0.5$ for the β transition, γ increase and x/L increment did not form a linear correlation. As shown in Figure 3.3.2, there are steeper cross-section transitions in the start 5

degrees γ interval ($45^\circ \rightarrow 50^\circ$) and the end γ interval of 5 degrees ($85^\circ \rightarrow 90^\circ$). An attempt was later made to allow more accurate transitions between the 1st and 2nd section and between the final and penultimate section by adding 4 intermediate sections respectively. The added sections are marked in red open squares as demonstrated in Figure 3.3.2. Therefore, 18 sections (see Figure 3.3.1a) were used in the sweeping and blending to create the final transition pipe model. A detailed 4-lobed transition development of the 18 sections and the start points is also available in Appendix 3.3 Cross-section Development of the 4-Lobed Transition Pipe.

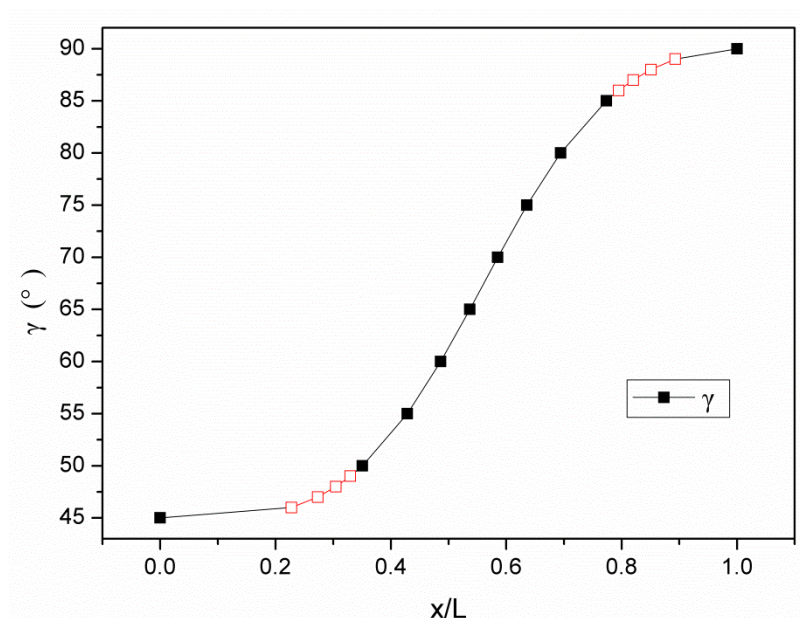


Figure 3.3.2 Graph of γ versus length for transition pipe

(Red open squares indicate sections inserted afterward)

3.3.2 Swirl Inducing Pipe Creation

The same swept blend method was adopted in creating the 200mm length, 50mm equivalent diameter swirl inducing pipe, which is half of the full swirl inducing pipe.

The swept blend process was carried out as below:

- 21 sections of fully developed 4-lobed cross-sections were sketched in the X-Y plane as shown in Figure 3.3.3a.
- The 21 sections were evenly distributed between the start and the end of the half swirl inducing pipe along Z-axis with the twist angle between the adjacent two sections were 9° .
- The distance between the adjacent two sections were evenly set to be $x/L=0.05$ (10mm). The twist degree with pipe length increase is shown in Figure 3.3.4 which exhibits a linear relationship.
- Specified a start point at each section and made sure the start points rotate clockwise. The feature swept the 2D face along Z trajectory onto the following face one by one and blended them into the swirl inducing pipe as shown in Figure 3.3.3c.

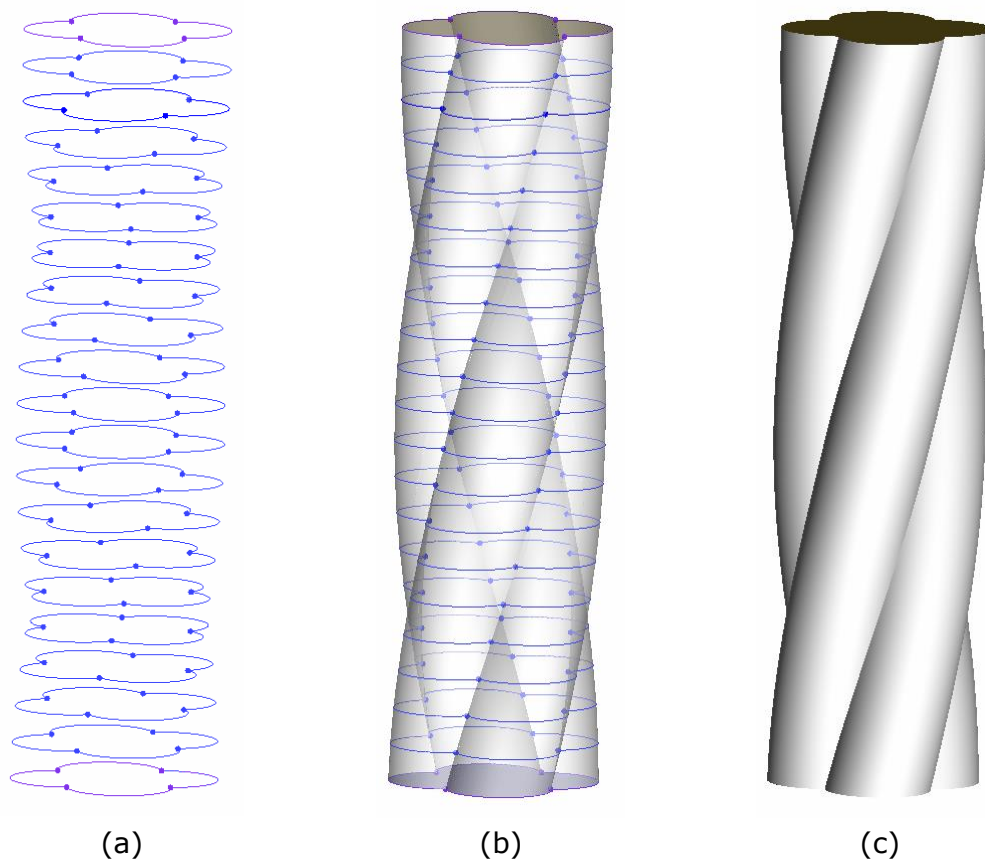


Figure 3.3.3 Demonstration of 21 sections used to sweep and blend into half of the full swirl inducing pipe

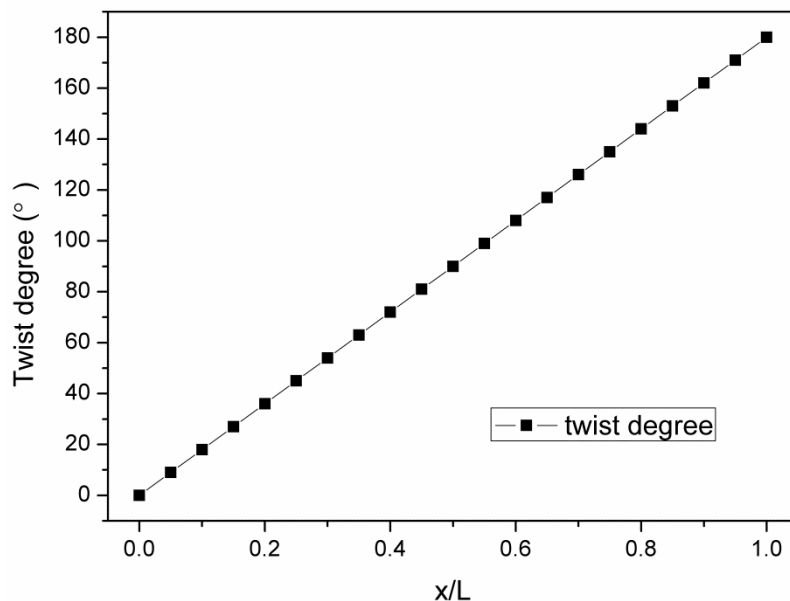


Figure 3.3.4 Graph of twist versus length for swirl inducing pipe

3.3.3 Optimized Swirl Pipe Creation

Ariyaratne (2005) connected either the transition prior to the 400mm length swirl inducing pipe as the entry transition (see Figure 3.3.5a) or after the 400mm length swirl inducing pipe as the exit transition (see Figure 3.3.5b). She found that the 4-lobed β transition with transition multiplier $n=0.5$ was optimum in both cases of entry and exit transition from several geometries tested. The entry transition was found to be able to increase swirl generated at the exit of the swirl pipe and reduce pressure losses. While the use of exit transition reduced exit pressure losses, decreased the swirl decay rate thereby sustaining the induced swirl for longer distance.

According to Ariyaratne's suggestion, a swirl pipe comprising a 400mm length swirl inducing pipe, an entry transition pipe prior to it and an exit transition pipe after it should be considered to be an 'optimised swirl pipe'. This type of optimised swirl pipe is not entirely understood and will be studied in this investigation.

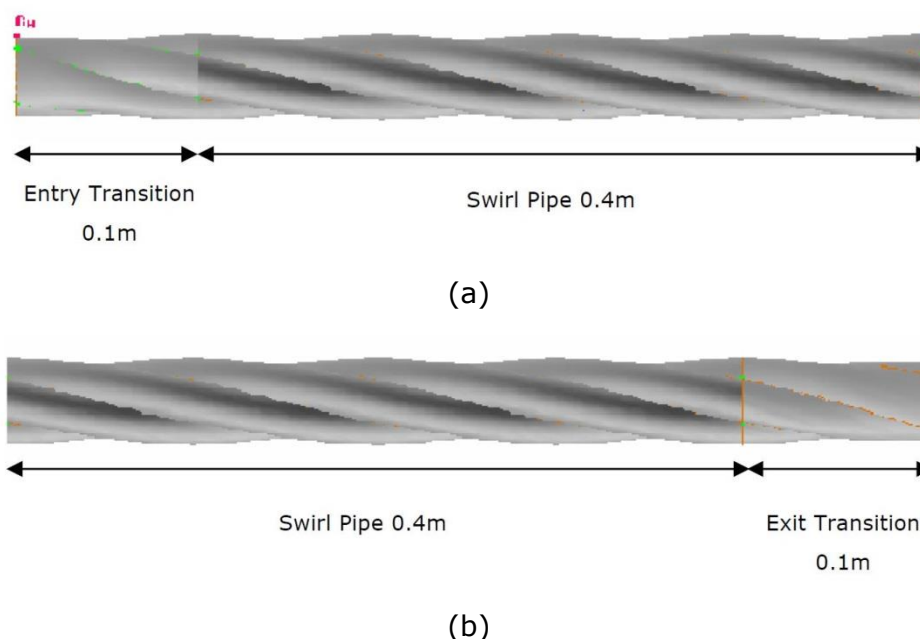


Figure 3.3.5 Entry transition pipe prior to (a) and exit transition pipe after (b) swirl inducing pipe (after Ariyaratne, 2005)

In the current work the optimised swirl pipe was created in the Pro/Engineer using an assemble tool which brings together several parts in such a way as to fully constrain them. That is, the relative rotation and location of the parts to each other has to be specified in all three dimensions. This is done primarily through two types of constraints: Mate and Align. The Mate constraint orients two planes or faces of two parts in parallel to each other in opposing direction allowing the 'outside' planes face each other. While the Align constraints two faces parallel to each other in the same direction. This means that the faces of the components would be on the same side of a datum plane.

In the assembly of a solid optimised swirl pipe:

- The 100mm length entry transition pipe was selected as the first component which is at the top of the hierarchical 'tree'.
- A 200mm length swirl inducing pipe was attached to the outlet of the entry transition.
- A second 200mm length swirl inducing pipe was connected to the

exposed 4-lobed face of the first swirl inducing pipe.

- A second 100mm length transition pipe was attached to the second swirl inducing pipe with the two 4-lobed faces opposite to each other.
- The joints of every two parts was constrained using two align and one mate constraints.
- The four components were then merged into one component and saved as a .STP file for use with ICED CFD.

The assembled optimised 4-lobed swirl pipe is displayed in Figure 3.3.6 which has a total length of 600mm, equivalent diameter of 50mm and a pitch to diameter ratio of 8:1.

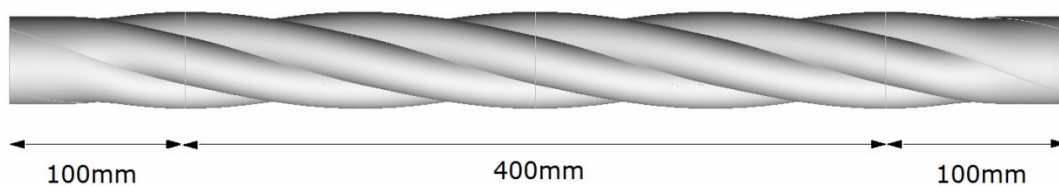


Figure 3.3.6 The optimized 600mm length 4-lobed swirl pipe

However, in this configuration:

- The swirl pipe has the lobed cross-section rotated by 540° (one and a half swirl) instead of 360° (one swirl), which was used in the previous designs.
- The longer swirl pipe results in more pressure loss due to the increase in contact area and thus friction.
- When the entry transition pipe was used in conjunction with the swirl pipe, a higher tangential velocity was generated. However, the induced swirl appeared to be constrained by the swirl inducing pipe geometry. A shorter length of swirl inducing pipe will therefore be required to generate an equivalent amount of swirl (Ariyaratne, 2005).

It is expected that with the inclusion of transitions, a shorter length of swirl inducing pipe than previously determined should be optimum. Therefore, to further optimize the swirl pipe, a configuration comprises a 100mm transition pipe initially, plus a 200mm swirl inducing pipe and finally a 100 transition pipe is proposed. This configuration, as shown in Figure 3.3.7, has one swirl, shorter length, and is expected to be more cost effective in swirl induction.

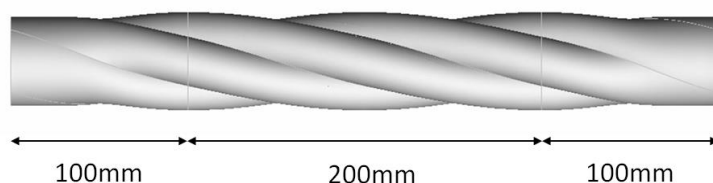


Figure 3.3.7 The further optimized 400mm length 4-lobed swirl pipe

The two swirl pipe configurations shown in Figure 3.3.6 and 3.3.7 were numerically compared in terms of pressure loss, swirl intensity, and swirl induction effectiveness in Chapter 5.

3.4 Conclusions

- Spreadsheets for transition pipe and swirl inducing pipe were generated according to the calculation.
- The solid 3D model of the transition pipe and swirl inducing pipe were created from the spreadsheets using Pro/Engineer.
- A 600mm length optimised swirl pipe and a 400mm length further optimised swirl pipe were introduced and assembled for further simulation and rapid prototyping.

CHAPTER 4: COMPUTATIONAL FLUID DYNAMICS METHODOLOGY

4.1 Introduction

Computational fluid dynamics or CFD is the analysis of systems involving fluid flow, heat transfer and associated phenomena such as chemical reactions by means of computer-based simulation. The technique is very powerful and spans a wide range of industrial and non-industrial application areas (H.K.Versteeg and W.Malalasekera, 2010). CFD has several unique advantages over experiment-based approaches to the fluid systems. For instance, it substantially reduces time and costs of new designs and has the ability to study systems where controlled experiments are difficult or impossible to perform. The CFD method is employed in the present research to supplement the experimental investigations because of its cost effectiveness and the limitations of the available experimental techniques.

In CFD, applying the fundamental laws of mechanics to a fluid flow, including turbulent ones, gives the governing equations for fluid flow which represent mathematical statements of the conservation laws of physics (H.K.Versteeg and W.Malalasekera, 2010, Bhaskaran and Collins, 2003):

- The mass of a fluid is conserved
- The rate of change of momentum equals the sum of the forces on a fluid particle (Newton's second law)
- The rate of change of energy is equal to the sum of the rate of heat addition to and the rate of work done on a fluid particle (first law of thermodynamics)

The partial differential equations for the three fundamental principles are the continuity equation, the momentum equations, and the energy equation respectively. They are termed the 'Navier-Stokes Equation'. Since this study assumes the swirl flows to be isothermal, only the continuity and momentum equations are concerned.

Continuity equation for mass conservation:

The continuity equation was derived by applying the law of conservation of mass to a fluid flow making sure that the rate of increase of mass inside the control volume is equal to the net rate of mass into and out of the control volume across its faces. The continuity equation for an incompressible flow, in Cartesian form is given by:

$$\frac{\partial \rho}{\partial t} + \nabla \cdot (\rho \vec{V}) = 0 \quad (4.1)$$

Where $\partial \rho / \partial t$ represents the rate of change of mass with time in an infinitesimal control volume; $\nabla \cdot (\rho \vec{V})$ describes the convection of the mass through the control volume.

Momentum equations for momentum conservation:

Apply the Newton's Second Law of Motion to the fluid flow and ensure that the rate of change of momentum of the fluid particles is equal to the total force due to surface stresses and body forces acting in an aligned direction of a chosen coordinate axis. The momentum equation is obtained in terms of the viscous stress acting on a particle in the fluid as:

$$\frac{\partial(\rho \vec{V})}{\partial t} + \rho(\vec{V} \cdot \nabla) \vec{V} = \rho \vec{f} + (-\nabla p + \nabla \cdot \tau_{ij}) \quad (4.2)$$

Where $\partial(\rho\vec{V})/\partial t$ represents the rate of change of momentum with time; $\rho(\vec{V} \cdot \nabla)\vec{V}$ describes the advection of momentum; $\rho\vec{f}$ represents the body forces (include gravity and buoyancy); $(-\nabla p + \nabla \cdot \tau_{ij})$ represents the forces due to pressure and stress gradients in the fluid.

It is not possible to solve the above partial differential equations (PDEs) analytically for most engineering problems. Therefore approximate modelling methods have been developed to calculate the statistical characteristics of the turbulent motion by discretising the flow equations to produce a numerical analogue of them.

The strategy of CFD is to replace the continuous problem domain with a discrete domain using a grid. In the discrete domain, each flow variable is defined only at the grid points (Bhaskaran and Collins, 2003). When the boundary and initial conditions that are specific to the flow problem being simulated have been applied, they can be solved using a variety of direct or iterative solution techniques producing a numerical simulation of the given flow problem (Shaw, 1992).

4.2 Modelling Turbulence

All flows encountered in engineering practice become unstable above a certain Reynolds number. For pipe flows, the Reynolds number is defined by $Re=(U \times D \times \rho)/\mu$ where U is velocity, ρ is density, and μ is viscosity. At low Reynolds numbers flows are laminar. At higher Reynolds numbers flows are observed to become turbulent. A chaotic and random state of motion develops in which the velocity and pressure fluctuate continuously with time within substantial regions of flow. The turbulent swirl flow in this study is a combination of vortex and axial motions. Due to the presence of a tangential velocity component, swirl flow is always accompanied by an increase in velocity fluctuations (Fokeer, 2006, Algifri

et al., 1988).

Turbulence causes the appearance of eddies in the flow with a wide range of length and time scales that interact in a dynamically complex way. Due to the importance of turbulence in engineering practice, several numerical methods have been developed to capture the important effects of the turbulence. The methods can be grouped into the following three categories (H.K.Versteeg and W.Malalasekera, 2010):

- **Turbulence models for Reynolds-averaged Navier–Stokes (RANS)**

equations: In this approach, prior to the application of numerical methods, the Navier–Stokes equations are time averaged. It was found that extra terms, the so-called Reynolds stresses, appear in the time-averaged (or Reynolds-averaged) flow equations due to the interactions between various turbulent fluctuations. These Reynolds stresses are modelled with classical turbulence models, among which the best known are the standard k - ϵ turbulence model and its variations, and the Reynolds stress model. This approach predicts the mean flow and the effects of turbulence on mean flow properties. The computing resources required for reasonably accurate flow computations are modest, so this approach has been the mainstay of engineering flow calculations over the last three decades. Besides, RANS turbulence models are the only modelling approach for steady state simulation of turbulent flows. Due to its shorter simulation time, simplified post-processing, and the importance and interest of time-averaged values from an industrial prospect, steady RANS is the most widely used approach for industrial flows.

- **Large eddy simulation:** LES is an intermediate form of turbulence calculations which tracks the behaviour of the larger eddies. The method

involves space filtering of the unsteady Navier–Stokes equations prior to the computations, which passes the larger eddies and rejects the smaller eddies. The motion of the largest eddies is directly resolved in the calculation in at least a portion of the domain, while eddies smaller than the mesh size are modelled by means of a so-called sub-grid scale model. Conceptually, LES is situated somewhere between DNS and RANS. LES is inherently an unsteady method and unsteady flow equations must be solved, so the demands on computing resources in terms of storage and volume of calculations are large. LES has the potential for improved accuracy when the resolution of the largest eddies is important or when unsteady data is needed. However, this method is computationally expensive due to the required higher grid resolution and small time steps for unsteady simulation which generates long run times and large volumes of data.

- **Direct numerical simulation (DNS):** these simulations compute the mean flow and all turbulent velocity fluctuations. The unsteady Navier–Stokes equations are solved on spatial grids that are sufficiently fine that they can resolve the Kolmogorov length scales at which energy dissipation takes place and with time steps sufficiently small to resolve the period of the fastest fluctuations. These calculations are highly costly in terms of computing resources, so the method is not used for industrial flow computations.

It is theoretically possible to resolve the Navier-Stokes equations for the turbulent swirl flow using Direct Numerical Simulation (DNS); however it is not feasible for practical engineering problems given that the volume of the computational domain used in this research is very large and it is prohibitive to obtain sufficiently fine grid resolution everywhere required for DNS.

Considering the intensive cost of NDS in terms of computing resource and the unaffordable run time for the calculation of the whole spectrum of turbulence which can be of small scales and high frequency, the alternative RANS and LES approaches will be adopted in this study for the investigation of swirl pipe induced swirl flow as both methods result in a modified set of Navier-Stokes equations that are computationally less expensive to solve.

The initial simulation work (in Chapter 5 and 6) will focus on the mean flow properties using a RANS approach since the time-averaged values are of interest for industrial applications. LES (in Chapter 7) will be used as a supplement to study the fluctuation property of some variables of the swirl flow. The principles and models in terms of the LES approach will be introduced in Chapter 7. This approach can be affordable to some extent as the filtering operation results in mesh resolution requirements that are much less restrictive than with DNS, though in practice, extremely fine meshes and large computer resource are still required.

4.2.1 RANS Approach

For most engineering purposes it is unnecessary to resolve the details of the turbulent fluctuations. Information about the time-averaged properties of the flow (e.g. mean velocities, mean pressures, mean stresses etc.) are almost always satisfied for most problems. Therefore, the vast majority of turbulent flow computations has been and for the foreseeable future will continue to be carried out with procedures based on the Reynolds-averaged Navier–Stokes (RANS) equations (H.K.Versteeg and W.Malalasekera, 2010).

In Reynolds averaging, the effects of fluctuation on the mean flow are investigated using the Reynolds decomposition (Reynolds averaging) approach. The Navier-Stokes equations are time averaged over a large enough time

compared to the typical timescale of turbulent fluctuation in order to average out the unsteadiness of a turbulent flow. Flow variables \mathbf{u} (hence u , v and w) and pressure p in the instantaneous (exact) Navier-Stokes equations are substituted by the sum of a mean and fluctuation component.

$$\mathbf{u} = \mathbf{U} + \mathbf{u}' \quad u = U + u' \quad v = V + v' \quad w = W + w' \quad p = P + p'$$

Where U is the time average of u (the steady component), u' is the fluctuation part (or perturbations, their average equals zero). Substituting the Reynolds decomposition into the equations for conservation of mass and momentum and taking the time average by applying the rules which govern time averages of fluctuating properties (H.K.Versteeg and W.Malalasekera, 2010). This yields the Reynolds Averaged Navier-Stokes Equations for incompressible flow:

$$\frac{\partial(u_i)}{\partial t} + \frac{\partial}{\partial x_j}(u_i u_j) = -\frac{1}{\rho} \frac{\partial p}{\partial x_i} + \frac{\partial}{\partial x_j} \left[\nu \left(\frac{\partial u_i}{\partial x_j} + \frac{\partial u_j}{\partial x_i} \right) \right] - \overline{u'_i u'_j} \quad (4.3)$$

The process of time averaging has introduced new terms $-\overline{u'_i u'_j}$ called Reynolds stress. This nonlinear Reynolds stress term requires additional modelling to close the RANS equation for solving, and has led to the creation of many different turbulence models of which the standard k - ϵ turbulence model and its variations (RNG k - ϵ model and Realizable k - ϵ model), and the Reynolds stress model are widely used.

In k - ϵ models, the Reynolds stress tensor can be calculated using the isotropic eddy viscosity assumption that the ratio between Reynolds stress and mean rate of deformation is the same in all directions. The k - ϵ model family are two equation models. Two transport equations, one for the turbulent kinetic energy k , and one for the rate of its dissipation ϵ , are solved. These are then used to calculate the turbulent viscosity, μ_t , to close the RANS equations. While, abandoning the assumption of isotropic eddy viscosity, the RSM closes the RANS

by solving transport equations for Reynolds stresses, together with an equation for the dissipation rate.

4.2.1.1 The Standard k- ϵ Model

The standard k- ϵ model, proposed by Launder and Spalding (1972) is a two-equation turbulence model that allows the determination of both the turbulent length and time scale by solving two separate transport equations. It is a semi-empirical model, and the derivation of the model equations relies on phenomenological considerations and empiricism.

The standard k- ϵ model has two model equations; one for kinetic energy k and one for its dissipation rate ϵ . k and ϵ are used to define velocity scale v and length l representative of the large-scale turbulence as follow:

$$\begin{aligned} v &= k^{1/2} \\ l &= \frac{k^{3/2}}{\epsilon} \end{aligned} \quad (4.4)$$

Applying dimensional analysis, the eddy viscosity is specified as:

$$\mu_t = C_p v l = \rho C_\mu \frac{k^2}{\epsilon} \quad (4.5)$$

where C_μ is a dimensionless constant.

The standard k- ϵ model uses the following transport equations for k and ϵ respectively:

$$\frac{\partial(\rho k)}{\partial t} + u_i \frac{\partial(\rho u_j k)}{\partial x_j} = \frac{\partial}{\partial x_j} \left(\frac{\mu_t}{\sigma_k} \frac{\partial k}{\partial x_j} \right) + \mu_t \frac{\partial u_i}{\partial x_j} \left(\frac{\partial u_i}{\partial x_j} + \frac{\partial u_j}{\partial x_i} \right) - \rho \epsilon \quad (4.6)$$

and

$$\frac{\partial(\rho\varepsilon)}{\partial t} + u_i \frac{\partial(\rho u_j \varepsilon)}{\partial x_j} = \frac{\partial}{\partial x_j} \left(\frac{\mu_t}{\sigma_\varepsilon} \frac{\partial \varepsilon}{\partial x_j} \right) + C_{\varepsilon 1} \frac{\varepsilon}{k} \mu_t \frac{\partial u_i}{\partial x_j} \left(\frac{\partial u_i}{\partial x_j} + \frac{\partial u_j}{\partial x_i} \right) - \rho C_{\varepsilon 2} \frac{\varepsilon^2}{k} \quad (4.7)$$

In words the equations are:

Rate of change of k or ε + Transport of k or ε by convection = Transport of k or ε by diffusion + Rate of production of k or ε - Rate of destruction of k or ε .

Production and destruction of turbulent kinetic energy are always closely linked. Dissipation rate ε is large where production of k is large. The model equation for ε assumes that its production and destruction terms are proportional to the production and destruction terms of the k-equation.

The inherent production of turbulence is what is responsible for the transfer of energy from the mean flow to the turbulence, and is counterbalanced by the interaction of the Reynolds stresses and mean velocity gradient. On the other hand, the destruction term represents the dissipation of energy into heat due to viscous nature of the flow.

The equations contain five adjustable constants: μ_t , σ_k , σ_ε , $C_{\varepsilon 1}$ and $C_{\varepsilon 2}$. The standard k- ε model employs values for the constants that are obtained by comprehensive data fitting for a wide range of turbulent flows:

$$\mu_t = 0.09 \quad \sigma_k = 1.00 \quad \sigma_\varepsilon = 1.30 \quad C_{\varepsilon 1} = 1.44 \quad C_{\varepsilon 2} = 1.92$$

The advantage of robustness, economy, and reasonable accuracy for a wide range of turbulent flows make the standard k- ε model popular for industrial flows. However this model does not perform very well for flows with boundary

layer separation, sudden changes in the mean strain rate such as swirling and rotating flows and flows over curved surfaces. Moreover, the k - ϵ model is based on the Boussinesq hypothesis, which inherently assumes that the turbulent viscosity is isotropic. This is a major source of error when using the k - ϵ model for simulating strong swirling flows as turbulent eddy viscosity is an anisotropic quantity which is affected by geometry.

4.2.1.2 RNG k - ϵ Model and Realizable k - ϵ Model

Both the RNG and realizable k - ϵ models are the variations of the standard k - ϵ model. The RNG turbulence model is derived from the instantaneous Navier-Stokes equations, using a mathematical technique called “renormalization group” (RNG) methods. The analytical derivation results in a model with constants different from those in the standard k - ϵ model, and additional terms and functions in the transport equations for k and ϵ . The RNG model includes the following refinements (ANSYS, 2011a):

- The RNG k - ϵ model has an additional term in its ϵ equation that improves the accuracy for rapidly strained flows.
- The effect of swirl on turbulence is included in the RNG model, enhancing accuracy for swirling flows.
- The RNG theory provides an analytical formula for turbulent Prandtl numbers, while the standard k - ϵ model uses user-specified, constant values.
- The standard k - ϵ model is a high-Reynolds number model, the RNG theory provides an analytically derived differential formula for effective viscosity that accounts for low-Reynolds number effects.

Therefore, the RNG k - ϵ model is more accurate and reliable for a wider class of flow than the standard k - ϵ model.

The realizable k - ϵ model proposed by Shih et al. (1995) differs from the standard k - ϵ model in two important ways:

- The realizable k - ϵ model contains an alternative formulation for the turbulent viscosity.
- A modified transport equation for the dissipation rate ϵ has been derived from an exact equation for the transport of the mean-square vorticity fluctuation.

The term “realizable” means that the model satisfies certain mathematical constraints on the Reynolds stresses, consistent with the physics of turbulent flows. Neither the standard k - ϵ model nor the RNG k - ϵ model is realizable.

Both the realizable and RNG k - ϵ models have shown substantial improvements over the standard k - ϵ model where the flow features include strong streamline curvature, vortices, and rotation. Since the model is still relatively new, it is not clear in exactly which instances the realizable k - ϵ model consistently outperforms the RNG model. However, initial studies have shown that the realizable model provides the best performance of all the k - ϵ model versions for several validations of separated flows and flows with complex secondary flow features (ANSYS, 2011a).

4.2.1.3 Reynolds Stress Model (RSM)

Reynolds stress model abandons the Boussinesq hypothesis of isotropic eddy viscosity. It closes the Reynolds-averaged Navier-Stokes equations by solving transport equations for the Reynolds stresses, together with an equation for the dissipation rate. This means that seven additional transport equations are required in 3D flows.

The transport equation for the transport of the Reynolds Stresses is (Speziale et al., 1991):

$$\begin{aligned} & \frac{\partial}{\partial t}(\rho \overline{u'_i u'_j}) + \frac{\partial}{\partial x_k}(\rho u_k \overline{u'_i u'_j}) = \\ & -\rho \left(\overline{u'_i u'_k} \frac{\partial u_j}{\partial x_k} + \overline{u'_j u'_k} \frac{\partial u_i}{\partial x_k} \right) - \frac{\partial}{\partial x_k} \left[\left(\mu + \frac{\mu_t}{\sigma_k} \right) \frac{\partial}{\partial x_k} (\overline{u'_i u'_j}) \right] + p \left(\frac{\partial u'_i}{\partial x_j} + \frac{\partial u'_j}{\partial x_i} \right) - \frac{2}{3} \delta_{ij} \rho \varepsilon \end{aligned} \quad (4.8)$$

Where the terms on the left hand side of Equation (4.8) are local time derivative and convection, the terms on the right hand side are stress production, diffusion, pressure-strain and dissipation respectively. μ and μ_t are the dynamic and eddy viscosity, with δ_{ij} being the Kronecker delta function.

The pressure-strain term is modelled by

$$\begin{aligned} p \left(\frac{\partial u'_i}{\partial x_j} + \frac{\partial u'_j}{\partial x_i} \right) = & -\rho \varepsilon \left(c_{s1} a_{ij} - c_{s2} \left(a_{ik} a_{kj} + \frac{1}{3} a_{mn} a_{mn} \delta_{ij} \right) \right) - c_{r1} P a_{ij} + \rho k S_{ij} (c_{r2} \\ & - c_{r3} \sqrt{a_{ij} a_{ij}}) + c_{r4} \rho k \left(a_{ik} S_{jk} + S_{ik} a_{jk} - \frac{2}{3} a_{mn} S_{mn} \delta_{ij} \right) + c_{r5} \rho k (a_{ik} \Omega_{jk} + a_{jk} \Omega_{ik}) \end{aligned} \quad (4.9)$$

where a_{ij} is the Reynolds-Stress anisotropy term, S_{ij} the strain rate and Ω_{ij} the vorticity, with $a_{ij} = \frac{\overline{u'_i u'_j}}{k} - \frac{2}{3} \delta_{ij}$, $S_{ij} = \frac{1}{2} \left(\frac{\partial u_j}{\partial x_i} + \frac{\partial u_i}{\partial x_j} \right)$, $\Omega_{ij} = \frac{1}{2} \left(\frac{\partial u_i}{\partial x_j} - \frac{\partial u_j}{\partial x_i} \right)$ and $P = (1/2) P_{kk}$, k is the turbulence kinetic energy, and ε the turbulence eddy dissipation rate computed from the additional transport equation

$$\frac{\partial \rho \varepsilon}{\partial t} + \frac{\partial}{\partial x_k} (\rho u_k \varepsilon) = \frac{\partial}{\partial x_k} \left[\left(\mu + \frac{\mu_t}{\sigma_\varepsilon} \right) \frac{\partial \varepsilon}{\partial x_k} \right] + \frac{\varepsilon}{k} (c_{\varepsilon 1} P - c_{\varepsilon 2} \rho \varepsilon) \quad (4.10)$$

The various constants used in this RSM are $\rho_k=0.68$, $\rho_\varepsilon=1.3$, $c_{\varepsilon 1}=1.45$, $c_{\varepsilon 2}=1.83$, $c_{s1}=1.7$, $c_{s2}=-1.05$, $c_{r1}=1.7$, $c_{r2}=0.9$, $c_{r3}=0.8$, $c_{r4}=0.625$, $c_{r5}=0.2$.

Since the RSM accounts for the effects of streamline curvature, swirl, rotation, and rapid changes in strain rate in a more rigorous manner than one-equation and two-equation models, it has greater potential to give accurate predictions for complex flows (ANSYS, 2011a).

4.2.2 Near Wall Treatment for Wall-Bounded Turbulence Flows

Turbulent flows are significantly affected by the presence of walls. In fluid dynamics, the boundary condition at a stationary wall is one of no-slip boundary condition, that all three components of the fluid velocity on a solid surface are equal to the respective velocity components of the surface (Lauga et al., 2005). In order to satisfy this, the mean velocity at the wall has to be zero, thereby creating a steep velocity gradient (from zero at the walls to the mean flow velocity at the core) very close to the wall. This gives rise to the so-called “near-wall region”.

The k - ϵ models and the RSM discussed above are designed for modelling turbulent core flows and therefore the prediction will be inaccurate in the “near-wall region”, which is a crucial region for the successful prediction of wall-bounded turbulent flows. Special wall modelling procedures are therefore needed to be implemented to make these turbulence models suitable for wall-bounded flows.

The turbulent boundary layer adjacent to a solid surface is composed of two regions (H.K.Versteeg and W.Malalasekera, 2010, ANSYS, 2011a):

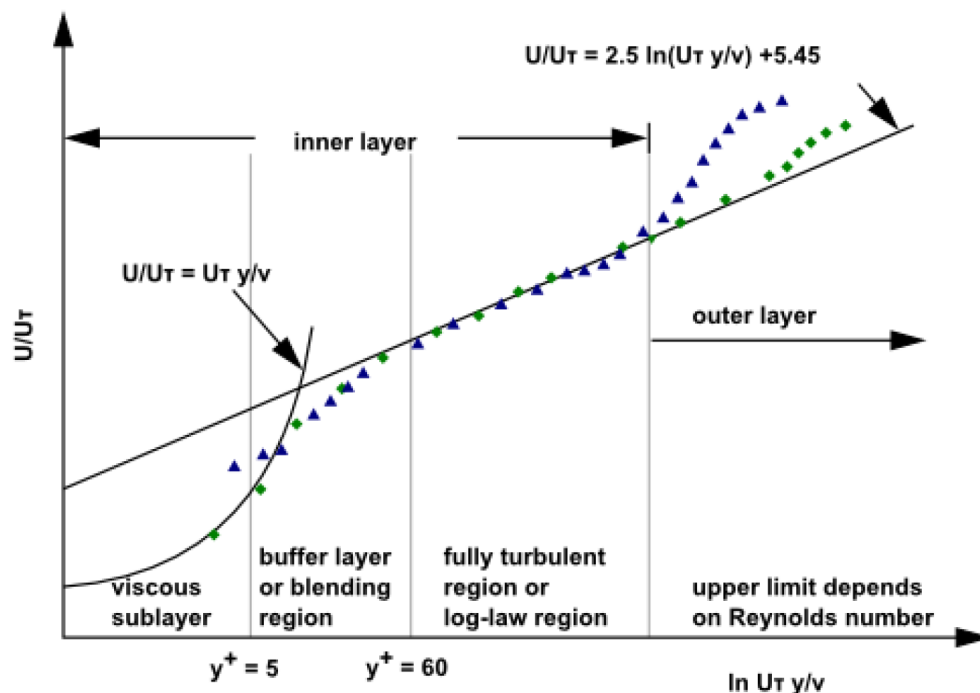


Figure 4.2.1 Near-Wall Region in Turbulent Flows (after ANSYS 2011a)

- The inner region:** 10-20% of the total thickness of wall layer; the shear stress is (almost) constant and equal to the wall shear stress τ_w . Within this region there are three zones. In order of increasing distance from the wall it has:
 - The linear (viscous) sublayer: the innermost layer where flow is almost laminar because the effects of turbulence are damped out by the wall itself. Viscous stresses dominate the flow adjacent to surface.
 - The buffer layer: viscous and turbulent stresses are of similar magnitude.
 - The log-law layer (or fully turbulent region): this is a region where the boundary layer and the external flow merge. Turbulence plays a major role.
- The outer region or law-of-the-wake layer:** inertia-dominated core flow far from wall; free from direct viscous effects.

In order to resolve the velocity gradient and better predict the flow behaviour in the near-wall region, a higher mesh density and special wall modelling

procedures are therefore required. The turbulence models previously discussed are primarily valid for fully turbulent flows. Close to the solid walls, there are inevitably regions where the local Reynolds number of turbulence is so small that viscous effects predominate over turbulent ones. Consideration must be given to make the models suitable for wall-bounded flows. Thus the overall success of all modern turbulence models is determined in large by the treatment of the boundary conditions at solid walls (Chen and Patel, 1988).

Generally, there are two approaches to model the near-wall regions, the wall function method and the near-wall modelling method (ANSYS, 2011a).

In the wall function method, the viscosity-affected inner region (viscous sublayer and buffer layer) is not resolved. Instead, semi-empirical formulas called “wall functions” are used to bridge the viscosity-affected regions between the wall and fully-turbulent region. The use of the wall functions obviates the need to modify the turbulence models to account for the presence of the wall.

In the near-wall modelling method, the turbulence models are modified to enable the viscosity-affected region to be resolved with a mesh all the way to the wall, including the viscous sublayer, namely the “near-wall modelling” approach.

4.2.2.1 Wall Functions

Depending on the choice of turbulent model, ANSYS FLUENT 14.0 offers the following choices of wall-function approaches:

- Standard Wall Functions
- Non-Equilibrium Wall Functions
- Scalable Wall Functions

1. Standard Wall Functions

The standard wall functions are based on the work of Launder and Spalding (1974), and have been most widely used in industrial flows. Standard wall functions are available with k- ϵ models and Reynolds Stress models.

In standard wall functions, the law-of-the wall for mean velocity yields

$$U^* = \frac{1}{k} \ln(Ey^+) \quad (4.11)$$

Where

$$U^* \equiv \frac{U_P C_\mu^{1/4} k_P^{1/2}}{\tau_W / \rho} \quad (4.12)$$

is the dimensionless velocity.

$$y^+ \equiv \frac{\rho C_\mu^{1/4} k_P^{1/2} y_P}{\mu} \quad (4.13)$$

is the dimensionless distance from the wall.

And

k = von Kármán constant (= 0.4187)

E = empirical constant (= 9.793)

C_μ = constant (= 0.09)

U_P = mean velocity of the fluid at the near-wall node P

k_P = turbulence kinetic energy at the near-wall node P

y_P = distance from point P to the wall

μ = dynamic viscosity of the fluid

τ_W = wall shear stress

The log-law is employed when $y^+ > 11.225$. When the mesh is that $y^+ < 11.225$ at the wall-adjacent cells, FLUENT applies the laminar stress-strain relationship that can be written as $U^+ = y^+$.

The wall boundary conditions for the solution variables, including mean velocity, temperature, species concentration, k , and ϵ , are all taken care of by the wall functions.

The standard wall functions work reasonably well for a broad range of wall-bounded flows. However, they tend to become less reliable when the flow situations depart from the ideal conditions that are assumed in their derivation. Among others, the constant-shear and local equilibrium assumptions are the ones that most restrict the universality of the standard wall functions. Accordingly, when the near-wall flows are subjected to severe pressure gradients, and when the flows are strongly non-equilibrium, the quality of the predictions is likely to be compromised.

The non-equilibrium wall functions are offered as an additional option, which can potentially improve the results in such situations.

2. Non-Equilibrium Wall Functions

In addition to the standard wall function described above, a two-layer-based, non-equilibrium wall function is also available (Kim and Choudhury, 1995). Non-equilibrium wall functions are available with k - ϵ models and Reynolds Stress Transport models.

The key elements in the non-equilibrium wall functions are as follows:

- Launder and Spalding's log-law for mean velocity is sensitized to pressure-gradient effects.
- The two-layer-based concept is adopted to compute the budget of turbulence kinetic energy ($\overline{G_k}, \overline{\varepsilon}$) in the wall-neighbouring cells.

The law-of-the-wall for mean temperature or species mass fraction remains the same as in standard wall functions. While the log-law for mean velocity sensitized to the pressure gradients is

$$\frac{\tilde{U} C_\mu^{1/4} k^{1/2}}{\tau_w / \rho} = \frac{1}{k} \ln \left(E \frac{\rho C_\mu^{1/4} k^{1/2} y}{\mu} \right) \quad (4.14)$$

Where

$$\tilde{U} = U - \frac{1}{2} \frac{dp}{dx} \left[\frac{y_v}{\rho k \sqrt{k}} \ln \left(\frac{y}{y_v} \right) + \frac{y - y_v}{\rho k \sqrt{k}} + \frac{y_v^2}{\mu} \right] \quad (4.15)$$

And y_v is the physical viscous sublayer thickness, and is computed from

$$y_v \equiv \frac{\mu y^+}{\rho C_\mu^{1/4} k_P^{1/2}} \quad (4.16)$$

$$y^+ = 11.225$$

The non-equilibrium wall function employs the two-layer concept in computing the budget of turbulence kinetic energy at the wall-adjacent cells, which is needed to solve the k equation at the wall-neighbouring cells. The wall-neighbouring cells are assumed to consist of a viscous sublayer and a fully turbulent layer.

The turbulence kinetic energy budget for the wall neighbouring cells depends on the proportions of the viscous sublayer and the fully turbulent layer, which varies widely from cell to cell in highly non-equilibrium flows. The non-equilibrium wall functions account for the effect of pressure gradients on the distortion of the velocity profiles. In such cases the assumption of local equilibrium, when the production of the turbulent kinetic energy is equal to the rate of its destruction, is no longer valid. Therefore, the non-equilibrium wall functions, in effect, partly account for the non-equilibrium effects that are neglected in the standard wall functions.

Due to the capability to partly account for the effects of pressure gradients, the non-equilibrium wall functions are recommended for use in complex flows involving separation, reattachment and impingement where the mean flow and turbulence are subjected to pressure gradients and rapid changes.

3. Scalable Wall Functions

Scalable wall functions avoid the deterioration of standard wall functions under grid refinement below $y^+ < 11$. These wall functions produce consistent results for grids of arbitrary refinement. For grids which are coarser than $y^+ > 11$, the standard wall functions are identical.

The purpose of scalable wall functions is to force the usage of the log law in conjunction with the standard wall functions approach. This is achieved by introducing a limiter in the y^+ calculations such that

$$\tilde{y}^+ = \text{MAX}(y^+, y_{limit}^+) \quad (4.17)$$

Where $y_{limit}^+ = 11.225$.

When the scalable wall functions is used, the y^+ formulation used for any standard wall function formula is replaced by \hat{y}^+ .

Limitations of the Wall Function Approach

The standard wall functions give reasonable predictions for the majority of high-Reynolds number wall-bounded flows. The non-equilibrium wall functions further extend the applicability of the wall function approach by including the effects of pressure gradient.

However, the above wall functions become less reliable when the flow conditions depart too much from the ideal conditions underlying the wall functions. Examples are as follows:

- Pervasive low-Reynolds-number or near-wall effects (e.g., flow through a small gap or highly viscous, low-velocity fluid flow).
- Massive transpiration through the wall (blowing/suction).
- Severe pressure gradients leading to boundary layer separations.
- Strong body forces (e.g., flow near rotating disks, buoyancy-driven flows).
- High three-dimensionality in the near-wall region (e.g., Ekman spiral flow, strongly skewed 3D boundary layers).

According to ANSYS FLUENT Theory Guide (2011a), if any of the above features listed prevail in the flow that is modelling, near-wall modelling approach combined with the adequate mesh resolution in the near-wall region should be employed.

4.2.2.2 Near-wall Modelling

In the near wall modelling approach, the turbulence models are modified to enable the viscosity-affected region to be resolved with a refined mesh all the way to the wall, including the viscous sublayer (ANSYS, 2011a).

If the near-wall mesh is fine enough to be able to resolve the viscous sublayer (typically with the first near-wall node placed at $y^+ \approx 1$), the enhanced wall treatment will be identical to the traditional two-layer zone model.

Enhanced Wall Treatment for the ε -equation is a near-wall modelling method that combines a two-layer model with enhanced wall functions to overcome the problem of near modelling. The enhanced wall treatment is available with all ε -equation models (except the Quadratic RSM) and all ω -equation models (ANSYS, 2011a).

The two-layer model is an integral part of the enhanced wall treatment and is used to specify both the ε and the turbulent viscosity in the near-wall cells. In this approach, the whole domain is subdivided into a viscosity-affected region and a fully-turbulent region. The demarcation of the two regions is determined by a wall-distance-based, turbulent Reynolds number, Re_y , defined as

$$Re_y = \frac{\rho y \sqrt{y}}{\mu} \quad (4.18)$$

where y is the wall-normal distance calculated at the cell centres.

In the fully turbulent region ($Re_y > 200$), the k - ε models or the RSM are adopted, while for the viscosity affected region, where $Re_y < 200$, the one-equation model of Wolfshtein is employed (Wolfshtein, 1969).

The enhanced wall treatment approach allows the fully turbulent law to be easily modified and extended to take into account other effects such as pressure gradients or variable properties. This approach also guarantees the correct asymptotic behaviour for large and small values of y^+ and reasonable representation of velocity profiles in the cases where y^+ falls inside the wall buffer region ($3 < y^+ < 10$) (Fokeer, 2006).

For the numerical investigation of the swirl inducing pipe, Ariyaratne (2005) used standard wall functions to optimize swirl pipe and transition pipe. She carried out a comparison to the use of non-equilibrium wall functions approach for the case of Swirl pipe (400mm) + Exit transition (100mm). It was observed that the trends were closely followed in both cases and the difference in final result was 3% greater pressure drop and 0.3% lower tangential velocity when standard wall functions were used.

Fokeer (2006) ran two identical cases, one employing the standard wall function and the other the non-equilibrium wall function. Distribution of static pressure and velocity magnitude throughout the model were compared and both wall functions produced very similar results. The maximum percentage difference between the two wall functions for static pressure and velocity magnitude parameters was only 0.9%. The standard wall function case converged 1% faster than the non-equilibrium wall function case. Since no significant advantage resulted from using a non-equilibrium wall function, Fokeer decided to employ the standard wall function.

Najafi et al. (2011) stated that for modelling the region close to the walls whose appropriate selection was of crucial importance in calculation of shear stresses, and the two layer zone models were employed. This near-wall flow modelling method by the two layer model of Norris and Reynolds was also used by Jensen et al. (2005) in their study of wall shear stress variation along a rig comprising

circular pipe, sudden and gradual expansion and contractions.

It is recommended to use the enhanced wall treatment for all models for which it is available. It provides the most consistent wall shear stress and wall heat transfer predictions with the least sensitivity to y^+ values (ANSYS, 2011b).

However, ANSYS FLUENT User's Guide (2011b) also states that, for swirling flows encountered in devices such as cyclone separators and swirl combustors, near-wall turbulence modelling is often a secondary issue, because the fidelity of the predictions in these cases is mainly determined by the accuracy of turbulence model in the core region. While in cases where wall activity participates in the generation of swirl, non-equilibrium wall functions can often improve the predictions since they use a law of the wall for mean velocity sensitized to pressure gradients.

4.3 Numerical Schemes

In ANSYS FLUENT, governing integral equations for the conservation of mass and momentum, and (when appropriate) for energy and other scalars such as turbulence and chemical species are solved by a control-volume-based technique that consists of:

- Division of the domain into discrete control volumes using a computational grid.
- Integration of the governing equations on the individual control volumes to construct algebraic equations for the discrete dependent variables ("unknowns") such as velocities, pressure, temperature, and conserved scalars.
- Linearization of the discretized equations and solution of the resultant linear equation system to yield updated values of the dependent variables.

4.3.1 Solver

To solve a fluid flow numerically, ANSYS FLUENT allows user to choose one of the two numerical methods: pressure-based solver and density-based solver.

The pressure-based solver traditionally has been used for incompressible and mildly compressible flows. On the other hand, the density-based approach was originally designed for high-speed compressible flows. Both approaches are now applicable to a broad range of flows (from incompressible to highly compressible). However, for high-speed compressible flows, the density-based formulation may give an accuracy advantage over the pressure-based solver.

Two algorithms exist under the pressure-based solver in ANSYS FLUENT: a segregated algorithm and a coupled algorithm. In the segregated algorithm the governing equations are solved sequentially, segregated from one another, while in the coupled algorithm the momentum equations and the pressure based continuity equation are solved in a coupled manner. In general, the coupled algorithm significantly improves the convergence speed over the segregated algorithm; however, the memory requirement for the coupled algorithm is more than the segregated algorithm.

The density-based solver in ANSYS FLUENT solves the governing equations of continuity, momentum, and (where appropriate) energy and species transport simultaneously as a set, or vector, of equations. Governing equations for additional scalars (e.g., turbulence or radiation quantities) will be solved sequentially. There are also two formulations existing under the density-based solver: implicit and explicit. The implicit and explicit density-based formulations differ in the way that they linearize the coupled equations.

Though both pressure-based and density-based solvers can be used for a broad range of flows, in some cases however one formulation may perform better than the other in yielding a solution more quickly or resolve certain flow features better (ANSYS, 2011b). Generally, the pressure-based solver provides more physical models or features that are not available with the density-based solver. In terms of this study on swirl pipe, some solution techniques that may be beneficial in swirling or rotating flow calculations are only available in the pressure based solver. For this reason, and since incompressible water is studied, the default pressure-based solver, which was also used by Ariyaratne (2005) and Fokeer (2006), will be adopted.

The pressure-based solver employs an algorithm which belongs to a general class of methods called the projection method (Chorin, 1968). In this method, the constraint of mass conservation (continuity) of the velocity field is achieved by solving a pressure (or pressure correction) equation that is derived from the continuity and the momentum equations in such a way that the velocity field, corrected by the pressure, satisfies the continuity. Since the governing equations are nonlinear and coupled to one another, the solution process involves iterations wherein the entire set of governing equations is solved repeatedly until the solution converges.

ANSYS FLUENT provides two pressure-based solver algorithms, a segregated algorithm, and a coupled algorithm. In this study, a segregated algorithm was employed as it is memory-efficient than the coupled algorithm.

4.3.1.1 The Pressure-Based Segregated Algorithm

In the segregated algorithm, the individual governing equations for the solution variables (e.g. $u, v, w, p, T, k, \varepsilon$ etc.) are solved sequentially. Each governing equation is “decoupled” or “segregated” from other equations while being

solved. The segregated algorithm is memory-efficient, because the discretized equations need only be stored in the memory one at a time. However, the solution convergence is relatively slow, as the equations are solved in a decoupled manner.

With the segregated algorithm, the iteration process consists of the following steps as demonstrated in Figure 4.3.1:

1. Update fluid properties (e.g., density, viscosity, specific heat) including turbulent viscosity (diffusivity) based on the current solution.
2. Solve the momentum equations one after another, using the recently updated values of pressure and face mass fluxes.
3. Solve the pressure correction equation using recently obtained velocity field and mass-flux.
4. Correct the face mass fluxes, pressure, and the velocity field using the pressure correction obtained from step 3.
5. Solve the equations for additional scalars, if any, such as turbulent quantities, energy, species, and radiation intensity using the current values of the solution variables.
6. Update the source terms arising from the interactions among different phases when multiphase is involved.
7. Check for convergence of the equations.

The steps are continued until the convergence criteria are met.

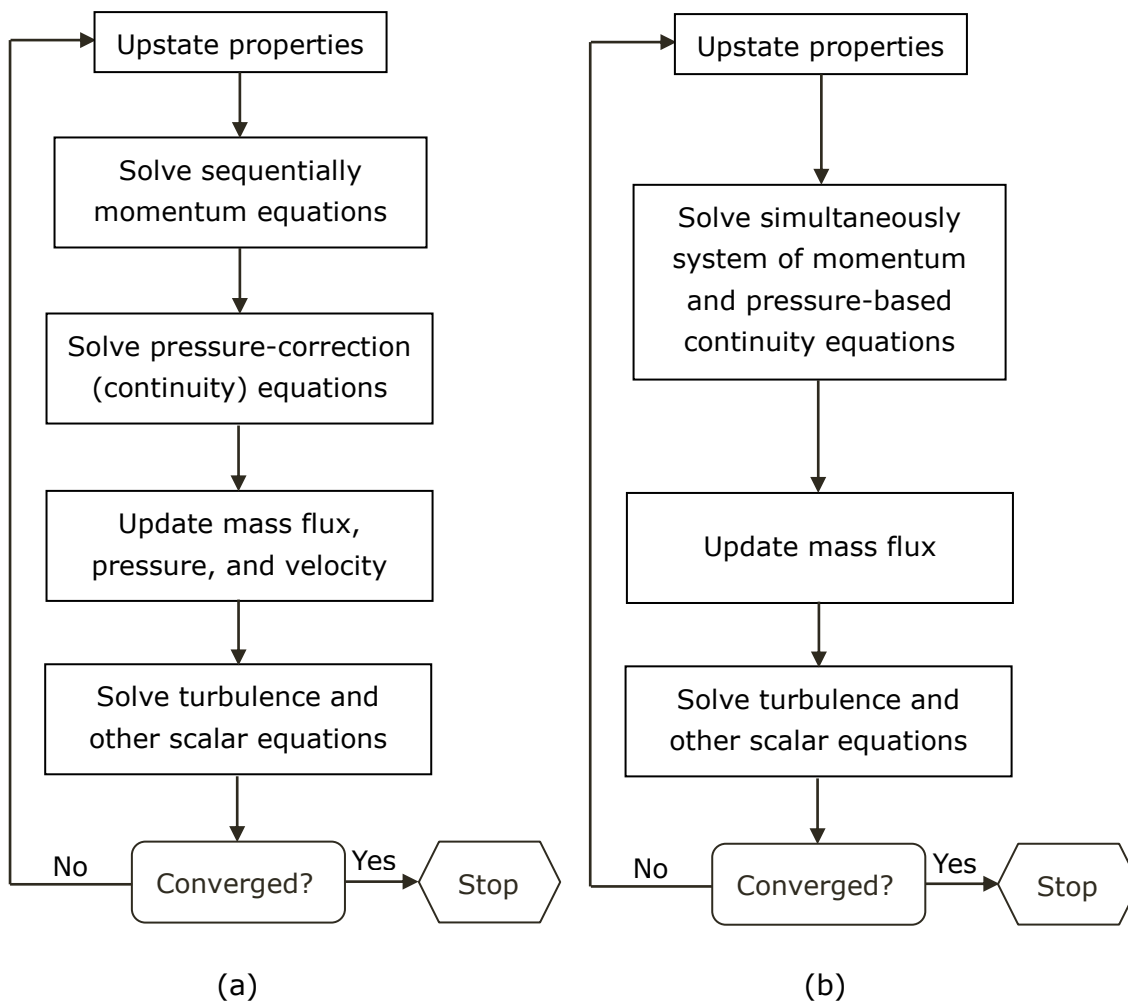


Figure 4.3.1 Overview of the Pressure-Based Segregated (a) and Coupled (b) Solution Methods

4.3.1.2 The Pressure-Based Coupled Algorithm

On the other hand, the pressure-based coupled algorithm solves a coupled system of equations comprising the momentum equations and the pressure-based continuity equation. Thus, steps 2 and 3 in the segregated solution algorithm are replaced by a single step in the coupled algorithm, in which the coupled system of equations is solved (refer to Figure 3.2.2 (b)). The remaining scalar equations are solved in a decoupled fashion as in the segregated algorithm.

Since the momentum and continuity equations are solved in a closely coupled manner, the rate of solution convergence significantly improves when compared to the segregated algorithm. However, the memory requirement increases by 1.5–2 times that of the segregated algorithm since the discrete system of all momentum and pressure-based continuity equations needs to be stored in the memory when solving for the velocity and pressure fields (rather than just a single equation, as is the case with the segregated algorithm).

4.3.2 Numerical Discretization

In order to solve a fluid flow numerically, the computational domain, including the surfaces and boundaries have to be discretized. This can be done using either one of three different methods (Versteeg and Malalasekera, 1995): Finite-Difference Method (FDM), Finite-Volume Method (FVM) or Finite-Element Method (FEM). Recent CFD packages, including ANSYS FLUENT, apply Finite-Volume Method more because it can be used on either a structured or unstructured mesh, rigorously enforces conservation, is directly relatable to physical quantities (mass flux, etc.), and is easier to program in terms of CFD code development.

ANSYS FLUENT uses a control-volume-based technique which converts a general scalar transport equation to an algebraic equation that can be solved numerically. In the FVM method, the numerical algorithm consists of the following steps (H.K.Versteeg and W.Malalasekera, 2010):

- Integration of the governing equations of fluid flow over all the (finite) control volumes of the domain.
- Discretisation – conversion of the resulting integral equations, which results in a system of algebraic equations that are written in matrix for convenience.
- Solution of the algebraic equations is then gained by an iterative method.

The discretized scalar transport equation contains the unknown scalar variable ϕ at the cell centre as well as the unknown values in the surrounding neighbour cells. This equation will, in general, be non-linear due to the convection term. Phenomena such as turbulence and chemical reactions introduce additional nonlinearities. The strategy used to handle the nonlinearity is to linearize the equations about a guess value of the solution and to iterate until the guess agrees with the solution to a specified tolerance level (Bhaskaran and Collins, 2003).

The linearized form of the discretized scalar transport equation can be written as $a_p \phi = \sum a_{nb} \phi_{nb} + b$, where the subscript nb refers to neighbouring cells, a_p and a_{nb} are the linearized coefficients for ϕ and ϕ_{nb} . The number of neighbours for each cell depends on the mesh topology, but will typically equal the number of faces enclosing the cell (boundary cells being the exception). Similar equations can be written for each cell in the mesh. This results in a set of algebraic equations with a sparse coefficient matrix. For scalar equations, ANSYS FLUENT solves this linear system using a point implicit (Gauss-Seidel) linear equation solver in conjunction with an algebraic multigrid (AMG) method.

4.3.2.1 Spatial Discretization

In the Finite-Volume Method, the computational domain is divided into a finite number of elements known as control volumes by the regular and irregular arrangement of nodes, known as the mesh. Flow parameters are resolved around these nodes, so that the fluid flow can be described mathematically by specifying its velocity at all points in space and time.

ANSYS FLUENT, by default, stores discrete values (e.g. pressure, velocities and turbulence) of the scalar at the cell centres. However, face values are required

for the convection terms and must be interpolated from the cell centre values. This is achieved through an upwind scheme. Upwinding means that the face value is derived from quantities in the cell upstream, or “upwind” relative to the direction of the normal velocity.

Upwind advection schemes

ANSYS FLUENT provides several upwind advection schemes for momentum, kinetic energy, dissipation rate and Reynolds Stresses: first-order upwind, second-order upwind, power law, QUICK and third-Order MUSCL scheme.

In the first-order upwind scheme, quantities at cell faces are determined by assuming that the cell centre values of any field variable represent a cell-average value and hold throughout the entire cell. Therefore, when first-order upwinding is selected, the face value is set equal to the cell-centre value of in the upstream cell.

When second-order upwind scheme is used, the higher-order accuracy quantities at cell faces are achieved through a Taylor series expansion of the cell-centred solution about the cell centroid. The face value is the sum of the cell-centred value and the product of its gradient in the upstream cell multiplies the displacement vector from the upstream cell centroid to the face centroid.

The power-law discretization scheme interpolates the face value of a variable using a solution the same as to a one-dimensional convection-diffusion equation. QUICK (Quadratic Upstream Interpolation for Convection Kinetics) type schemes are based on a weighted average of second-order-upwind and central interpolations of the variable. The third-Order MUSCL scheme was conceived from the original MUSCL (Monotone Upstream-Centred Schemes for Conservation Laws) by blending a central differencing scheme and second-order upwind.

ANSYS FLUENT states that, when flow is aligned with the mesh, the numerical diffusion will be naturally low; a first-order scheme yields better convergence without any significant loss of accuracy. However, when flow is not aligned with the mesh, the first-order convective discretization increases numerical discretization error. The second-order scheme generally obtains more accurate results especially for complex flows. In summary, while the first-order discretization generally yields better convergence than the second-order scheme, it generally will yield less accurate results, especially on triangular/tetrahedral meshes.

The QUICK and third-order MUSCL discretization schemes may provide better accuracy than the second-order scheme for rotating or swirling flows. In general, however, the second-order scheme is sufficient and the QUICK and third-order MUSCL schemes will not provide significant improvements in accuracy. The power law scheme will generally yield the same accuracy as the first-order scheme.

Note that when LES are used, the bounded central differencing and central differencing schemes are available.

Pressure interpolation schemes

Similarly, the face values of pressure are computed from the cell values adopting pressure interpolation schemes. The ones available in ANSYS FLUENT, when pressure-based solver is used, include: standard, second-order, body-force-weighted, linear and the PRESTO! (PREssure STaggering Option) scheme.

The standard scheme works well when the pressure variation between cell centres is smooth. When there are jumps or large gradients in the momentum

source terms between control volumes, the pressure profile has a high gradient at the cell face, and cannot be interpolated using standard scheme. The standard scheme will have trouble handling flows with a large body force (such as strongly swirling flow) and the presence of curvature.

The second-order scheme reconstructs the face pressure in the manner used for second-order accurate convection terms. This scheme may provide some improvement over the standard and linear schemes, but it may have some trouble if it is used at the start of a calculation and/or with a bad mesh. This method is not applicable for porous medium and the use of the VOF (Volume of Fluid) or mixture model for multiphase flow.

The body-force-weighted scheme computes the face pressure by assuming that the normal gradient of the difference between pressure and body forces is constant. This works well if the body forces are known a priori in the momentum equations (e.g., buoyancy and axisymmetric swirl calculations).

The linear scheme computes the face pressure as the average of the pressure values in the adjacent cells. The PRESTO! scheme uses the discrete continuity balance for a “staggered” control volume about the face to compute the “staggered” (i.e., face) pressure.

Generally, for problems involving large body forces, the body-force-weighted scheme is recommended. While For flows with high swirl numbers, high-Rayleigh-number natural convection, high-speed rotating flows, flows involving porous media, and flows in strongly curved domains, the PRESTO! scheme is recommended.

Pressure-velocity coupling

The momentum equation is normally solved with a guessed pressure field, and therefore the resulting face flux, does not satisfy the continuity equation. This is rectified by applying a pressure-velocity coupling algorithm, which uses a combination of continuity and momentum equations to derive an equation for pressure (or pressure correction) so that the corrected face flux satisfies the continuity equation.

When pressure-based segregated solver is used, ANSYS FLUENT provides three segregated types of algorithms: SIMPLE, SIMPLEC and PISO.

The SIMPLE algorithm uses a relationship between velocity and pressure corrections to enforce mass conservation and to obtain the pressure field. It substitutes the flux correction equations into the discrete continuity equation to obtain a discrete equation for the pressure correction in the cell. The SIMPLEC procedure is similar to the SIMPLE procedure however it offers different expression for the face flux correction.

The PISO (Pressure-Implicit with Splitting of Operators) scheme is based on the higher degree of the approximate relation between the corrections for pressure and velocity. It improves the efficiency of calculation allowing the new velocities and corresponding fluxes to satisfy the momentum balance after the pressure-correction equation is solved by including neighbour correction and skewness correction.

According to ANSYS FLUENT User's Guide, steady-state calculations will generally use SIMPLE or SIMPLEC, while PISO is recommended for transient calculations. PISO may also be useful for steady-state and transient calculations on highly skewed meshes.

4.3.2.2 Temporal Discretization

For modeling unsteady flows, the governing equations must be discretized in both space and time. The spatial discretization for the time-dependent equations is the same as the steady-state case. While the discretization in time are realized adopting the temporal discretization by splitting the time in the continuous flow into discrete time steps.

Temporal discretization involves the integration of every term in the differential equations over a time step Δt . For a variable ϕ , the time evolution can be expressed as:

$$\frac{\partial \phi}{\partial t} = F(\phi) \quad (4.19)$$

where the function F incorporates any spatial discretization.

First-Order Implicit

If the time derivative is discretized using backward differences, the first-order accurate temporal discretization is given by:

$$\frac{\phi^{n+1} - \phi^n}{\Delta t} = F(\phi) \quad (4.20)$$

Once the time derivative has been discretized, the Implicit Time Integration can be used to evaluate $F(\phi)$: in particular, which time level of ϕ should be used in evaluating F . The method is to evaluate $F(\phi)$ at the future level:

$$\frac{\phi^{n+1} - \phi^n}{\Delta t} = F(\phi^{n+1}) \quad (4.21)$$

This implicit equation can be solved iteratively at each time level before moving to the next time step. This fully implicit scheme is advantageous in that it is unconditionally stable with respect to time step size.

Second-Order Implicit

The second-order discretization is expressed as:

$$\frac{3\phi^{n+1} - 4\phi^n + \phi^{n-1}}{2\Delta t} = F(\phi) \quad (4.22)$$

Where

ϕ = a scalar quantity

$n + 1$ = value at the next time level, $t + \Delta t$

n = value at the current time level, t

$n - 1$ = value at the previous time level, $t - \Delta t$

Since the same Implicit Time Integration is used to evaluate $F(\phi)$, this temporal discretization method is named the Second-Order Implicit.

For the second-order discretization, Bounded Second Order Implicit Time Integration is also available. This refers to the Bounded Second Order Implicit. This formulation is only used in the pressure-based solver not available with the density-based solver.

Generally speaking, the First Order Implicit formulation is sufficient for most problems. Either Second Order Implicit or Bounded Second Order Implicit gives improved accuracy. The Bounded Second Order Implicit formulation provides the same accuracy as the Second Order Implicit formulation, however it provides better stability.

4.4 CFD Model Formulation

4.4.1 CFD Software Package

ANSYS FLUENT academic code 14.0 (ANSYS, 2011b) is employed in simulating the swirl flow induced by the optimized 4-lobed swirl pipe. The ANSYS FLUENT code is written in C computer language and makes full use of the flexibility and power offered by this language. The code is a state-of-the-art computer program for modeling fluid flow, heat transfer, and chemical reactions in complex geometries (ANSYS, 2013b).

ANSYS Fluent uses a client/server architecture which enables it to run as separate simultaneous processes on a personal workstation which has two 3.3GHz 4 core processors, 48GB memory with a 64-Bit Window 7 operating system. The academic version of ANSYS FLUENT offers parallel solver (local machine) which enables the user to compute a solution using 4 processors on the same workstation.

ANSYS FLUENT offers insight into how the swirl pipe will behave in the real cleaning industry before a single prototype is built.

4.4.2 Enabling Assumptions

Prior to setting up and running a CFD simulation, assumptions need to be made to reduce the complexity of the flow problem in terms of the physical and chemical phenomena that need to be considered to a manageable level whilst preserving the salient features of the problem at hand (H.K.Versteeg and W.Malalasekera, 2010). For the RANS approach, the following assumptions are made to simplify the single phase swirl flow as follows:

- The flow is single phase water only flow
- The flow is steady and isothermal
- The flow is incompressible
- The pipe walls are hydraulically smooth
- The walls are assumed to be stationary, no slip wall

4.4.3 Flow Domain

The configuration of the modelled pipe flow geometry for use with ANSYS FLUENT was created with Pro/Engineer 4.0. Since modelling the whole rig would be computationally intensive and time-consuming, only the top horizontal section of the experimental rig (the rig will be introduced in Chapter 8) is modelled.

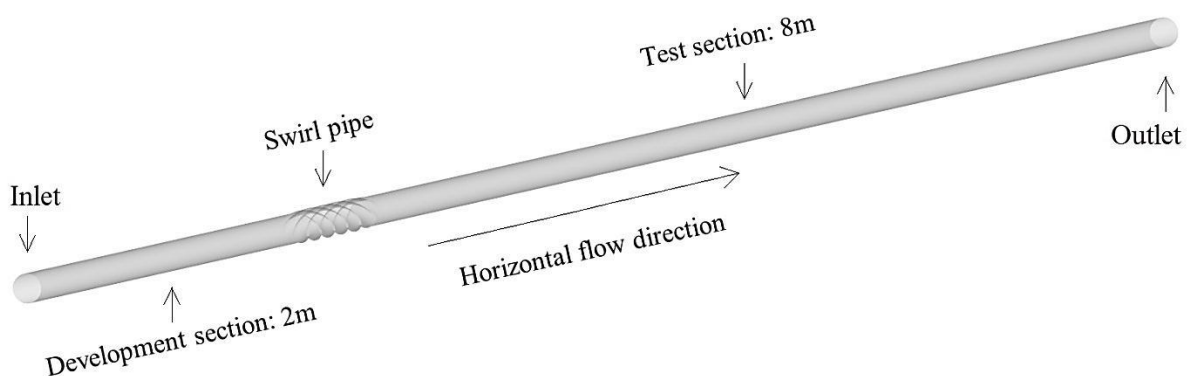


Figure 4.4.1 Configuration of simulation geometry

- The 2m straight circular pipe prior to the swirl pipe serves as development section to ensure the flow has a fully developed viscous boundary layer before entering the swirl pipe.
- The 8m horizontal straight circular pipe downstream of the swirl pipe is the test section.
- The circular pipe has a diameter of 50mm.
- The swirl pipe has an equivalent diameter of 50mm and its cross-sectional areas are constant and equal to the circular pipe.
- The circular face of the inlet and outlet are created in the XY-plane, the

fluid flows in the horizontal Z direction.

It is important to establish a fully developed viscous boundary layer. When this is achieved, the flow is fully-developed and there is no variation of the velocity profile in the axial direction. Previous researcher Ariyaratne (2005) ran a simulation over a 0.5m circular pipe and used the 'outlet' velocity profile obtained as the 'velocity profile'. The 'velocity profile' was then applied to the inlet of 0.1m or 0.2m circular pipes that were connected prior to the swirl pipes or control (circular) pipes. Therefore, the development section of the pipe geometries Ariyaratne used has an equivalent length of 0.6m or 0.7m.

In the current study, attempts were made to further ensure fully turbulent flow by increasing the length of the development section into 1m, 1.5m and 2m. The simulation results showed that, without the use of a 'velocity profile', a 1.5m length circular pipe prior to the swirl pipe was able to reach a steady velocity profile before entering the swirl pipe. As can be seen from Figure 4.4.2, the velocity profiles in the planes 1.5m, 1.6m, 1.7m and 1.8m downstream of the inlet are identical indicating that the flow is fully developed at these distances from the inlet. Considering a proper safety margin, a development section of 2m without 'velocity profile' was finally used for all cases.

To ensure the swirl motion decayed completely before researching the outlet of the computational domain, test sections of length of 3m, 5m, 6m and 8m were attempted. It was found, especially for a larger inlet velocity, a test section of 8m was required to cover the decay process of the induced swirl flow.

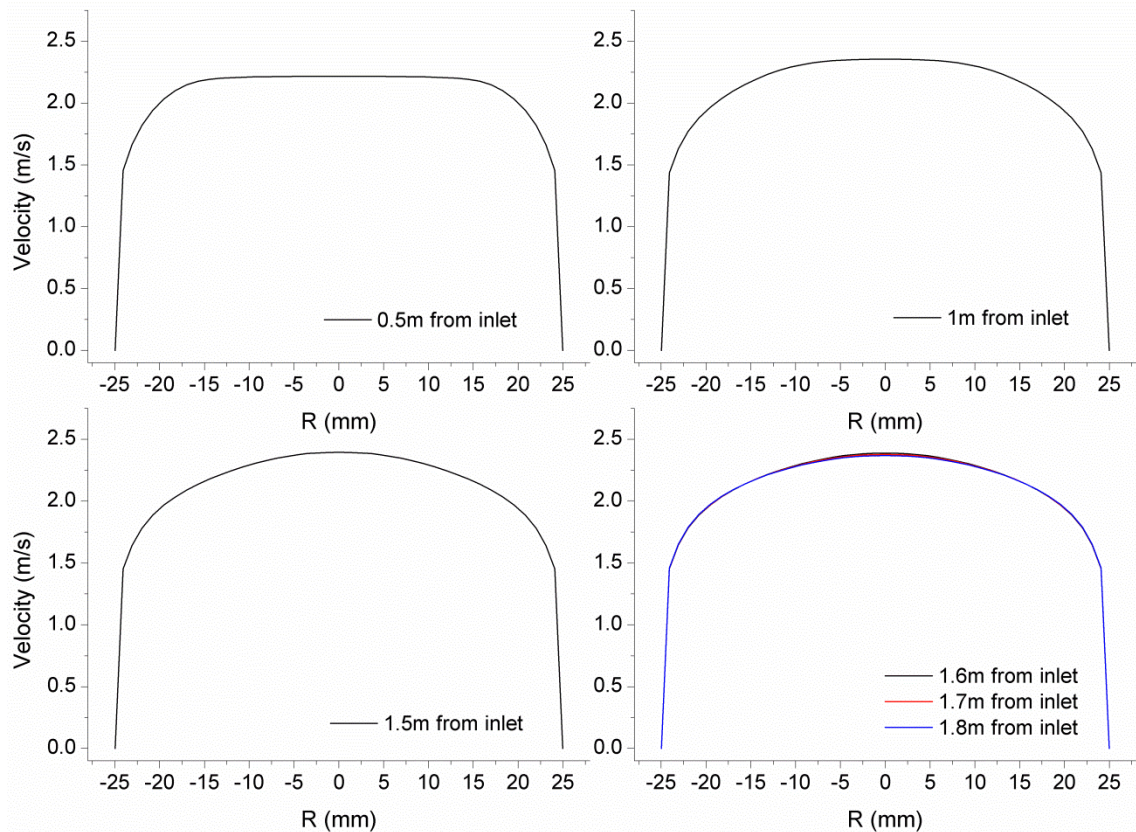


Figure 4.4.2 Velocity profiles downstream of circular pipe inlet

4.4.4 Meshing

As has been discussed in section 4.3.2.1, before the governing equations can be numerically solved, the flow domain including the surface of all the boundaries need to be discretised into a finite number of elements known as control volumes by the regular or irregular arrangement of nodes, namely the mesh. Flow parameters are resolved around these nodes, so that the fluid flow can be described mathematically by specifying its velocity at all points in space and time.

How the mesh is arranged within the domain is largely influenced by the structure of the domain and the positions of the critical regions where there are high gradients in the space of the flow, typically fine mesh are required at these locations to describe the rapid variation accurately.

The mesh is typically made up of nodes from 3D elements such as 4-noded tetrahedrons, 5-noded pyramids, 6-noded prisms (or wedges) and 8-noded hexahedrons. Two types of mesh structures can be arranged from these 3D elements. They are:

Regular structured grid (structured) where:

- The meshes are typically made up of hexahedrons.
- The node points are regularly arranged throughout a cuboid, which can be stretched to fit the particular geometry of the problem as if the mesh is made of rubber.
- Any point in the mesh connects to the same neighbouring points after the stretching process.
- Implicit relationship exists between the label of a cell or a point and the labels of its neighbours in a structured mesh, which enables data to be found easily.

Irregular structured grid (unstructured) where:

- The meshes are often made up of tetrahedrons.
- Node points are filled within the space of concern without being connected with a regular topology.
- The information that any particular node is attached to an element cannot be known from the form of the mesh.
- A numerical table must exist which labels the arrangement of the mesh by listing which nodes are attached to each element.

The advantage of a structured mesh is that it enables the solver program to run faster than when an unstructured mesh is used. In addition, the hexahedral cells within the structured mesh can be built to align with the flow thereby minimising the numerical diffusion.

On the other hand, the use of an unstructured mesh significantly reduces the amount of time spent generating meshes as it is created by automatic mesh generation algorithms. Secondly, unstructured mesh can handle more complex geometries due to its flexibility. Thirdly, an unstructured mesh made up of triangular or tetrahedral cells created for complex geometries often has far fewer cells than the equivalent structured mesh consisting hexahedral cells.

Because the geometry of the swirl inducing pipe and the transition pipes contain sharp angles at the intersection of the lobes and the lobed cross section extends helically around and along the pipe axis making the geometry very complex. Therefore previous researcher Ariyaratne (2005) used meshes comprised unstructured tetrahedral elements for all geometries of swirl, transition and circular pipes employing Gambit software. Ariyaratne also investigated other potentially better meshes using structured hexahedral elements however no alternatives were found.

The mesh Fokeer (2006) generated for meshing the 3-lobed swirl pipe was also based on the unstructured hexahedral mesh. Though, Fokeer used a region of fine mesh, called the boundary layer mesh, along the solid wall surfaces of the 3-lobed swirl pipe and the circular pipes, enabling the modelling of the rapid velocity variation through the boundary layer.

Due to the complex geometry of the swirl pipes, previous researchers Ganeshalingam (2002) and Jones (2002) used unstructured tetrahedral mesh for their studies.

However, it was found that:

- When an unstructured tetrahedral mesh is used, the flow can never be aligned with the grid, which causes numerical diffusion.

- An unstructured mesh made up of tetrahedral cells also tends to have a large aspect ratio, which affect the skewness of the cell, and in turn hinder the accuracy and convergence (Ariyaratne, 2005).
- The unstructured mesh requires more elements for refinement compared to a structured mesh of the same geometry, leading to higher computing cost (Fokeer, 2006).

In this study, the accurate prediction of flow parameters in the boundary layer, such as wall shear stress, are of crucial importance. However, when an accurate prediction of a boundary layer is required, the boundary layer meshes should consist of quads, hexes, or prisms, and the use of pyramid or tetrahedral cells immediately adjacent to the wall should be avoided (Bakker, 2002). Therefore, a method of meshing the computational domain using structured hexahedral elements has to be found.

4.4.4.1 Attempts Made Using Gambit

According to the above discussion, the unstructured tetrahedral cells Ariyaratne used is not applicable to this study as strict mesh control is required in the boundary layer. Therefore, attempts were made to mesh the swirl pipe and circular pipes using structured hexahedral elements adopting the Gambit software. However, no satisfactory solution was found.

In the **first** attempt, the geometry of the flow domain was divided into 3 sections: the development section, the swirl pipe and the test section of circular pipe with every two neighbouring sections sharing one 'internal' face. Therefore two sheared internal faces were within the geometry to make the flow domain continuous between the adjacent two sections. The swirl inducing pipe was firstly meshed using hexahedral cells with boundary layer mesh included along the solid wall surface. The circular pipes were meshed by sweeping the two

surface meshes of the swirl pipe forward or backward along the geometry. It was found that:

- As shown in Figure 4.4.3(a), the mesh of the circular pipes followed the nodes arrangement pattern of the swirl pipe resulting in uneven nodes distribution across the circular pipe cross-section.
- Highly skewed cells existed in four regions of the circular pipe which are in accordance with the four intersections of the lobes (see Figure 4.4.3(b)).
- Highly skewed cells were also found in the intersections of lobes. The poor mesh quality would impede accuracy and convergence of the solution (see Figure 4.4.3(c)).

Due to the poor mesh quality, this method was not employed.

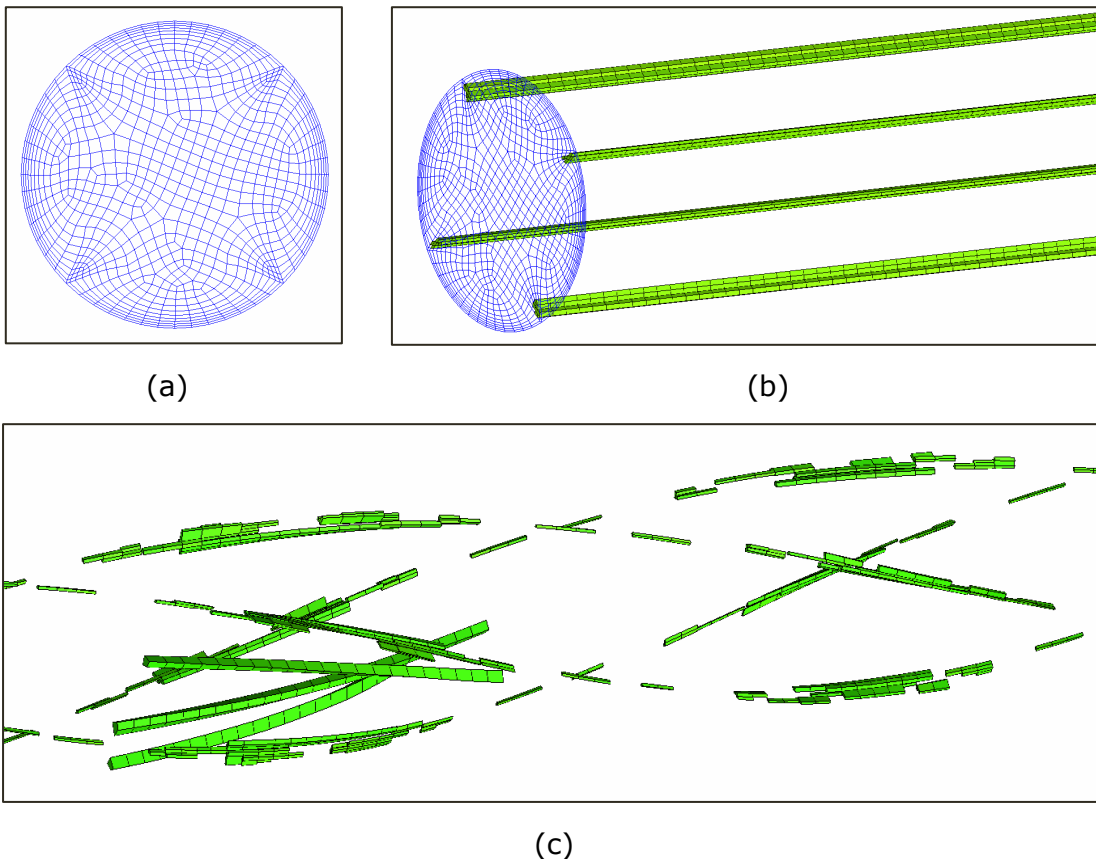


Figure 4.4.3 Circular Pipe face Mesh and Distribution of Highly Skewed Cells

In order to eliminate effects of 'internal' face sheared by the adjacent two sections, a **second** attempt was made to build and mesh the three sections separately without any sheared faces between sections. The meshes of the three sections were imported into FLUENT and the 'Grid interface' feature was applied at the interface of the adjacent two sections to allow the three sections to be bridged together. The Grid interface enables the exchange of all parameters in governing equations between the adjacent two sections.

This method:

- Allowed the nodes arrangement to fit for the different geometries of the three sections respectively.
- Provided the improved mesh quality though still not satisfactory.
- Ensured flow continuity between three geometries through the use of 'Grid interface'.

However, the grid interfaces of the circular pipe and the swirl pipe that were attached together have different nodes arrangement patterns therefore the nodes of the two interfaces do not exactly align with each other (see Figure 4.4.4). The use of this non-conformal mesh interface violates normal best practice and may cause flow discontinuity at the swirl/circular pipe interface.

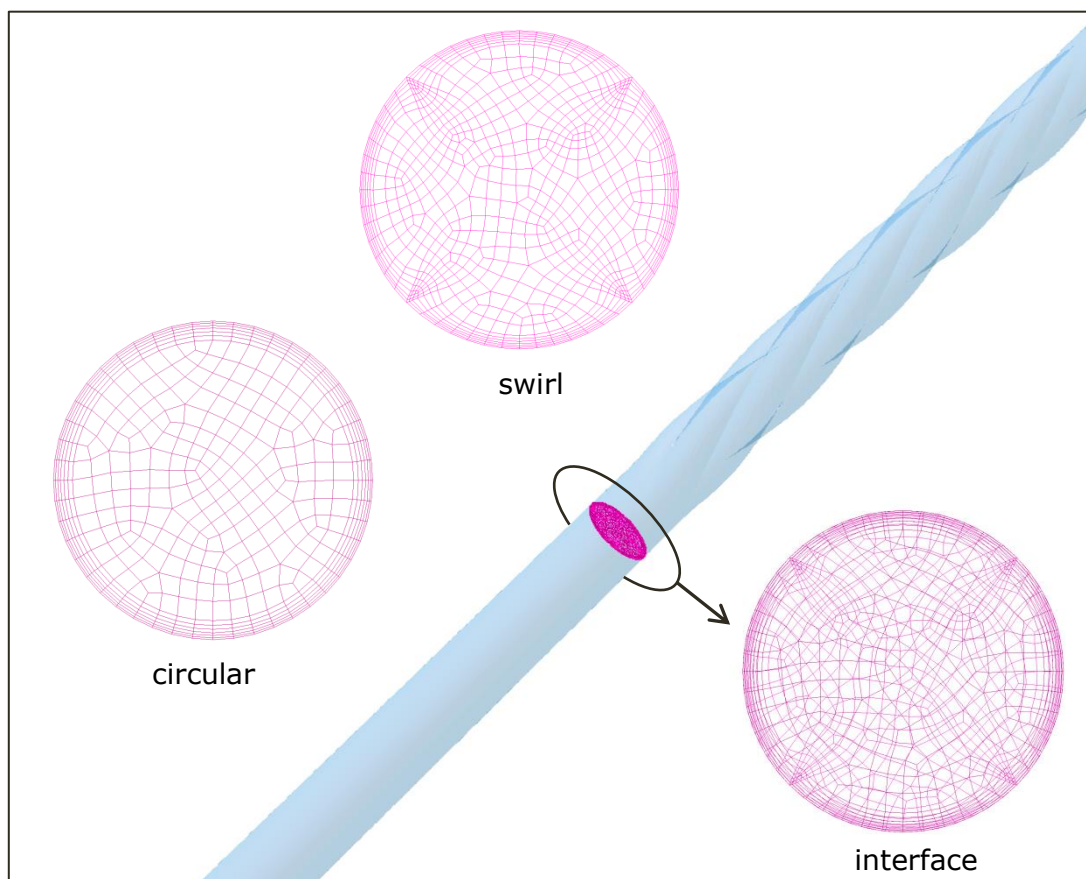


Figure 4.4.4 A detail view of the interface at the swirl/circular pipe intersection

The mesh generated was tested using a standard $k-\epsilon$ model and the standard wall functions. The simulation results showed that, there were no discontinuities in terms of axial, tangential velocity and pressure in the vicinity of swirl/circular pipe interface. However, wall shear stress discontinuity did exist at the swirl/circular pipe interface as shown in Figure 4.4.5. Due to the importance of accurate prediction of wall shear stress for this study and the unsatisfactory mesh quality, this method was deemed unacceptable.

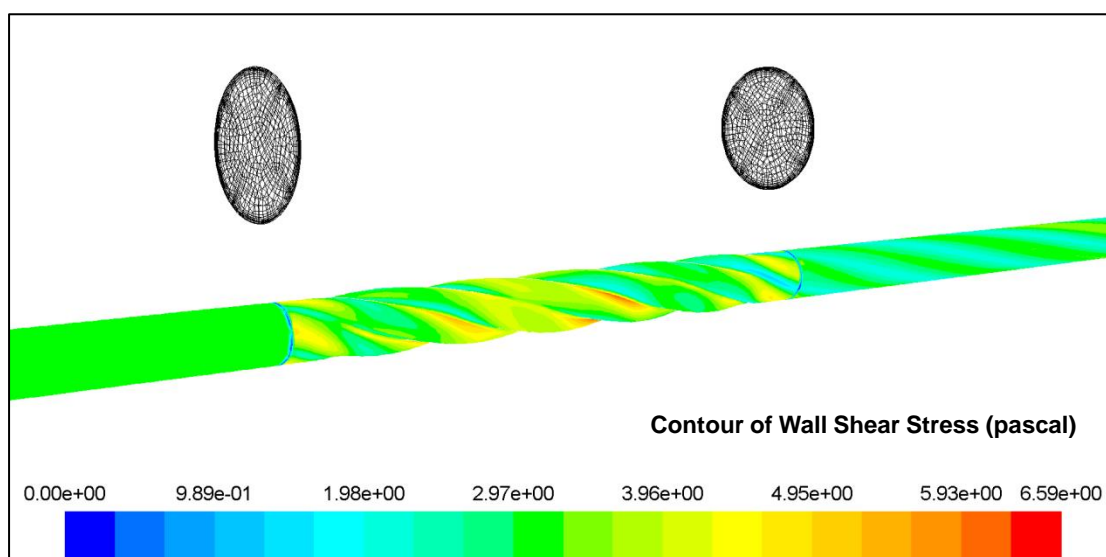


Figure 4.4.5 Discontinuity in contour of wall shear stress at the circular/swirl and swirl/circular interfaces

The **third** attempt was to firstly merge the three sections into an integrated geometry. The inlet and outlet faces of the geometry were then meshed using quadrilateral cells with boundary layer mesh applied in the wall region. The whole geometry was then meshed by sweeping the two face meshes of inlet and outlet as 'source' throughout the whole domain. The surface meshes of the inlet, the cross-section of the circular and swirl pipe are shown in Figure 4.4.6a to Figure 4.4.6c respectively. It can be found that the fine mesh region in the inlet mesh where boundary layer mesh was applied stopped being concentrated only near the wall area as it was swept toward the swirl pipe. This is against the purpose of the use of boundary layer mesh in order to accurately model the rapid velocity variation and the wall shear stress in the near wall region. Another drawback of the grid was the high skewed mesh spotted in the intersections of the lobes. Generally, the Equi-Angle, which is a normalised measure of skewness, should be less than 0.65 for hexahedral cells. Figure 4.4.6d showed that poor mesh cells with an Equi-Angle value larger than 0.65 existed in the intersections of the lobes in the swirl pipe. Considering the difficulties in controlling the mesh refinement in the boundary layer region and the existence

of highly skewed cells which may affect the simulation accuracy and convergence, this meshing method was deemed not sufficient.

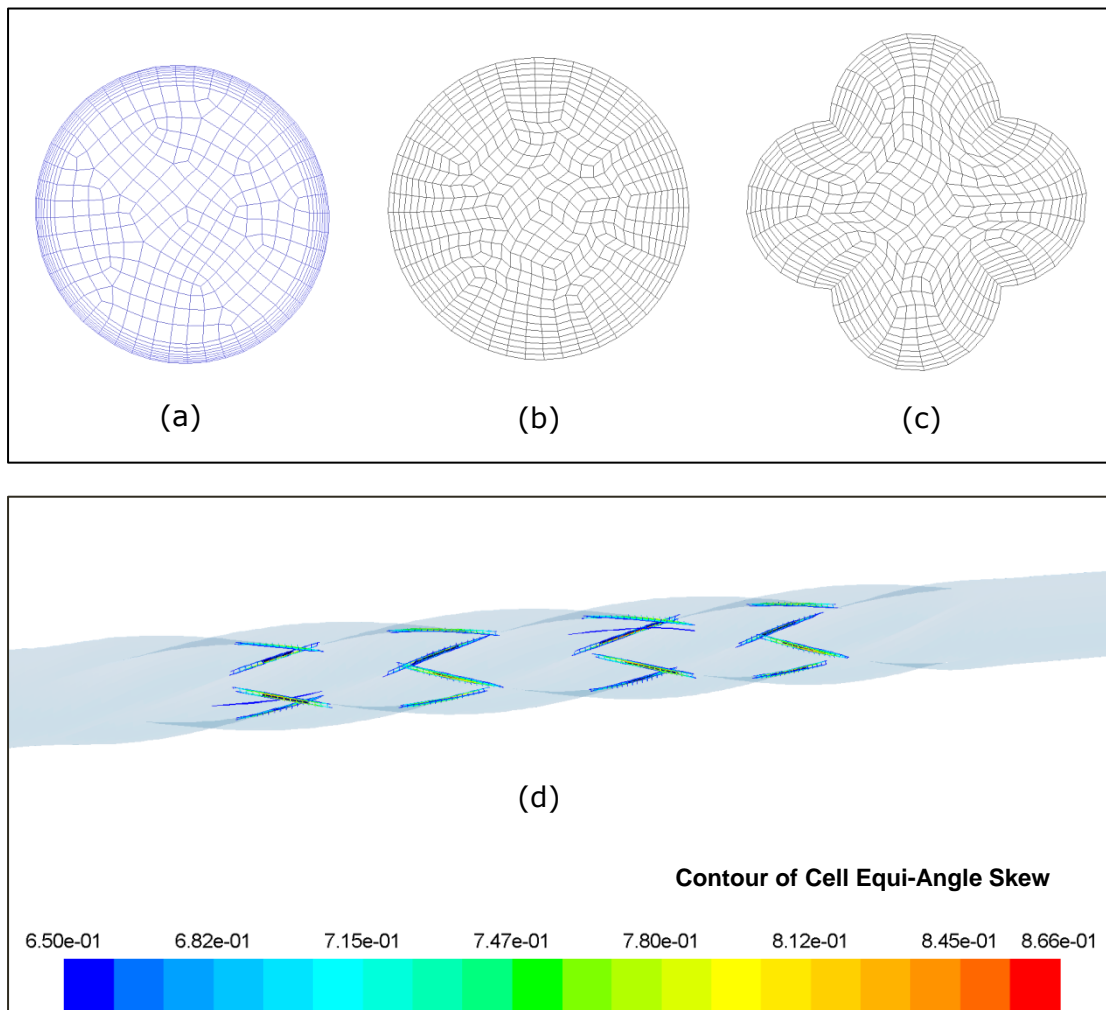


Figure 4.4.6 Face meshes of swirl inducing pipe, transition pipe, and circular pipe

4.4.4.2 Multi-Block Structured Mesh by ICEM

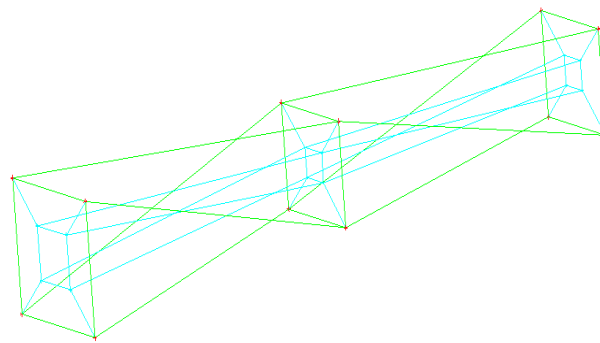
Afterward, a multi-block structured mesh was considered for the discretization of the swirl and circular pipes. This method is a compromise between computing cost and flexibility where the computational domain is subdivided into different blocks which can be structurally meshed using hexahedral cells. This method is complex but more computer efficient than an unstructured mesh and it facilitates control in specifying refinement needed along certain surfaces or walls, especially for meshing around complex geometries.

ICEM CFD (The Integrated Computer Engineering and Manufacturing code for Computational Fluid Dynamics) (ANSYS, 2013d) mesh generation software was used to mesh the computational domain with structured hexahedral cells. ICEM CFD uses a primarily top-down blocking approach to efficiently mesh complex models using all hexahedral cells without the need to subdivide the geometry. The ICEM CFD offers the capability to parametrically create grids from geometry by the association of blocks with topologically similar geometries of the computational domain.

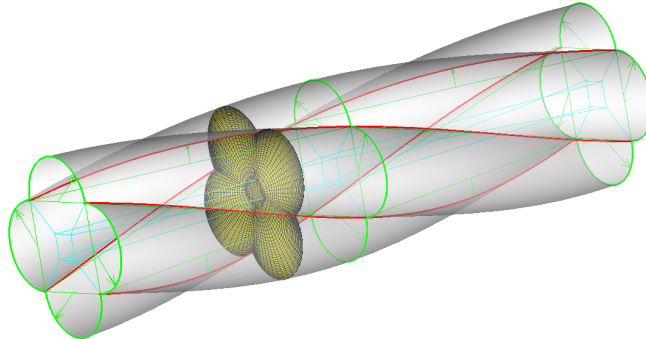
A general process used in meshing the flow geometry shown in Figure 4.4.1 is summarized as below:

- Firstly import the .STP file into ICEM CFD and modify its position to ensure that the inlet is located in the origin of coordinates and the flow direction is in parallel with Z axis.
- Create a block to contain the whole geometry.
- Split the block into three blocks corresponding to the 2m cylindrical pipe, the 0.6m (or 0.4m) optimized swirl pipe and the 8m cylindrical test section.
- The block corresponding to the 0.6m (or 0.4m) swirl pipe was sub-split into 6 (or 4) blocks with each sub-block having a length of 100mm (each lobe rotates 90° over the 100mm length).
- Rotate each sub-block through 90° by moving clockwise the vertexes of the sub-block to fit the rotation of the lobes. Make sure the edges of sub-blocks and curves of the swirl pipe stretch in the same direction as shown in Figure 4.4.7a.
- Associate vertexes, edges and faces of blocks to the points, curves and surface of the topologically similar geometries. The arrows in Figure 4.4.7b show the associations.

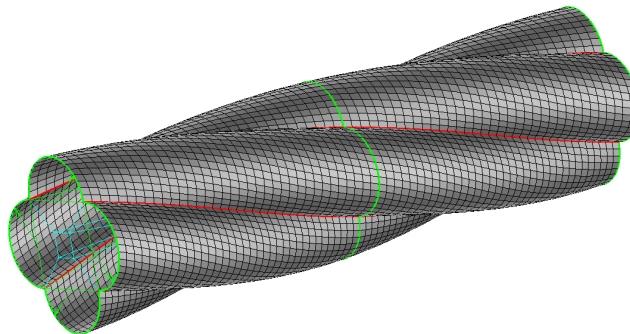
- Further split all the blocks and sub-blocks into O-grid blocks where the mesh radially propagates from the pipe centre towards the outer wall domain. This will result in an orthogonal mesh to better capture near-wall or boundary layer flow.
- Set up nodes number of the edges and mesh law; pre-mesh the geometry; check the mesh quality; smooth the mesh if necessary; convert to mesh; select solver and output mesh file for use with ANSYS FLUENT.



(a) Rotated O-grid blocks



(b) Association between blocks and geometry

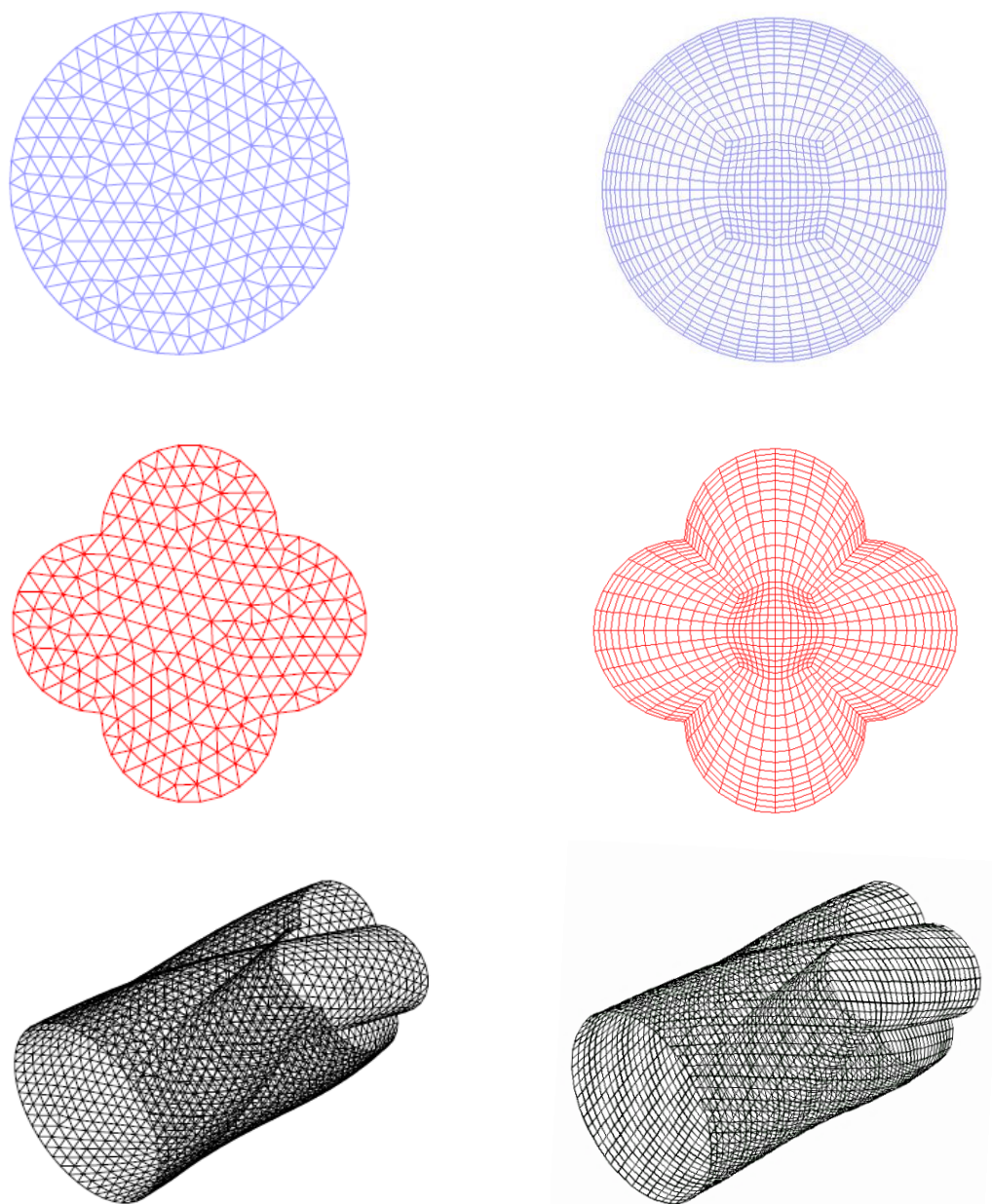


(c) surface mesh at the intersection of lobes

Figure 4.4.7 Face meshes of swirl inducing pipe, transition pipe, and circular pipe

Figure 4.4.7c demonstrates the surface mesh at the intersection of lobes in a section of swirl pipe showing that the block is well fitted to the geometry.

A detail cross-sectional view of the O-grid mesh is shown in Figure 4.4.8b. Figure 4.4.8 also presents a comparison of mesh generated by an unstructured tetrahedral grid and structured hexahedral grid.



(a) unstructured tetrahedral grid

(b) Structured hexahedral grid

Figure 4.4.8 Swirl pipe meshes with unstructured grid by Ariyaratne (2005) and structured hexahedral grid with O-block

The advantages of the structured hexahedral grid using O-block over the previously used unstructured tetrahedral grid are that it:

- Allows the mesh to be arranged in a way that faithfully reflects the geometric characteristics of the flow domain.
- Provides control of the fine regular mesh in the boundary layer which facilitates accurate prediction of wall shear stress in the near-wall region.
- Minimises the numerical diffusion since the structured hexahedral mesh was built to align with the flow.
- Improves largely the mesh quality which promotes solution convergence.

4.4.4.3 Mesh Adaption for Wall Functions

There are two approaches to model the near-wall regions, the enhanced wall treatment method and the wall function method. If the enhanced wall treatment is used, the near-wall mesh should be sufficiently fine everywhere to be able to resolve the viscous sub-layer, a very thin region next to a wall, typically only 1% of the boundary layer thickness. Typically, the first near-wall node should be placed at $y^+ \approx 1$, where y^+ is the non-dimensional distance of a point from the wall (ANSYS, 2011a). This condition is difficult to achieve due to the high three-dimensionality in the lobe interaction region of the swirl pipe.

Therefore, the wall function approach will be used, and non-equilibrium wall functions will be chosen as they give an improved prediction than standard wall functions. Besides, the wall function method allows specifying the roughness of the internal pipe surface to represent the internal surface finish of stainless pipes typically found within the closed processing systems.

The wall functions approach uses the 'log law' whereby the mean velocity is taken as a logarithmic function of the distance from the wall in the fully

turbulent region. The log-law is valid for y^+ between 30 and 60. Therefore, it is important to carry out mesh adaption for wall functions to make sure the first node where the velocity is calculated is located in the log-law region. This was done by adjusting the distances from the first node of the mesh to the wall to generate a series of mesh files. The meshes were then tested independently in simulations with same boundary conditions and solver settings. After the solution converged, y^+ values were calculated to check which mesh allows the y^+ to be in the right range, and if not continue the adaption.

From Figure 4.4.9, for a velocity of 2m/s, the distance from the first node of the mesh to the wall being 0.8mm would place y^+ between 30 and 60 for development section and the test section. The y^+ value is slightly larger than 60 in the vicinity of the four lobe peaks of the swirl pipe. This should not affect the simulation results as it only accounts for a small portion of the swirl pipe and the y^+ is close to 60. Besides, other reference suggests that the layer where y^+ takes values between 30 and 500 is the log-law layer (H.K.Versteeg and W.Malalasekera, 2010).

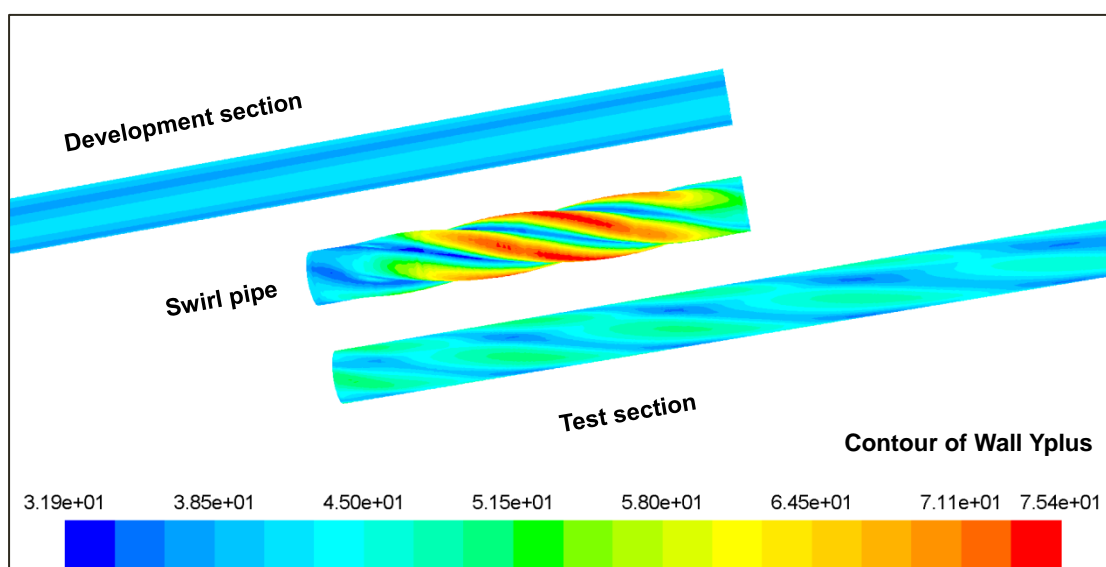


Figure 4.4.9 y^+ contours for computational domain geometry (2m/s inlet velocity)

Table 4.4.1 Y^+ value for different sections of the geometry at different inlet velocities

Inlet velocity	Distances from first node to wall (mm)	Y^+ value		
		Development section	Swirl pipe	Test section
1m/s	1.4	34.3< Y^+ <47.9	25.58< Y^+ <59.7	33.7< Y^+ <45.1
1.5m/s	1	35.7< Y^+ <50.9	27.2< Y^+ <64.6	34.2< Y^+ <48.9
2m/s	0.8	37.2< Y^+ <53.9	31.9< Y^+ <75.4	35.5< Y^+ <51.6
2.5m/s	0.6	34.1< Y^+ <50.8	30.1< Y^+ <70.8	32.7< Y^+ <48.3
3m/s	0.5	33.4< Y^+ <50.8	29.5< Y^+ <70.49	32.1< Y^+ <47.9

It was found this 0.8mm value was not applicable for other velocities. So another four series of y^+ adaption were carried out for the 1m/s, 1.5m/s, 2.5m/s and 3m/s cases respectively. The distance from the first row of the mesh to the pipe wall and the corresponding y^+ value for the three sections are summarized in Table 4.4.1. The y^+ is reasonable between 30 and 60 for all cases.

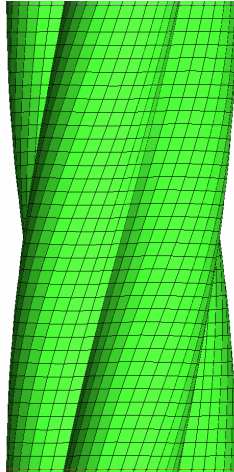
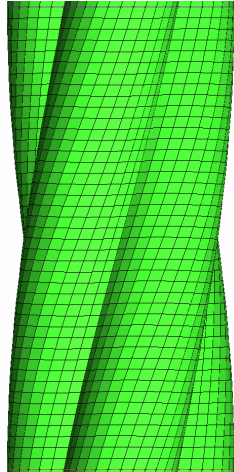
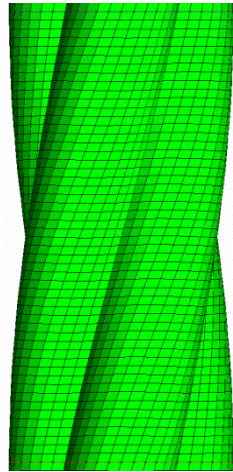
4.4.4.4 Mesh Independence Test

To ensure that the errors associated with the size of mesh were minimized, a quick mesh independence test was carried out. This was done by refining the mesh height in the direction parallel with the swirl pipe and circular pipes (Z axis) until the change of the parameters monitored decreases to the order of 1%. The mesh size in the cross-section plane (X-Y plane) was made sufficiently fine already in order to meet the Y^+ requirement at the wall. For instance, in the mesh generated for the 1m/s flow velocity, the largest mesh size in the cross-section plane is 1.51mm; this is already smaller than the finally used mesh height of 2mm. Therefore, mesh independence test for cross-section mesh is not necessary.

In the mesh independence tests, the initial mesh height of 3mm was refined by shortening the mesh height to 2.5mm and 2mm. The three mesh files were imported to the CFD models and numerically compared. All the solver parameters including flow and boundary conditions were same for each test case. The average tangential velocity and wall shear stress, etc. at planes downstream of the swirl pipe exit were checked. Table 4.4.2 presents a summary of the results. The percentages are a comparison of the value to that obtained from the refined mesh-2. From the table, the differences in the value of parameters obtained from refined mesh-1 and refined mesh-2 are mostly within the order of 1%. Refined mesh-1 should be reasonably concluded as

mesh independent. However, considering the importance of the accurate simulation of tangential velocity and wall shear stress in this study, the refined mesh-2 with a mesh height of 2mm was used for all RANS based simulations.

Table 4.4.2 A summary of the mesh independence test results

Model parameters: 600mm length swirl pipe Pipe diameter 50mm Single phase water Inlet velocity 1.5m/s					
		Initial mesh 3mm	Refined mesh-1 2.5mm	Refined mesh-2 2mm	
		Total no. of cells	2819460	3382960	4227720
		Items			
Pressure (pa)	0.1m after	2466.5513 (-1.39)	2429.9509 (-0.11%)	2432.6831	
	0.3m after	2352.1868 (-0.13%)	2354.0349 (-0.05%)	2355.1926	
Axial velocity (m/s)	0.1m after	1.5335 (-0.44%)	1.5260 (-0.06%)	1.5269	
	0.3m after	1.5183 (-0.07%)	1.5186 (-0.05%)	1.5193	
Tangential velocity (m/s)	0.1m after	0.2307 (-4.27%)	0.2183(-1.34%)	0.2212	
	0.3m after	0.1864 (-2.15%)	0.1880 (-1.31%)	0.1905	
Wall shear stress (pa)	Swirl pipe exit	5.42 (-1.63%)	5.45 (-1.08%)	5.51	
	0.3m after	5.37 (-1.28%)	5.39 (-0.91%)	5.44	

4.4.4.5 Checking Mesh Quality

Checking the quality of the mesh is essential as it plays a significant role in the accuracy and the stability of the numerical computation (ANSYS, 2011b). For the hexahedral mesh elements, the EquiAngle Skew and the Aspect Ratio are

normally used for checking its quality.

Skewness is one of the primary quality measures for a mesh. It determines how close a face or cell of triangle is to an ideal equilateral triangle or a quad is to an ideal equiangular quad (ANSYS, 2013c). The Equi-Angle Skew is a normalised measure of skewness defined as:

$$Q_{EAS} = \max\left(\frac{Q_{max} - Q_{eq}}{180 - Q_{eq}}, \frac{Q_{eq} - Q_{min}}{Q_{eq}}\right) \quad (4.23)$$

where

Q_{max} = largest angle in face or cell.

Q_{min} = smallest angle in face or cell.

Q_{eq} = angle for equiangular face or cell, E.g., 60 for triangle, 90 for square.

According to the definition of skewness, a value of 0 indicates an equilateral cell (best) and a value of 1 indicates a completely degenerate cell. Degenerate cells (slivers) are characterized by nodes that are nearly coplanar. Cells with a skewness value above 1 are invalid.

For the Q_{EAS} value between 0 and 1, Table 4.4.3 gives the mesh qualities with respect to a range of skewness values.

Table 4.4.3 Skewness ranges and cell quality

Skewness	Cell Quality
1	degenerate
0.9–<1	bad (sliver)
0.75–0.9	poor
0.5–0.75	fair
0.25–0.5	good
>0–0.25	excellent
0	equilateral

Table 4.4.4 reports the Equiangle skewness ranges of cells of the meshes for 1m/s, 2m/s and 3m/s flow velocities in the form of the number of elements and percentages. A clearer histogram of Q_{EAS} distribution is also available in Figure

4.4.10. According to the evaluation criterion, most mesh cells are of excellent or good quality with only less than 0.03% of the mesh elements being fair. There are no poor elements in the mesh.

Table 4.4.4 Skewness ranges and cell quality

Equiangle skew	1m/s		2m/s		3m/s	
	No. of elements	Percentage	No. of elements	percentage	No. of elements	percentage
<i>0→0.05</i>	1804411	42.6370%	2465272	45.6572%	2803904	51.9288%
<i>0.05→0.1</i>	1094768	25.8686%	1357690	25.1446%	1256131	23.2638%
<i>0.1→0.15</i>	523299	12.3652%	610995	11.3157%	524379	9.7116%
<i>0.15→0.2</i>	436777	10.3207%	486896	9.0174%	404308	7.4879%
<i>0.2→0.25</i>	158544	3.7463%	169683	3.1426%	176108	3.2615%
<i>0.25→0.3</i>	61471	1.4525%	107265	1.9866%	68356	1.2660%
<i>0.3→0.35</i>	51630	1.2200%	94777	1.7553%	94785	1.7554%
<i>0.35→0.4</i>	49818	1.1772%	52346	0.9695%	13715	0.2540%
<i>0.4→0.45</i>	6946	0.1641%	8956	0.1659%	10783	0.1997%
<i>0.45→0.5</i>	43358	1.0245%	44361	0.8216%	45598	0.8445%
<i>0.5→0.55</i>	814	0.0192%	1050	0.0194%	1272	0.0236%
<i>0.55→0.6</i>	102	0.0024%	122	0.0023%	87	0.0016%
<i>0.6→0.65</i>	74	0.0017%	80	0.0015%	72	0.0013%
<i>0.65→0.7</i>	20	0.0005%	27	0.0005%	22	0.0004%
<i>0.7→0.75</i>	0	0%	0	0%	0	0%
<i>0.75→0.8</i>	0	0%	0	0%	0	0%
<i>0.8→0.85</i>	0	0%	0	0%	0	0%
<i>0.85→0.9</i>	0	0%	0	0%	0	0%
<i>0.9→0.95</i>	0	0%	0	0%	0	0%
<i>0.95→1</i>	0	0%	0	0%	0	0%

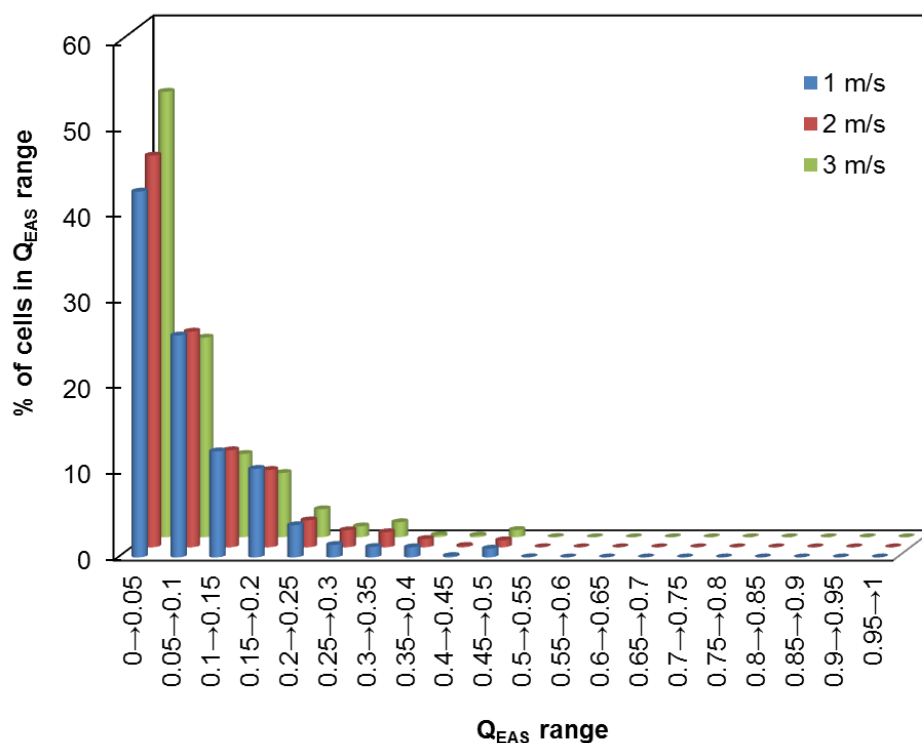


Figure 4.4.10 Histogram of Q_{EAS} quality distribution

Another important indicator of the mesh quality is the Aspect Ratio which is a measure of the stretching of a cell. It is computed as the ratio of the maximum value to the minimum value of any of the following distances: the normal distances between the cell centroid and face centroids, and the distances between the cell centroid and nodes.

There is no unified criterion on a certain Aspect Ratio under which the mesh is considered acceptable. However, some references argued that whilst large Aspect Ratios may be acceptable in some problems, a general rule of thumb might be to avoid Aspect Ratios in excess of 5:1 (Selvam and Govindaswamy, 2001).

Figure 4.4.11 shows the histogram of Aspect Ratio distributions of the cells of the mesh generated for simulating swirl flow with 1m/s, 2m/s and 3m/s velocities. It is clear that the Aspect Ratio of the cells within the meshes for 1 m/s and 2m/s flow velocities are all less than 4. For the mesh generated for flow with a velocity of 3 m/s, only 3.79% of the cells have an Aspect Ratio exceeds

5 with the largest value being 7.25. The relatively large Aspect Ratio for the 3 m/s case is due to the very fine boundary layer mesh at the near wall region. Compared with the 1 m/s and 2 m/s cases, the mesh used for the 3 m/s case has an even finer mesh in the boundary layer which results in more flat hexahedrons along the pipe wall thus increasing the Aspect Ratio.

Further refinement of the mesh for the 3 m/s case may decrease the Aspect Ratio. However it is deemed unnecessary considering the increase in computational cost and time for calculation. Moreover, the meshes for all cases lead to convergence of the solutions with no difficulties.

Therefore, it can be concluded that the meshes generated for all cases successfully pass the mesh quality test.

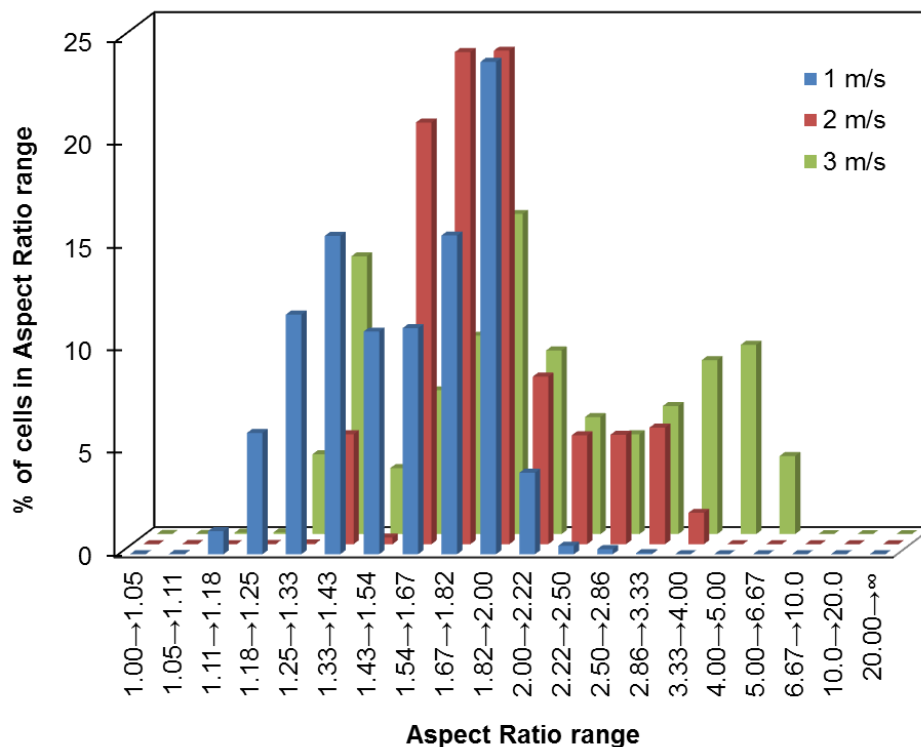


Figure 4.4.11 Histogram of Aspect Ratio quality distribution

4.4.5 Boundary Conditions

4.4.5.1 Operation Conditions

The operating conditions allow the user to set the operating pressure, include the effects of gravity and specify other operating variables. Following the FLUENT documentation, the zero operating pressure was used which would minimise errors due to the small pressure drop across the flow domain compared to atmospheric pressure. The gravity acting on the negative y-axis at 9.81 m/s^2 was included. The operating density was not specified, thus permitting the solver to calculate it by averaging over all cells.

4.4.5.2 Inlet Boundary Conditions

At the inlet, a uniform mean flow velocity boundary condition was applied. The material used was single phase, incompressible water with its density and viscosity being specified as 998.2 kgm^{-3} and $1.003 \times 10^{-3} \text{ kgm}^{-1}\text{s}^{-1}$ respectively. The turbulence of the flow was specified in terms of intensity and hydraulic diameter at the inlet. The turbulence intensity is defined as the ratio of the root-mean-square of the velocity fluctuations to the mean velocity. It was calculated by (ANSYS, 2011b):

$$I = 0.16 \times (Re)^{-1/8}, \quad Re = (U \times D \times \rho) / \mu$$

Where Re is the Reynolds number, U is the average velocity, ρ is the density, and μ is the viscosity.

The hydraulic diameter was set to be the same as the pipe diameter of 50mm.

A series of simulations was carried out with varying velocities from 1m/s to 3m/s. The corresponding Reynolds number and turbulence intensity are listed in Table 4.4.5.

Table 4.4.5 Simulation conditions at inlet

Inlet velocity (m/s)	Reynolds number	Turbulence intensity (%)
1	49,760	4
1.5	74,641	3.9
2	99,521	3.8
2.5	124,401	3.7
3	149,282	3.6

4.4.5.3 Outlet Boundary Conditions

A pressure outlet boundary condition with zero uniform static pressure was imposed at the outlet of the computational model. This boundary condition results in a better rate of convergence when backflow occurs during iteration. The turbulence was specified in terms of intensity and hydraulic diameter at the outlet in the same way as the inlet.

4.4.5.4 Wall Boundary Conditions:

The pipe walls were specified as being stationary and no-slip walls to match the simulation conditions. The no-slip condition for viscous fluids is that at a solid boundary, the fluid will have zero velocity relative to the boundary.

The wall roughness of the development section and the test section was set by specifying the roughness height, K_s , as 1.237×10^{-6} m which is the same value as the measured roughness of transparent Perspex pipes used in the experimental rig. The roughness was measured employing a surface roughness tester. The internal surface roughness of the swirl pipe was specified as 9×10^{-6} m which is the measured roughness of the stainless steel swirl pipe produced through investment casting. The two roughness values are small enough that the walls can be considered as hydraulically smooth.

4.4.6 Solution Methodology

4.4.6.1 Solver Setting

The steady state simulations were carried out with single phase water with the flow being assumed to be steady, incompressible and isothermal. The pressure-based segregated solver was used as it is recommended for incompressible flows. Reynolds Stress Model (RSM) was used in all cases, unless stated, otherwise the LES method was used. For the near wall treatment, initially the standard wall function was used to implement the wall boundary condition which was later improved by employing the non-equilibrium function. The SIMPLE discretization technique was applied for the pressure-velocity coupling and a second order upwind scheme was employed for the viscous terms. The following sections provide further details of the solver parameters.

4.4.6.2 Turbulence Model and Wall Treatment

As has been discussed in section 4.2.1 that the RSM accounts for the effects of streamline curvature, swirl, rotation, and rapid changes in strain rate in a more rigorous manner than one-equation and two-equation models, it has greater potential to give accurate predictions for complex flows (ANSYS, 2011a). The flow being modelled is swirling and in such turbulent flows viscosity is typically anisotropic, therefore the most reliable turbulence model, the Reynolds Stress Model (RSM) was chosen (Najafi et al., 2011, Fokeer et al., 2010).

For modelling the regions close to the walls, whose appropriate selection is of crucial importance in the calculation of shear stress, a two-layer-based, non-equilibrium wall function was employed which can partly account for the effects of pressure gradients in the wall area. Non-equilibrium wall functions are recommended for use in complex flows where the mean flow and turbulence are subjected to pressure gradients and rapid changes. In such flows,

improvements can be obtained, particularly in the prediction of wall shear and heat transfer (ANSYS, 2011a).

It was found that direct use of the RSM and the Non-Equilibrium wall functions with second order discretization at the start lead to divergence of the solution. Attempts were made to facilitate convergence by initially using the standard $k-\epsilon$ model with standard wall functions to obtain a baseline solution which was then improved by applying the Realizable $k-\epsilon$ model together with the Non-Equilibrium functions. After that, RSM was applied to further improve the solution until it reasonably converged.

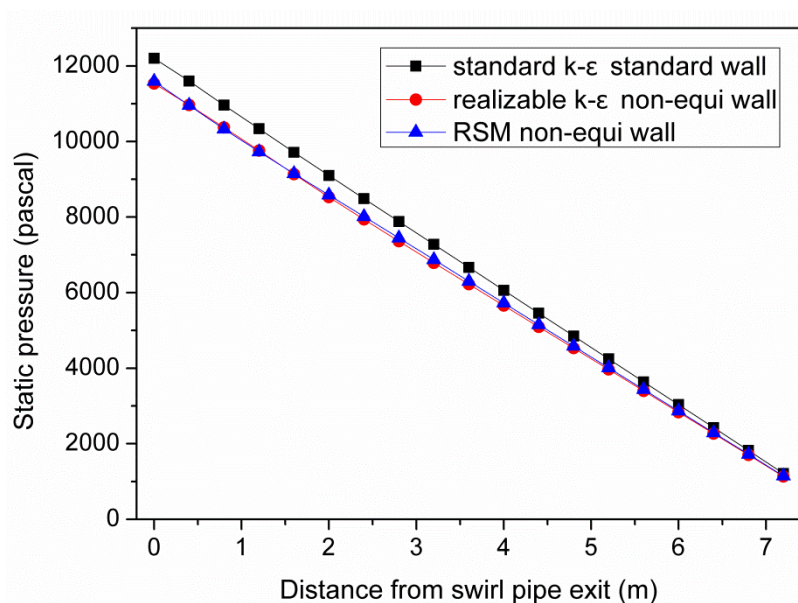


Figure 4.4.12 Pressure downstream of swirl pipe for various turbulence models and wall functions (3m/s inlet velocity)

Figure 4.4.12 shows the distribution of static pressure downstream of the swirl pipe obtained using various turbulence models and wall functions. It can be seen that the biggest difference occurs at the location where flow emerges from the swirl pipe with the realizable $k-\epsilon$ model and the Non-Equilibrium wall functions giving the most conservative prediction followed by RSM and the Non-Equilibrium wall functions (0.49% larger) and, finally, the standard $k-\epsilon$ model and standard wall functions (5.77% larger). Figure 4.4.12 may suggest that, for the prediction of pressure, the selection of wall function may play an

important role since when the Non-Equilibrium wall functions are selected, the use of the realizable k - ϵ model or RSM makes a very small difference; whilst with the standard wall function a clear difference is observed. This difference may be attributed to the advantage of the non-equilibrium wall function which can partly account for the effects of pressure gradients in the wall area.

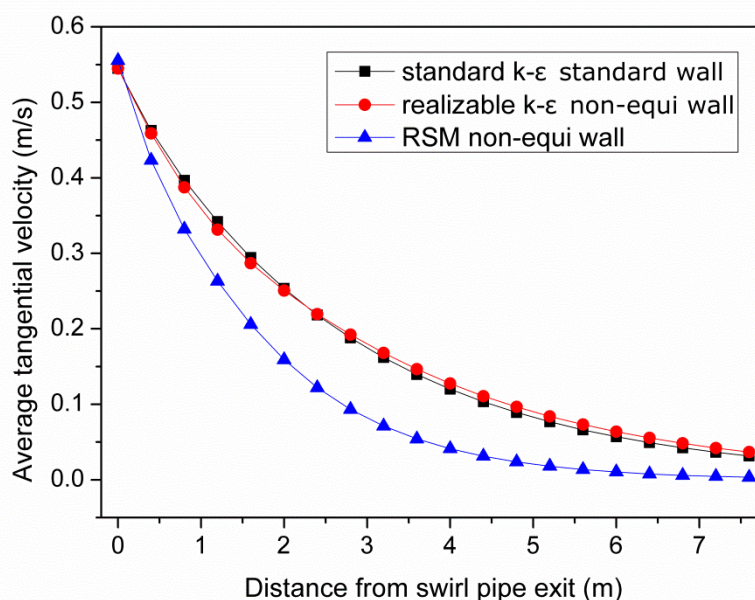


Figure 4.4.13 Tangential velocity downstream of swirl pipe for various turbulence models and wall functions (3m/s inlet velocity)

Figure 4.4.13 depicts the variation of average tangential velocity in the planes downstream of the swirl pipe for various turbulence models and wall functions. it shows that the RSM and Non-Equilibrium wall functions combination gives the largest prediction of initial tangential velocity just downstream of the swirl pipe followed by realizable k - ϵ model (1.89% lower) and, finally, the standard k - ϵ model (1.92 lower). However, the tangential velocity predicted by the RSM model decreases faster with increasing downstream distance with a maximum difference of 17.3% lower than that obtained by the standard k - ϵ model and maximum 17.8 % lower than that predicted by the realizable k - ϵ model. From the figure, despite the use of different wall functions, the standard k - ϵ model and realizable k - ϵ model gives similar predictions of tangential velocity. On the other hand, although same Non-Equilibrium wall functions are chosen, the use of the RSM results in a clear difference in predicted tangential velocity compared

to the realizable k - ε model. Figure 4.4.13 indicates the importance of the turbulence model in predicting the turbulent flow region. The difference between the RSM and k - ε models is due to the difference in how the models handle the turbulent swirl flow induced by the swirl pipe. Conceptually, RSM should give more reliable predictions.

4.4.6.3 Advection Schemes for Viscous Terms

Three identical cases were run with each case employing First order upwind, Second order upwind and QUICK schemes respectively for viscous terms (the momentum, kinetic energy, dissipation rate and Reynolds Stresses). The variation of static pressure and tangential velocity determined by the three schemes are presented below.

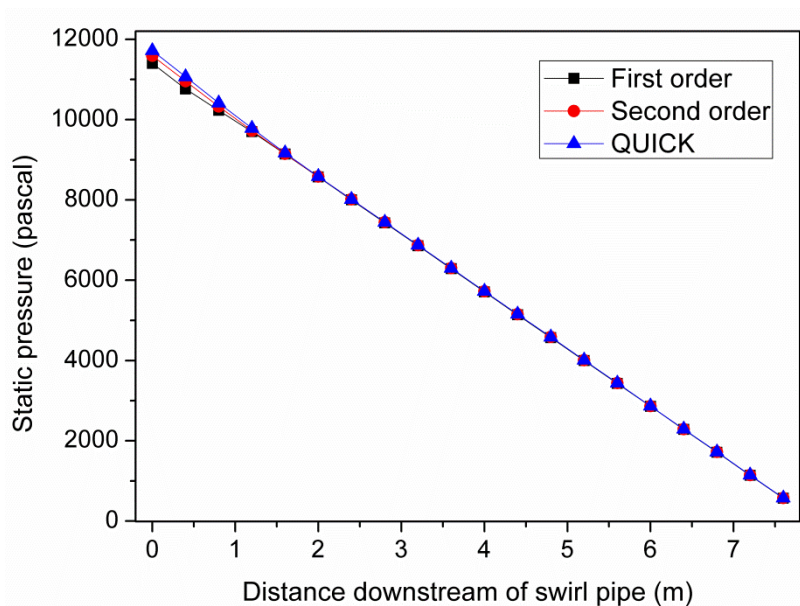


Figure 4.4.14 Pressure downstream of swirl pipe for various advection schemes (3m/s inlet velocity)

Figure 4.4.14 shows that the three schemes yield very close pressure downstream of the swirl pipe with the main difference occurring at the exit of the swirl pipe where the QUICK scheme gives the highest pressure followed by second order (1.07% lower) and first order schemes (2.71% lower).

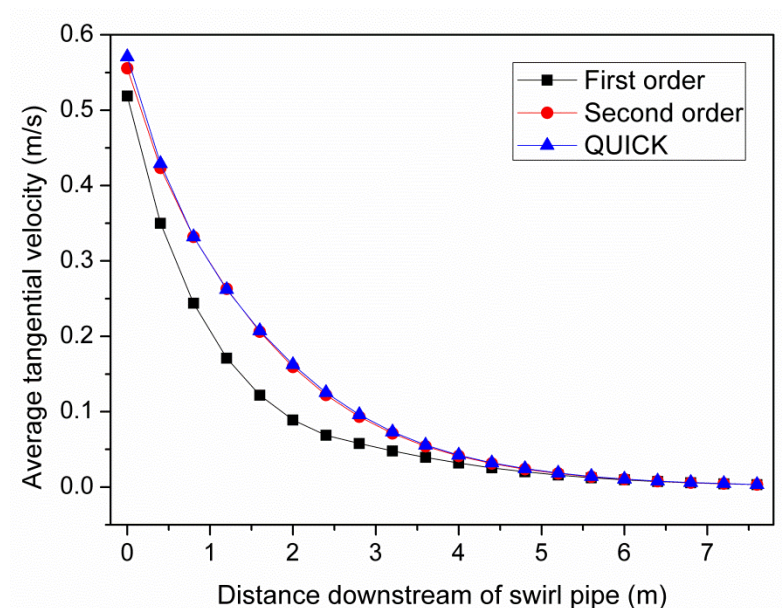


Figure 4.4.15 Tangential velocity downstream of swirl pipe for various advection schemes (3m/s inlet velocity)

From Figure 4.4.15, the first order scheme yields the most conservative prediction for tangential velocity with a maximum difference of 45.26% lower than that obtained by the QUICK scheme. Whilst the second order and QUICK schemes provide close tangential velocity downstream of the swirl pipe with the largest difference being 2.79% lower for second order upwind scheme.

In general, the QUICK scheme does not provide significant difference in the monitored variables than the second order method. Considered the extra time (32% longer) required for the solution to reasonably converge for the QUICK, the second-order scheme is deemed to be sufficient and will be used as it provides a good compromise between accuracy and solution time.

4.4.6.4 Pressure Interpolation Scheme

As has been stated in section 4.3.2.1, the standard pressure interpolation scheme will have trouble handling flows with large body forces (such as strongly swirling flow) and the presence of curvature, therefore this scheme was not considered. The second order was employed as it is reported to provide

improvement over standard and linear schemes. Later on, attempts were made to improve the solution by adopting the PRESTO! and the body-force-weighted scheme. It was found that for this particular case, the PRESTO! and body-force-weighted schemes have difficulties converging the solution. Nevertheless, the simulation results were compared after 3000 iterations when the monitored parameters reached a stable value. The distribution of static pressure and tangential velocity downstream are presented in Figure 4.4.16 and Figure 4.4.17 respectively. It shows that the three interpolation schemes yield very close prediction for static pressure with a negligible maximum difference of 0.35% between them. The difference in predicted tangential velocity is relatively clearer though still small with an improvement of maximum 7.7% (+0.004 m/s) and 3.5% (+0.002 m/s) for PRESTO! and body force weighted schemes respectively. Due to the difficulty in the solution convergence employing PRESTO! and body force weighted schemes and the limited improvements they provided, it was therefore decided to still employ the second order pressure discretisation scheme for future simulations.

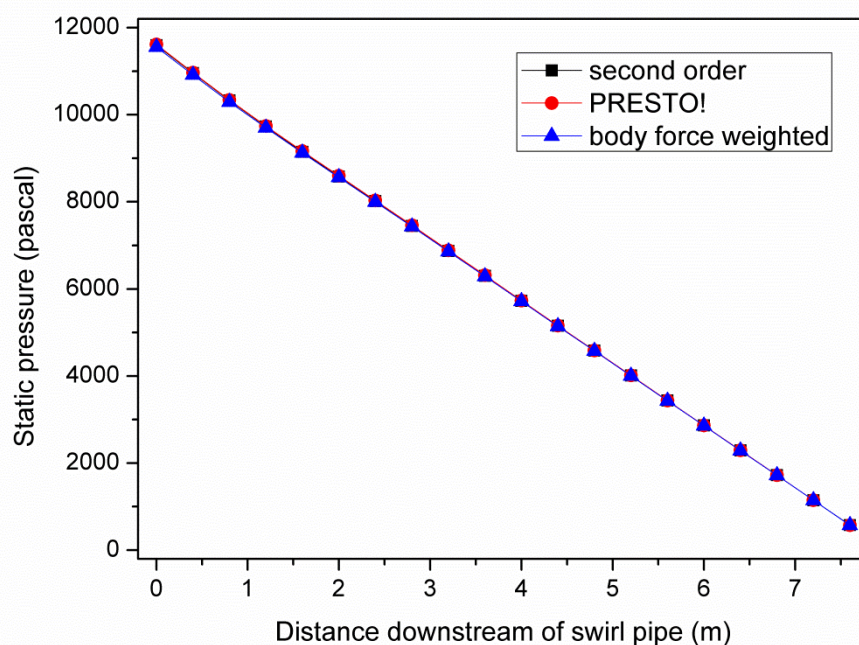


Figure 4.4.16 Pressure downstream of swirl pipe for various pressure interpolation schemes (3m/s inlet velocity)

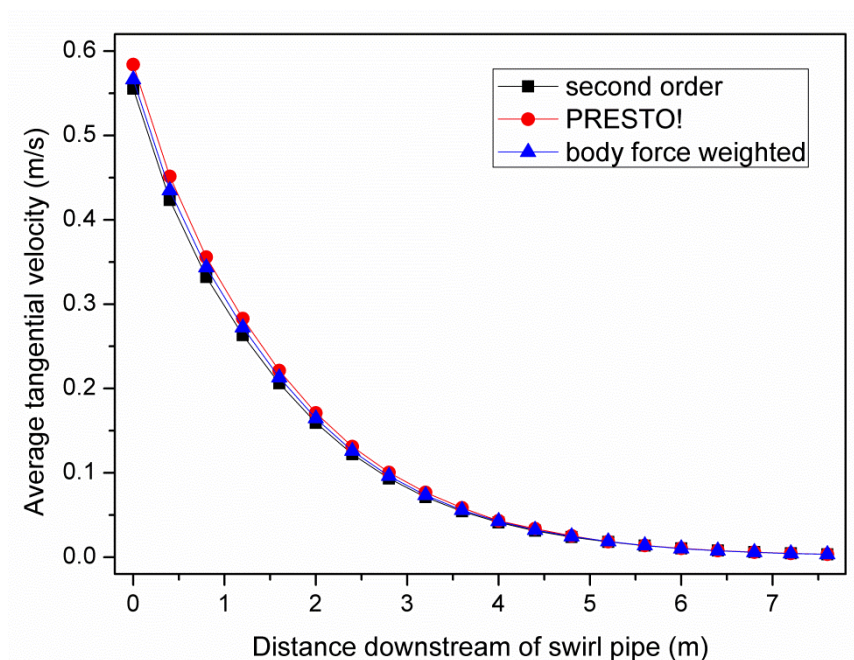


Figure 4.4.17 Tangential velocity downstream of swirl pipe for various pressure interpolation schemes (3m/s inlet velocity)

4.4.6.5 Pressure-velocity Coupling Scheme

Since the PISO scheme is recommended for transient calculations, only the SIMPLE and SIMPLEC algorithm were considered for the steady state simulations. The difference was compared by running two identical cases, each employing SIMPLE or SIMPLEC pressure-velocity coupling schemes respectively. Figure 4.4.18 shows that the SIMPLE and SIMPLEC schemes yield almost identical results with the maximum difference in pressure and tangential velocity being 0.06% and 0.04% respectively lower for the SIMPLE scheme. Since no advantage resulted from the use of SIMPLEC pressure-velocity coupling schemes, it was decided to employ the SIMPLE pressure-velocity coupling schemes.

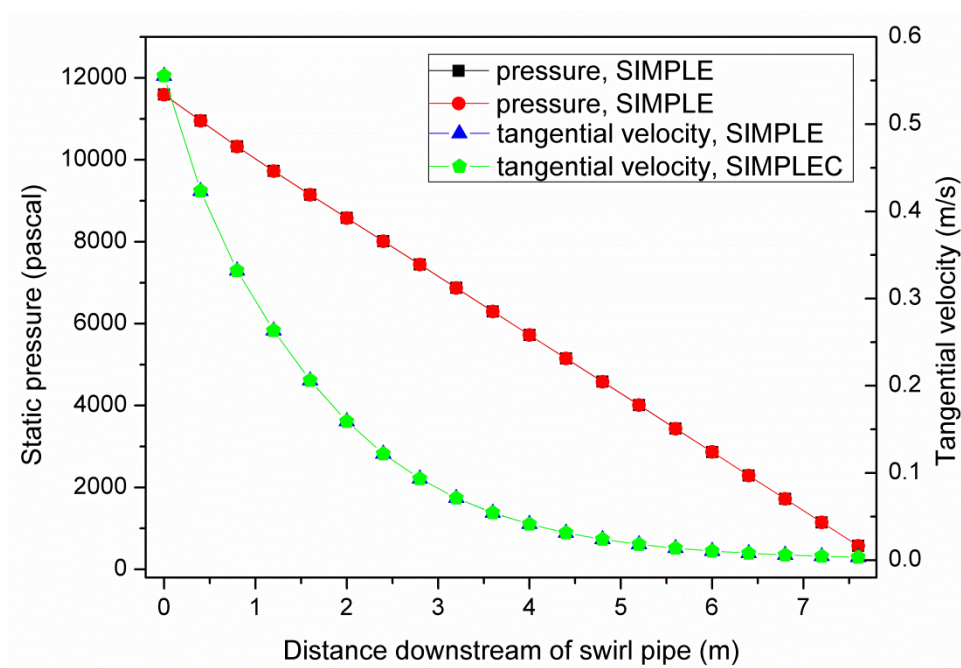


Figure 4.4.18 Pressure and tangential velocity after swirl pipe for various Pressure-velocity coupling schemes (3m/s inlet velocity)

4.4.7 Judging Convergence

The iterative process is repeated until the change in the variable from one iteration to the next becomes so small that the solution can be considered converged. There are no universal metrics for judging convergence; however it is common to require the scaled residuals to be in the order of 10^{-3} to 10^{-4} or less for convergence.

It should be noted that residual definitions that are useful for one class of problem are sometimes misleading for other classes of problems. Therefore it is a good idea to judge convergence not only by examining residual levels, but also by monitoring relevant integrated quantities and checking for mass and energy balances.

Generally, there are three indicators that convergence has been reached:

1. The residuals have decreased to a sufficient degree.

The solution has converged when the convergence criterion for each variable has been reached. The default criterion is that each residual will be reduced to a value of less than 10^{-3} . In this study, the convergence criterion used for all cases was that the scaled residuals of x , y , z velocities, k , and ϵ , and Reynolds stresses have decreased by four orders of magnitude. Figure 4.4.19 shows the scaled residuals for a final simulation model of the swirl flow where a value of 10^{-4} has been reached for all variables.

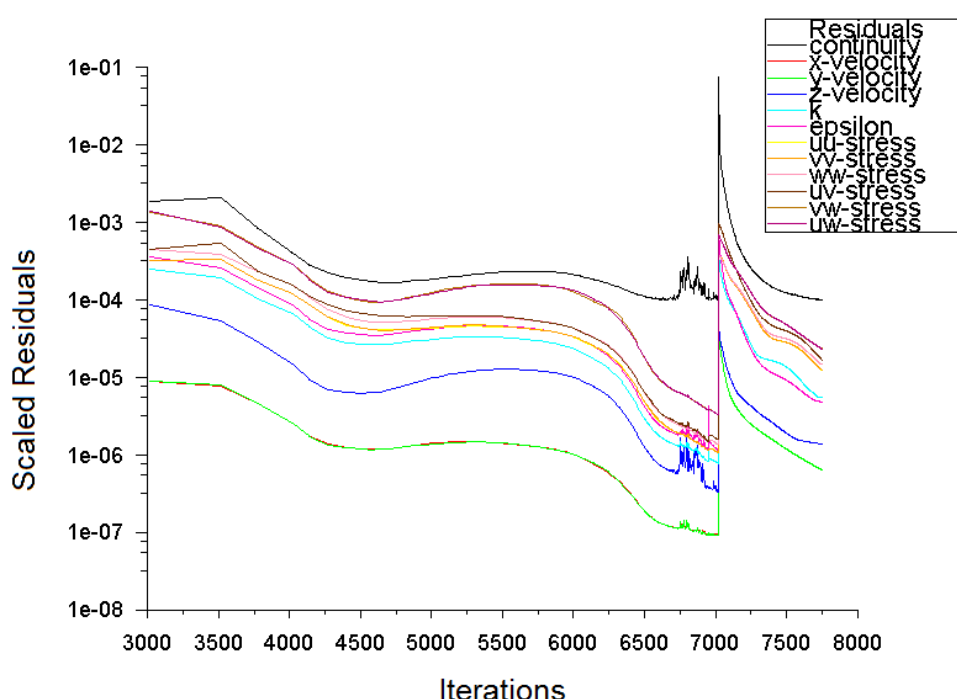


Figure 4.4.19 Scaled residuals for a final simulation model

2. The solution no longer changes with more iterations.

Sometimes the residuals may not fall below the convergence criterion set in the case setup. However, monitoring the representative flow variables through iterations may show that the residuals have stagnated and do not change with further iterations. This could also be considered as convergence.

Figure 4.4.20 shows the inlet pressure convergence of the last 100 iterations as

the solution was proceeding. The convergence of the wall shear stress at the position 0.5m downstream of the swirl pipe was also checked which is presented in Figure 4.4.21. It is clear that the two variables have levelled out.

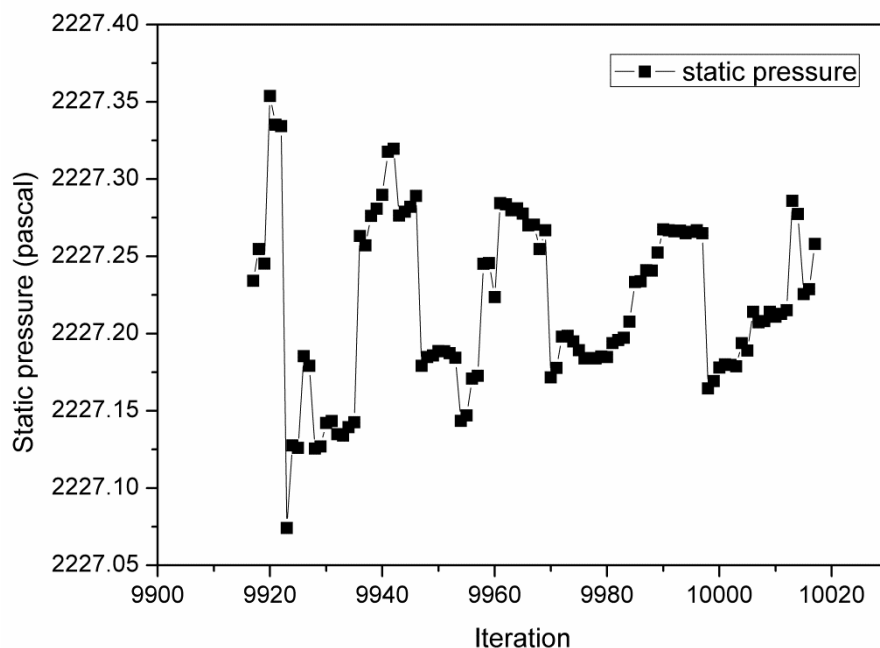


Figure 4.4.20 Variation of static pressure at inlet as solution proceeding (last 100 iterations)

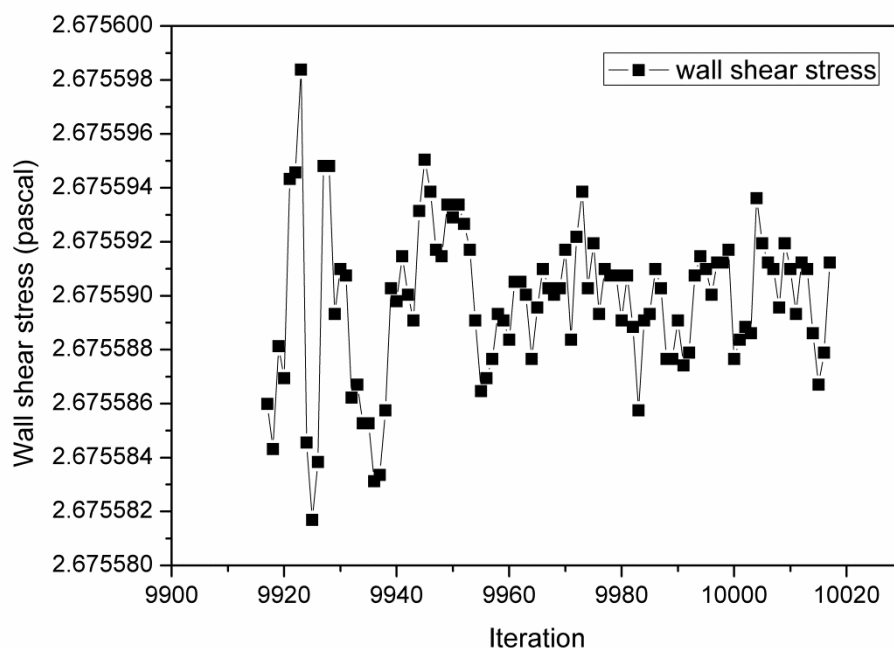


Figure 4.4.21 Variation of wall shear stress 0.5m downstream of swirl pipe with iteration number (last 100 iterations)

3. The overall mass, momentum, and scalar balances are obtained.

The mass imbalance was checked for all cells and was generally in the range of 10^{-8} (Figure 4.4.22). Additionally, the mass imbalance between the inlet and outlet was examined as the solution was proceeding. The mass imbalance, as shown in Figure 4.4.23, converged to zero as expected.

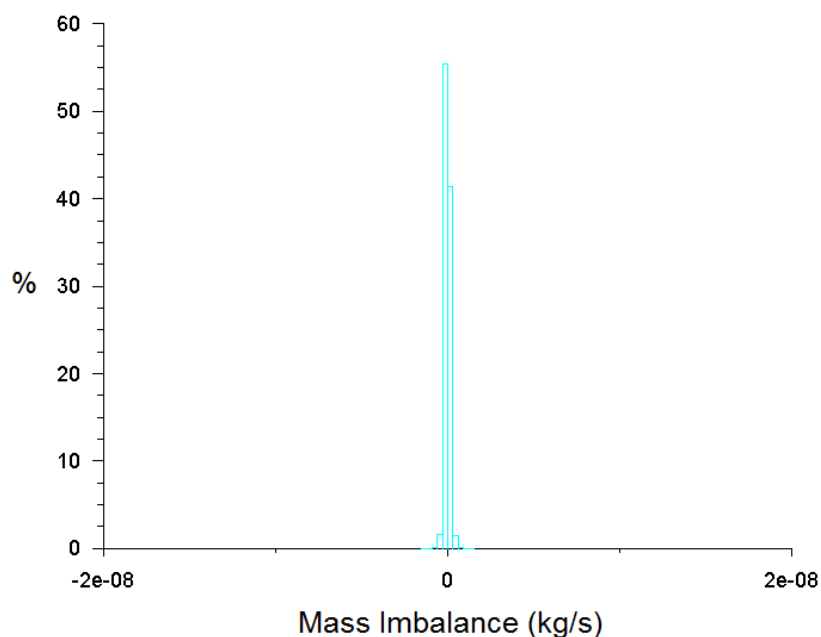


Figure 4.4.22 Histogram of mass imbalance

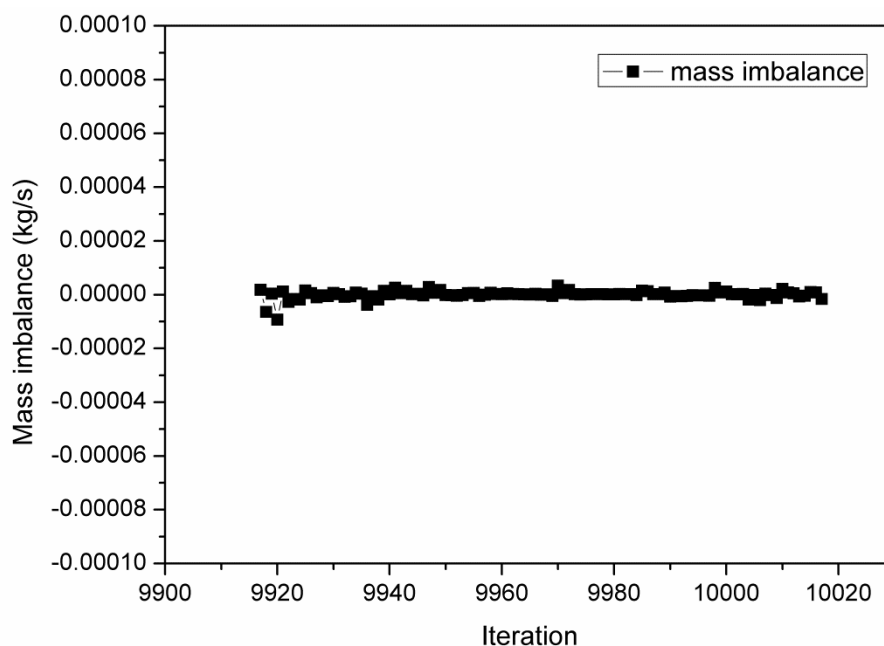


Figure 4.4.23 Variation of mass imbalance (inlet-outlet) as solution was proceeding (last 100 iterations)

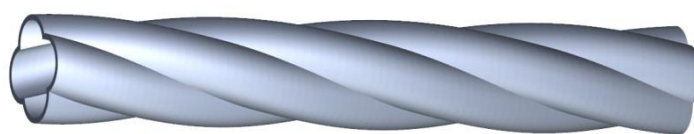
4.5 Conclusions

- CFD was applied to model the swirl flow induced by the optimised 4-lobed swirl pipe. The principles and methods underlying CFD were introduced in this chapter.
- The k - ϵ and RSM Turbulence models for Reynolds-averaged Navier-Stokes (RANS) equations were described and compared. In the 'near-wall region' where turbulence models fail to give accuracy prediction, the near wall treatment methods were presented.
- In this study, the finite volume method based ANSYS FLUENT code was used to solve the governing equations. The numerical methods of the solvers and the numerical discretization technique applied were covered.
- The formulation of the model used for simulating the swirl flow was described in detail including enabling assumptions, configuration of the flow domain and boundary conditions, etc.
- Various approaches attempted to discretise the flow domain using structured hexahedral mesh were explained, of which a Multi-Block structured mesh using ICEM CFD was adopted. To ensure errors associated with the mesh are minimised, mesh adaption for wall functions, mesh independence tests and mesh quality tests were carried out.
- For the solution of the swirl flow field, the turbulence models and wall functions were tested and compared, with the RSM turbulence and Non-Equilibrium wall functions being employed in the final model. The discretization schemes for the viscous terms, pressure-velocity coupling and pressure interpolation were evaluated and selected respectively.
- Convergence of the solution was identified by monitoring the scaled residuals, flow variables and mass balances.

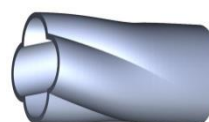
CHAPTER 5: FURTHER OPTIMISATION OF THE 4-LOBED SWIRL PIPE

5.1 Introduction

It has been stated previously that, based on the evaluation criteria of Swirl Effectiveness, Ganeshalingam (2002) recommended a 4-lobed swirl inducing pipe with a P:D ratio of 8 and the length of 400mm as an optimal design. As shown in Figure 5.1.1a, this optimal swirl inducing pipe has an equivalent diameter of 50mm and has the 4-lobed cross-section rotated by 360° through a length of 400mm.



(a) Optimal Swirl inducing pipe, 400mm length, P:D=8



(b) Entry transition pipe, (c) Exit transition pipe

Figure 5.1.1 Optimal Swirl inducing pipe and transition pipes

It was found that there were high entry and exit pressure losses across this optimal swirl inducing pipe when connected to circular pipes due to the sudden change in cross-section from lobed to circular and vice versa. Transition geometries prior to and after the swirl pipe were suggested to eliminate these pressure losses. This should further improve the applicability of the swirl inducing pipes. However the transition section should be short and effective. Otherwise it will increase overall pressure drop and, in the case of exit transition,

may decrease swirl intensity.

Ariyaratne (2005) designed and optimized a transition pipe for use as an entry and exit duct with the optimal swirl inducing pipe. The transition pipes either before or after the swirl inducing pipe were found to reduce entry and exit pressure losses by providing a gradual transition from circular to lobed cross-section. They also increased induced swirl and reduced swirl decay. As shown in Figure 5.1.1b and Figure 5.1.1c, the transition pipe's cross-section changes from circular to 4-lobed shape and vice versa gradually. The area of the cross-sections is constant and equal to that of the swirl inducing pipe. The length of transition pipe is 100mm, and each lobe rotates by 90°.

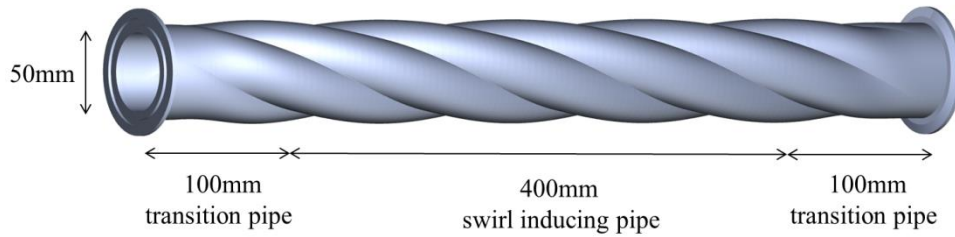
Based on the study of Ariyaratne (2005), a swirl pipe configuration of 100mm entry transition prior + 400mm swirl inducing pipe + 100mm exit transition pipe after (as shown in Figure 5.1.2a) should be deemed to be optimum. However, in this configuration:

- The entry and exit transition pipes are used in place of the cylindrical pipes making the total length of the swirl pipe 600mm instead of 400mm. The longer swirl pipe results in more pressure loss due to the increase in contact area and thus friction.
- The swirl pipe has the lobed cross-section rotated by 540° (one and a half swirl) instead of 360° (one swirl), as in the previous design.
- Ariyaratne (2005) stated that when the entry transition pipe was used in conjunction with the swirl pipe, a higher tangential velocity was generated. However, the induced swirl appeared to be constrained by the swirl inducing pipe geometry. Ariyaratne therefore suggested that a shorter length of swirl inducing pipe will therefore be required to generate an equivalent amount of swirl.
- In this chapter, we numerically investigated the swirl development within this 600mm length swirl pipe and found that the swirl intensity induced

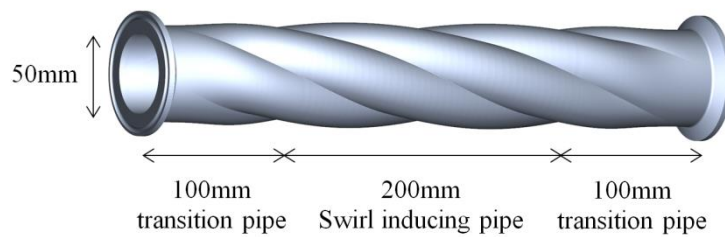
reaches the highest value in the middle of the 400mm swirl inducing pipe (0.3m in the X axis in Figure 5.3.3), and starts to decrease in the second half of the swirl inducing pipe (0.3m to 0.5m in the X axis in Figure 5.3.3). It suggested that the second half of the swirl inducing pipe constrains and weakens the development of the swirl.

Therefore, with the inclusion of transitions, a shorter length of 200mm swirl inducing pipe should provide improved swirl induction effectiveness. A swirl inducing pipe shorter than 200mm will decrease pressure loss but also result in decreased overall swirl intensity. While a swirl inducing pipe longer than 200mm will constrain and weaken the swirl induced and also give rise to greater pressure loss. Therefore, a swirl pipe configuration of 100mm entry transition pipe + 200mm swirl inducing pipe + 100 exit transition pipe was proposed. Other lengths of swirl pipes were not considered as they are less effective in swirl induction resulting in lower initial swirl intensity at swirl pipe exit. This configuration, as shown in Figure 5.1.2b, has one swirl, a total length of 400mm and an equivalent diameter of 50mm.

This chapter presents a numerical comparison of the two configurations of horizontally mounted four-lobed swirl pipes in terms of swirl induction effectiveness into flows passing through them. Pressure losses, swirl development within the two swirl pipes, and their swirl effectiveness are analysed and compared. Besides, comparisons of swirl decay and wall shear stress downstream of the swirl pipes for various velocities were also covered. A more detailed numerical comparison of the two swirl pipes was presented in a conference at San Francisco USA, June 07-08, 2015 (Li et al., 2015). The conference paper is referred to Appendix 5.1 for easy reference.



(a) 100+400+100 swirl pipe, 600mm length, one and a half swirl



(b) 100+200+100 swirl pipe, 400mm length, one swirl

Figure 5.1.2 Two configurations of swirl pipes

5.2 Numerical Method and Models

Configurations of the two modelled pipe flow systems employing the 600mm length and 400mm length swirl pipes respectively are shown in Figure 5.2.1. The numerical method, models used and the meshing method are described in the Chapter 4 section 4.4. A series of simulations were carried out with inlet velocities of 1m/s, 2m/s and 3m/s. The solver parameters and boundary conditions are summarised in Table 5.2.1.

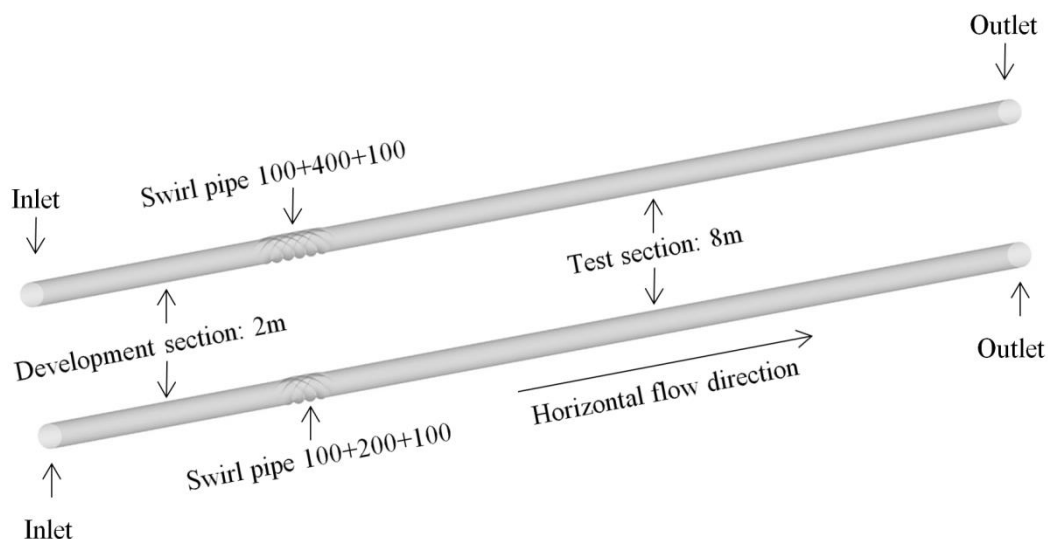


Figure 5.2.1 Configuration of simulation geometries

Table 5.2.1 Models and parameters used for the simulations

Items	Parameters
Solver	Pressure-based Segregated Solver
	Steady state simulation
	Absolute velocity formulation
Material	Water: Density= 998.2kg/m^3 , Viscosity= $0.001003\text{kg/m}^{\text{s}}$
Viscous model	RSM, Non-Equilibrium wall functions
Operating conditions	Operating pressure=0 Pascal
	Gravity= 9.81m/s^2
Boundary conditions	<ul style="list-style-type: none"> INLET: Velocity inlet boundary condition
	Velocity magnitude=1, 2, 3 m/s
	Turbulence Intensity=4%, 3.8% and 3.6% respectively
	Hydraulic Diameter = 50 mm
	<ul style="list-style-type: none"> OUTLET: Pressure outlet boundary condition
	Gauge Pressure=0 Pascal
Solution methods	Turbulence specification method: k and epsilon
	<ul style="list-style-type: none"> WALL: wall boundary condition
	Stationary no slip wall
	Roughness height= $9 \times 10^{-6}\text{m}$ for swirl pipe;
	$1.237 \times 10^{-6}\text{m}$ for circular pipes
	<ul style="list-style-type: none"> Second order upwind for momentum, kinetic energy, dissipation rate and Reynolds Stresses
Solution methods	Pressure interpolation: Second order
	Pressure-Velocity coupling: SIMPLE(Semi-Implicit Method for Pressure-Linked Equations)

The convergence criterion used for all cases was that the scaled residuals of x , y , z velocities, k , and ϵ , and Reynolds stresses have decreased by four orders of magnitude. The mass flow rate at the outlet was monitored and the solution was deemed to have reached a steady state when this parameter achieved a constant value over a large number of iterations.

5.3 Results and Discussions

5.3.1 Pressure Drop

The pressure loss across the lobed swirl pipe itself is greater than circular pipe due to the additional turbulence generated through artificial roughness of the non-circular pipe surfaces (Ganeshalingam, 2002, Ariyaratne, 2005). The energy lost is partly converted into angular momentum of the swirling flow. Figure 5.3.1 demonstrates the pressure drop of the flow within the 600mm and 400mm length swirl pipes for flows with velocities being 3m/s, 2m/s, and 1m/s respectively.

From Figure 5.3.1, it can be seen that:

- A larger inlet velocity causes larger pressure drop in both the 100+400+100 swirl pipe and the 100+200+100 swirl pipe.
- For a given flow velocity, the overall pressure drop caused by the 100+400+100 swirl pipe is always larger than that caused by the 100+200+100 swirl pipe due to its larger contact area with fluid and thus pipe friction.
- The differences in production of pressure drops by the two swirl pipes are more obvious in flows with higher velocities.
- The entry and exit transition pipes result in less pressure loss compared with the swirl inducing pipe. This is clearer for high velocity flows.

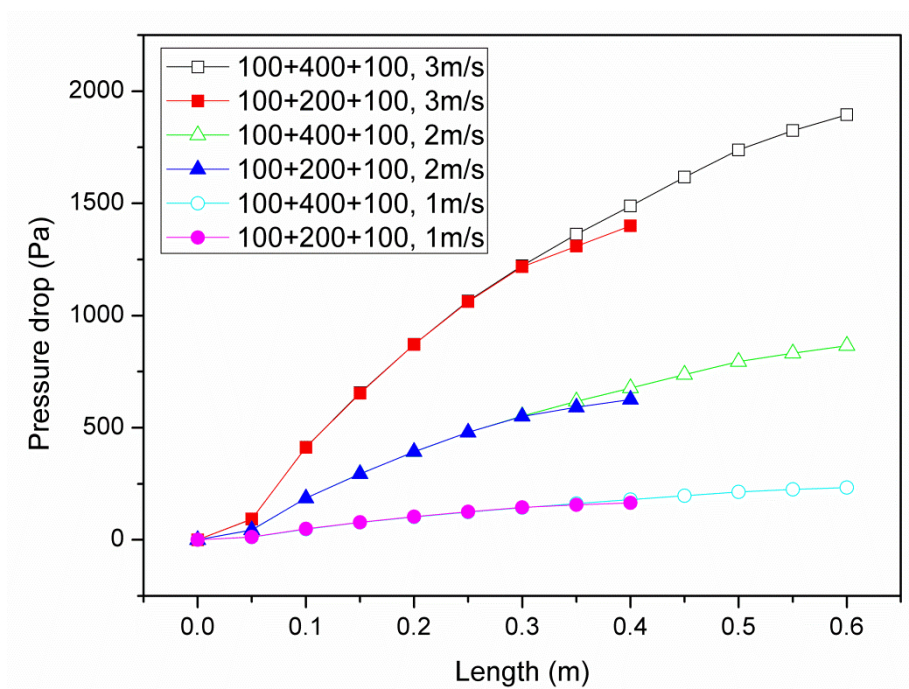


Figure 5.3.1 Pressure drop across the two swirl pipes in flows with various inlet velocities

Table 5.3.1 gives the overall pressure losses caused by the 600mm length and 400mm length swirl pipes in flows with various velocities. Compared to the 100+200+100 swirl pipe, the 100+400+100 swirl pipe resulted in additional pressure losses of 41%, 38% and 35% respectively for flows with 1m/s, 2m/s and 3m/s velocities.

Table 5.3.1 Comparison of the two swirl pipe in swirl induction

Velocity (m/s)	Pressure drop (Pascal)		Final tangential velocity (m/s)		Final swirl intensity		Swirl effectiveness	
	600mm swirl pipe	400mm swirl pipe	600mm swirl pipe	400mm swirl pipe	600mm swirl pipe	400mm swirl pipe	600mm swirl pipe	400mm swirl pipe
1	233.24	165.25	0.156	0.156	0.106	0.106	0.228	0.321
2	866.2	625.86	0.33	0.345	0.115	0.125	0.265	0.398
3	1894.99	1399.5	0.545	0.555	0.129	0.133	0.305	0.428

5.3.2 Swirl Development within Swirl Pipes

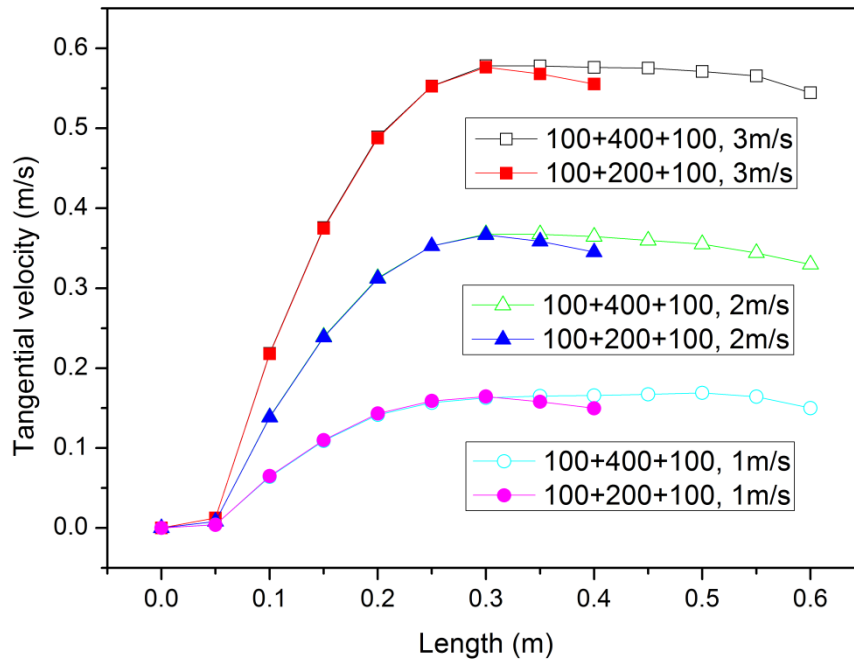


Figure 5.3.2 shows the development of tangential velocity within the 100+400+100 swirl pipe and 100+200+100 swirl pipe for the three inlet velocities of 3m/s, 2m/s and 1m/s. It is clear that:

- Both swirl pipes induce greater tangential velocities in flows with higher velocities.
- For both swirl pipes, exit transition pipes cause a decrease in tangential velocity.
- For the three inlet velocities and for the 100+400+100 swirl pipe, a sharper tangential velocity increase is seen from the middle of the entry transition pipe (0.05m in the X axis) and reaches the highest value in the vicinity of the middle of the 400mm swirl inducing pipe (0.4m in the X axis). The tangential velocity decreases slightly in the second half of the swirl inducing pipe indicating that it is acting as a constraint to the induced tangential velocity.
- While in the case of 100+200+100 swirl pipe, the whole 200mm swirl

inducing pipe contributes to the tangential velocity development with the largest value appearing at the join of the swirl inducing pipe and the exit transition pipe and the largest values in tangential velocity are almost the same as the 100+400+100 swirl pipe.

- The final tangential velocities at the exit of the 100+200+100 swirl pipe are slightly larger than that of the 100+400+100 pipe for inlet velocities of 2m/s and 3m/s. For a flow of 1m/s velocity, no difference in the final tangential velocity was identified.

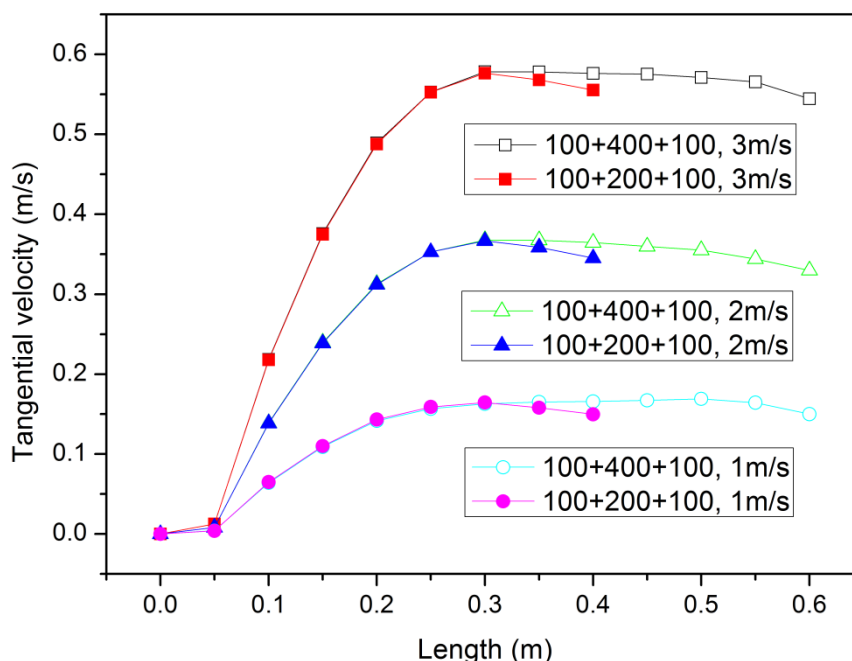


Figure 5.3.2 Tangential velocity distribution within the two swirl pipes for various inlet velocities

Figure 5.3.3 depicts the variation of swirl intensity within the two swirl pipes for the three velocities. Generally, for both swirl pipes, the first 0.3m length contributes to swirl induction with the swirl intensity value and its variation almost identical. The highest swirl intensity value appears in the 0.3m in the X axis for both swirl pipes. However, starting from 0.3m in the X axis, for the 600mm swirl pipe, both the second half of the swirl inducing pipe and the exit

transition pipe act as a constraint to the swirl induced previously. While for the 400mm length swirl pipe, only the exit pipe constrain the swirl induce. Due to the presence of the second half of the swirl inducing pipe in the 600mm length swirl pipe, which did not contribute to but weaken the swirl induction, the final swirl intensity at the exit of the 100+400+100 pipe is smaller than that of the 100+200+100 swirl pipe especially for larger flow velocities. The detailed initial swirl intensity downstream of both pipes for the three velocities is listed in Table 5.3.1. This confirmed again that, in the case of 100+400+100 swirl pipe, the second half of the swirl inducing pipe constrains and weakens the development of swirl and therefore needs to be removed. Besides, it was found the 400mm length swirl pipe also gives rise to greater swirl intensity and wall shear stress to the downstream which also lasts for longer downstream distance. The detailed numerical comparison of the 400mm and 600mm length swirl pipes in terms of the downstream wall shear stress and swirl intensity is discussed in a conference paper which is attached in Appendix 5.1 for easy reference (Li et al., 2015).

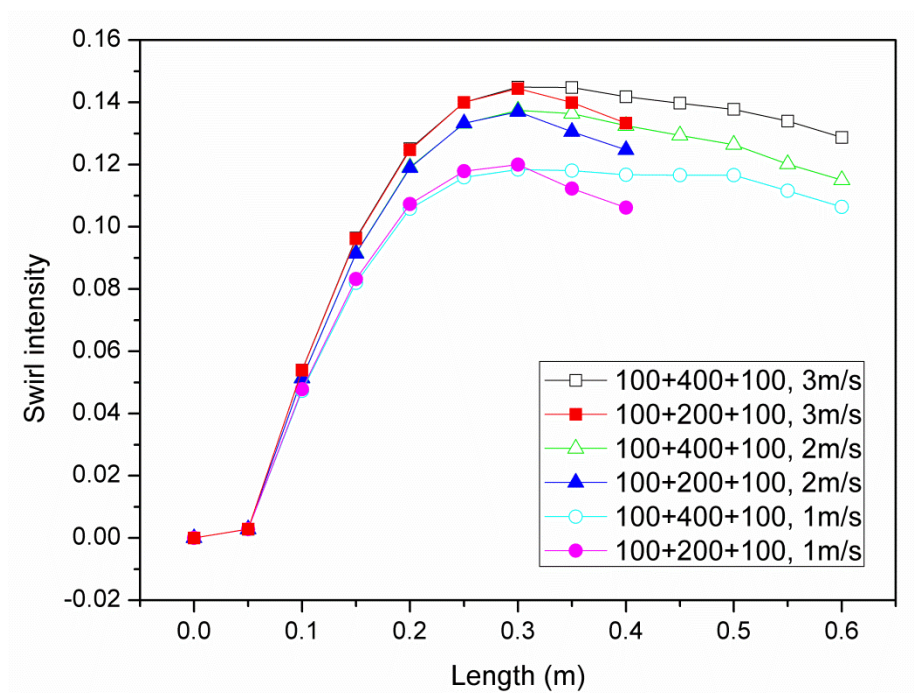


Figure 5.3.3 Swirl intensity distribution within the two swirl pipes for

various inlet velocities

5.3.3 Swirl Effectiveness

Ganeshalingam (2002) defined a Swirl Effectiveness parameter based on the ratio of the swirl intensity produced to the pressure loss, and used it in all swirl effectiveness calculations. The effectiveness of swirl induction was deemed to be the swirl intensity that could be induced for a given pressure drop. This parameter is also used in this research for the comparison of the two swirl pipe configurations in terms of swirl induction effectiveness.

$$\text{Swirl Effectiveness} = \frac{\text{Swirl Intensity}}{\frac{\Delta P}{\frac{\rho \times u^2}{2}}} \quad (5.1)$$

Where ΔP is pressure drop, ρ is density, and u is flow velocity.

Figure 5.3.4 shows the swirl effectiveness variation for both pipes with the three different inlet velocities. At each position, the value is calculated as the overall swirl effectiveness from the inlet of the swirl pipe to that specific position.

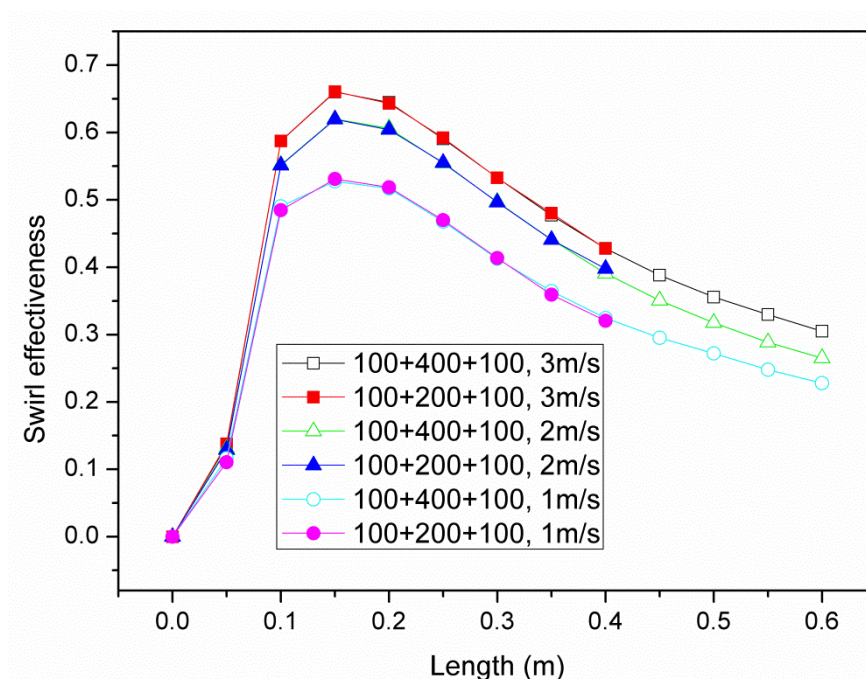


Figure 5.3.4 Swirl effectiveness variation within the two swirl pipes for

various inlet velocities

In the entry transition pipe for the two swirl pipes, there is a quick increase in swirl effectiveness. This is due to the gradual transition from circular to the lobed cross-section which reduces frictional losses from the pipe walls thereby producing a more effective swirl induction from a smaller pressure drop.

The quick increase in swirl intensity prevails within the swirl inducing pipe that it is immediately adjacent to the entry transition pipe where the swirl effectiveness reaches its highest value in this duration (0.1~0.15m). The high swirl effectiveness value benefits from the averaging of pressure losses caused by the entry transition pipe and the swirl inducing pipe section (0.1~0.15m).

Afterward, the increase in swirl intensity slows down until it reaches a maximum value in the vicinity of 0.3m in the horizontal axis as shown in

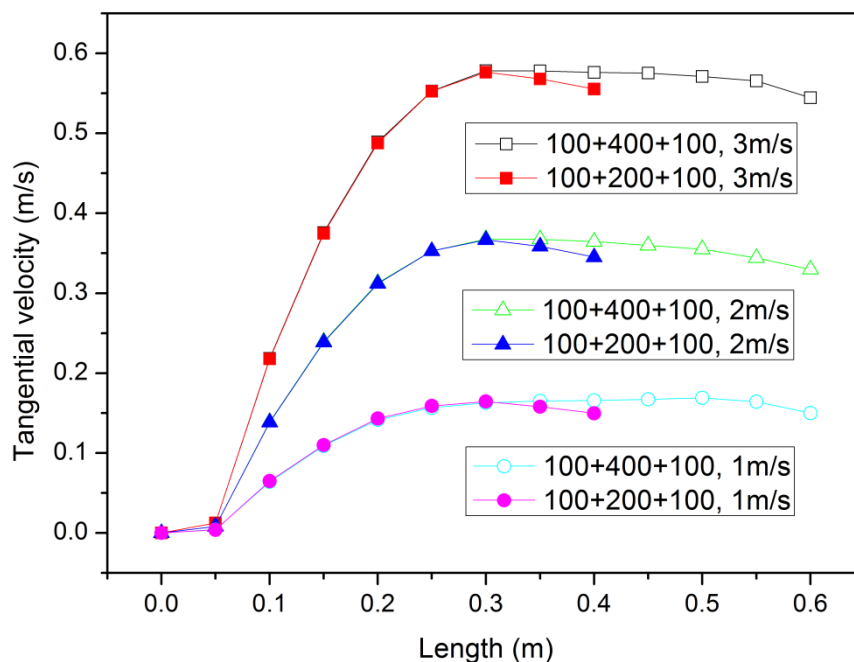


Figure 5.3.2 where the swirl inducing pipe still contributes to swirl induction despite of the drop in swirl effectiveness (which is due to the increase in the average pressure loss). Until this position, the two swirl pipes have almost identical swirl induction effectiveness.

Downstream of the 0.3m position, the second half of the swirl inducing pipe and the exit transition pipe of the 100+400+100 swirl pipe is restricting the swirl motion that has been generated. However, only the exit transition pipe of the 100+200+100 swirl pipe is restricting the swirl. Due to the constraining effects and extra pressure loss caused by the second half of the 400mm swirl inducing pipe, the overall swirl effectiveness of the 100+400+100 pipe is lower than that of the 100+200+100 pipe. The swirl effectiveness values for the two pipes under the three conditions can be referred to Table 5.3.1.

5.3.4 Swirl Decay

The induced swirl flow decayed with increasing distance downstream the swirl pipe and reverted back to the upstream flow profile at different distances downstream according to the inlet velocities. The decay of swirl is caused by the transport of angular momentum to the pipe wall. Figure 5.3.5 depicts the average tangential velocity distribution downstream of both the 100+400+100 swirl pipe and the 100+200+100 swirl pipe for inlet velocities of 3m/s, 2m/s and 1m/s. It is clear for both the two swirl pipes that tangential velocity decreases with increasing distance downstream and finally decreases to zero where the swirl effect fades away. It is also clear that the effectiveness of both the two swirl pipes is more prominent for flows with larger velocities. However, for the same inlet velocities, the initial tangential velocities downstream of 100+200+100 swirl pipe and along the circular pipe are slightly larger than that of when 100+400+100 swirl pipe is used, this is even true in flows with a larger velocity.

Figure 5.3.6 presents the swirl intensity calculated at swirl pipe exit and planes downstream of the two swirl pipe exits. It is clear for both the two pipes that swirl intensity decreases with increasing distance downstream of the swirl pipe exit with larger swirl intensity observed both at the swirl pipe exit and downstream of it in flows with higher velocities (Reynolds number). The swirl

decay rate is in good agreement with exponential trend with the decay rate of swirl flow induced by 100+400+100 swirl pipe in flows with inlet velocity of 3m/s, 2m/s and 1m/s being 0.0332, 0.0356, and 0.0398 while the decay rate for 100+200+100 swirl pipe are 0.0328, 0.0349 and 0.0398. It is clear that, for the inlet velocity of 2m/s and 3m/s, 100+200+100 swirl pipe has a superior swirl induction effect as it induces larger initial swirl intensity downstream and has a smaller swirl decay rate than when 100+400+100 swirl pipe is used. However, for the inlet velocity of 1m/s, the advantage of 100+200+100 swirl pipe is negligible.

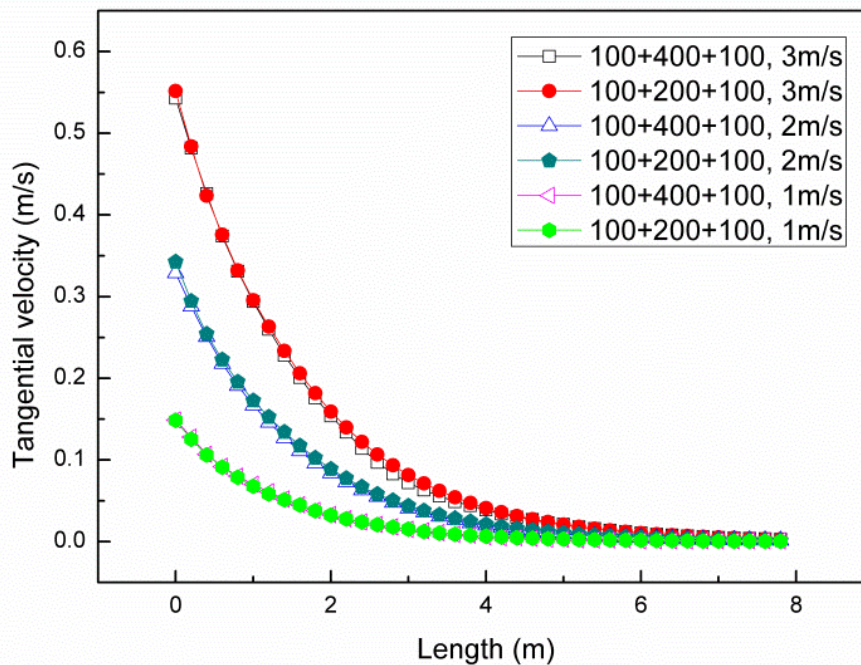


Figure 5.3.5 Tangential velocity distribution downstream of the two swirl pipes for various inlet velocities

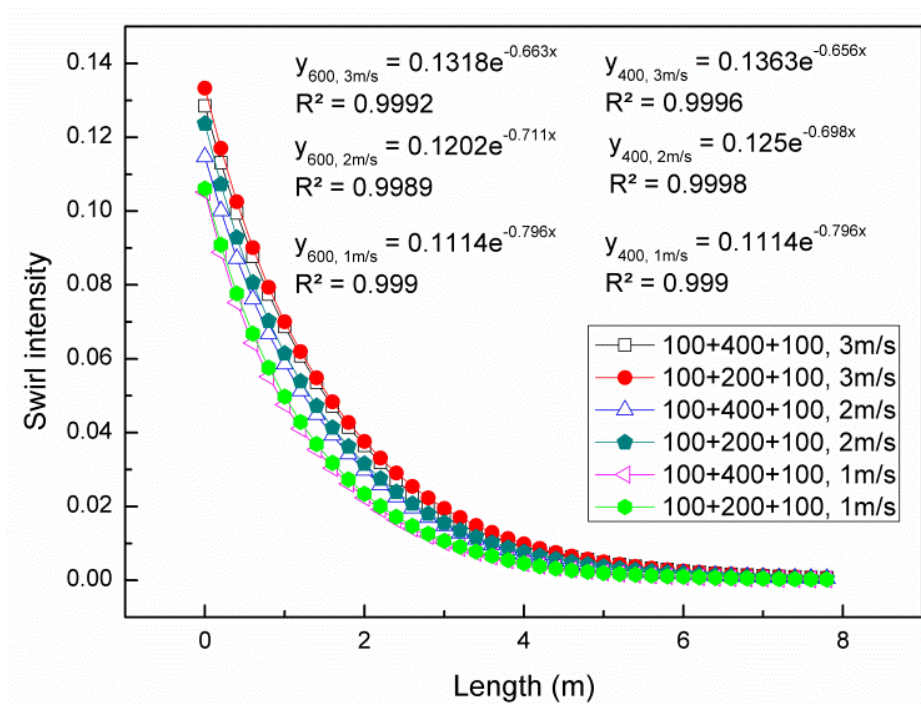


Figure 5.3.6 Swirl intensity variation downstream of the two swirl pipes for various inlet velocities

5.3.5 Wall shear stress

The effects of the two swirl pipes on increasing shear stress at the pipe surface are also investigated and compared as we intend to apply this swirl pipe into Clean-In-Place procedures, in which the wall shear stress was reported to be the local tangential force acting on the soil on the surface and remove them.

From Figure 5.3.7, it is clear that flow passing through both the two swirl pipes will generate tangential shear stress at the wall and direct to the downstream. The tangential shear stress will decay and finally fades away with a similar variation trend of tangential velocity as shown in Figure 5.3.5, which suggests that tangential wall shear stress is closely associated with tangential velocity thus swirl intensity. It can be noticed that an increase of inlet velocity from 1 m/s to 3 m/s causes a sharp rise in tangential wall shear stress downstream of the two swirl pipes; this may suggest that the effect of the swirl pipe on tangential shear stress is more prominent in flows with a higher Reynolds

number.

It is also clear from Figure 5.3.7 that the initial tangential wall shear stress and the values downstream of the 100+200+100 swirl pipe are slightly larger than that of 100+400+100 swirl pipe and this is clearer in flows with larger inlet velocities.

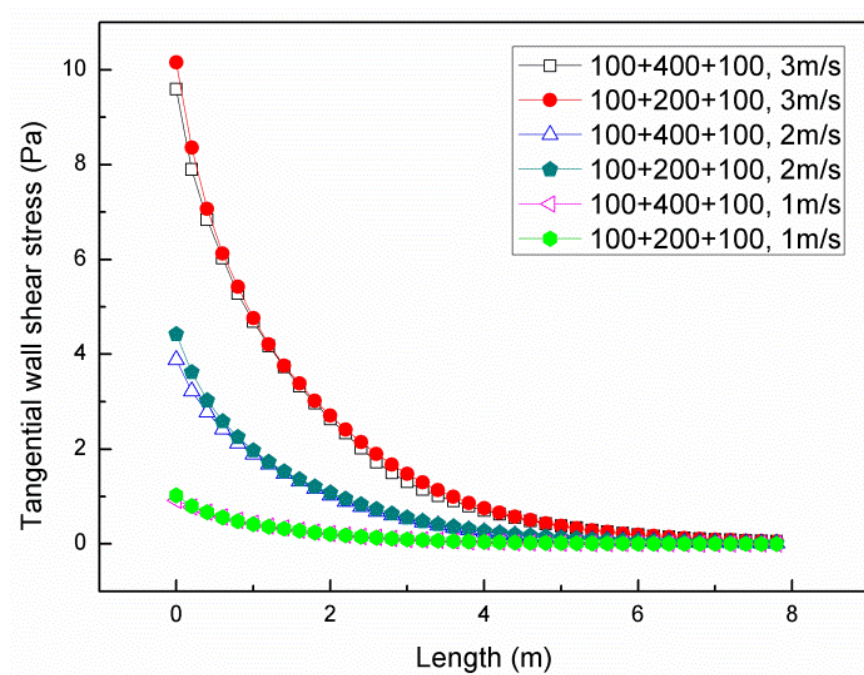


Figure 5.3.7 Tangential wall shear stress distribution downstream of the two swirl pipes for various inlet velocities

Figure 5.3.8 depicts the average non-dimensional tangential wall shear stress along the pipe downstream of the two swirl pipe exits for various inlet velocities. It shows that the trend of variation for non-dimensional tangential wall shear stress is similar to that of swirl intensity as shown in Figure 5.3.6. This further indicates that the presence and variation of tangential wall shear stress is mainly dependent on swirl intensity. One again, the 100+200+100 swirl pipe is slightly better in increasing non-dimensional tangential wall shear stress than the 100+400+100 swirl pipe due to the relatively larger swirl intensity induced.

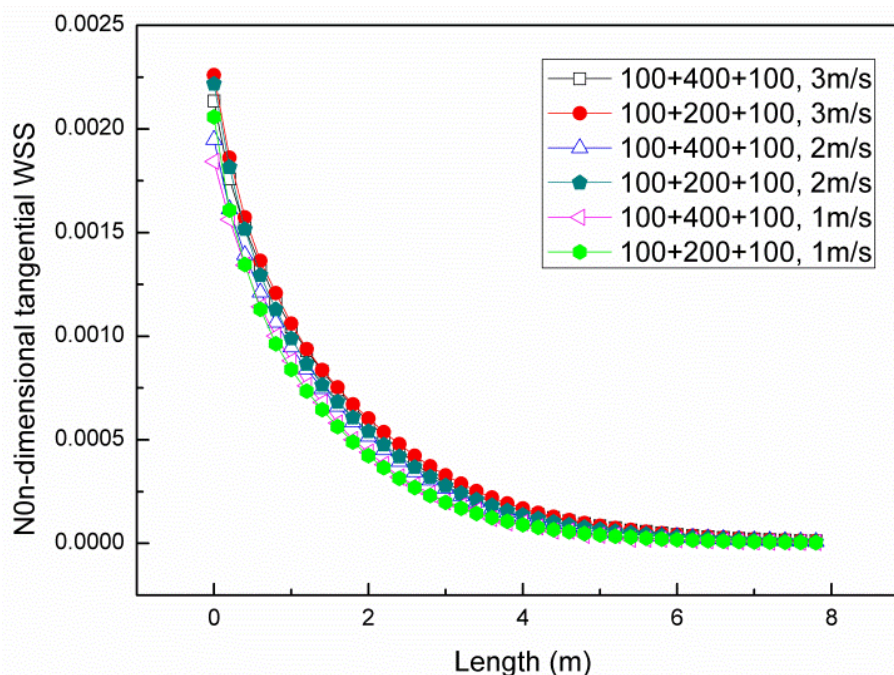


Figure 5.3.8 Non-dimensional tangential WSS distribution downstream of the two swirl pipes for various inlet velocities

Figure 5.3.9 presents the average axial wall shear stress downstream of the two swirl pipe exits for various inlet velocities. It shows that the two swirl pipes also has the effect of increasing axial wall shear stress downstream them but in a very slight way and lasts for a short distance compared with tangential wall shear stress. The effect of the swirl pipes on axial wall shear becomes less obvious with decreasing inlet velocity (Reynolds number). Their effect is almost negligible for flows with an inlet velocity of 1 m/s. with the same inlet velocities, 100+200+100 swirl pipe induces a slightly higher axial wall shear stress increase than that of 100+400+100 swirl pipe, however, its advantage stops being obvious in flows with lower velocities.

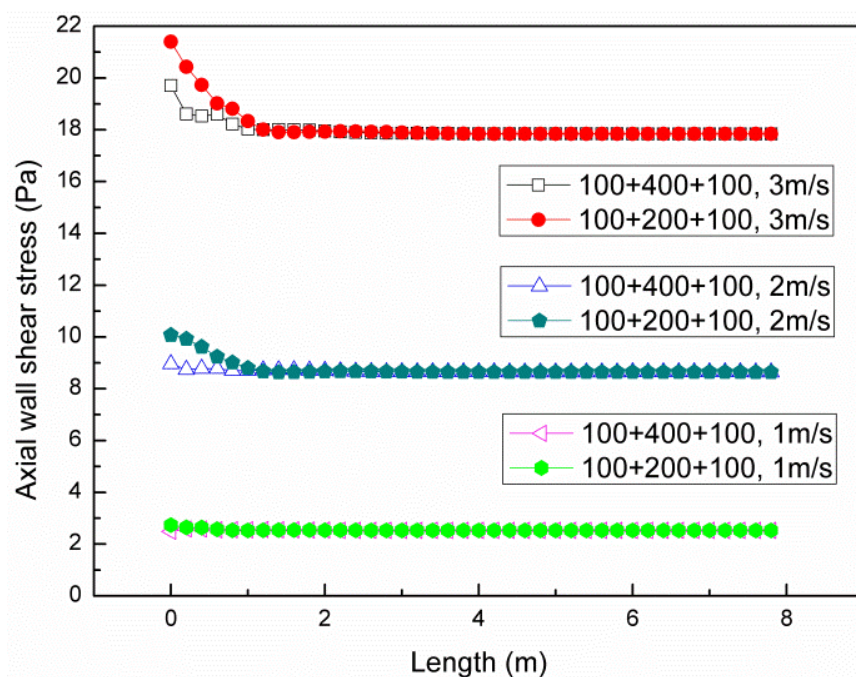


Figure 5.3.9 Axial wall shear stress distribution downstream of the two swirl pipes for various inlet velocities

Figure 5.3.10 shows the total wall shear stress, which is the combined action of the tangential and axial shear stress component acting on the pipe surface, downstream of the two swirl pipes. It is clear that swirl pipes locally increases mean wall shear stress downstream of it, with the increased value and effective distance more remarkable for a faster inlet flow velocity (a large Reynolds number and large swirl intensity). For a flow velocity of 3m/s which is typically the velocity of cleaning fluid circulating in a Clean-In-Place procedure, 100+400+100 swirl pipe raises mean shear stress at the wall from 17.8 Pascal prior swirl pipe inlet to 22 Pascal (23.5% increase) just downstream of it. The wall shear stress decays in accordance with swirl intensity, and in the point 1m (20D) downstream swirl pipe exit the increase in wall shear stress is 5%. While the 100+200+100 swirl pipe rises wall shear stress from 17.8 Pascal before it to 23.7 Pascal (33.1% increase) downstream of it and maintains at least 5% increase in mean wall shear stress in the position 1.1m (22D) downstream of it . Such it can be concluded that 100+200+100 swirl pipe is better in increasing

and maintaining wall shear stress downstream it than that of 100+400+100 swirl pipe. However, the advantage of 100+200+100 swirl pipe on increasing total wall shear stress is not that obvious in flows with lower velocities, and for an inlet velocity of 1m/s, the different is almost negligible.

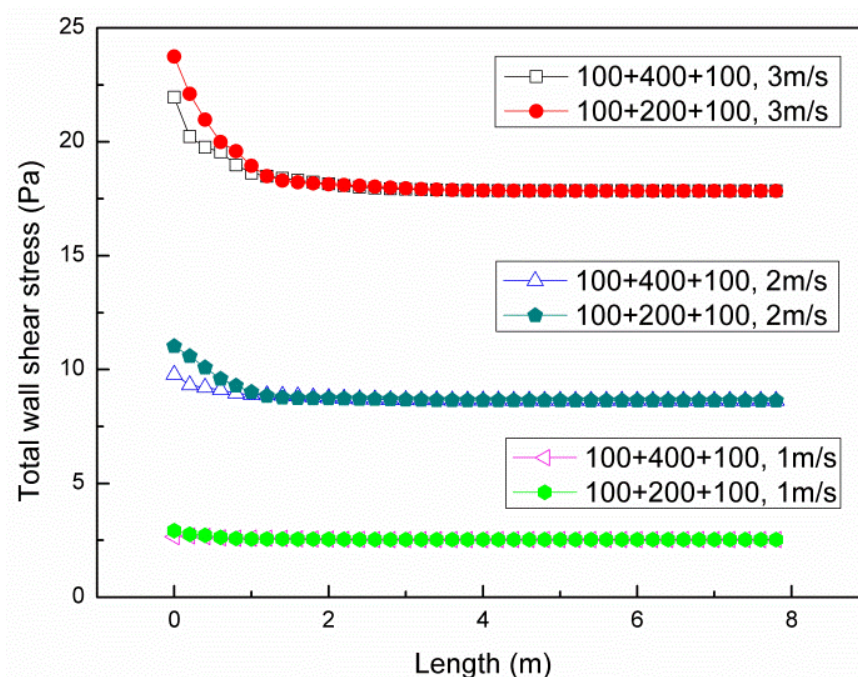


Figure 5.3.10 Total wall shear stress distribution downstream of the two swirl pipes for various inlet velocities

From the above discussion, the 100+200+100 swirl pipe induces slightly greater or the same level of swirl into flows passing through it for less pressure losses than the longer 100+400+100 pipe. It is also clear that the 100+200+100 swirl pipe is more cost effective in increasing wall shear stress downstream of it than when a 100+400+100 swirl pipe. This swirl pipe configuration is 'optimized' in swirl induction and will therefore be used for the following investigations.

5.4 Conclusions

- The overall pressure drop caused by the 100+400+100 swirl pipe is larger than the 100+200+100 swirl pipe for the same inlet velocities due

to the longer swirl inducing pipe.

- For the 100+400+100 swirl pipe, the second half of the 400mm swirl inducing pipe serves as a constraint to the swirl induced resulting in lower (same level as for 1m/s velocity) initial tangential velocity or swirl intensity at the exit of swirl pipe than the 100+200+100 swirl pipe.
- The overall swirl effectiveness of the 100+200+100 swirl pipe is greater than that of the 100+400+100 swirl pipe.
- The induced tangential velocity, swirl intensity and the effective distances are larger downstream of the 100+200+100 swirl pipe than when 100+400+100 swirl pipe is used with its advantage is more true in flows with larger Reynolds Number.
- Swirl pipes impose a tangential wall shear stress within itself and direct to downstream, its value and variation trend is dependent on swirl intensity. The induced tangential wall shear stress after the 100+200+100 swirl pipe is larger than when 100+400+100 swirl pipe is used due to the relatively larger swirl intensity.
- The axial and total wall shear stress are also larger downstream of the 100+200+100 swirl pipe than that of the 100+400+100 swirl pipe with its advantage being more true in flows with a larger inlet velocity.
- A shorter length of 200mm swirl inducing pipe used in conjunction with the entry and exit transition sections is suggested to be more cost effective in swirl induction, and will therefore be employed for further research.

CHAPTER 6: RANS-BASED SIMULATION OF SWIRL FLOW DOWNSTREAM OF THE OPTIMISED SWIRL PIPE

6.1 Introduction

This chapter presents a computational fluid dynamics model of the swirl flow that is induced in a fluid flow passing through the horizontally mounted optimized four-lobed 400mm length swirl pipe. The steady state CFD model based on the RANS approach provides time-averaged properties of the swirl flows (e.g. mean velocities, mean pressures, mean stresses etc.). Analysis will focus on the variation of flow parameters downstream of the swirl pipe as this is the duration where CIP may benefit from the use of swirl pipe.

Pressure loss, tangential velocity, swirl type, swirl intensity and its decay rate of the swirl flow downstream of the swirl pipe are investigated in flows with various inlet velocities. Special attention is paid to the potential of the swirl flow on improving CIP efficiency by increasing the mean wall shear stress to the downstream without increasing the operation velocity. The wall shear stress is a measure of the mechanical action of fluid flow on a process surface with the mean wall shear stress especially relevant as a measure of cleaning efficiency in straight pipes, large parts of pumps, valves and so on (PathogenCombat, 2011).

The numerical results indicate that the swirl pipe may improve efficiency of CIP procedures by locally increasing mean wall shear stress to the downstream without the need to increase the flow velocity, consequently shortening the downtime for cleaning, and reducing the costs for chemicals and power energy.

6.2 Simulation Setup

Configuration of the modelled pipe flow system is demonstrated in Figure 6.2.1. A detailed description of the simulation geometry is covered in Chapter 4 section 4.4.3. The numerical method, turbulence models and wall functions used, the meshing method, the solver parameters and the solution convergence criteria employed were the same as used in Chapter 5.

In the inlet of the flow domain, velocities of 1m/s, 1.5m/s, 2m/s, 2.5m/s and 3m/s were specified. The corresponding Reynolds number and turbulence intensity at inlet of the five conditions are listed in Table 6.2.1. The simulations results were processed using a CFD-Post package (ANSYS, 2013a) after all the solutions were reasonably converged. The simulation results of the swirl flow parameter downstream of the optimized swirl pipe are presented in following sections.

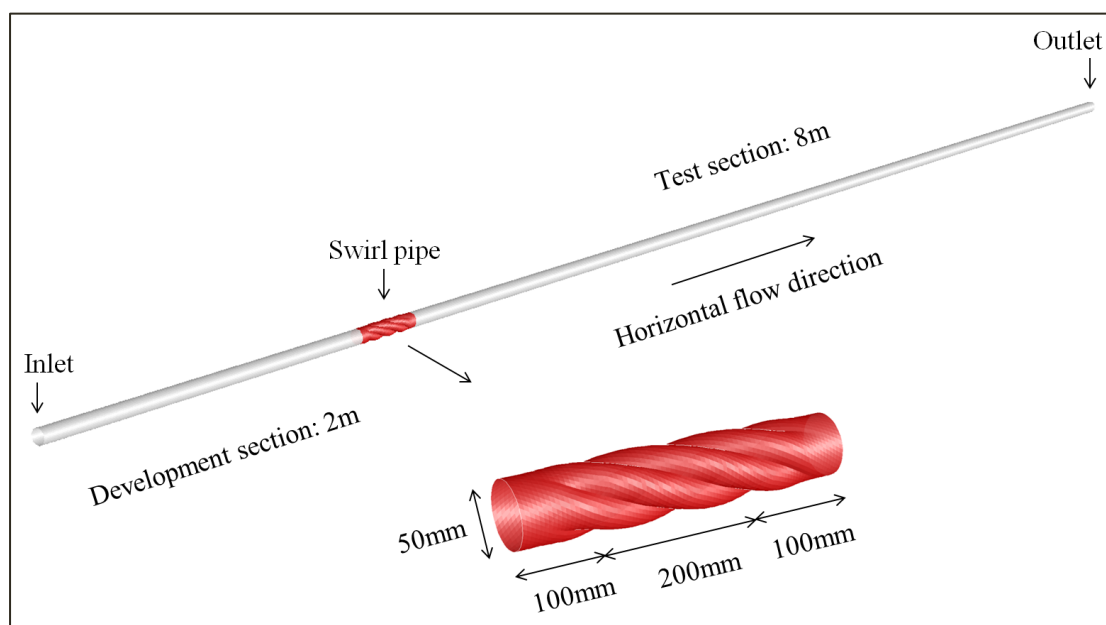


Figure 6.2.1 Configuration of simulation geometry

Table 6.2.1 Simulation conditions at inlet

Inlet velocity (m/s)	Reynolds number	Turbulence intensity (%)	Hydraulic diameter (mm)
1	49,760	4	50
1.5	74,641	3.9	50
2	99,521	3.8	50
2.5	124,401	3.7	50
3	149,282	3.6	50

6.3 Results and Discussions

6.3.1 Pressure Drop

Pressure is the force applied to a unit area of surface. In a dynamic system, pressure typically is defined using three terms, the static pressure, the dynamic pressure and the total pressure. The static pressure can be identified for every point in a body of fluid, regardless of whether the fluid is in motion or not. The dynamic pressure is associated with the velocity or the flow of the fluid. The total pressure is the sum of the static pressure and the dynamic pressure.

For the current flow system where the circular and swirl pipe have a constant cross-sectional area, the dynamic pressure is constant throughout the system for a given flow velocity. The static pressure was used to understand the flow behaviour within the top horizontal section of the rig that was modelled.

Figure 6.3.1 shows the variation of averaged static gauge pressure over the area of the planes downstream of the inlet throughout the whole flow system. The CFD results show that the value of pressure and its loss along the pipe system are proportional to the velocity (Reynolds number) of the flow. The swirl pipe (2m~2.4m in X axis) causes a more significant drop in pressure than the circular pipes; this is more obvious in flows with larger Reynolds number.

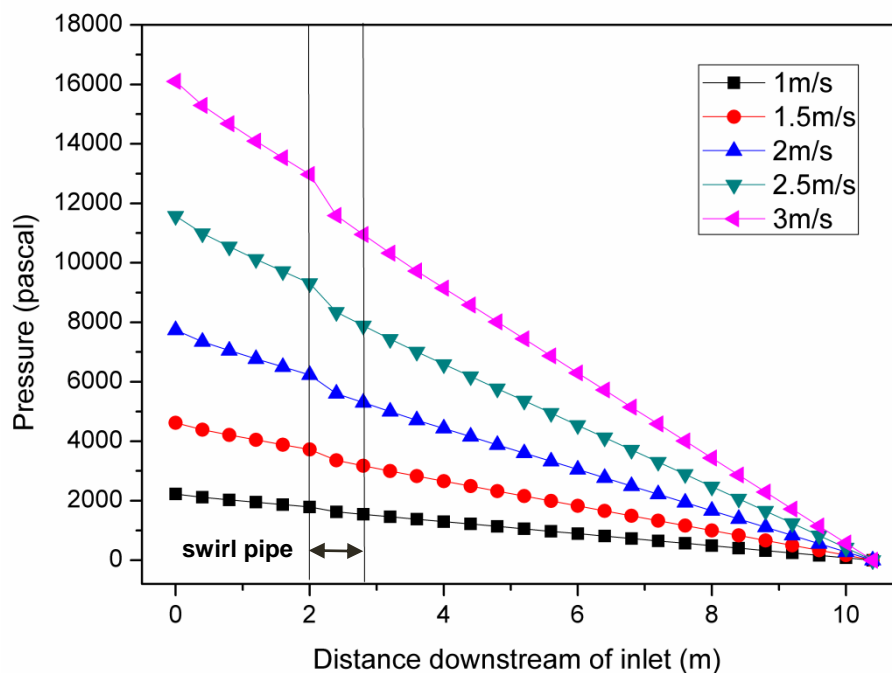


Figure 6.3.1 Static pressure variation in the horizontal pipe system for various inlet velocities

Table 6.3.1 summarizes the per unit length pressure loss within the duration 1 meter prior the swirl pipe, the swirl pipe and the durations of 0~1m, 1~2m, 2~3m ... 6~7m downstream of the swirl pipe. It can be seen that the pressure losses across the 4-lobed swirl pipe are greater than that of the circular pipes (2.1~2.45 times corresponding to 1~3m/s velocity). The greater pressure losses are due to the additional turbulence generated through the artificial roughness of the non-circular pipe cross-sections of the swirl pipe.

Table 6.3.1 The unit length pressure losses for swirl and circular pipes

ΔP Velocity	1m prior, Pa/m	Swirl pipe, Pa/m	0~1m after, Pa/m	1~2m after, Pa/m	2~3m after, Pa/m	3~4m after, Pa/m	4~5m after, Pa/m	5~6m after, Pa/m	6~7m after, Pa/m
1 m/s	198.4	413.1	206.5	201.5	202.9	202.7	202.4	202.8	202.8
1.5m/s	406.9	907.2	449.4	417.0	414.2	415.4	414.4	415.2	415.2
2 m/s	679.5	1564.7	753.6	696.3	690.7	693.1	691.2	692.4	692.6
2.5m/s	1012.8	2426.7	1125.4	1035.6	1026.9	1030.0	1027.3	1030.2	1030.7
3 m/s	1406.3	3457.8	1568.0	1441.6	1425.2	1432.4	1427.7	1428.8	1430.0

Table 6.3.1 also shows that, for the circular pipes, the unit length pressure losses just downstream of the swirl pipe are slightly greater than that occurred in the circular pipe prior the swirl pipe, this is more true in flows with higher velocities. The increase in pressure loss downstream of swirl pipe declines with increasing downstream distance as the swirl effects fades away.

The increase in pressure losses may be due to the swirling flow regime which decreases the thickness of the boundary layer resulting in an increase in shear stress at the wall. It is documented that, in cylindrical pipe flow, the wall shear stress has a proportional relation to the pressure loss in that $\tau_w = \frac{\Delta P d}{4L}$ (Sleigh and Goodwill, 2008), where d is pipe diameter, L is the length of pipe corresponding to pressure loss. Therefore, the greater pressure loss in the circular pipe downstream of the swirl pipe indicates that the swirl pipe increases wall shear stress in the duration just downstream of it.

6.3.2 Tangential Velocity

The swirl pipe adds a rotating momentum to the flow within itself and the circular pipe downstream of it, turning the fluid clockwise in addition to the axial velocity along the pipe. The velocity component, which mainly affects the swirl flow field, is the tangential velocity component, which has a distribution dependent on the swirl generation mechanism (Najafi et al., 2011). Generally three well known methods may be employed in order to produce swirl flow (Gupta et al., 1984):

- In the first method, passing through a rotational section, fluid flow acquires tangential momentum and enters the pipe in the form of a swirl flow.
- In method two, fluid flow enters the pipe through fixed blades (vanes), which are mounted inside of the pipe with a specified angle.
- The third method is that fluid flow enters the pipe by means of a tangential inlet so that it can acquire rotational momentum and enter the pipe in the form of a swirl flow.

The swirl pipe induces swirl into flow in a way similar to the first method, but the swirl pipe does not rotate, rather it is the helical geometry of the swirl pipe that forces the fluid which passes through it to rotate within itself and the circular pipe downstream.

Tangential velocity contour plots in the radial and axial directions for various flow velocities are illustrated in Figure 6.3.2 with the interval distance of the adjacent cross-sections being $4D$ (0.2m). It shows that the swirl pipe induces swirl (tangential velocity) within itself and the swirl prevails for some distance downstream and decays gradually. In the radial direction, where swirl exists, the tangential velocity is zero at the centre of the pipe. This increases to the highest value in the near wall region and then decreases to zero at the pipe wall. The contours exhibit a characteristic quadrangular shape which is attributed to the 4-lobed swirl pipe. However, this quadrangular nature is more difficult to identify the further away from the swirl pipe exit. The contour also shows that the orientation of quadrangular contour changes with distance downstream, indicating a rotating flow. Figure 6.3.2 depicts that the tangential velocity induced by the swirl pipe are greater in flows with larger velocity which also prevails for a longer downstream distance.

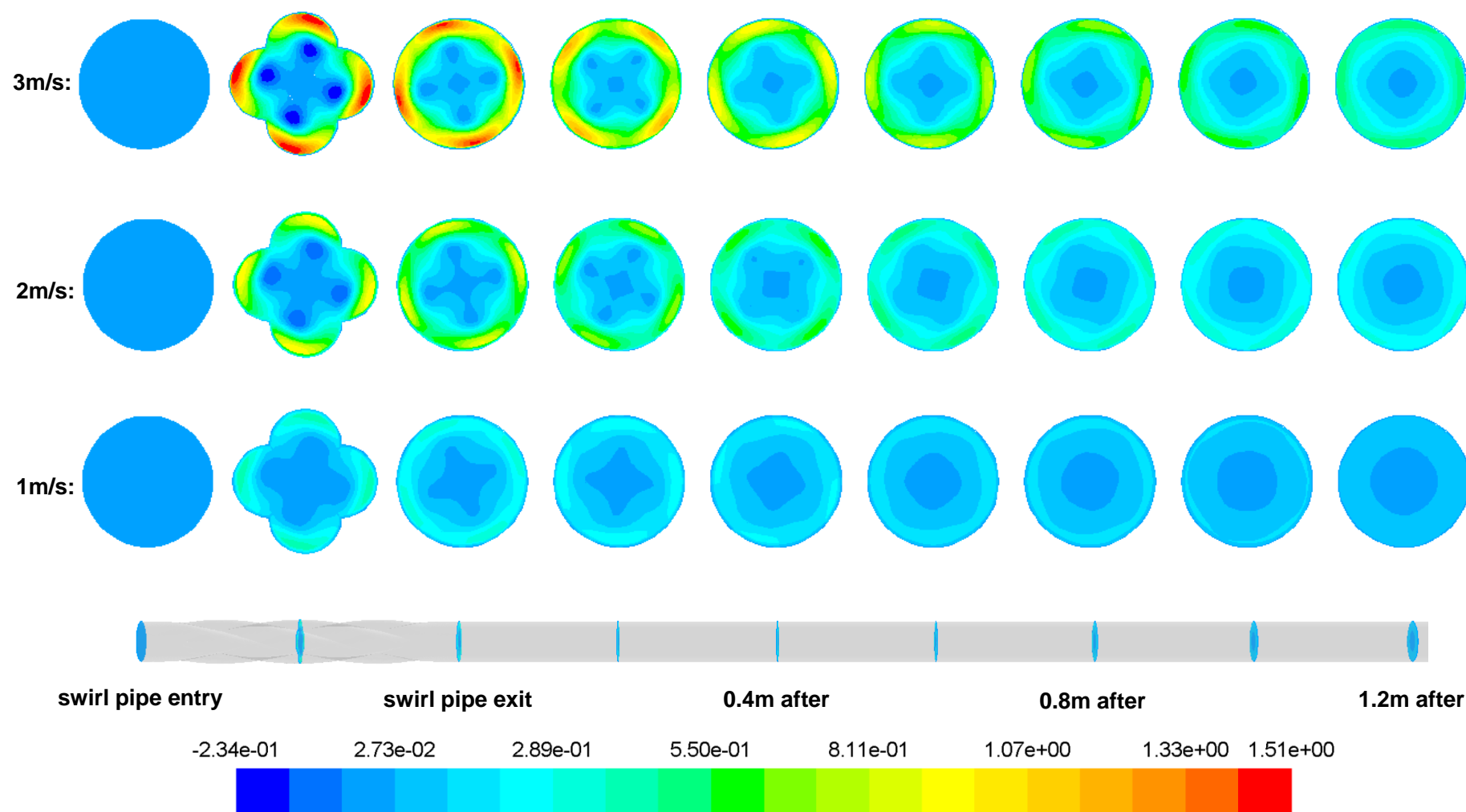


Figure 6.3.2 Tangential velocity (m/s) distribution within and downstream swirl pipe for various velocities

Based on the radial distribution of tangential velocity field, three swirl types can be distinguished as shown in Figure 6.3.3 (Steenbergen and Voskamp, 1998):

- Concentrated Vortex (CV)- rotation concentrated near the pipe centre
- Solid Body (SB)- almost uniform rotation
- Wall Jet (WJ)- angular momentum concentrated near the wall

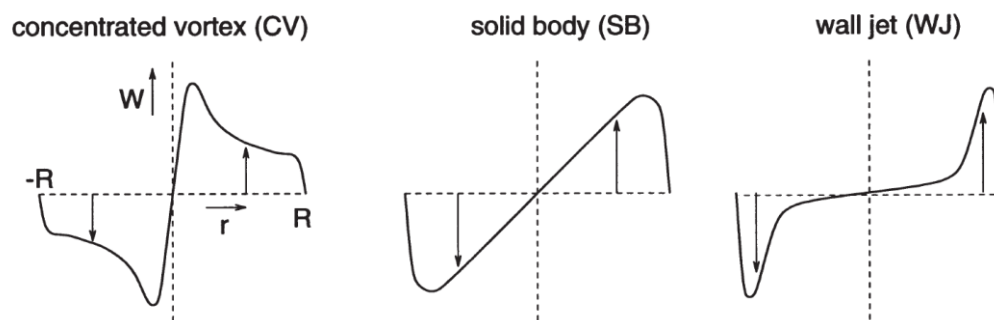


Figure 6.3.3 Classification of swirl types (After Steenbergen and Voskamp, 1998)

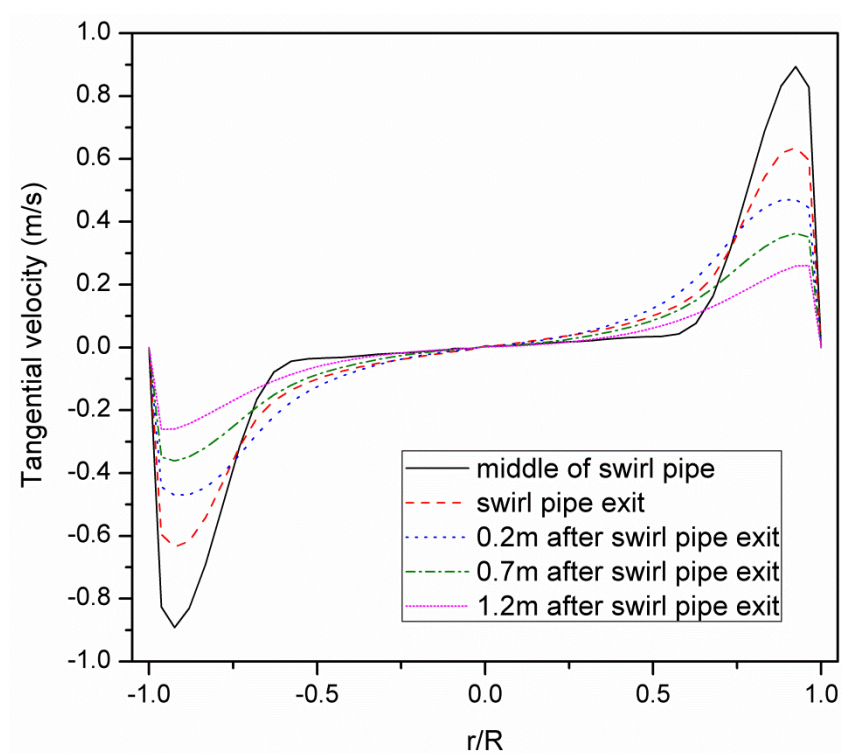


Figure 6.3.4 Tangential velocity profiles in radial direction (2m/s inlet velocity)

Figure 6.3.4 shows the radial distribution of tangential velocity in several cross-sectional flow planes within the swirl pipe and downstream of it (2m/s inlet velocity for instance). It is clear that, compared with Figure 6.3.3, the swirl type inside the swirl pipe itself is in good agreement with wall jet definition. However, it gradually develops into a solid body type. 1.2m after the swirl pipe exit the type of swirl is better fitted to a solid body.

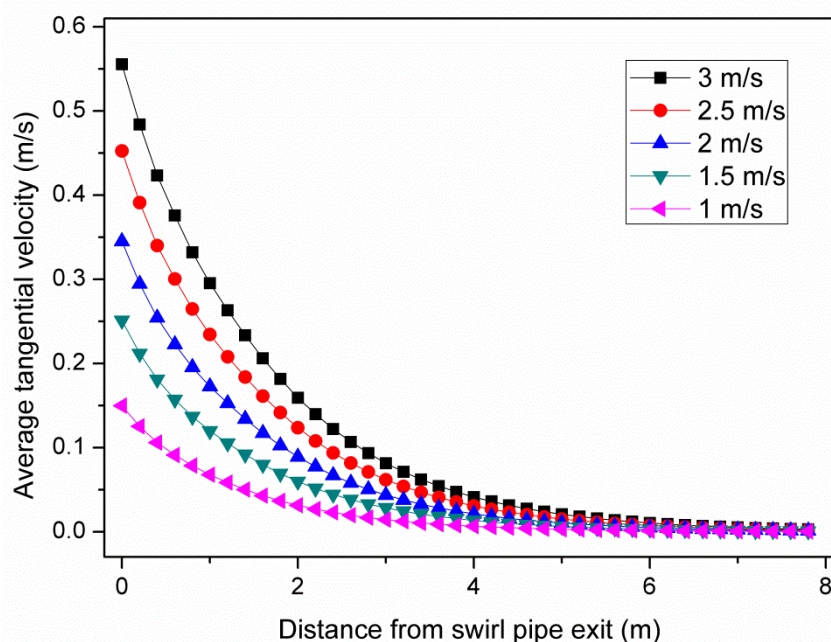


Figure 6.3.5 Tangential velocity variation downstream of swirl pipe exit

Figure 6.3.5 depicts the average tangential velocity distribution downstream of the swirl pipe for various inlet velocities. It is clear from the plot that tangential velocity decreases with increasing downstream distance and finally decreases to zero where the swirl effect fades away. Figure 6.3.5 also shows that a greater initial tangential velocity at the exit of swirl pipe was generated with a larger flow velocity. An attempt was made to find the relation between the initial tangential velocity and the inlet velocity by linear fitting of the five pairs of data. The fitting resulted in a straight line with a coefficient of determination close to 1. However this straight line makes no engineering sense at zero parameters because it indicates a positive tangential velocity value with an inlet velocity of zero. Therefore the (0, 0) point was included and several fittings were

considered. Exponential and logarithmic fitting were excluded as they cannot go through zero point. A linear fitting was tried with good coefficient of determination. However, it seems that the increasing rate of initial tangential velocity increases with increasing inlet velocities and a linear fitting cannot reflect this trend. Therefore it is determined to use a polynomial fit at the time which should provide a relatively accurate relation of the initial tangential velocity and the inlet velocity. Figure 6.3.6 shows a positive correlation of initial tangential velocity with inlet velocity indicating that the swirl pipe has a more pronounced effect in flows with larger velocities.

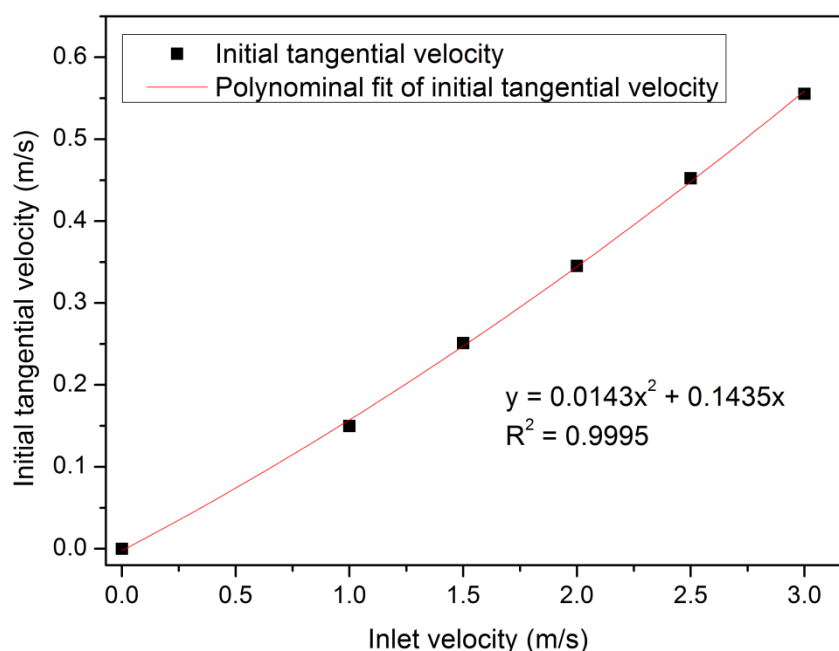


Figure 6.3.6 Correlation of initial tangential velocity with inlet velocity

If a tangential velocity of 0.05 m/s is regarded as small enough to be ignored, the downstream duration of swirl effects with various inlet velocities can be seen in Figure 6.3.7 that the effective distances are 3.7m(74D), 3.3m(66D), 2.8m(56D), 2.2m(44D) and 1.4m(28D) respectively for flows at speed of 3m/s, 2.5m/s, 2m/s, 1.5m/s and 1m/s. In order to find out the relation between the effective distance and inlet velocity, initially a straight line was used to fit the 6 points (zero point being included) with good coefficient of determination; however it was observed that the increasing rate of effective duration

downstream of the swirl pipe decreases with increasing inlet velocities and a straight line cannot reflect this trend. Therefore it was decided to use a polynomial fitting. Figure 6.3.7 shows that the swirl effect prevails a longer downstream distance in flows with larger velocities. However, the descending increasing rate of the curve may also suggests that the pipe wall exerts greater resistance to the swirl flow generated in flows with larger velocities resulting in a decreased increasing rate of swirl effective distance.

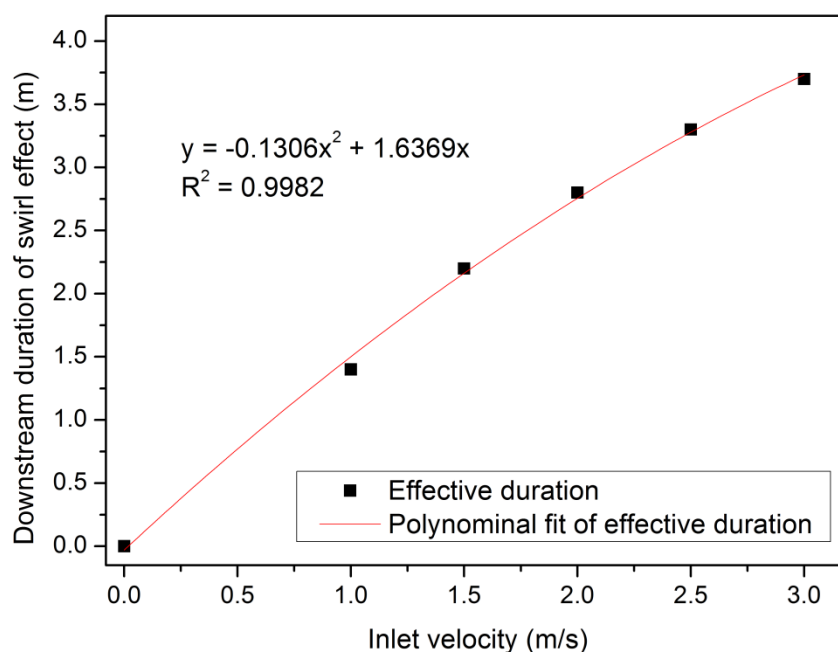


Figure 6.3.7 Correlation of swirl pipe effect distance with inlet velocities

6.3.3 Swirl Decay

The induced swirl flow decays with increasing distance downstream the swirl pipe and reverts back to the upstream flow profile at different pipe diameters downstream according to the inlet velocities. The decay of swirl is caused by the transport of angular momentum to the pipe wall (Steenbergen and Voskamp, 1998).

To quantify the swirl intensity S of the swirl flow, the numerator and

denominator in equation $S = \frac{\int_0^R uwr^2 dr}{R \int_0^R u^2 r dr}$ (equation 2.3.1, Chapter 2) were calculated in CFD-post by integrating uwr and u^2 over planes downstream of the swirl pipe exit. Figure 6.3.8 presents the swirl intensity calculated at swirl pipe exit and planes 4D, 8D, 12D, 16D and so on downstream of the swirl pipe exit. It can be seen from the figure that swirl intensity decreases with increasing distance downstream of the swirl pipe exit with larger swirl intensity observed both at the swirl pipe exit and downstream of it in flows with higher velocities (Reynolds number).

The swirl decay rate is in good agreement with exponential trend of $S = S_0 e^{\beta \frac{x}{D}}$ (equation 2.3.2, Chapter 2), where S_0 is the initial swirl intensity, and β is the swirl decay rate. The swirl decay rates for inlet velocity of 1m/s, 1.5m/s, 2m/s, 2.5m/s and 3m/s are 0.040, 0.036, 0.035, 0.034 and 0.032 respectively. It is clear that the swirl decay rate decreases with increasing inlet velocities, indicating that swirl prevails for a longer downstream distance in flows with a larger Reynolds number. A detailed correlation of swirl decay rate with flow Reynolds number is presented in Figure 6.3.9.

Steenbergen and Voskamp (1998) concluded that in turbulent swirl flow in smooth pipes at a swirl number within $0 \leq S \leq 0.18$, the swirl decay rate is related to the friction factor of the pipe f' . They suggested a value of $\beta = [(1.49 \pm 0.07) \times f']$ for $0 \leq S \leq 0.18$ (experiments were carried out with water at $50,000 < Re < 300,000$, $S_0 = 0.18$).

The friction factor f' can be obtained by solving the Colebrook equation and the Blasius equation $f_D = \frac{0.3164}{Re^{0.25}}$ which is valid for $Re = 3 \times 10^3 \sim 1 \times 10^5$. The value of β calculated in terms of f' for swirl flows at various speeds are shown in Table 6.3.2.

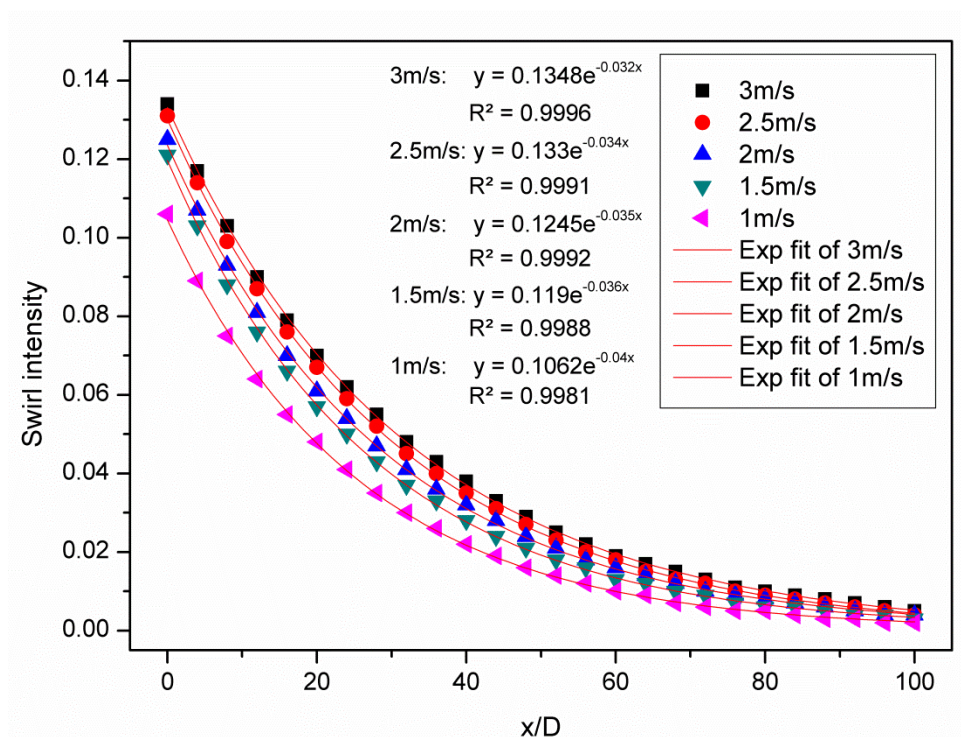


Figure 6.3.8 Swirl intensity variation downstream of swirl pipe exit

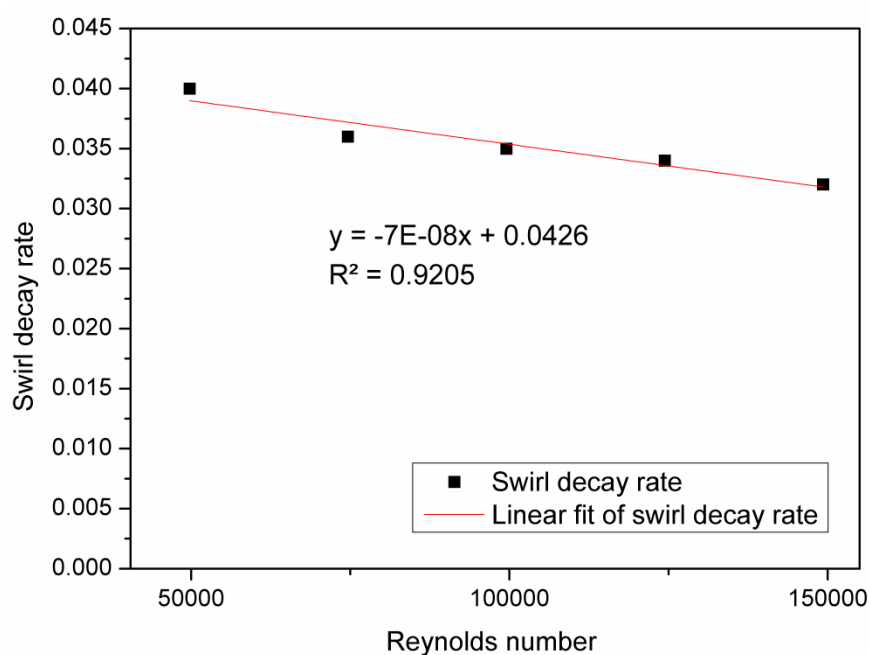


Figure 6.3.9 Correlation of swirl decay rate with Reynolds number

Table 6.3.2 Swirl decay rate calculated in terms of friction factor

Velocity	Reynolds number	CFD	Colebrook equation		Blasius equation	
		β	f'	β	f'	β
1 m/s	49,760	0.04	0.021	$1.90f'$	0.0211	$1.90f'$
1.5m/s	74,641	0.036	0.0192	$1.88f'$	0.0191	$1.88f'$

2 m/s	99,521	0.035	0.0181	$1.93f'$	0.0178	$1.97f'$
2.5m/s	124,401	0.034	0.0173	$1.97f'$	0.0168	$2.02f'$
3 m/s	149,282	0.032	0.0167	$1.92f'$	0.0161	$1.99f'$

The values of decay rate are higher than the expected value suggested by Steenbergen and Voskamp. This may attribute to the fact that Colebrook equation and the Blasius equation tend to underestimate the friction factor value as they are primarily dedicated for calculating friction factor in non-swirling cylindrical pipe flow. In the case of swirl flow, the two equations may underestimate the friction factor. Another possible reason might be the difference in the swirl induction method of the current geometrically induced swirl flow. However, there is no unanimous agreement regarding this point. Kitoh (1991) and Steenbergen and Voskamp (1998) concluded that swirl intensity is independent of the mechanism of swirl generation while Najafi (2011) stated that the swirl intensity decay rate is not solely a function of Reynolds number, but depends on the type of the swirl generation as well.

6.3.4 Wall Shear Stress

Published work reports that Clean-In-Place efficiency of closed processing equipment depends, among other criteria, on the hydrodynamic effect. The cleaning liquid generates local tangential force acting on the soil on the surface and acts as a carrier for the chemicals and heat (Jensen et al., 2007). The removal kinetics is a function of the fluid detergent velocity and of the wall shear stress (Gallot-Lavallée et al., 1984, Graßhoff, 1992, Visser, 1970, Sharma, 1991). In general, there is a threshold value of both mean and local wall shear stress above which cleaning is considered efficient. The threshold is defined as the lowest mean wall shear stress sufficient to remove the specific type of soil on the pipe surface (PathogenCombat, 2011). A so-called critical wall shear stress for removal of specific microorganisms on various surfaces was also reported by

Duddridge (1982), Powell and Slater (1982) and Fowler and McKay (1980).

Cleaning fluids moving along a solid boundary incurs a shear stress on that boundary. The no-slip condition dictates that the speed of the fluid at the boundary is zero, but at some height from the boundary the flow speed must equal that of the fluid. The region between these two points is aptly named the boundary layer. For all Newtonian fluids in laminar flow, the shear stress is proportional to the strain rate in the fluid where the viscosity is the constant of proportionality. The shear stress is imparted onto the boundary as a result of this loss of velocity (Day, 2004, Timoshenko and Stephen, 1983).

6.3.4.1 Tangential Wall Shear Stress

The shear stress, for a Newtonian fluid, is defined by the normal velocity gradient at the wall as: $\tau_w = \mu \frac{\partial u}{\partial y}$, where μ is dynamic viscosity of the fluid, u is velocity of the fluid along the boundary and y is height above the boundary.

For swirl flow, angular momentum is transported into the pipe wall, generating a sharp tangential velocity gradient in the wall area as shown in Figure 6.3.4. It is expected this tangential velocity gradient will induce tangential wall shear stress acting on the pipe surface in addition to the axial wall shear stress that is parallel to the straight circular pipe. This was proven by the numerical results of the average tangential wall shear stress downstream of the swirl pipe exit as depicted in Figure 6.3.10, which were calculated by expression of tangential wall shear in terms of wall shear X and wall shear Y in the CFD-post. It is clear that flow passing through the swirl pipe will generate tangential shear stress at the wall and direct to the downstream. The tangential shear stress will decay and finally fade away with a similar variation trend of tangential velocity as shown in Figure 6.3.5, which suggests that tangential wall shear stress is closely associated with tangential velocity thus swirl intensity. It can be noticed that an

increase of inlet velocity from 1 m/s to 3 m/s causes a sharp rise in tangential wall shear stress downstream of swirl pipe; this suggests that the effect of the swirl pipe on tangential shear stress is more prominent in flows with a higher Reynolds number.

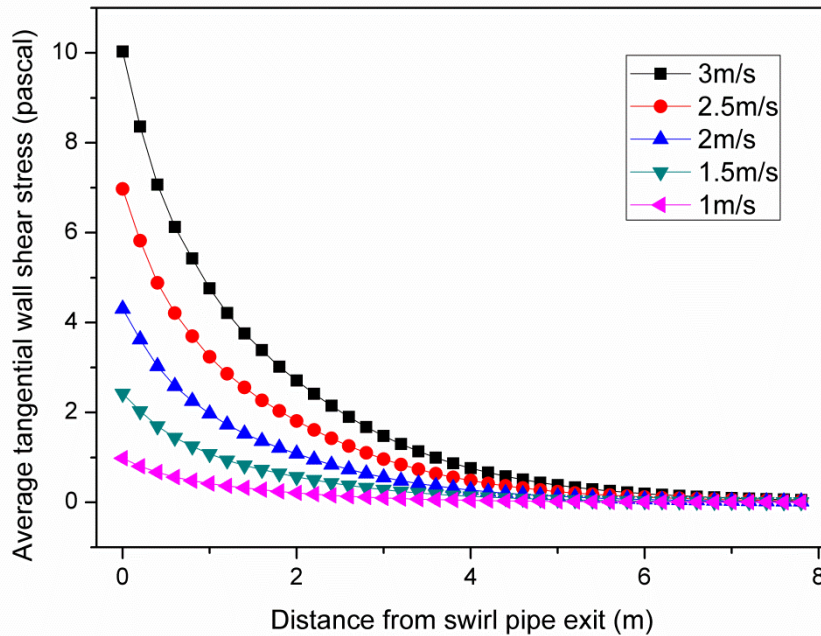


Figure 6.3.10 Tangential WSS variation downstream of swirl pipe exit

Figure 6.3.11 depicts the average non-dimensional tangential wall shear stress along the cylindrical pipe downstream of the swirl pipe exit for various inlet velocities. It shows that the trend of variation for non-dimensional tangential wall shear stress is similar to that of swirl intensity as shown in Figure 6.3.8. The correlation coefficient of the swirl intensity and the non-dimensional tangential wall shear stress downstream of the swirl pipe is calculated through the following correlation function:

$$Correl(X,Y) = \frac{\sum(x - \bar{x})(y - \bar{y})}{\sqrt{\sum(x - \bar{x})^2 \sum((y - \bar{y})^2)}} \quad (6.3.1)$$

where \bar{x} and \bar{y} are the means of array x and array y.

The correlation coefficients are 0.998726, 0.998783, 0.999239, 0.999419 and 0.999484 for swirl flows at speed of 3m/s, 2.5m/s, 2m/s, 1.5m/s and 1 m/s

respectively. The high correlation coefficients further confirm that the presence and variation of tangential wall shear stress is closely dependent on swirl intensity.

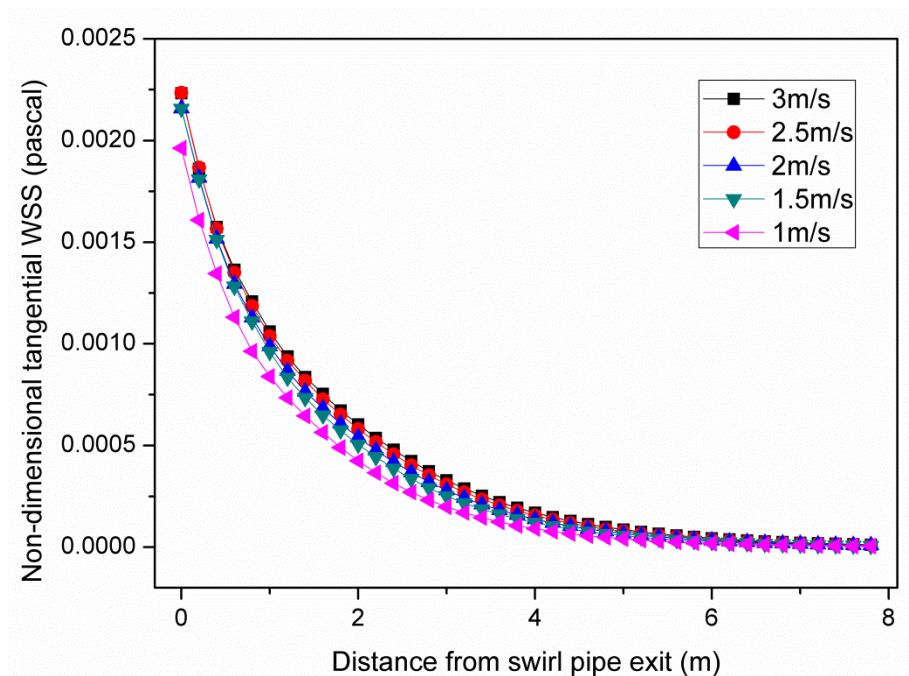


Figure 6.3.11 Non-dimensional tangential WSS variation downstream of swirl pipe exit

6.3.4.2 Axial Wall Shear Stress

Figure 6.3.12 depicts the average axial wall shear stress downstream of the swirl pipe exit for various inlet velocities. It shows that the swirl pipe also has the effect of increasing axial wall shear stress downstream it but in a very slight way and lasts for a shorter distance compared with tangential wall shear stress. The increase in axial wall shear stress can be explained by the change of axial velocity profile downstream of the swirl pipe exit as shown in Figure 6.3.13. It is clear that the peak axial velocities downstream of the swirl pipe exit are higher than before the swirl pipe inlet. This is especially true at cross-flow planes close to the exit of the swirl pipe, with the effect diminishing with downstream distance. The increase in axial velocity in the core area causes a sharper normal velocity gradient at the wall consequently slightly increasing axial wall shear

stress. The effect of the swirl pipe on axial wall shear becomes less obvious with decreasing inlet velocity (Reynolds number). Its effect is almost negligible for flows with an inlet velocity of 1.5 m/s and 1 m/s. From Figure 6.3.12, the axial wall shear stress is more sensitive to flow velocity (Reynolds number). For cross-flow planes where axial wall shear stress is constant for various inlet velocities, the correlation of axial wall shear stress and flow velocities can be plotted as shown in Figure 6.3.14. As the exponential and logarithmic fittings cannot go through zero point and a straight line cannot reflect the increased increasing rate of axial wall shear stress with increasing Reynold number, the polynomial fit becomes a reasonable choice. Figure 6.3.14 shows that generally the axial wall shear stress is positively correlated to the Reynolds number of the flow and the increasing rate of axial wall shear stress is faster in flows with larger Reynolds number. This is expected as a larger Reynolds number means greater turbulence of the flow and hence stronger impact at the wall.

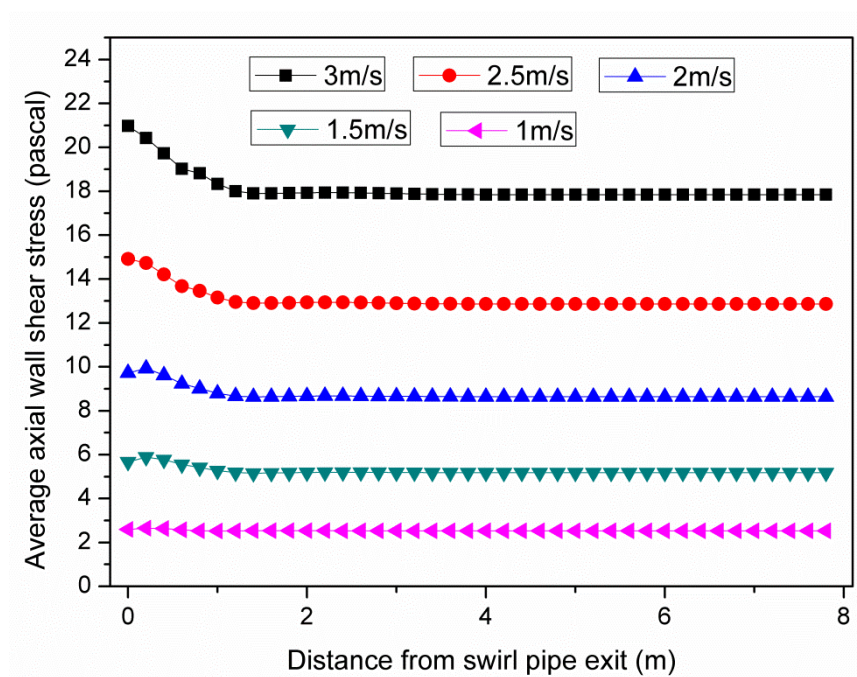


Figure 6.3.12 Axial wall shear stress variation downstream of swirl pipe exit

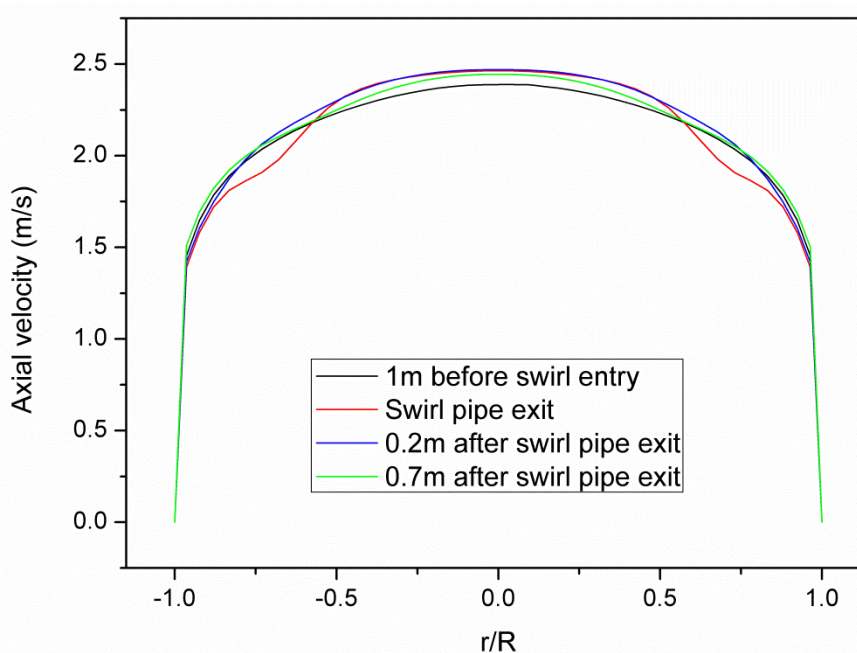


Figure 6.3.13 Axial velocity profiles in radial direction (2m/s velocity)

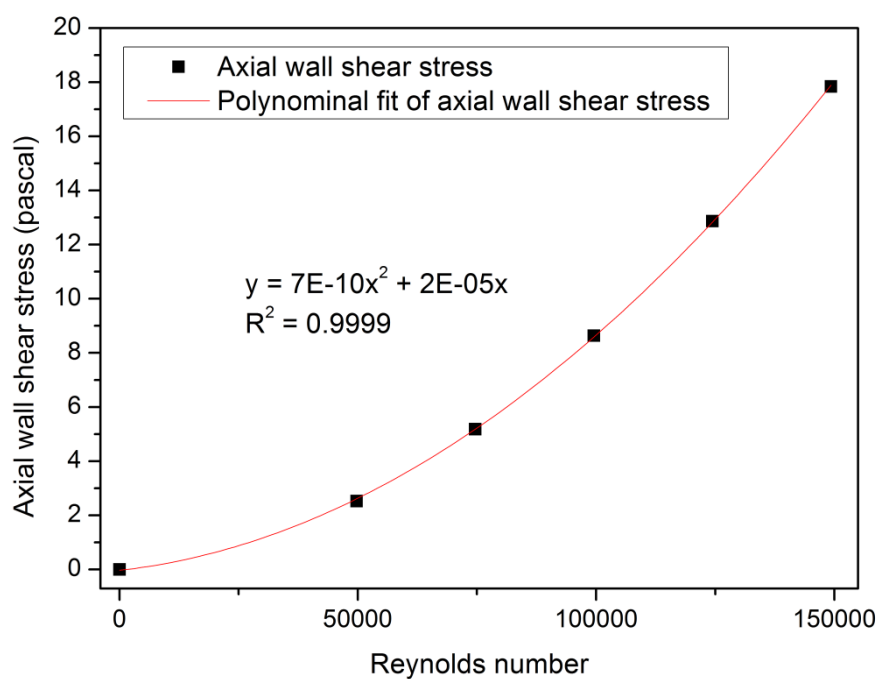


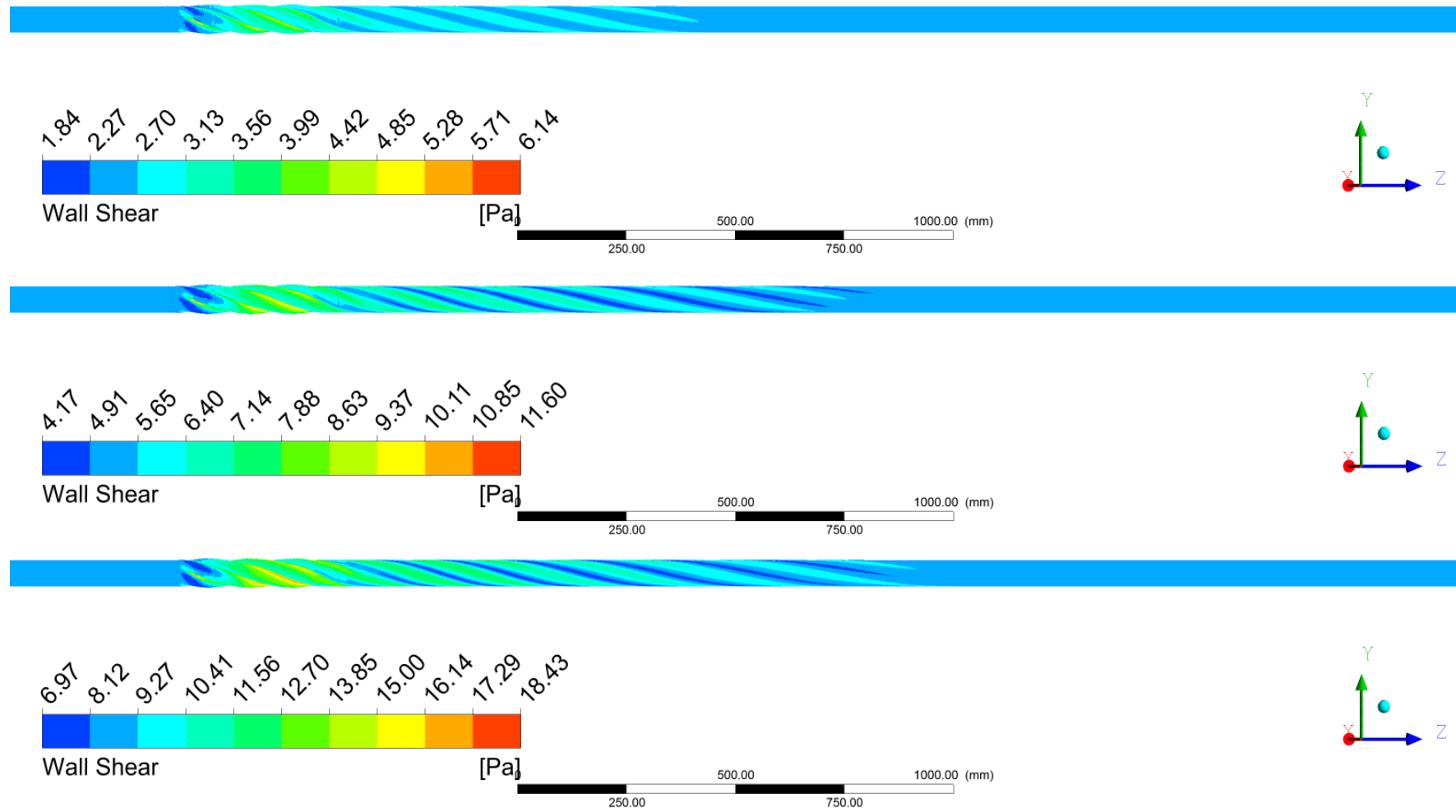
Figure 6.3.14 Correlation of average axial WSS with Reynolds number

6.3.4.3 Total Wall Shear Stress

The wall shear stress of the swirl flow is the combined action of the tangential and axial shear stress component acting on the pipe surface. Figure 6.3.15 shows the wall shear stress contours within and downstream of the swirl pipe for

inlet velocities of 1 m/s, 1.5 m/s, 2 m/s, 2.5 m/s, and 3 m/s respectively from top to bottom. A scale up of 1.2 is applied to the X-Y plane in order to see clearly the wall shear stress distributions. From the contours, an increase of wall shear stress is observed starting from the swirl pipe inlet, with the largest value existing within the swirl pipe at the intersection of lobes where the non-circular wall results in additional resistance to the flow. Downstream of the swirl pipe exit, the increase in wall shear stress prevails following the spiral pattern of the swirl pipe with a longer effective distance and larger wall shear stress increase observed in flows with higher inlet velocity. From Figure 6.3.15, the pitch to diameter ratio of the spiral distribution pattern of wall shear stress also increases with increasing downstream distance reflecting the decay of swirl flow.

The shear stress at the circumference of the pipe wall downstream of the swirl pipe exit is not evenly distributed but has four peaks and valleys as shown in Figure 6.3.16, with the gap between the peak and valley more obvious at circumferences close to the swirl pipe exit. The wave-like variation of wall shear stress along the pipe circumference is expected from the uneven distribution of axial and tangential velocity contours within the cross-flow planes as shown in Figure 6.3.17. At the four corners of the characteristic quadrangular shape in both axial and tangential velocity contours, velocities are higher than other areas indicating a sharper velocity gradient at the wall, resulting in greater wall shear stress increase in the four corners.



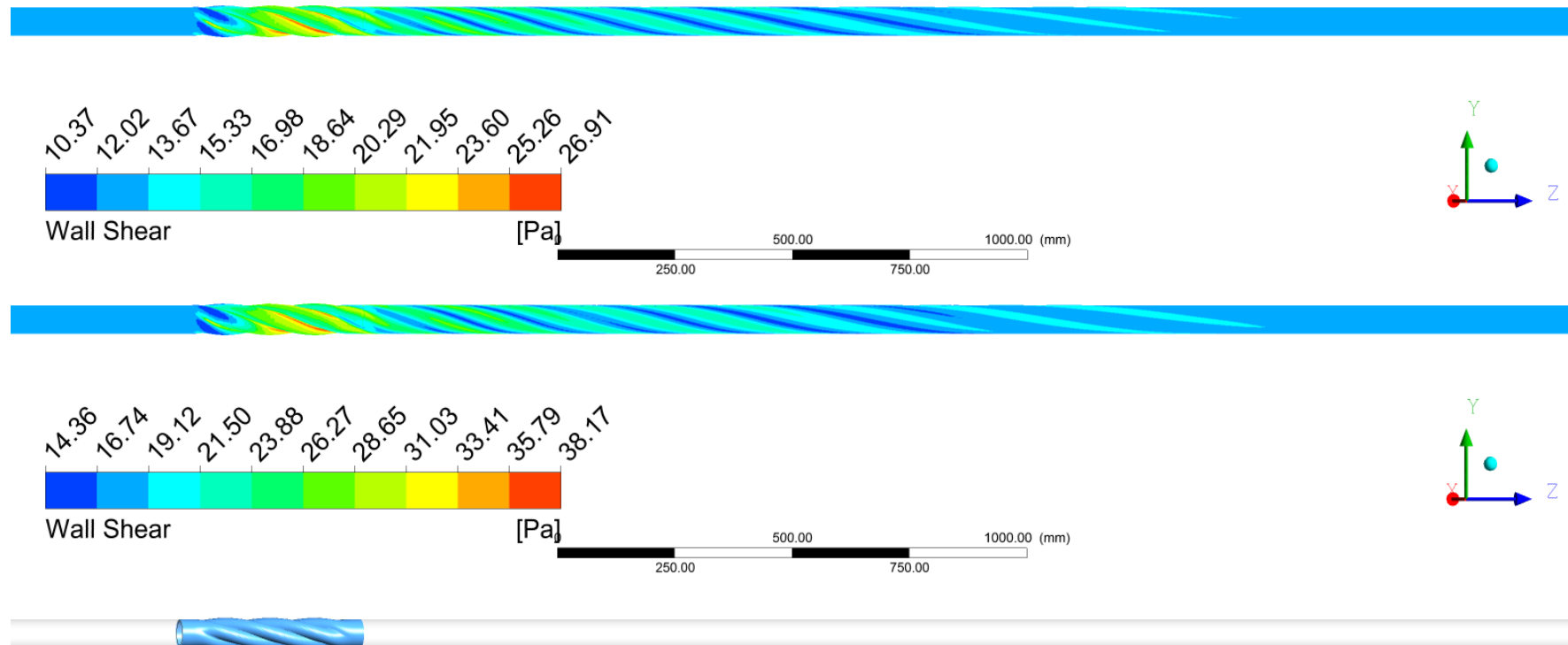


Figure 6.3.15 Contours of WSS at interior wall of swirl pipe and downstream for inlet velocities of 1m/s, 1.5m/s, 2m/s, 2.5m/s, 3m/s respectively from top to bottom

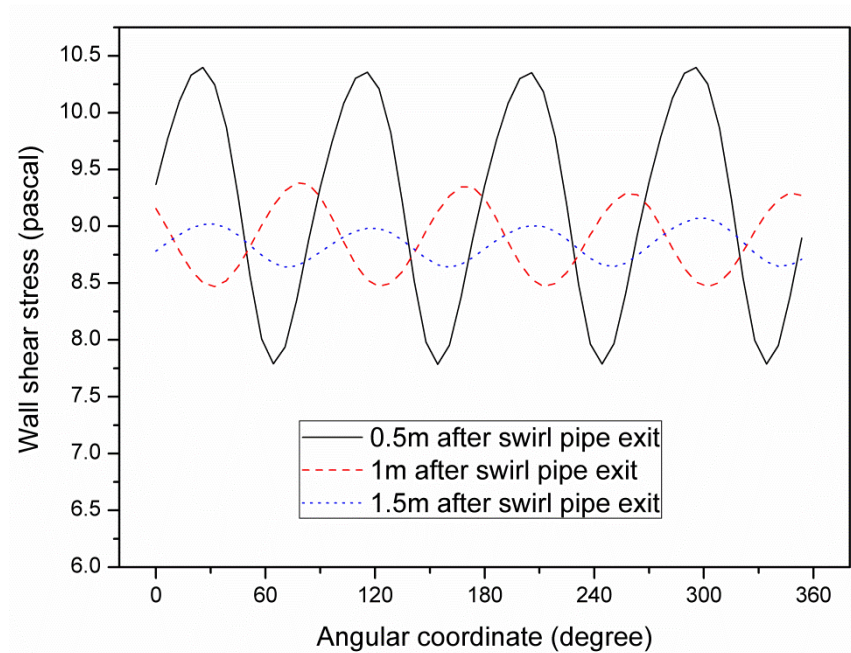


Figure 6.3.16 Circular distribution of WSS at 0.5m, 1m, and 1.5m downstream of swirl pipe exit (2m/s inlet velocity)

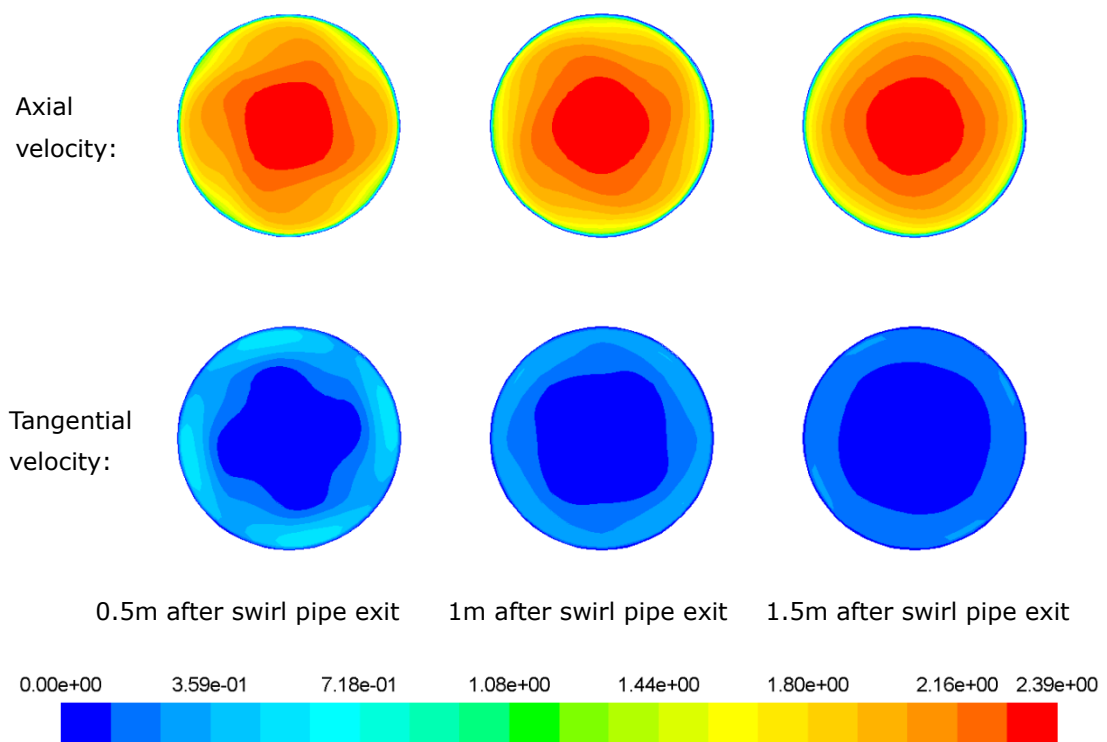


Figure 6.3.17 Contours of axial and tangential velocity at cross-flow planes 0.5m, 1m, and 1.5m downstream of swirl pipe exit (2m /s inlet velocity)

The mean wall shear stress downstream of the swirl pipe exit is calculated for the various inlet velocities as it is reported to be a measure of cleaning efficiency in straight pipes, large parts of pumps, valves and so on. The plot is presented in Figure 6.3.18. It is clear that swirl pipe locally increases mean wall shear stress downstream of it, with the increased value and effective distance more remarkable for a faster inlet flow velocity (thus a large Reynolds number and large swirl intensity). For flow at a lower speed of 1m/s, the increase in wall shear stress is not obvious.

At the flow velocity of 3m/s which is typically the velocity of cleaning fluid circulating in a Clean-In-Place procedure, swirl pipe raises mean shear stress at the wall from 17.8 Pascal prior swirl pipe entry to 23.3 Pascal (30.9% increase) just downstream of swirl pipe exit; and within 1.1m (22D) downstream swirl pipe exit, mean wall shear stress has an increase of at least 5%. For inlet velocities of 2.5m/s, 2m/s, 1.5m/s and 1m/s, the effective distance within which the wall shear stress has at least 5% increase are 1m (20D), 0.9m (18D), 0.6m (12D) and 0.5m (10D) respectively. The 5% increase of wall shear stress, though small, can be important in improving Clean-In-Place efficiency in the closed processing system. Due to the decay nature of the geometrically induced swirl flow, the application of swirl pipe should be particularly useful in the areas that are most difficult to clean in the pipe system, as the cleaning time is dependent on the degree of cleanliness of such areas.

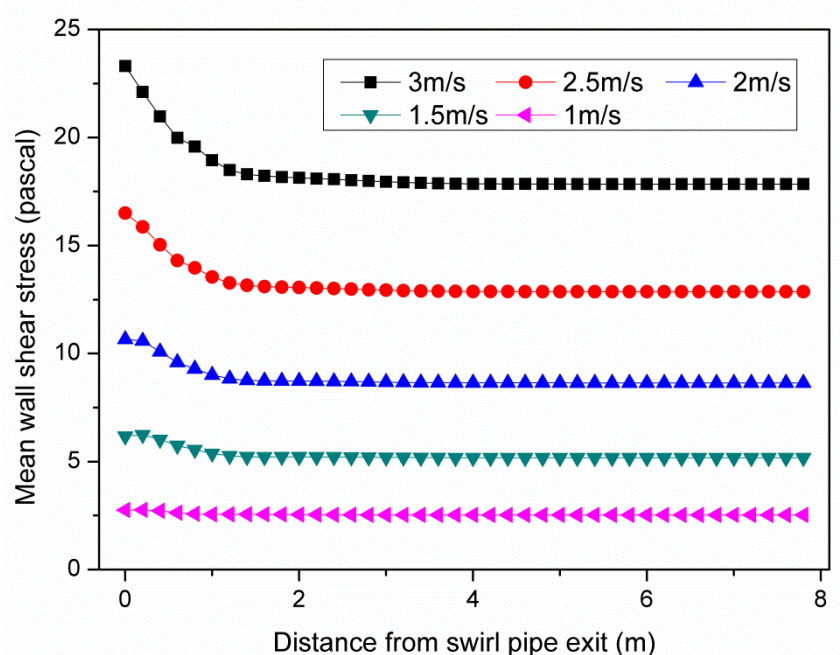


Figure 6.3.18 Wall shear stress variation downstream of swirl pipe exit for various inlet velocities

Besides locally increasing the maximum and mean wall shear stress of cleaning fluid without increasing the flow velocity, swirl pipe should also enhance the transport of heat and cleaning agent, typically 0.5% sodium hydroxide and/or phosphoric acid, to the pipe wall area, enhancing its contact with fouling at wall. This is expected as the current swirl pipe is developed from a swirly shaped pipe found in marine boilers which is used to improve heat exchanger efficiency. The cleaning agent and its operating temperature induce a decrease in the adhesion strength of fouling to the pipe surface, facilitating fouling removal when a wall shear stress is applied.

From the above discussion, swirl pipes mounted in the closed processing system have the potential to locally increase CIP efficiency in the stage of cleaning without increasing the overall flow speed. While in the stage of food or beverage processing, where flow velocity is much lower, the existence of the swirl pipe would not have much influence on the material passing through it.

Compared with other swirl induction methods, the swirl pipe is much easier to

install into the pipe system by flanges or clamps, and more importantly the local intervention of swirl pipe has minimal intrusion to the flow which avoids the insertion of any objects which would otherwise be mounted inside the pipe, such as blades, helical ribs and honeycomb structures that might contribute to problems regarding the fouling and cleaning of the pipes.

6.4 Conclusions

In this chapter, the potential of a swirl flow induced by an optimised four-lobed swirl pipe on improving Clean-In-Place efficiency has been numerically investigated. The objective has been the prediction of swirl intensity and its decay law downstream of the swirl pipe, the shear stress at the pipe wall exerted by the geometrically induced swirling flow and its relationship with swirl intensity and the Reynolds number.

The geometrically induced swirl flow property with respect to tangential velocity, swirl intensity and shear stress at wall were analysed. The following results have been obtained:

- Swirl pipe imparts a tangential velocity into flow passing through it with the swirl effect more prominent in flows with a large Reynolds number. The tangential velocity contour forms a characteristic quadrangular shape due to the 4-lobed cross section of swirl pipe. Its swirl type fits to a 'solid body' downstream of the swirl pipe exit.
- The swirl decay rate of swirl pipe induced swirling flow is in good agreement with exponential trend with the decay rate decreasing with increasing Reynolds number. The decay rate is a little higher than the expected value suggested in the literature which may attribute to the fact that Colebrook equation and the Blasius equation tend to underestimate the friction factor value.

- Swirl pipe imposes a tangential wall shear stress within itself and direct to downstream, its value and variation trend is dependent on swirl intensity.
- Axial wall shear stress is mainly proportional to the Reynolds number, though the presence of the swirl pipe slightly increases its value within and downstream of it.
- The wall shear stress value along the pipe circumference forms a wave-like distribution, with the gap between peak and valley more obvious at circumferences close to the swirl pipe exit.
- Swirl pipe locally increases mean wall shear stress downstream of it, with the increased value and effective distance more remarkable for flow with a larger Reynolds number.

From the simulation results, swirl pipe should be able to improve the cleaning efficiency of Clean-In-Place procedures in closed processing systems by locally increasing wall shear stress downstream of it without increasing overall velocities of cleaning fluid. The beneficial effects of swirl pipe are more obvious in flows with higher velocities where both the effective distance and wall shear stress increase are larger than lower velocities. The swirl pipe should be particularly useful in the areas that are most difficult to clean in the pipe system, as the cleaning time is dependent on the degree of cleanliness of such areas.

CHAPTER 7: LARGE EDDY SIMULATION OF SWIRL FLOW DOWNSTREAM OF THE OPTIMISED SWIRL PIPE

7.1 Introduction

So far, the simulation study of the swirl flows induced by swirl pipes were restricted to the RANS approach, which is the mainstay for engineering flow calculations owing to its modest requirement on computing resource, reasonably accurate prediction and simplified post-processing. However, it was found the RANS cannot capture the turbulent velocity fluctuations with time, giving only the mean flow field and the effects of turbulence on mean flow properties (H.K.Versteeg and W.Malalasekera, 2010). For this reason, the time-dependent property of the swirl flow was not revealed and reported by previous researchers on swirl pipe. As the swirl flow induced by the swirl pipe is inherently unsteady and three-dimensional, it is therefore important to understand the unsteady property of the swirl flow and perhaps its correlation with CIP procedures in closed processing systems.

In this chapter the Large Eddy Simulation (LES) approach was attempted in order to understand the unsteadiness of the geometrically induced swirl flow. LES has had very limited impact on industrial flows due to the very high grid resolution requirement and the prohibitive computational cost in terms of long run times and large volumes of data. However it has the potential for improved accuracy when resolving the largest eddies is important, and more importantly it provides unsteady data needed to see the fluctuation in the flow variables.

The general concepts and models concerning LES were introduced. The vortex

core regions within the swirl flow were identified. The instantaneous and time averaged pressure drop, tangential velocity and swirl decay of the unsteady swirl flow were analysed and compared with the RANS results. The instability of the flow variables was revealed. Special attention was paid to the increase of the mean wall shear stress just downstream of the swirl pipe and the enhancement of the fluctuation rate of the wall shear stress further downstream of the swirl pipe.

7.2 Large Eddy Simulation

Turbulent flows are characterized by eddies with a wide range of length and time scales. The smaller eddies are nearly isotropic and have a universal behaviour. They are less dependent on the geometry, with the smallest eddies are responsible for the dissipation of the turbulence kinetic energy. On the other hand, the large eddies, which interact with and extract energy from the mean flow, are more anisotropic. Their behaviours are dictated by the geometries and boundary conditions of the flow involved.

It is possible, in theory, to resolve directly the whole spectrum of turbulence scales using a direct numerical simulation (DNS) approach where no modelling is required. However, DNS is unaffordable for practical engineering problems involving high Reynolds number flows because the cost needed for DNS to resolve the whole range of scales is proportional to Re^3 . Obviously, for flows with high Reynolds number, the cost becomes prohibitive.

Large eddy simulation (LES) offers a different approach to the computation of turbulent flows which accepts that the larger eddies need to be computed for each problem are resolved with a time-dependent simulation. On the other hand, the universal behaviours of the smaller eddies are modelled with a compact Subgrid-Scale Model.

7.2.1 Filtering Operation

Different from time-averaging used in the RANS approach, the LES uses a spatial filtering operation to separate the larger and smaller eddies. The operation involves the application of a filtering function and a certain cut-off width to the unsteady Navier-Stokes equations. During the spatial filtering, those eddies with a length scale greater than the cut-off width are retained and will be resolved in an unsteady flow computation. While the information related to the turbulent eddies which are smaller than the cut-off width is destroyed.

The LES performs the spatial filtering operation by means of a filter function $G(x, x', \Delta)$ as below (H.K.Versteeg and W.Malalasekera, 2010):

$$\bar{\phi}(x, t) \equiv \int_{-\infty}^{\infty} \int_{-\infty}^{\infty} \int_{-\infty}^{\infty} G(x, x', \Delta) \phi(x', t) dx'_1 dx'_2 dx'_3 \quad (7.2.1)$$

Where $\bar{\phi}(x, t)$ = filtered function

$\phi(x', t)$ = original (unfiltered) function

Δ = filter cutoff width

The filtering operation is an integration carried out in the three-dimensional space. It is designed to split an input into a desirable, retained part and an undesirable, rejected part.

The commonest forms of the filtering function in three-dimensional LES are Top-hat (or box filter), Gaussian filter and Spectral cut-off. Of which the Top-hat filter is used in finite volume implementation of LES which is defined as:

$$G(x, x', \Delta) = \begin{cases} 1/\Delta^3 & |x - x'| \leq \Delta/2 \\ 0 & |x - x'| > \Delta/2 \end{cases} \quad (7.2.2)$$

The cut-off width Δ of the filter determines what is retained and what is rejected.

In most practical (and commercial) implementations of LES, for three-dimensional CFD computation with the finite volume method, the cut-off width is often taken to be the cubic root of the grid cell volume (and no explicit filtering is performed):

$$\Delta = \sqrt[3]{\Delta x \Delta y \Delta z} \quad (7.2.3)$$

where Δx , Δy , Δz are the length, width and height of the grid cells respectively.

Applying the filtering operation to the governing equations obtains the filtered equations of the flow motion. For incompressible Newtonian fluid flow they are:

$$\begin{aligned} \frac{\partial \bar{u}_i}{\partial x_i} &= 0, \\ \frac{\partial \bar{u}_i}{\partial t} + \frac{\partial}{\partial x_j} (\bar{u}_i \bar{u}_j) &= -\frac{1}{\rho} \frac{\partial \bar{p}}{\partial x_i} - \frac{\partial \tau_{ij}}{\partial x_j} + \nu \frac{\partial^2 \bar{u}_i}{\partial x_j \partial x_j} \end{aligned} \quad (7.2.4)$$

where $\tau_{ij} = \overline{u_i u_j} - \bar{u}_i \bar{u}_j$ is the sub-grid-scale stress that must be modelled by Sub-Grid-Scale Models.

7.2.2 Sub-Grid-Scale Models

The spatial filtering gives rise to sub-grid-scale (SGS) stresses due to the interaction effects between the larger, resolved eddies and the smaller unresolved ones. The sub-grid-scale stresses are unknown and require modelling.

ANSYS FLUENT offers sub-grid-scale turbulence models employing the Boussinesq hypothesis as in the RANS models that the turbulent stresses is proportional to the mean rate of strain. They compute the sub-grid-scale turbulence stress using (Conway et al., 2000):

$$\tau_{ij} - \frac{1}{3} \tau_{kk} \delta_{ij} = -2\mu_t \bar{S}_{ij} \quad (7.2.5)$$

where μ_t is the sub-grid-scale turbulent viscosity. τ_{kk} is the isotropic part of the sub-grid-scale stress. It is not modelled but added to the filtered static pressure term. δ_{ij} is the Kronecker delta ($\delta_{ij} = 1$ if $i = j$ and $\delta_{ij} = 0$ if $i \neq j$). \bar{S}_{ij} is the local rate-of-strain of the resolved flow $\bar{S}_{ij} = \frac{1}{2} \left(\frac{\partial \bar{u}_i}{\partial \bar{x}_j} + \frac{\partial \bar{u}_j}{\partial \bar{x}_i} \right)$.

ANSYS FLUENT provides the following models for μ_t : the Smagorinsky-Lilly model, the dynamic Smagorinsky-Lilly model, the Wall-Adapting Local Eddy-Viscosity (WALE) model, the Algebraic Wall-Modeled LES Model (WMLES) model, and the dynamic kinetic energy subgrid-scale model (ANSYS, 2011a). The most common and simplest explicit SGS is that of the Smagorinsky-Lilly model (Smagorinsky, 1963).

7.2.2.1 Smagorinsky-Lilly Model

In the Smagorinsky-Lilly model, the eddy-viscosity μ_t is modelled by

$$\mu_t = \rho L_s^2 |\bar{S}| \quad (7.2.6)$$

where $|\bar{S}| \equiv \sqrt{2\bar{S}_{ij}\bar{S}_{ij}}$, L_s is the mixing length for sub-grid scales which is computed using

$$L_s = \min(kd, C_s \Delta) \quad (7.2.7)$$

where k is the von Kármán constant, d is the distance to the closest wall, Δ is the local grid scale which is computed according to the volume of the computational cell using $\Delta = V^{1/3}$, C_s is the Smagorinsky constant.

Lilly (1967) carried out a theoretical analysis of the decay rates of isotropic turbulent eddies in the inertial subrange of the energy spectrum and suggested values of C_s between 0.17 and 0.21. However, in the presence of shear, near solid boundary or in transitional flows, this value was found to cause excessive

damping of large-scale fluctuations and must be decreased (Piomelli, 1999). A C_s value around 0.1 was found to give the best results for a wide range of flows, which is the default value in ANSYS FLUENT.

7.2.2.2 Dynamic Smagorinsky-Lilly Model

The Smagorinsky-Lilly Model is purely dissipative that the direction of energy flow is exclusively from eddies at the resolved scales towards the sub-grid scales. It does not allow for the intermittent transport of energy from the small scales to the large ones. This backscattering phenomenon is important when modelling transition. Germano et al. (1996) and Lilly (1967) introduced a dynamic modelling idea which can account for the backscatter.

In the dynamic model, the model constant C is dynamically computed as the calculation progresses based on the energy content of the smallest resolved scale. This is accomplished by applying to the equations of motion a test filter whose filter width $\hat{\Delta}$ is typically equal to twice the grid filter width Δ ($\hat{\Delta} = 2\Delta$). Both the grid filter and the test filter produce a resolved flow field. The difference between the two resolved fields is the contribution of the small scales whose size is in between the grid filter and the test filter. The information related to these scales is used to compute the model constant.

Both the sub-test stresses T_{ij} and the sub-grid stresses τ_{ij} are modelled using Smagorinsky-Lilly Model assuming that the constant C is the same for both filtering operations.

$$\begin{aligned}\tau_{ij} - \frac{1}{3}\delta_{ij}\tau_{kk} &= -2C\Delta^2|\bar{S}|\bar{S}_{ij} \\ T_{ij} - \frac{1}{3}\delta_{ij}T_{kk} &= -2C\hat{\Delta}^2|\hat{S}|\hat{S}_{ij}\end{aligned}\tag{7.2.8}$$

The grid filtered SGS and the test-filtered SGS are related by the Germano

identity that (Germano et al., 1996):

$$T_{ij} - \hat{\tau}_{ij} = L_{ij} = \widehat{\bar{u}_i \bar{u}_j} - \widehat{\bar{u}_i} \widehat{\bar{u}_j} \quad (7.2.9)$$

where L_{ij} (the contribution from the region between test-filter and grid-filter scale) is computable from the resolved large eddy field.

Lilly (1967) suggested a least-squares approach to evaluate local values of C:

$$C^2 = \frac{\langle L_{ij} M_{ij} \rangle}{\langle M_{ij} M_{ij} \rangle}$$

with $M_{ij} = -2\hat{\Delta}^2 |\widehat{\bar{S}}| \widehat{\bar{S}}_{ij} + 2\Delta^2 |\widehat{\bar{S}}| \widehat{\bar{S}}_{ij}$

(7.2.10)

The angular brackets $\langle \rangle$ indicate an averaging procedure which is to avoid numerical instability. The model constant C obtained using the dynamic Smagorinsky-Lilly model varies in time and space over a fairly wide range. In ANSYS FLUENT, it is clipped at zero and 0.23 by default.

7.2.2.3 Algebraic Wall-Modeled LES Model (WMLES)

Despite the wide use in the academic community, LES has had very limited impact on industrial simulations for high Reynolds number, wall-bounded flows due to the prohibitive computational cost to resolve energy-carrying eddies in the near-wall region. Hybrid RANS-LES approaches have been developed which significantly reduce the computational cost of such configurations. These include the Detached-Eddy Simulation (DES) and its recent modification the delayed DES (DDES), and wall-modelling in LES (WMLES) (Shur et al., 2008).

The wall-modelling approach is based on the RANS calculation in the inner layer. The inner-layer RANS is solved in a grid that is refined in the wall-normal direction and is embedded in the outer-layer, coarse LES mesh. Which provides instantaneous wall shear stresses and heat fluxes at the wall to the concurrent

outer-layer LES as approximate wall boundary conditions replacing the standard no-slip velocity boundary conditions at a solid surface (Templeton et al., 2006, Kawai and Larsson, 2010). The outer part of the boundary layer is covered by a modified LES formulation.

ANSYS FLUENT optimizes an Algebraic WMLES formulation which was originally proposed by Shur et.al. (2008). In this model, the eddy viscosity is calculated with the use of a hybrid length scale:

$$\mu_t = \min \left[(k d_w)^2, (C_{smag} \Delta)^2 \right] \cdot S \cdot \left\{ 1 - \exp \left[- \left(y^+ / 25 \right)^3 \right] \right\} \quad (7.2.11)$$

where $k=0.41$ and $C_{smag}=0.2$ are constants, d_w is the wall distance, S is the strain rate, y^+ is the normal to the wall inner scaling, and Δ is the sub-grid length-scale.

The LES model is based on a modified grid scale to account for the grid anisotropies in the wall-modelled flows:

$$\Delta = \min \{ \max [C_w d_w, C_w h_{max}, h_{wn}], h_{max} \} \quad (7.2.12)$$

where h_{max} is the maximum edge length of the cell, h_{wn} is the grid spacing in the wall-normal direction and $C_w=0.15$ is an empirical constant.

The main advantage of the WMLES formulation is the improved Reynolds number scaling that the classical resolution requirements for wall resolved LES is avoided by WMLES and the CPU effort is substantially reduced (ANSYS, 2011a).

7.3 Simulation Setup

7.3.1 Meshing

The geometry of the computational domain used in the LES is the same as that used in the RANS approach. The multi-block, structured meshing scheme described in section 4.4.4 is used in the spatial discretization of the geometry. Near the wall, the largest scales in the turbulent spectrum are nevertheless geometrically very small and require a very fine grid and a small time step. Therefore, a much finer mesh is generated so as to meet the excessively high resolution requirements for the wall boundary layers, typically $y^+ \leq 1$ is required for near-wall grid points.

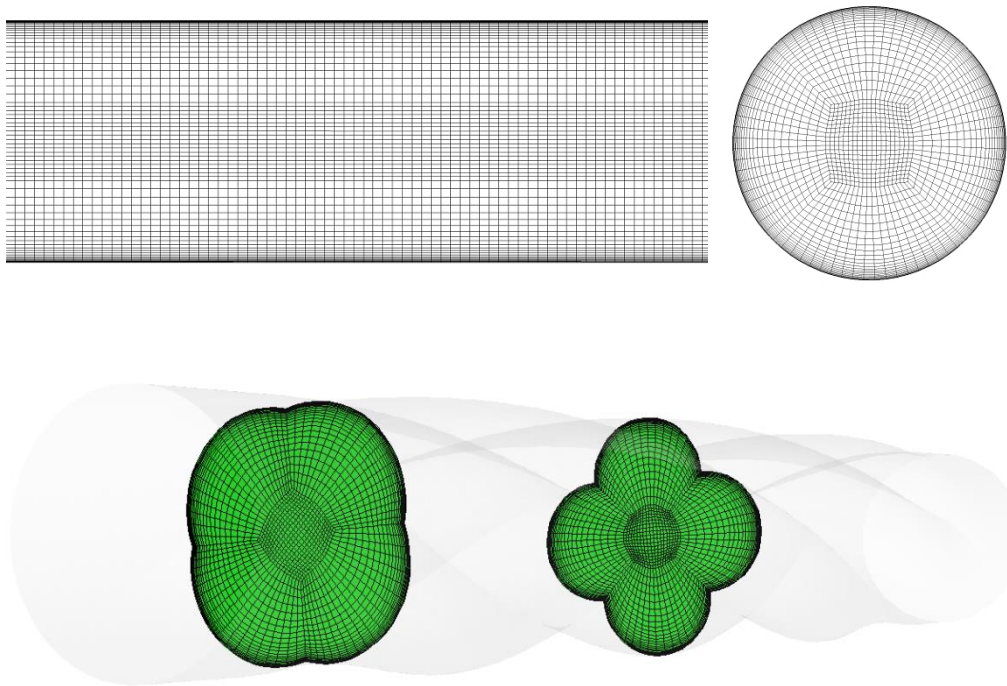


Figure 7.3.1 Fine grid in the near wall region of cylindrical pipe and swirl pipe for LES

Initially a very small distance of 0.02mm from the wall to the first node of the mesh was specified with a growth ratio of 1.1 towards pipe centre. It was found that degenerate cells (slivers) appeared along the pipe wall which would impede convergence of the solution. Attempts were made to improve the mesh quality

by gradually increasing the distance between the wall and the first node of the mesh from 0.02mm, 0.03mm, 0.04mm to 0.05mm. Simulation tests suggested that at a value of 0.05mm the solution was reasonably converged and the y^+ value was in an acceptable range.

In addition, the grid was not only refined in the wall normal direction (X-Y plane) but also refined in the Z direction so as to resolve turbulence in the wall parallel plane. In the stream wise direction, grid refinement was carried out by shortening the mesh height to 1.5mm and 1mm. It was found a grid with a mesh height of 1mm demands excessively large computing resources in terms of storage and volume of calculation for the LES that the current workstation is not suited for this task. Therefore a mesh height of 1.5mm is used in the stream wise direction. Figure 7.3.1 shows the final grid in the wall normal and wall parallel direction for the geometry of the computational domain.

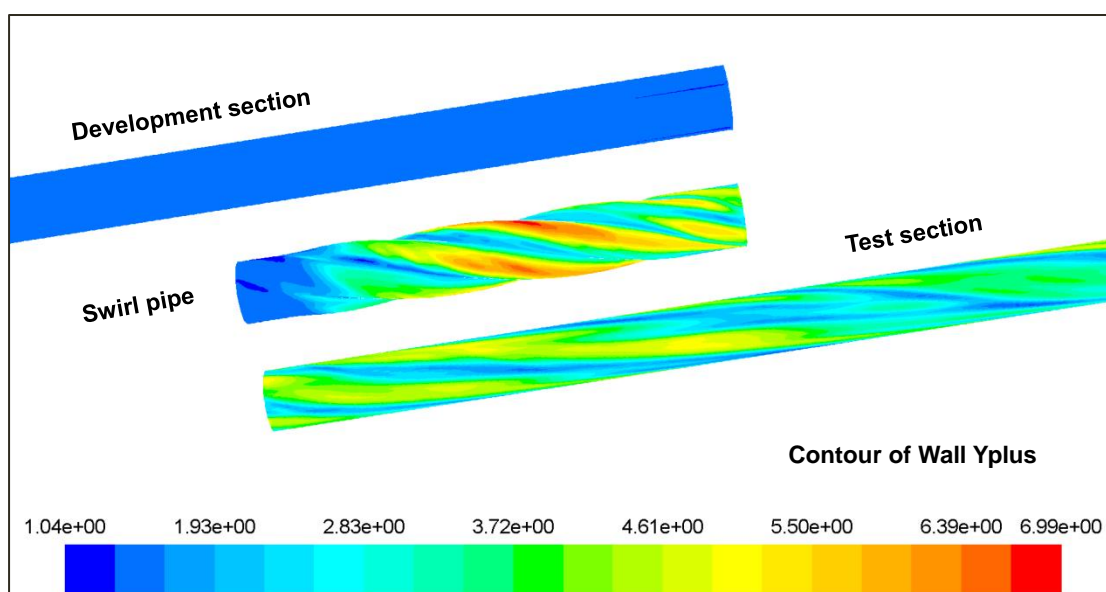


Figure 7.3.2 y^+ contours of computational domain geometry for LES (2m/s inlet velocity)

Figure 7.3.2 shows the y^+ contours of the sections of the flow geometry. The y^+ values are between 1.3-5.24, 1.15-6.82, and 1.04-5.24 for the development section, swirl pipe and test section respectively. Though the y^+ value is greater than 1, it is the finest grid that can be reached due to the limitation of the

computing power of the current workstation. In practice, a y^+ value less than 10 may be acceptable for engineering flows.

7.3.2 Initial Conditions for LES

Large eddy simulation involves running a transient solution from the initial condition using an appropriate time step size. The solution must be run long enough to become independent of the initial condition and to enable the statistics of the flow field to be determined.

At the inlet, the No Perturbations fluctuating velocity algorithm is employed that the stochastic components of the flow at the velocity inlet boundaries are neglected. This option is suitable as the level of turbulence at the inflow boundary does not play a major role in the accuracy of the overall solution. The outlet boundary condition is less troublesome and a pressure outlet boundary condition is specified at the outlet. The pipe walls are specified as being stationary and the no-slip walls condition is used.

In this study, the large eddy simulation started by running a steady state RANS simulation using a standard $k-\epsilon$ model together with a near wall modelling approach which enables the viscosity-affected region to be resolved with the fine mesh all the way to the wall, including the viscous sub-layer. After convergence of the solution, the turbulence model was changed into a realizable $k-\epsilon$ model and RSM and run until the flow field was reasonably converged. Then an instantaneous velocity field was generated out of the steady state RANS results as the initial condition for the LES. This approach creates a much more realistic initial field for the LES run. In addition, it will reduce the time needed for the LES simulation to reach a statistically stable state.

7.3.3 Discretization for LES

Activate LES, and ANSYS FLUENT will turn on the unsteady solver option. The

Bounded Second Order Implicit formulation was chosen for temporal discretization as it provides better stability despite the same accuracy as the Second Order Implicit formulation. Frequently a time-dependent problem has a very fast “startup” transient that decays rapidly. Therefore, a conservatively small time step size Δt was set initially for the first number of time steps. The Δt was gradually increased to 0.01s as the calculation proceeded.

To verify that the choice for Δt was proper, the contour of the Courant number was checked after the calculation is complete. The Courant number was found reasonably within a value of 40 in the most sensitive transient regions of the domain. This meets the requirement that it should not exceed a value of 20-40 (ANSYS, 2011b).

As for the spatial discretization, the first-order upwind or power law scheme should be avoided, as they may overly damp out the energy of the resolved eddies. The central-differencing based schemes are recommended for all equations when LES model is used. Here the bounded central-differencing scheme was used for momentum which is the default option for use with LES. The second order pressure discretisation scheme was employed for Pressure interpolation. The SIMPLE scheme was used for pressure-velocity coupling.

7.3.4 Choice of SGS Model

Three identical cases were run each employing Smagorinsky-Lilly, Dynamic Smagorinsky-Lilly and WMLES Sub-Grid-Scale Model respectively. A time step size of 0.01s and 200 time steps ($0.01 \times 200 = 2s$) were set for the transient solution. Data sampling for time statistics was enabled in order to obtain the mean flow quantities. It allows for the calculation of the mean or root-mean-square of the variables by collecting time statistics at each sampling interval while performing the simulation. The variation of the mean wall shear stress and the mean tangential velocity downstream of the swirl pipe for the

three cases and the RANS approach are presented in Figure 7.3.3 and 7.3.4.

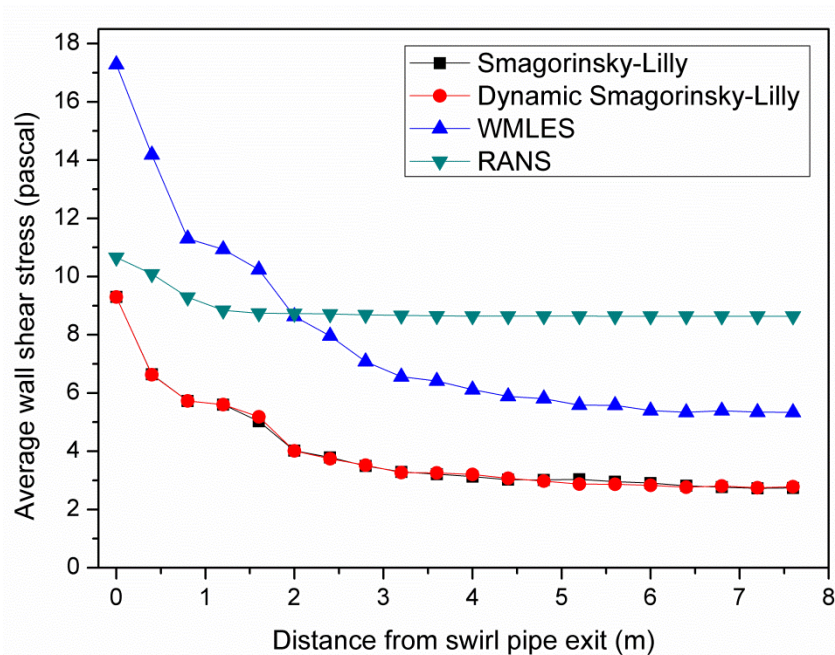


Figure 7.3.3 Comparison of wall shear stress distribution for various SGS models and RANS (2m/s inlet velocity)

The configurations employing the Smagorinsky-Lilly or Dynamic Smagorinsky-Lilly SGS models belong to the category of Wall-Resolved LES where very fine grid spacing is needed close to the wall to filter out the smallest turbulent scales and to get the near-wall structures resolved. Figure 7.3.3 shows that the Smagorinsky-Lilly and Dynamic Smagorinsky-Lilly model give almost identical underestimation on wall shear stress downstream of swirl pipe despite the dynamic constant C used for the Dynamic Smagorinsky-Lilly model.

The reason for this may be due to the high resolution requirements for the wall boundary layers with the current mesh not being fine enough for the Wall-Resolved LES. Because near the wall, even the 'large' eddies become relatively small and require a Reynolds number dependent resolution.

When resolving the exterior flow, the grid resolution is weakly dependent on the Reynolds number as $Re^{0.4}$ (Chen, 2011). When the LES is implemented on coarse grids near the wall, errors arise from numerical discretization and SGS

modelling. The velocity gradient in the near-wall region is under predicted by a discretization scheme using no-slip boundary conditions on coarse grids. This leads to underestimation of the wall shear stress and incorrect kinetic energy production, and distortion of the exterior LES (Chen, 2011).

No-slip boundary conditions cannot be applied directly at high Reynolds numbers if the mesh is too coarse in the near-wall region as the distance between the first point off-wall and the wall is much larger than the characteristic length-scales of the modelled zone (Monfort et al., 2010).

Alternatively, the WMLES approach replaces the no-slip boundary condition with approximate wall boundary conditions by RANS calculation in the inner layer. The RANS calculation is an in-time-accurate calculation and provides instantaneous wall shear stresses and heat fluxes at the wall to the concurrent outer-layer LES as approximate wall boundary conditions (Kawai and Larsson, 2010). From Figure 7.3.3, the WMLES approach provides increased wall shear stress predictions than the Wall-Resolved method. The simulation values are closer to the RANS results however it has a larger initial wall shear stress just downstream of the swirl pipe exit which has a steeper decrease along the streamwise direction than the RANS with some fluctuation in values. This is expected as the LES is inherently an unsteady method which is more robust in capturing unsteadiness in turbulence.

Figure 7.3.4 shows that the WMLES and the RANS approach give close prediction on tangential velocity of the swirl flow. While the Smagorinsky-Lilly and the Dynamic Smagorinsky-Lilly SGS models tend to overestimate the swirl effect of the flow. This suggests that, when these models are used, there will be a mismatch between the near wall region and the exterior flow as a stronger swirl flow should yield larger wall shear stresses at the internal pipe surface. Therefore, it is decided to use the WMLES SGS model for the LES, which should

give more reliable predictions than the Smagorinsky-Lilly or Dynamic Smagorinsky-Lilly SGS model.

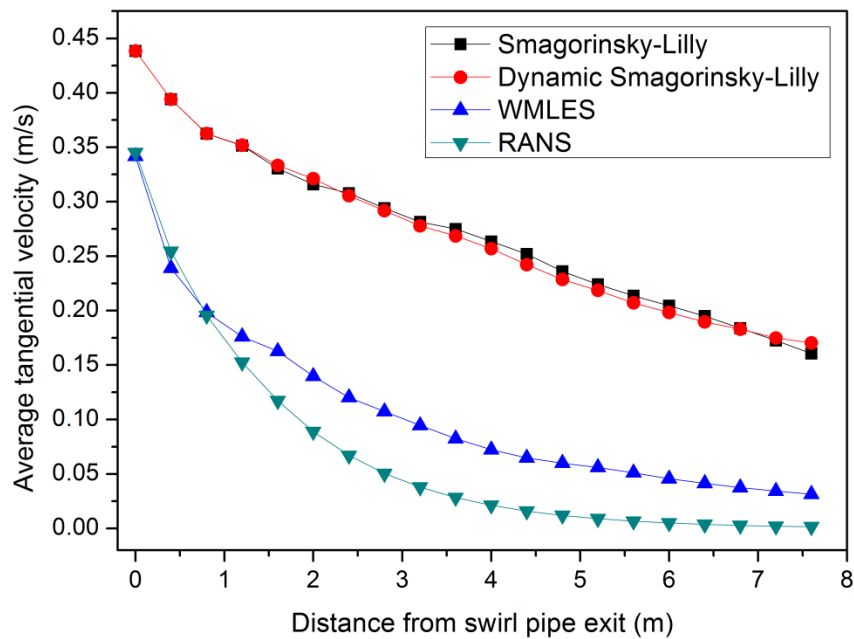


Figure 7.3.4 Comparison of tangential velocity distribution for various SGS models and RANS (2m/s inlet velocity)

7.4 Results and Discussions

7.4.1 Unsteady Swirl Flow

The unsteady RANS approach was used to capture the unsteadiness of the swirl flow, however it was found that with the proceeding solution, the flow statistics, and the contours monitored, became stable and stopped changing with flow time. It gave the same results as the steady RANS approach.

It is claimed that RANS is not applicable for handling unsteady flows unless there is a spectral gap between the unsteadiness and the turbulence. To capture the unsteadiness using unsteady RANS, the averaging period should be much smaller than the time scale of the unsteady mean motion. Meanwhile, the time period should be orders of magnitude higher than the time scale of the random fluctuations for the time averaging to make sense (Wegner et al., 2004). The

unsteady RANS may capture the unsteadiness with the use of periodic or time dependent boundary. However, in this study with constant inlet velocity, unsteady RANS failed to present a fluctuating swirl flow field.

LES, on the other hand, is an inherently time dependent method. Hence, it handles unsteady flows well. Figure 7.4.1 shows a comparison of axial and tangential velocity contours obtained by RANS and the instantaneous contours by LES. The LES gives more detailed turbulent swirl flow field than the RANS. In the LES method, the characteristic quadrangular shaped distribution of the axial velocity contours is more robust than the RANS with a clear indication of four vortex cores at the four corners of the quadrangle corresponding to the four lobes of the swirl pipe. However, in the cross-flow planes further downstream, the flow pattern becomes chaotic indicating the mixing of the four vortex cores.

The four vortex cores are clearer in the velocity vectors in cross-flow planes 0.2m, 0.5m and 1m downstream of the swirl pipe as shown in Figure 7.4.2. The LES clearly captures four rotating movement of the four vortex cores (marked with \times) within the flow field. It is also clear that the location of the vortex cores change with increasing downstream distance, indicating that the four vortices rotate about the pipe's geometrical axis forming an integrated swirling effect throughout the downstream duration of the swirl pipe. The swirl effect decays with downstream distance due to the retarding force from the friction of the internal pipe surface. The vortex cores become ambiguous by reasons of swirl decay and mixing of vortexes. Animation of velocity contour showed that the vortex centres varies slightly around their rotation axis indicating the unsteady nature of the turbulent flow. The unsteadiness of flow is more remarkable in cross-flow planes further downstream of the swirl pipe.

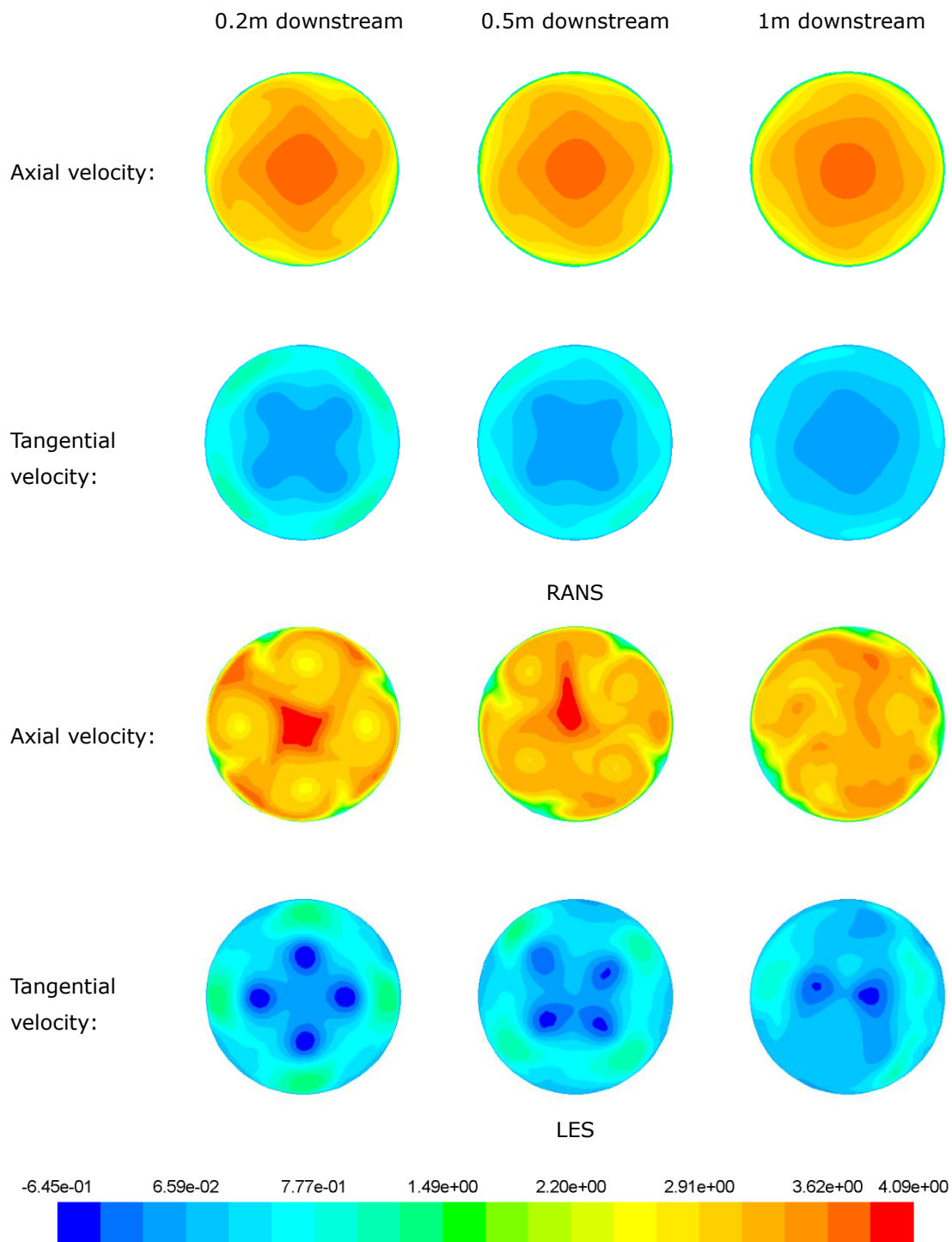


Figure 7.4.1 Comparison of axial and tangential velocity contours obtained by RANS and LES (2m/s inlet velocity)

Figure 7.4.3 shows the pathline of swirl flow downstream of swirl pipe. From the figure, four vortical regions of flow formed within the swirl pipe in which the flow is rotating about the curved axes as shown in Figure 7.4.4. The four curved axes are in the centres of the four lobed regions of the swirl pipe which extend

helically about the geometrical axis of the swirl pipe and the downstream circular pipe. Downstream of the swirl pipe, the four vortices prevail following the pattern as in the swirl pipe, rotating respectively about the four curved axes extended from the centre of the four lobed regions. Because the four curved axis rotate about the axis of the downstream circular pipe, the four rotational vortexes revolve about the circular pipe axis forming an integrated swirl flow throughout the flow field.

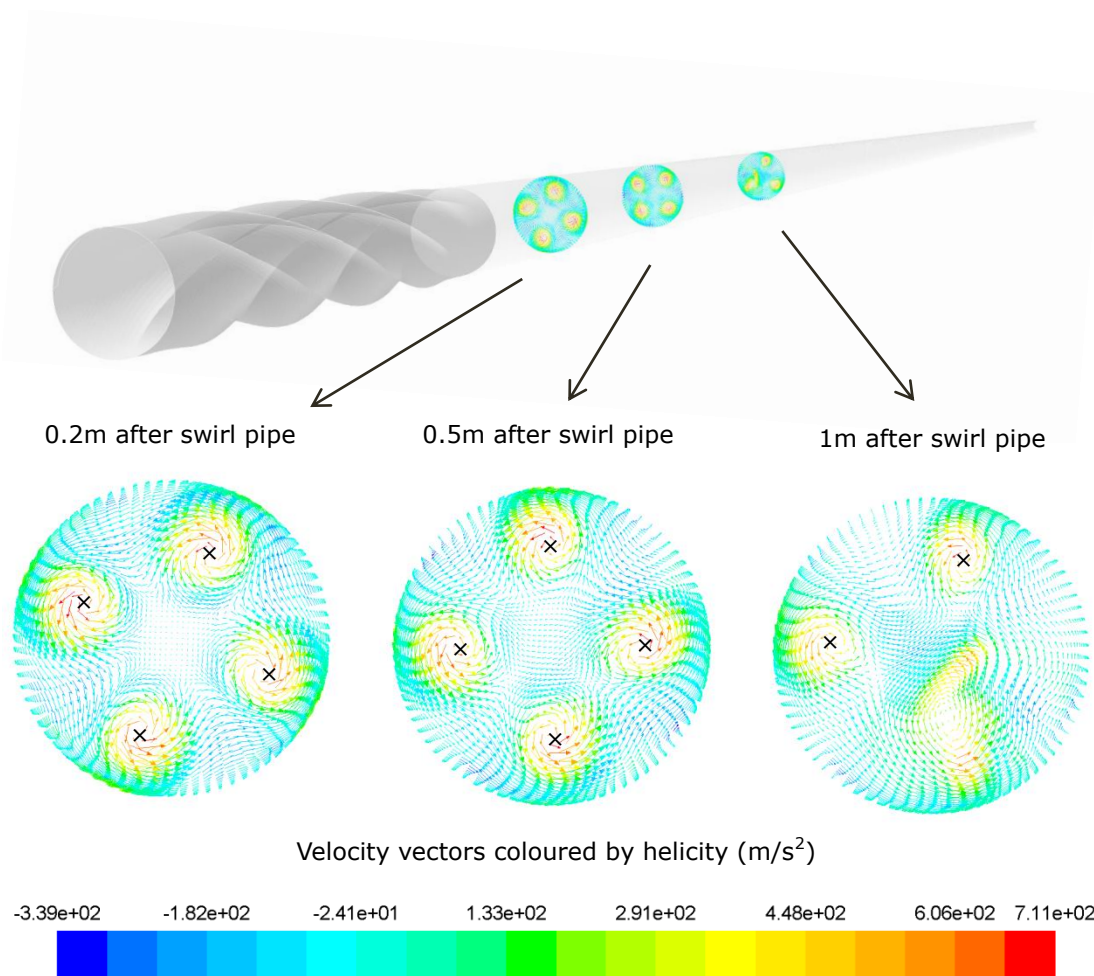


Figure 7.4.2 Velocity vectors in cross-flow planes 0.2m, 0.5m and 1m downstream of the swirl pipe (2m/s inlet velocity)

The vortices formed passing through the swirl pipe, move forward, twist and interact in complex ways. Animation of the velocity magnitude indicates that, further downstream of the swirl pipe where the swirl effect is less prominent, the pattern of spiral flow becomes chaotic and fades away. However, in this duration, the flow velocity fluctuates faster in space and time suggesting stronger unsteadiness.

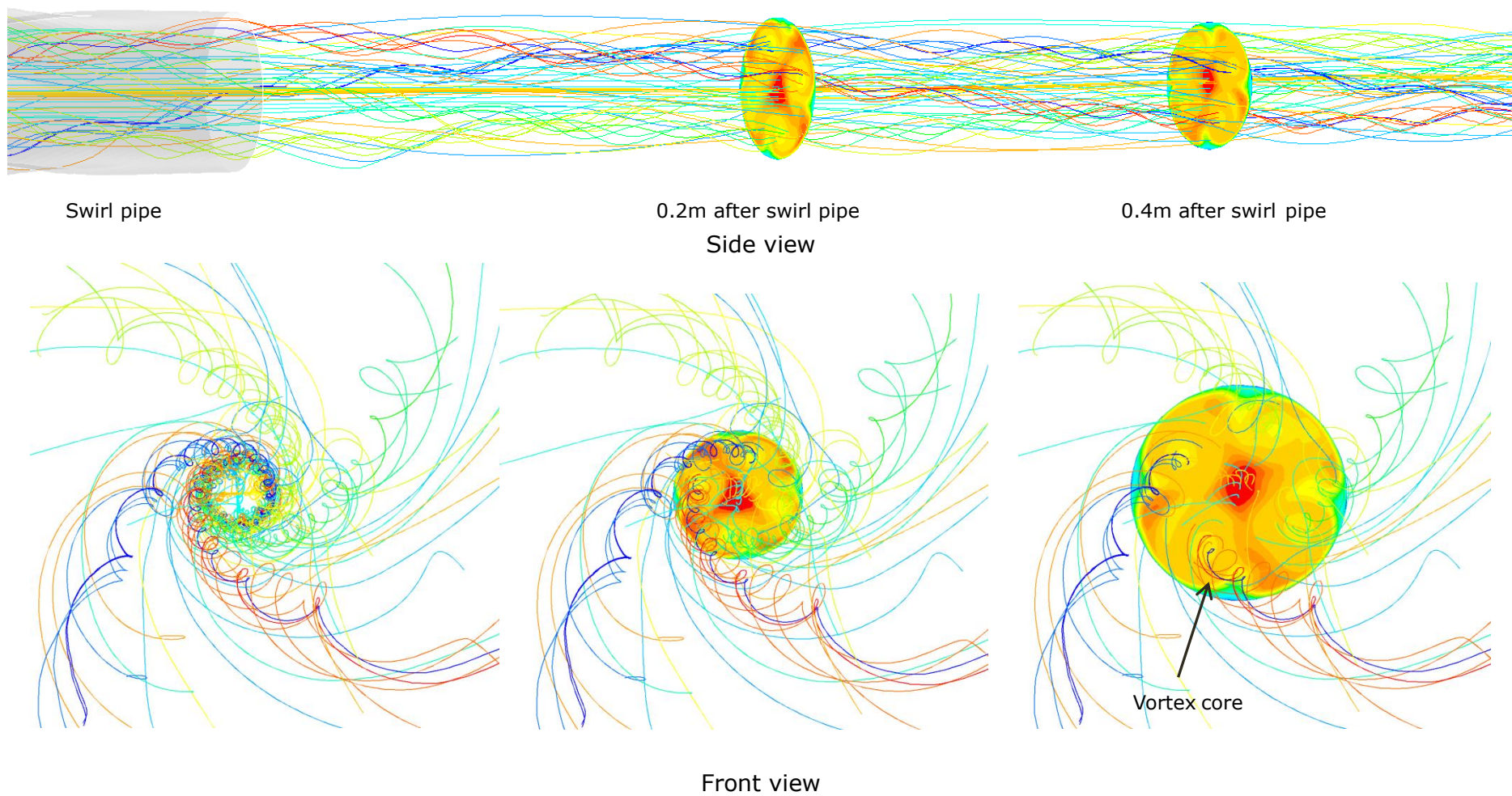


Figure 7.4.3 Pathline of swirl flow downstream of swirl pipe showing vortices (2m/s inlet velocity)

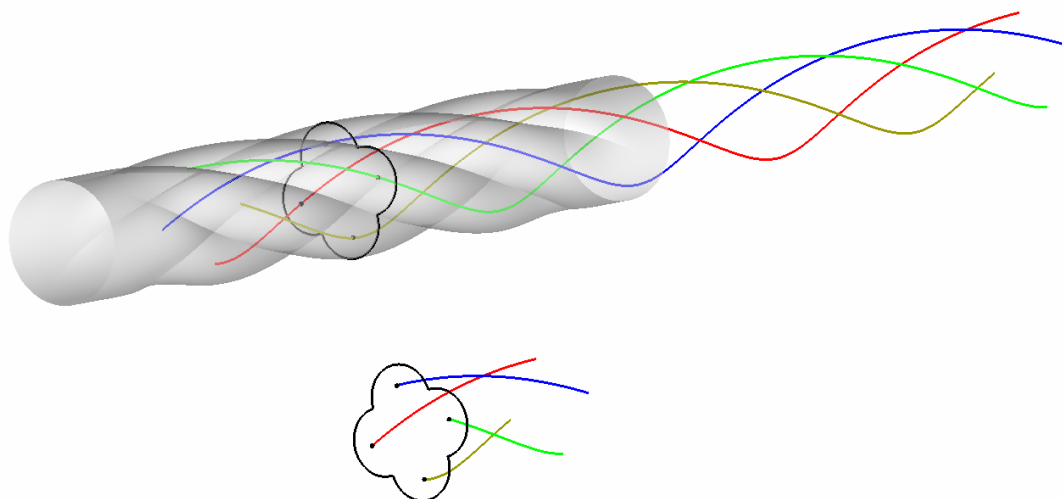


Figure 7.4.4 The four curved axes about which the four vortices rotate

It is reported that swirl flows applied in many engineering application such as modern gas turbines, aero propulsion systems, often exhibit a three-dimensional time-dependent hydrodynamic instabilities called processing vortex core (PVC): a rotating movement of the vortex centre about the system's geometrical axis (Wegner et al., 2004). The appearance of vortices such as the PVC improve the mixing as it creates larger turbulent scales which translate through into the dissipation range of the energy cascade (O'Doherty and Gardner, 2005, Viguera-Zuñiga et al., 2012). The four vortices captured in the LES should be able to enhance the local turbulence intensity downstream of the swirl pipe, which is a favourable feature for CIP procedures as the cleaning efficiency benefits from promotion of turbulent flow or enhancement of flow disturbance (PathogenCombat, 2011).

Froud et al (1995) experimentally investigated the PVC in flow patterns produced in, and past the exhaust of a swirl burner under piloted premixed combustion conditions and stated that the PVC dominates the flow and mixing patterns. Their study showed that the centre of the vortex flow is displaced from the central axis of the burner, creating the PVC phenomena as the centre of the vortex precesses around the central axis of symmetry. As a consequence of the displacement of the vortex centre, flow between the PVC centre and the wall is

squeezed, producing a considerable increase in tangential velocity. Similar conclusion was also reported by Huang and Yang (2009).

From the tangential velocity contours shown in Figure 7.4.1, the strong tangential velocity concentrates in the four regions between vortex core and the pipe wall. The considerable increase in tangential velocity may be caused by the rotational movement of the vortex centre squeezing the flow field at the side against the pipe wall.

7.4.2 Pressure Drop

The variation of time averaged pressure (over 2 seconds), the instantaneous pressure predicted by LES and the pressure predicted by RANS are shown in Figure 7.4.5. For both the LES and RANS method, the pressure drop within the swirl pipe is greater than the circular pipes; this is more obvious in flows with larger velocities (Reynolds number). However, the LES approach tends to underestimate (18%-23% lower) the overall pressure drop especially in flows with higher velocities.

The difference between LES and RANS may attribute to the following two reasons:

- Firstly, the different methods in near-wall region treatment with the RANS approach using semi-empirical wall functions to bridge the viscosity-affected regions between the wall and fully-turbulent region; while the LES employed a Hybrid RANS-LES approach to resolve energy-carrying eddies in the near-wall region.
- Secondly, in the RANS approach, wall roughness of the swirl pipe and circulars pipes were specified as the same value as the experimental rig. While in the LES, such values cannot be specified and the pipe wall was treated as a hydraulic smooth pipe.

Nevertheless, in RANS, the roughness height of 1.237×10^{-6} m for circular pipe and 9×10^{-6} m for swirl pipe are small enough that the walls are hydraulically smooth. In a smooth pipe flow, the viscous sub-layer completely submerges the effect of roughness height of the pipe. In this condition, the friction factor λ is a function of the Reynolds number and is independent of the effect of surface roughness on the flow (Rao and Kumar, 2007). Therefore, it's more likely that the difference in pressure drop prediction is caused by the different near-wall region treatments employed by RANS and LES.

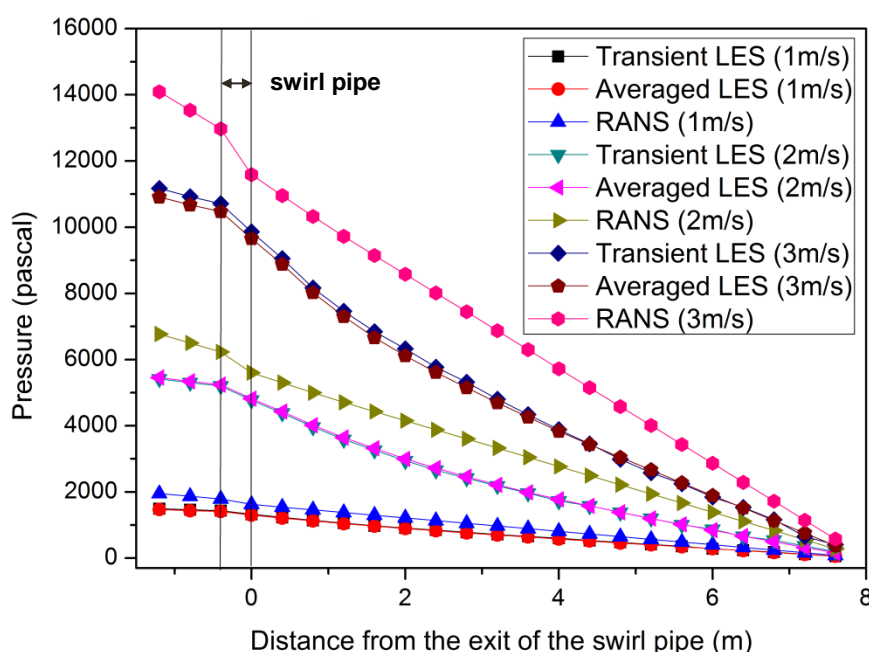


Figure 7.4.5 Static pressure variation in the flow system for various inlet velocities predicted by LES and RANS

It is also clear from Figure 7.4.5 that, for the LES, the pressure drops faster in the circular pipe just downstream of the swirl pipe (indicated by the steeper slope) than further downstream (relatively smaller slope). As discussed in section 6.3.1, a greater pressure drop just downstream of swirl pipe was also observed in the RANS approach, but it is less significant. It is therefore expected that, the inherently time dependent LES method should give a more radical prediction of the increase in wall shear stress in the duration just downstream of the swirl pipe than the RANS.

7.4.3 Tangential Velocity

Figure 7.4.6 depicts the area averaged tangential velocity over cross-flow planes downstream of the swirl pipe obtained by RANS and LES (time averaged value over 2 seconds and instantaneous value respectively) for various inlet velocities. The figure shows that:

- The initial tangential velocities are almost identical in both methods with greater tangential velocities being induced in flows with larger velocities, which also prevail for longer downstream duration.
- The tangential velocity induced decreases with increasing downstream distance for both the RANS and LES. However, in the LES method, the tangential velocity decreases more slowly, prevailing for a longer downstream distance at a relatively larger value.
- From the transient LES results, the instantaneous tangential velocity fluctuates about the time averaged LES value, revealing the unsteady nature of the turbulent swirling flow. The fluctuation degree increases with increasing flow velocity, indicating greater turbulence intensity in flows with a larger Reynolds number.
- The transient LES results also suggests that a greater fluctuation in tangential velocity takes place in cross-flow planes that are further downstream of the swirl pipe where the vortex cores interacts and dissipates. While just downstream of the swirl pipe, the tangential velocity is relatively stable. It seems like the flow just downstream of the swirl pipe is stabilized by the swirl.

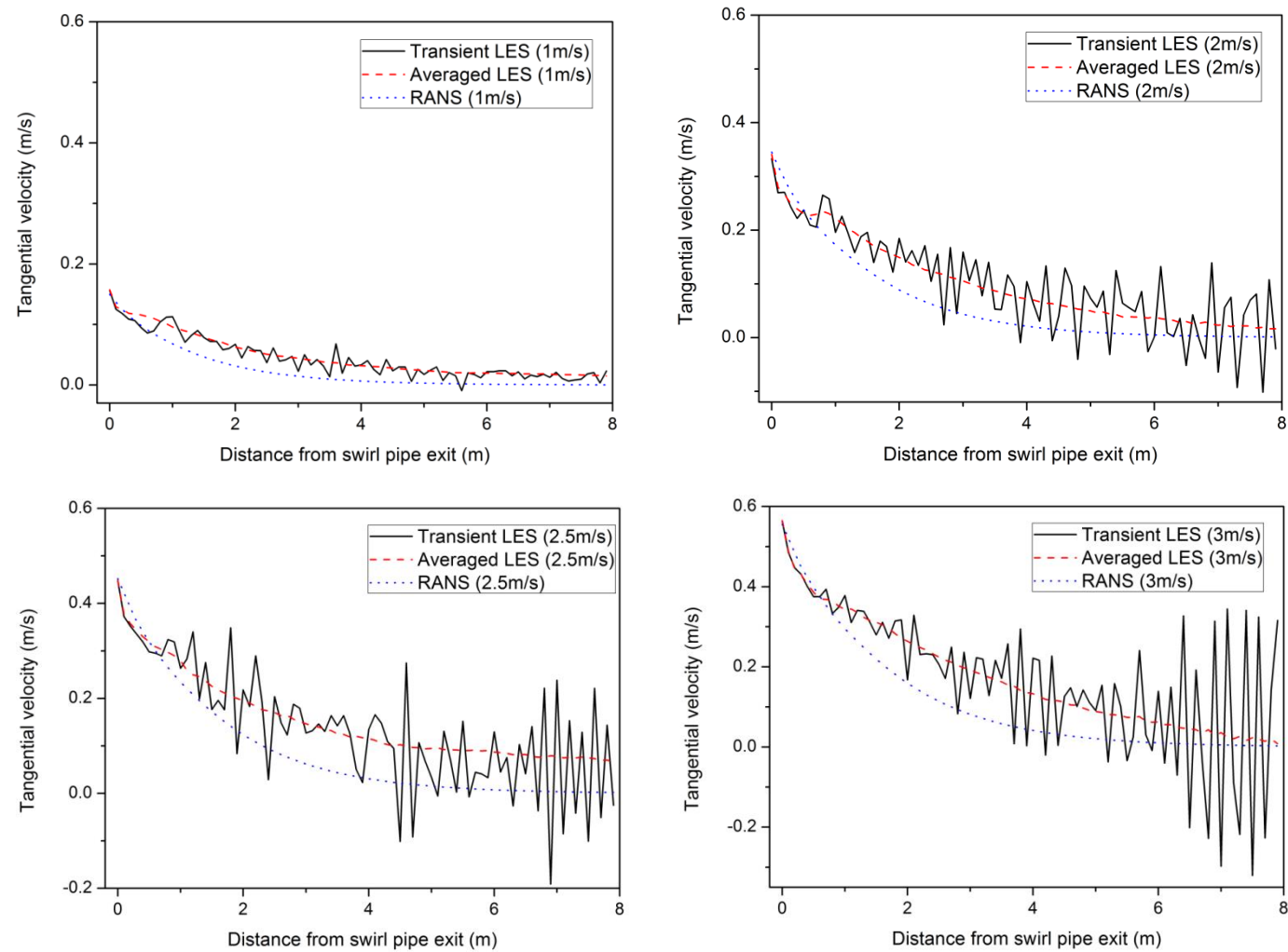


Figure 7.4.6 Tangential velocity variation downstream of swirl pipe exit for LES and RANS

7.4.4 Swirl Decay

Figure 7.4.7-7.4.11 present the swirl intensity calculated at the swirl pipe exit, and planes 2D, 4D, 6D and so on downstream of the swirl pipe for various inlet velocities using RANS, time averaged LES and transient LES. It is clear from the plots:

- The initial swirl intensity is almost identical for both RANS and LES with its value positively proportional to flow velocity (Reynold number).
- The swirl intensity decreases with increasing distance downstream of the swirl pipe for both RANS and LES. However, in LES, the swirl decays slower than RANS permitting the swirl effect to prevail for a longer distance at relatively stronger swirl intensity.
- The instantaneous swirl intensity obtained by LES shows fluctuation about the time averaged value with greater fluctuation spotted in cross-flow planes where the swirl effect is less dominant. This is especially true in flows with larger velocities (Reynold number).

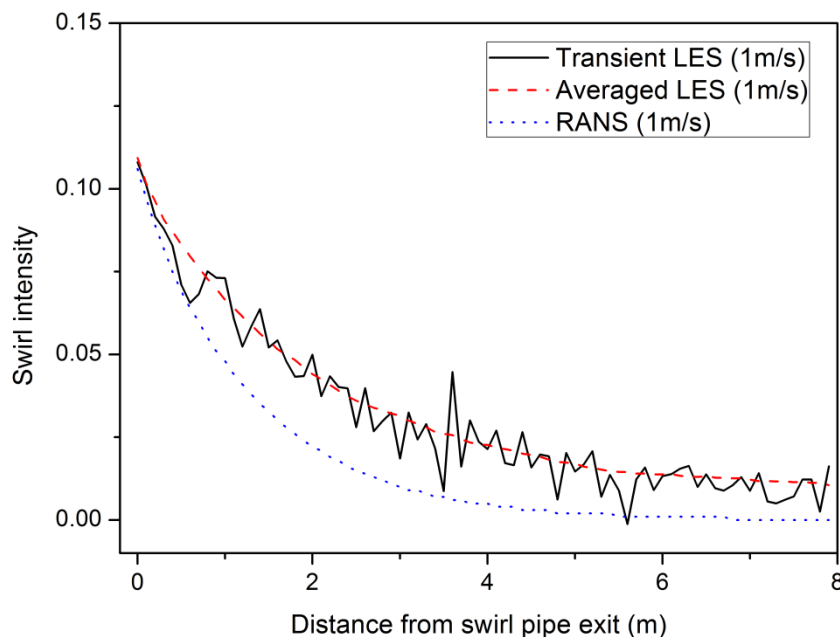


Figure 7.4.7 Swirl intensity variation downstream of swirl pipe exit for LES and RANS (1m/s inlet velocity)

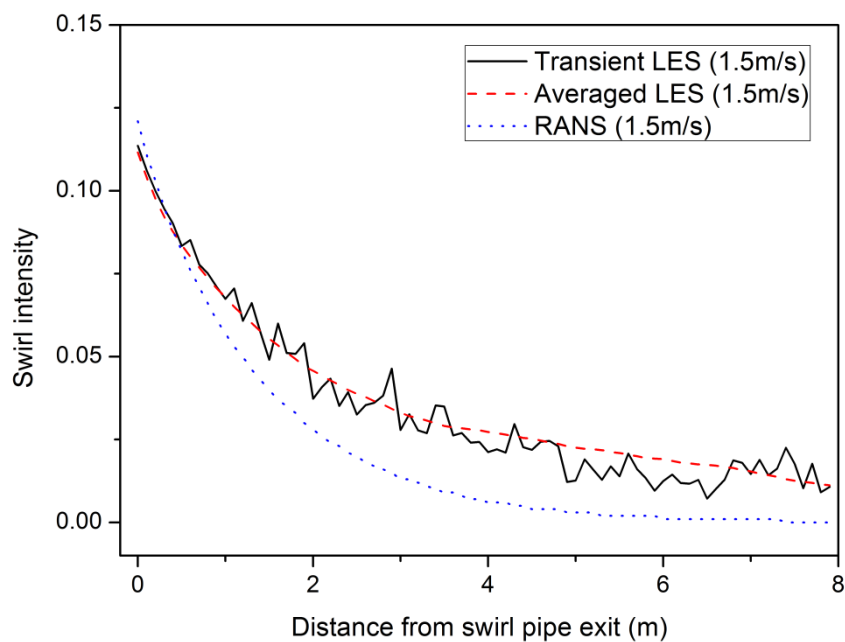


Figure 7.4.8 Swirl intensity variation downstream of swirl pipe exit for LES and RANS (1.5m/s inlet velocity)

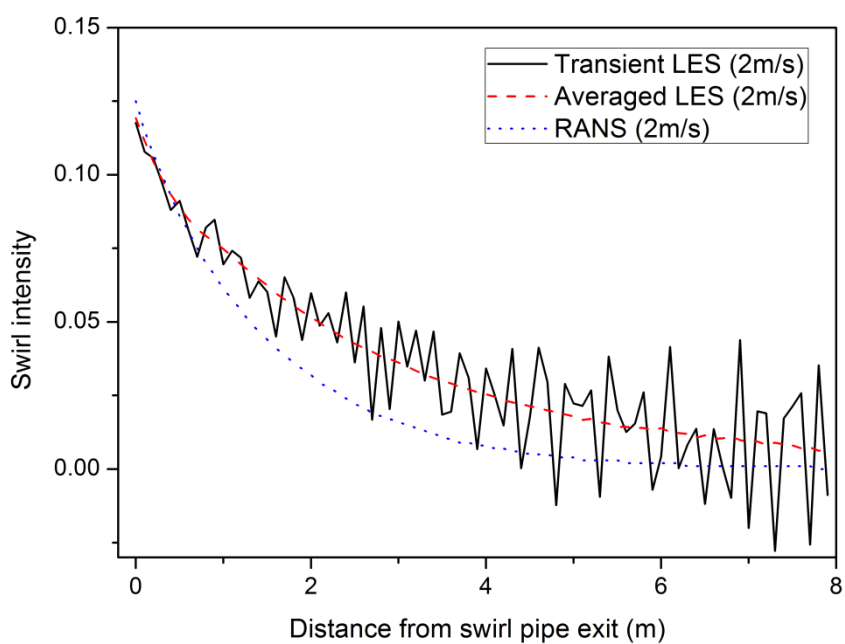


Figure 7.4.9 Swirl intensity variation downstream of swirl pipe exit for LES and RANS (2m/s inlet velocity)

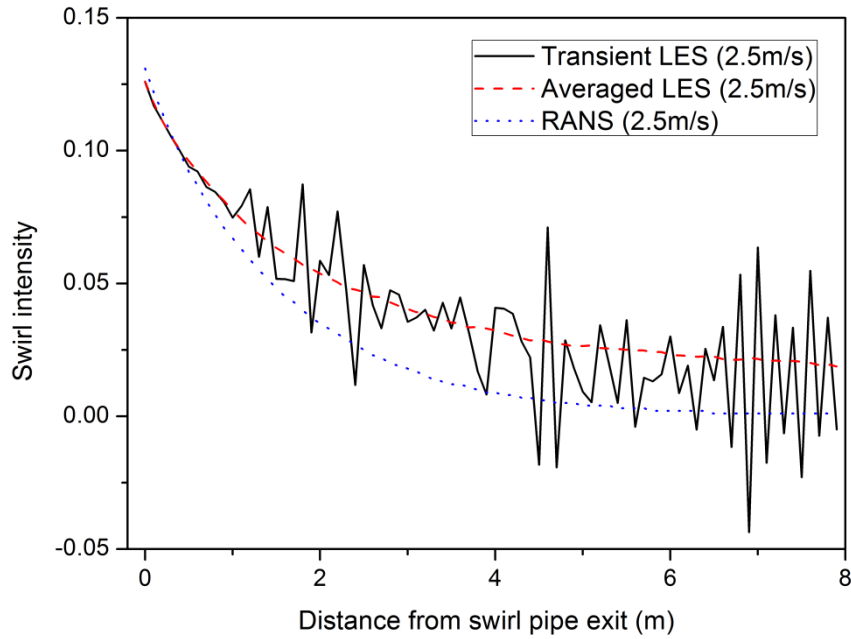


Figure 7.4.10 Swirl intensity variation downstream of swirl pipe exit for LES and RANS (2.5m/s inlet velocity)

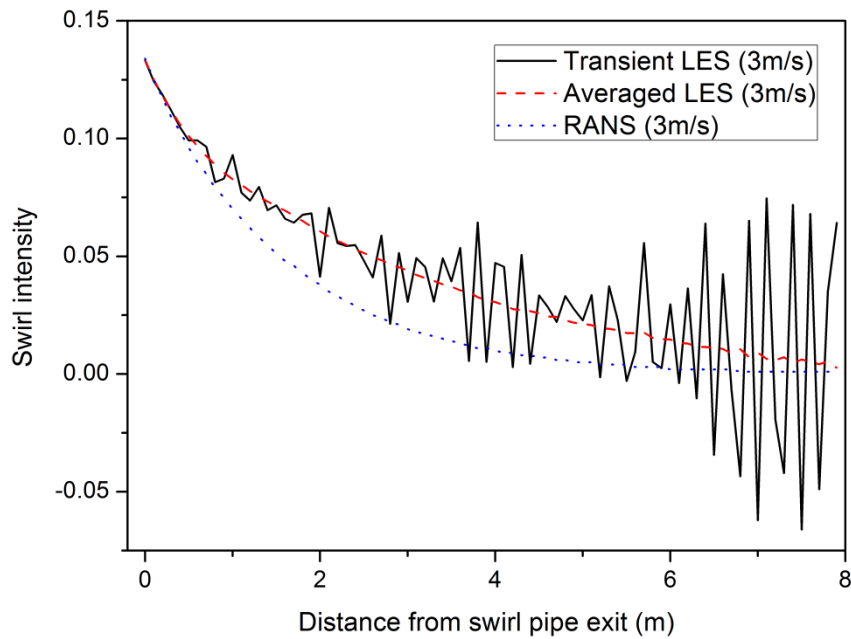


Figure 7.4.11 Swirl intensity variation downstream of swirl pipe exit for LES and RANS (3m/s inlet velocity)

Figure 7.4.12 demonstrates that the swirl decay rate predicted by LES (averaged value over 2 seconds) is in good agreement with exponential trend. The swirl decay rate is 0.019, 0.018, 0.018, 0.017 and 0.017 for flow velocity of

1m/s, 1.5m/s, 2m/s, 2.5m/s and 3m/s respectively. The swirl decay rate decreases with increasing velocity indicating that the application of the swirl pipe is more effective in flows with higher velocities. Compared with the corresponding RANS results of 0.040, 0.036, 0.035, 0.034 and 0.032, the swirl decay rate predicted by LES is smaller suggesting a more robust swirl flow.

For a hydraulically smooth pipe the friction factor can be approximated by the Blasius equation $f_D = \frac{0.3164}{Re^{0.25}}$ (valid for $Re=3 \times 10^3 \sim 1 \times 10^5$). The swirl decay rate is related to the friction factor f' as $0.90f'$, $0.94f'$, $1.01f'$, $1.02f'$ and $1.06f'$ respectively for 1m/s, 1.5m/s, 2m/s, 2.5m/s and 3m/s flow velocities. This swirl decay value is smaller compared to $\beta = [(1.49 \pm 0.07) \times f']$ (for $0 \leq S \leq 0.18$) suggested by Steenbergen and Voskamp (1998). However, this result is not entirely reliable as the Blasius equation is mainly applicable to non-swirling flows where the pipe friction factor is largely the same everywhere throughout the pipe. While in the case of swirl flow, there may be an uneven distribution of the friction factor due to the variation of flow regimes throughout the flow system. Secondly, it is not entirely understood what the surface roughness of the pipes were in the LES model. The approximation of the friction factor using Blasius equation may introduce further discrepancy between LES and the empirical equation.

Theoretically, the LES, based on spatial filtering, has the potential for improved accuracy when the resolution of the largest eddies is important as these eddies have the most energy and fluxes and are explicitly calculated, leaving only the small eddies, with little energy and fluxes to be modelled. Since the larger eddies in the turbulent swirling flow is inherently unsteady and three-dimensional, the LES is likely to be more accurate than the RANS.

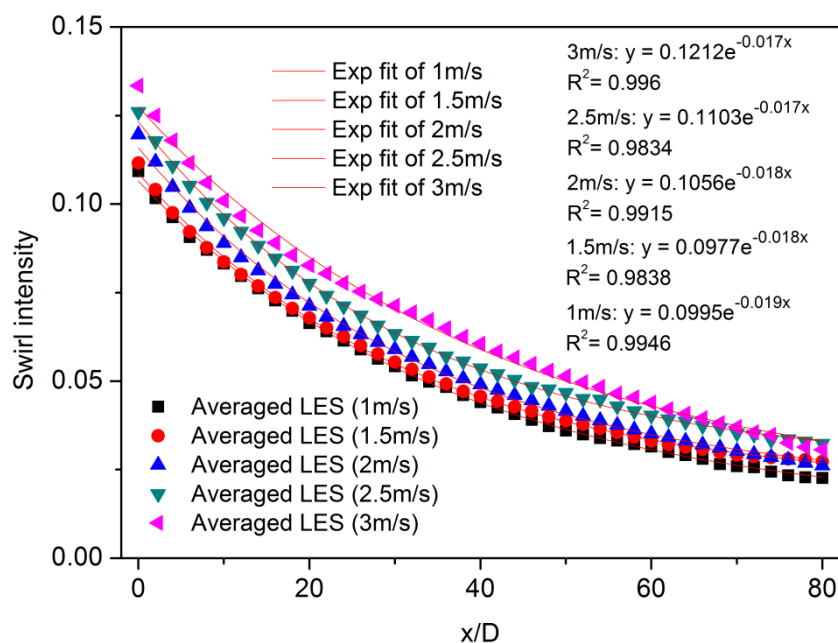


Figure 7.4.12 Swirl intensity decay trend downstream of swirl pipe exit obtained by LES for various inlet velocities

7.4.5 Wall Shear Stress

Figure 7.4.13 and 7.4.14 display the contours of instantaneous and time averaged wall shear stress exerted on the swirl pipe and circular pipe surfaces obtained by LES for inlet velocities of 1m/s, 1.5m/s, 2m/s, 2.5m/s and 3m/s from top to bottom. From the contours:

- It is clear the swirl pipe raises the wall shear stress on its internal surface which prevails in the downstream circular pipe with the increase in wall shear stress and its distance downstream proportional to the flow velocity (Reynolds number). The results indicate that the swirl pipe has a more significant effect in flows with higher velocities.
- Downstream of the swirl pipe, the wall shear stress distribution is not uniform but follows the spiral pattern of the swirl pipe. The four regions that experienced greatest wall shear stress extend helically about the circular pipe axis forming a four-stranded-rope distribution. The spiral distribution attributes to the four lobes of the swirl pipe and is the

extension of their effects on the circular pipe downstream.

- From the instantaneous contours shown in Figure 7.4.13, the spiral pattern of wall shear stress distribution stops being clear with increasing downstream distance and becomes chaotic in space and time. This indicates greater fluctuation of the flow in the duration that is further downstream of swirl pipe where the vortices dissipate and the swirl intensity becomes sufficiently weak.
- In the durations where the swirl intensity is zero or sufficiently small, there is still a wall shear stress increase due to the stronger instability of the flows and this increase of the wall shear stress prevails for some distance dependent on the flow velocity.
- Comparing the instantaneous and the time averaged contours, it seems the spiral pattern just downstream of the swirl pipe varies only slightly over time. The animations made during the solution of the LES also showed that the wall shear stress fluctuation just downstream of the swirl pipe is smaller than that further downstream, although the fluctuations do increase with increasing inlet velocities. This again suggests that the stronger swirl just downstream of the swirl pipe tends to stabilize or depress the fluctuation of the flow.
- It has been reported, the rotating flow will be stable if the angular momentum flux $\rho w r$ increases with r (solid body rotation) (Syred, 2006). Where the w is the tangential velocity at a specific radius r , m/s. As has been shown in Figure 6.3.4 the tangential velocity increases with r and the swirl gradually develops into a solid body type downstream of the swirl pipe. Therefore, the flow regime is relatively stable just downstream of the swirl pipe. This may explain why the wall shear stress distribution pattern stays relatively unchanged in the duration just downstream of the swirl pipe.

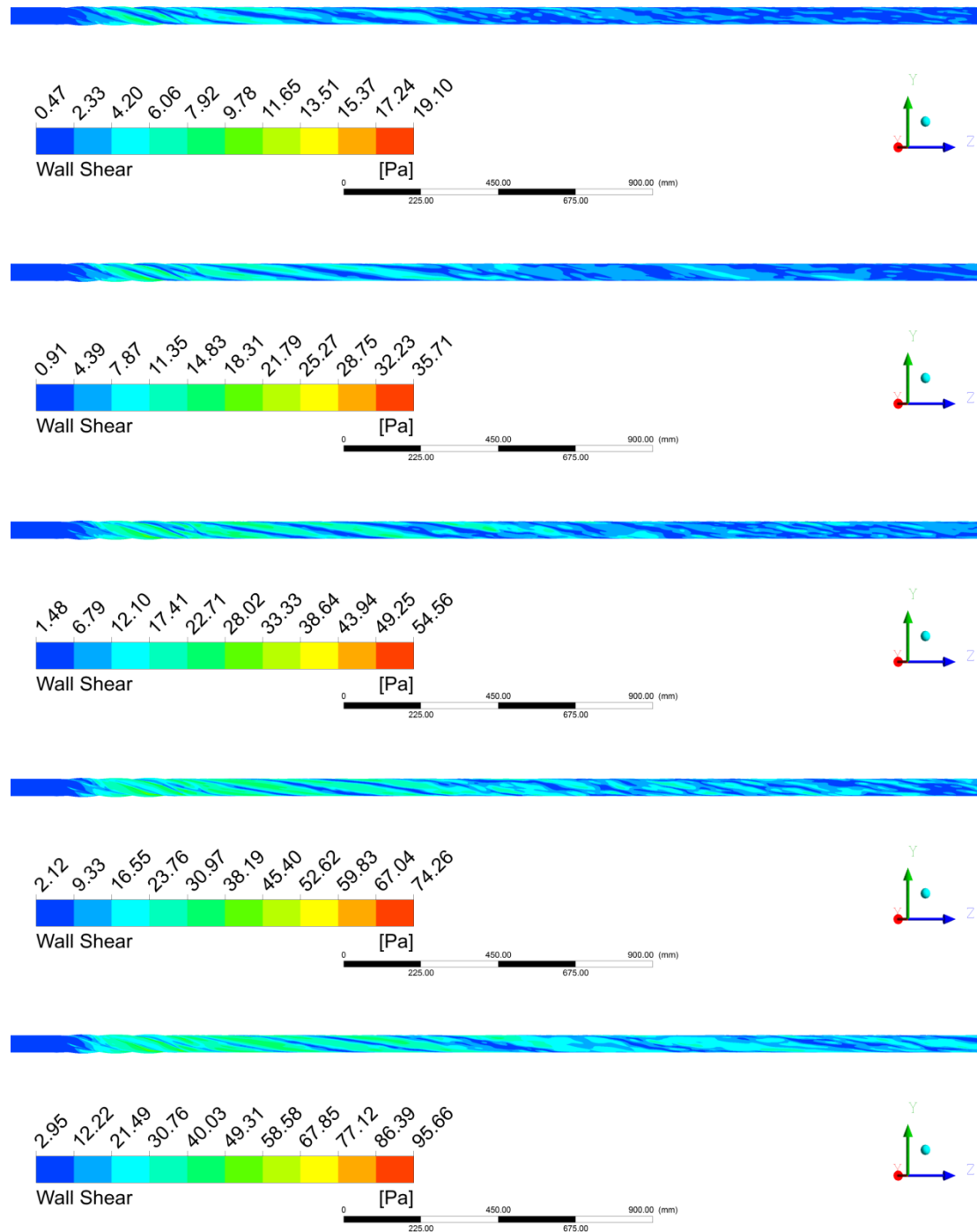


Figure 7.4.13 Contours of instantaneous wall shear stress in swirl pipe and circular pipes obtained by LES for inlet velocities of 1m/s, 1.5m/s, 2m/s, 2.5m/s, 3m/s respectively from top to bottom

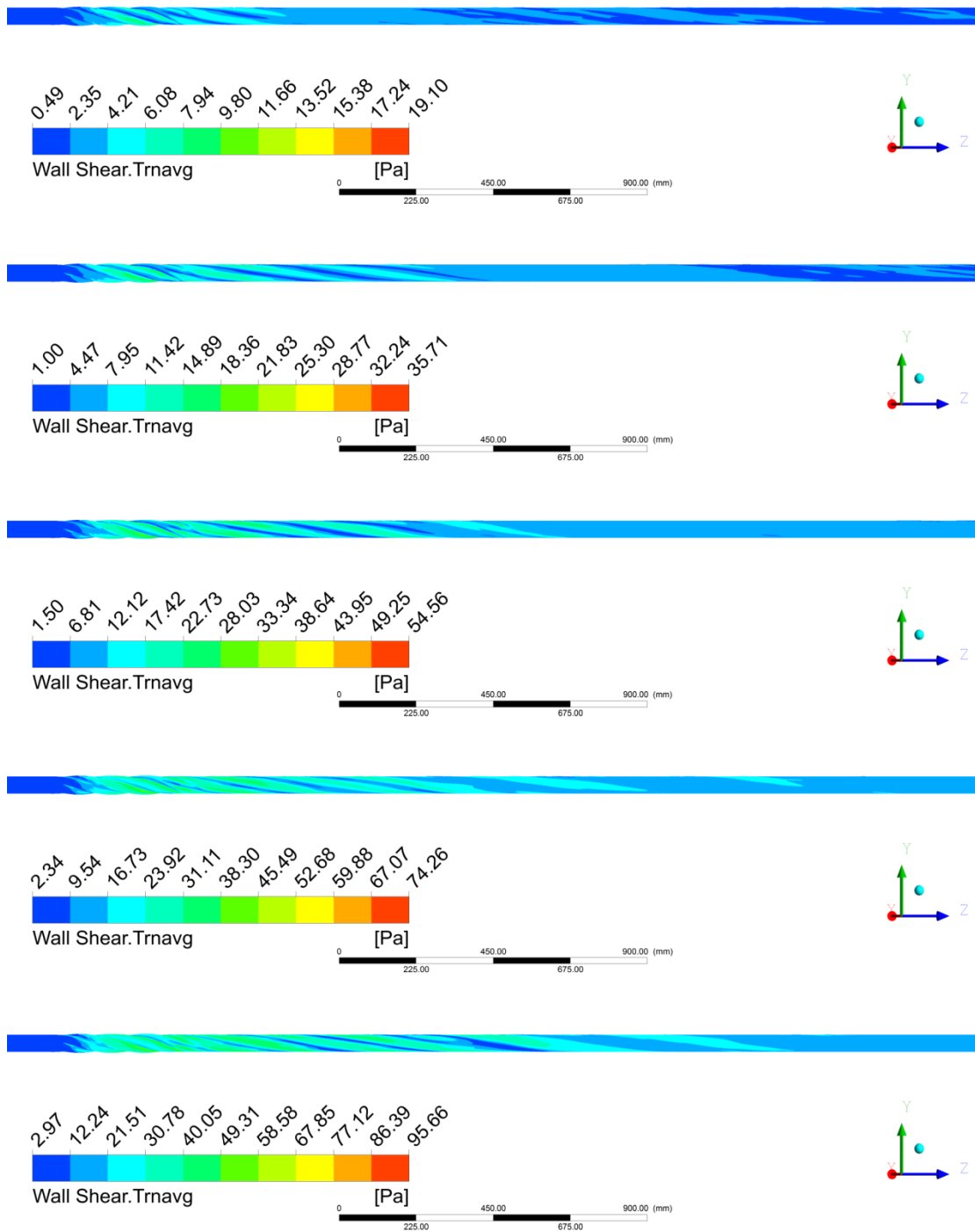


Figure 7.4.14 Contours of time averaged wall shear stress in swirl pipe and circular pipes obtained by LES for inlet velocities of 1m/s, 1.5m/s, 2m/s, 2.5m/s, 3m/s respectively from top to bottom

Figure 7.4.15 shows the vortex core regions inside the pipe system for various inlet velocities. The vortex cores demonstrated is an isosurface of the strength of swirling motion around a local axis, which are used to visualize and understand vortex regions. The isosurface of swirling strength were coloured by tangential velocity in order to show how it changes throughout the vortex core regions.

From the isosurface, four vortex cores can be identified which are formed inside the lobed area of the swirl pipe and precess rotationally about the curved axis in the centre of the lobes as illustrated in Figure 7.4.4. Getting out of the swirl pipe, the vortex cores precess for a distance following the same pattern as within the swirl pipe however decay and fade away with increasing downstream distance. Stronger vortices are observed in flows with larger inlet velocities which also tend to precess for a longer distance.

Figure 7.4.15 illustrates that greater tangential velocity (indicated by the red and yellow colours) appears in the four spiral regions between the four rotating vortex core regions and the pipe wall. This is because the flow between the rotating vortex core centres and the wall is squeezed, producing a considerable increase in tangential velocity (Froud et al., 1995, Huang and Yang, 2009). The tangential velocity (consequently swirl intensity) gives rise to a tangential wall shear stress. As has been concluded previously that the presence and variation of tangential wall shear stress is closely dependent on swirl intensity (tangential velocity), it is therefore understood why the increase of wall shear stress downstream of the swirl pipe forms a spiral pattern distribution.

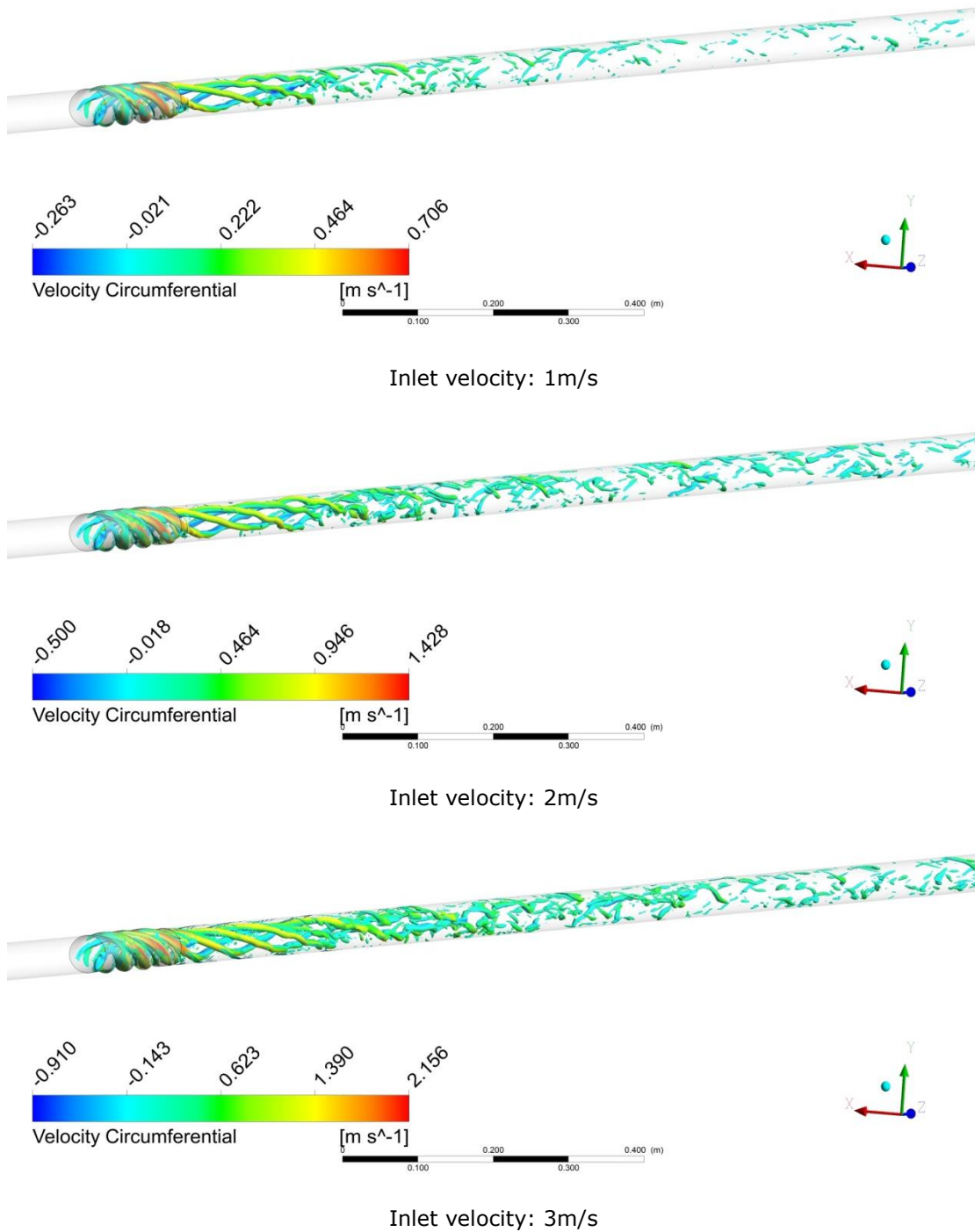


Figure 7.4.15 The four vortex core regions within swirl pipe and downstream circular pipe for inlet velocities of 1m/s, 2m/s and 3m/s respectively from top to bottom

Instantaneous and time averaged mean wall shear stress downstream of swirl pipe exit obtained by LES and the RANS results are presented in Figure 7.4.16. The figure demonstrates that, for both LES and RANS, there is a clear mean wall shear stress increase downstream of the swirl pipe with the increased value and the prevailing distance being larger for flows with faster velocities.

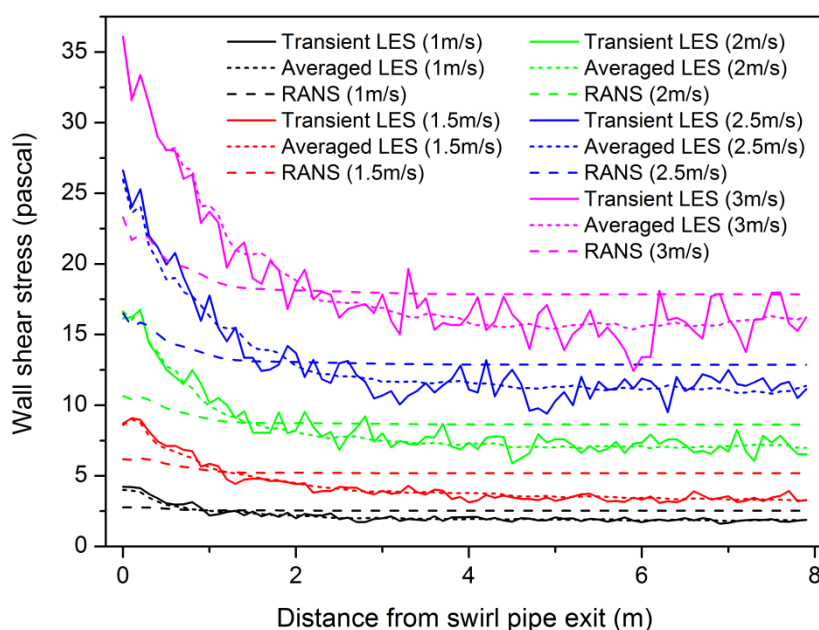


Figure 7.4.16 Wall shear stress variation downstream of swirl pipe exit obtained by LES and RANS for various inlet velocities

The LES gives greater wall shear stress prediction in the duration just downstream of the swirl pipe which also varies more swiftly along the circular pipe. Comparing to the wall shear stress value 1m prior to the outlet of the flow system (7m~8m in the x axis) where the time average wall shear stress value is relatively stable for all velocities, the initial wall shear stress just downstream of the swirl pipe increases by 54%(2.2 Pa), 61%(5.3 Pa), 57% (9.5Pa), 58%(15Pa) and 53%(20Pa) respectively for inlet velocities of 1m/s, 1.5m/s, 2m/s, 2.5m/s and 3m/s. The LES results suggest a more robust and dynamic swirl flow. While the RANS gives more conservative prediction with the initial wall shear stress just downstream of the swirl pipe being 35%, 36%, 36%, 28% and 31% lower than the LES results for inlet velocities of 3m/s, 2.5m/s, 2m/s, 1.5m/s and 1m/s respectively.

The transient LES result demonstrates that the wall shear stress fluctuates about the time averaged value as it decays, showing peaks and valleys along the stream-wise direction. The amplitude of the fluctuation increases with increasing flow velocity, indicating stronger instability of the flow. For a given velocity, especially for larger ones, the wall shear stress has a more pronounced fluctuation further downstream of the swirl pipe. This is more clearly illustrated in Figure 7.4.17 the wall shear stress variation over time (2s) at circumferences of the swirl pipe exit, 0.4m, 0.8m, 1.6m, 3.2m, 4.8m and 6.4m downstream of the swirl pipe. Figure 7.4.17 shows that the mean wall shear stress at circumferences just downstream of the swirl pipe (swirl pipe outlet, 0.4m and 0.8m downstream) is large but stays relatively steady over time. However, as the wall shear stress decreases with increasing downstream distance, the circumferences further downstream (1.6m, 3.2m, 1.8m and 6.4m downstream) start to experience stronger fluctuation in wall shear stress.

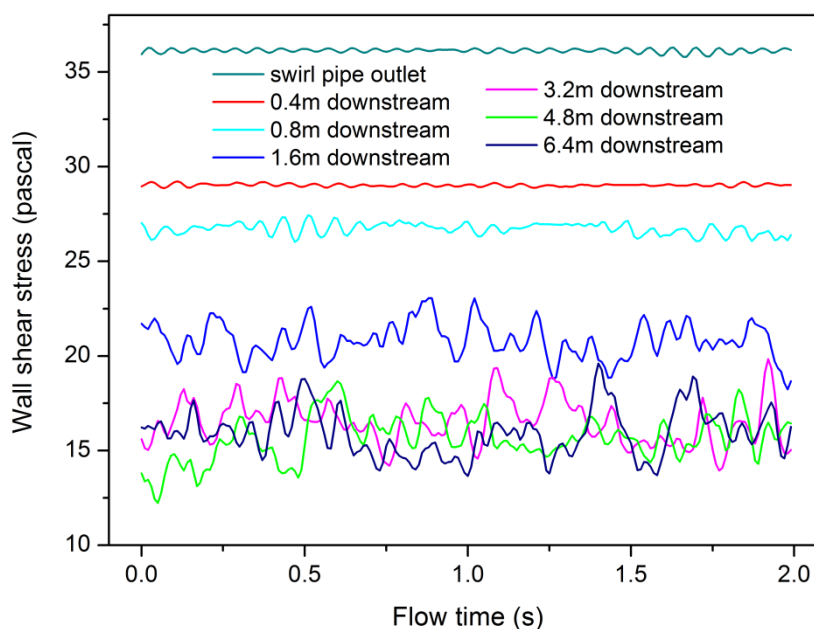


Figure 7.4.17 wall shear stress variation over time at circumferences of the swirl pipe exit and its downstream (3m/s inlet velocity)

The averaged wall shear stress at circumferences 1m and 0.5m prior to the swirl pipe, the swirl pipe exit, 0.4m, 0.8m, 1.2m, 1.6m, 2m, 2.4m ... and 7.6m after the swirl pipe were monitored and recorded every 0.01s over 2s as the LES solution was proceeding. At each circumference, the 200 wall shear stress data were normalized by dividing their mean. This is to eliminate the effects of different wall shear stress levels at different circumferences on the fluctuation rates. The normalized fluctuation rate of the wall shear stress was calculated by

$$\text{Normalized fluctuation rate} = \left[\frac{1}{N-1} \sum_{i=1}^N (\tau'_{wi} - \overline{\tau'_w})^2 \right]^{1/2} \quad (7.4.1)$$

where the τ'_{wi} is the normalized wall shear stress and the $\overline{\tau'_w}$ is its mean. The equation is actually the standard deviation of the normalized data. A similar equation was used by Su et al. (2010). However no normalization was applied as the flow they studied was non-swirling with no level difference of wall shear stress over circumferences.

The variation of the normalized wall shear stress fluctuation rate throughout the system for various inlet velocities is depicted in Figure 7.4.18 to 7.4.22. This demonstrates that the swirling flow downstream of the swirl pipe generally gives rise to stronger fluctuations in the wall shear stress than the non-swirling flow prior to the swirl pipe. Just downstream of the swirl pipe, the fluctuation rate is relatively low (as the flow tends to be stabilized by the stronger swirl in this duration) which increases with increasing downstream distance and then maintains at a larger fluctuation level up to the outlet of the circular pipe though experiencing ups and downs. It is not clear how long the fluctuation would last after getting out of the outlet due to the limitation of the length of the simulation domain. However it should be expected the stronger flow fluctuation would prevail for some further distance thereafter especially for flows with larger inlet velocities.

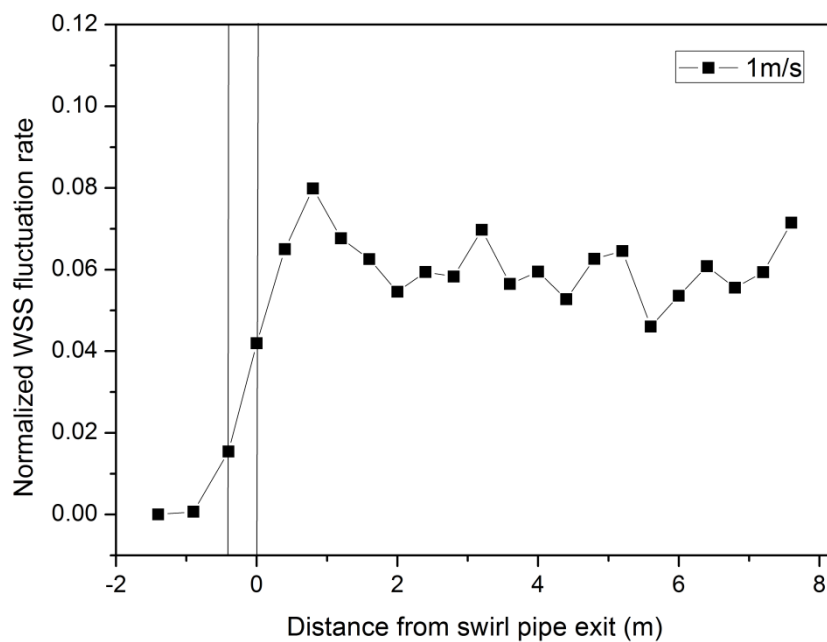


Figure 7.4.18 Variation of normalized wall shear stress fluctuation rate in swirl and circular pipes (1m/s inlet velocity)

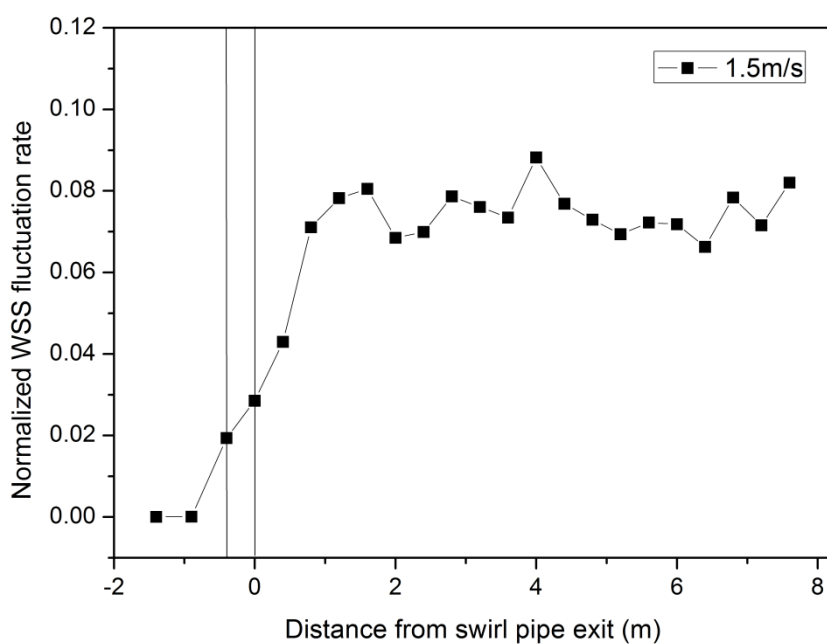


Figure 7.4.19 Variation of normalized wall shear stress fluctuation rate in swirl and circular pipes (1.5m/s inlet velocity)

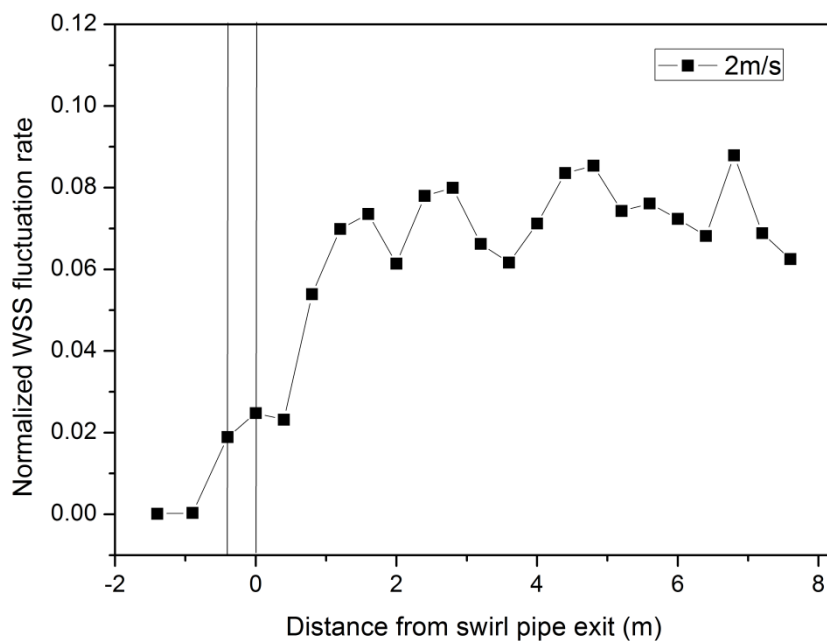


Figure 7.4.20 Variation of normalized wall shear stress fluctuation rate in swirl and circular pipes (2m/s inlet velocity)

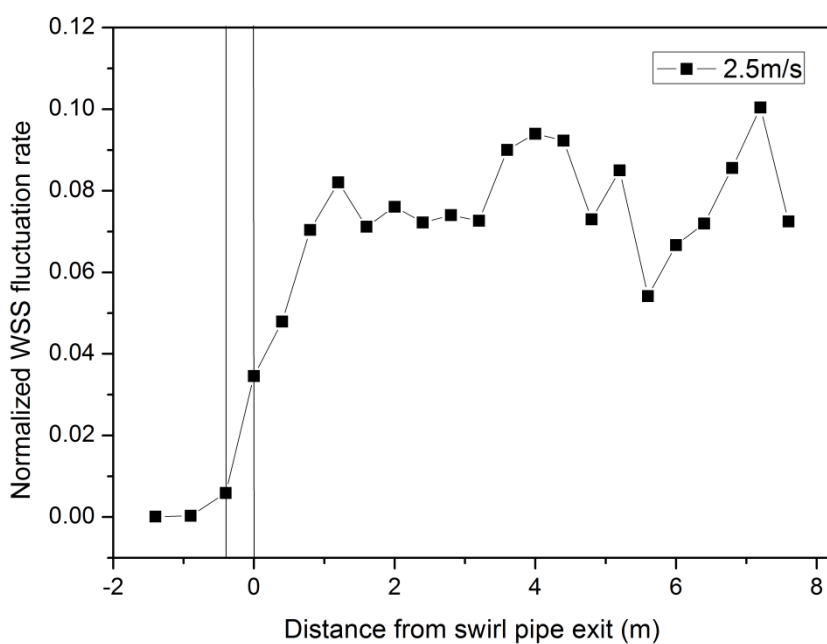


Figure 7.4.21 Variation of normalized wall shear stress fluctuation rate in swirl and circular pipes (2.5m/s inlet velocity)

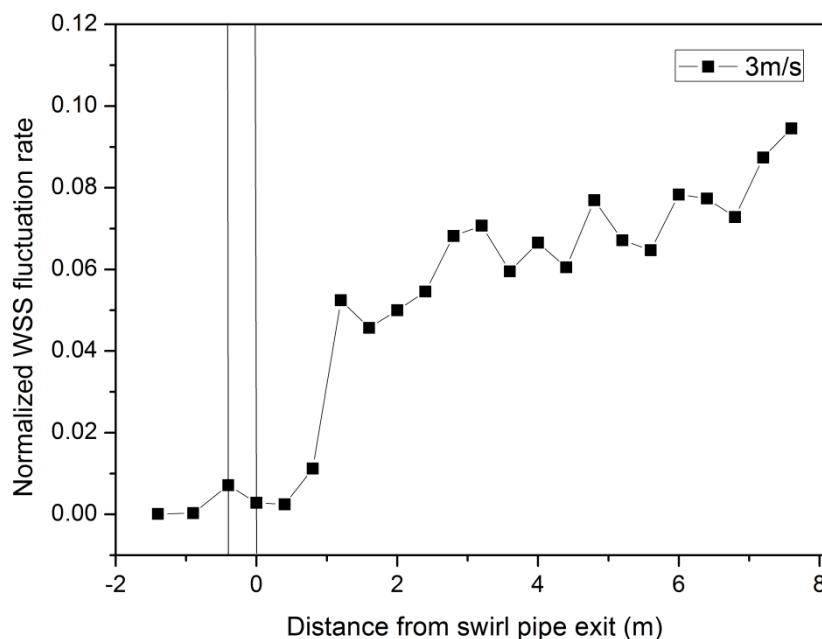


Figure 7.4.22 Variation of normalized wall shear stress fluctuation rate in swirl and circular pipes (3m/s inlet velocity)

It is well documented that the wall shear stress is a measure of the mechanical action of fluid flow acting on the soil on the internal pipe surface (Jensen et al., 2007). And the mean wall shear stress is especially relevant as a measure of cleaning efficiency in straight pipes, large parts of pumps, valves and so on (Paz et al., 2013, PathogenCombat, 2011).

Some studies showed that the fluctuation in the value of the wall shear stress was of major importance for CIP processes. Bari and Veale (2012) claimed that a wall shear stress as low as 0.15 Pa can be cleanable for their application given a high fluctuation level. L  lievre et al. (2002) reported the effect of the fluctuation rate on bacterial removal, indicating that some low wall shear stress zones could be considered as cleanable given that in these areas, a high level of turbulence, hence a high fluctuation rate, was observed. They therefore suggested that to predict cleaning, it is necessary to take into account not only the mean local wall shear stress, but also its fluctuation rate. Jensen et al. (2005) suggested that a combination of the mean wall shear stress and the fluctuating part of the wall shear stress can be used for evaluating cleaning properties.

The LES results showed that, without increasing the overall inlet velocity, the swirl pipe increases mean wall shear stress downstream and the increase prevails for a distance as the swirl decays. Within this distance, the swirl pipe is expected to improve the cleaning efficiency of Clean-In-Place procedures in closed processing systems without greatly increasing energy consumption, thus potentially reducing time and cost for the company.

While in the further downstream duration where the swirl effect is less dominant and the wall shear stress increase is less significant, the flow experiences a high level of turbulence, resulting in a high fluctuation rate in the wall shear stress. The internal pipe surface during this phase could also be considered cleanable as local enhancement of turbulence intensity is reported to improve CIP efficiency in closed processing systems (PathogenCombat, 2011). Therefore the swirl pipe retains the potential in CIP enhancement at the further downstream duration by local introduction of flow disturbance, consequently high wall shear stress fluctuation rate.

In this section, with the help of LES, which is an inherent unsteady method, the mean and fluctuation rate of the wall shear stress downstream of the swirl pipe was explored. The LES presented a more robust and promising swirling flow. The beneficial effects of swirl pipe were identified not only in increasing the mean wall shear stress just downstream but also by inducing a high fluctuation rate of the wall shear stress in further downstream where the increase in mean wall shear stress is less significant. As both of these factors contribute to process equipment cleaning, it is expected the local application of the swirl pipe could enhance CIP procedures in closed processing systems over a longer downstream distance than previously believed.

7.5 Conclusions

In this chapter, a LES model with WMLES as Sub-Grid-Scale model was established with the aim of understanding the unsteady property of the swirl flow induced by the swirl pipe. The time averaged and unsteady property of flow variables was examined. The general variation trend of the flow parameters was consistent with the RANS. However, some new findings have been noted:

- Four vortex core regions were identified forming inside the lobes of the swirl pipe which precess spirally about the circular pipe axis for some distance and then dissipate.
- Compared to RANS, the LES approach underestimate (18%-23% lower) the overall pressure drop within the flow system.
- The initial tangential velocities predicted by LES were found almost identical with the RANS however they decrease more slowly, prevailing for a longer downstream distance at a relatively larger value.
- The instantaneous tangential velocity was found fluctuating about the time averaged LES value with a greater fluctuation in the tangential velocity observed in the cross-flow planes that are further downstream of the swirl pipe where the swirl effect is less dominant.
- In the LES model the swirl was better retained as a smaller swirl decay rate than RANS was predicted, suggesting a more robust and vigorous swirl flow.
- The fluctuation level of the swirl intensity increased as the swirl decayed. It may suggest that the flow subjected to strong swirl tends to be more stable.
- The increase of the wall shear stress within the swirl pipe and the downstream circular pipe formed a spiral pattern distribution. This may be due to the flow between the rotating vortex core centres and the wall being squeezed, producing a considerable increase in tangential velocity

which consequently gives rise to a tangential wall shear stress.

- The LES predicted a greater mean wall shear stress just downstream of the swirl pipe which also varies more swiftly along the circular pipe.
- The normalized wall shear stress fluctuation rate with time was calculated and showed that further downstream the swirl effect is less dominant and the wall shear stress increase is less significant but the flow experiences a high level of turbulence, resulting in a high fluctuation rate in the wall shear stress.
- As the increase of either the mean or the fluctuation rates of the wall shear stress contribute to pipeline cleaning, it is expected the local application of the swirl pipe could be a promising approach to enhance the CIP procedures in closed processing systems.

CHAPTER 8: VALIDATION OF THE COMPUTATIONAL FLUID DYNAMICS RESULTS

8.1 Introduction

This chapter concerns the experimental validation of the simulation results, mainly the pressure drop and wall shear stress obtained in chapter 6 and 7. Pressure drop measurement is relatively easier to implement in flow measurement and is useful to validate some aspects of a flow field. The wall shear stress is the governing hydrodynamic factor influencing CIP efficiency in a closed processing system and therefore it is important to be measured.

The pressure drops across the optimised swirl pipe in various flow velocities were measured employing a pair of pressure transmitters. The experimental results were compared to the CFD models and the pressure drops across previously used swirl induction pipes.

The wall shear stresses in the swirl flows were measured using a fast response Constant Temperature Anemometer (CTA) system comprising a Glue-on hot-film probe and a MiniCTA 54T42. The hot-film sensor is capable of obtaining the mean wall shear stress and its fluctuation rate. Before measurement, the hot-film probe was calibrated in cylindrical pipe flows where the wall shear stress is directly proportional to the streamwise pressure gradient.

8.2 Dealing with Errors and Uncertainties in CFD

At the end of a simulation, the user needs to make a judgement whether the results are “good enough”. In estimating the trust and confidence in CFD modelling, the definitions of error and uncertainty have been widely accepted

(AIAA, 1998, Oberkampf and Trucano, 2002, H.K.Versteeg and W.Malalasekera, 2010).

- **Error:** a recognisable deficiency in a CFD model that is not caused by lack of knowledge. This includes:
 - Numerical errors - roundoff errors, iterative errors, discretisation errors
 - Coding errors – mistakes or ‘bugs’ of the software.
 - User error – human errors through incorrect use of the software.
- **Uncertainty:** A potential deficiency in a model that is caused by a lack of knowledge. This is caused by:
 - Input uncertainty – inaccuracies due to limited information or approximate representation of geometry, boundary conditions, material properties, etc.
 - Physical model uncertainty – inconsistencies between real flows and CFD due to inadequate representation of physical or chemical processes or due to simplifying assumptions in the modelling process (e.g. treated as incompressible or steady flow).

Among them, the user errors can be reduced or avoided to a large extent through appropriate training and experience. The reduction of coding errors relies on the software engineering/quality assurance.

For the errors and uncertainty that are unavoidable in CFD modelling, methods were developed to quantify the level of confidence in the CFD results. This involves the process of verification and validation (H.K.Versteeg and W.Malalasekera, 2010):

- **Verification:** the process of determining that a model implementation accurately represents the developer’s conceptual description of the

model and the solution to the model. Put it briefly 'solving the equations right'. This process quantifies the errors.

- **Validation:** the process of determining the degree to which a model is an accurate representation of the real world from the viewpoint of the intended uses of the model. In short it is 'solving the right equations'. This process quantifies the uncertainty.

In the modelling of swirl flow induced by the swirl pipe, efforts have been made to minimize the 'errors' in terms of iterative convergence and discretisation. This includes:

- Second order accuracy applied to all viscous terms
- Global residuals control of at least four orders of magnitude
- Structured hexahedron mesh to ensure minimal numerical diffusion
- Mesh adaption for wall functions (for RANS)
- Mesh independence test
- Second order accuracy for temporal discretization (for LES)
- Sufficiently small time step size (for LES)

In the reduction of possible input uncertainty on the boundary conditions, considerations have been taken on:

- Extending the development section of the domain so that the inlet boundary is sufficiently far from the swirl pipe and will not affect the flow in this region.
- Including the effects of gravity on flow.
- Specifying surface roughness of the swirl pipe and cylindrical pipe with the same value as the experimental rig in the RANS model.
- Generating an instantaneous velocity field out of a steady state RANS model as the initial condition for the LES.

In the case of quantitative assessment of physical model uncertainty, it requires comparison of the CFD results with high-quality experimental results (Oberkampf and Trucano, 2002). Thus the ultimate test of a CFD model is a comparison between its output and experimental data. If the difference between computed and experimental values looks sufficiently small the CFD model is considered to be validated. For this reason, a hydraulic rig was designed and established to validate the CFD results.

8.3 Hydraulic Rig Layout

The hydraulic rig is designed to validate the numerical model by measuring the following parameters in flows with different velocities in the horizontal direction:

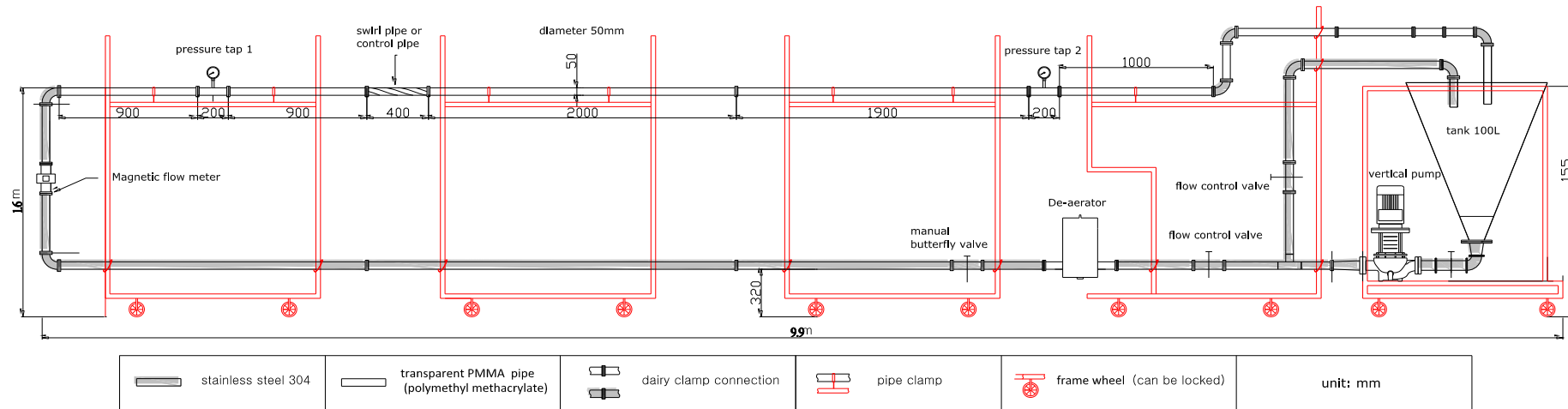
- Pressure drop due to the presence of the swirl pipe (using pressure transmitters).
- Mean wall shear stress downstream of the swirl pipe (using a Hot Film probe).
- Fluctuation rate of wall shear stress downstream of the swirl pipe (using a Hot Film probe).

The layout and dimension of the rig is shown in Figure 8.3.1. All the experimental work was carried out on the top horizontal section of the rig.

- The hydraulic rig is composed of sanitary stainless steel pipes, transparent Perspex pipes, a swirl pipe, bends, valves, a de-aerator, tank, pump, frequency convertor and sensors with the purpose of circulating water at various velocities.
- The internal pipe diameter of both stainless steel and Perspex pipes is 50 mm. The tank has a capacity of 100L and is filled with 80L water. The vertical centrifugal pump has a capacity of $30\text{m}^3/\text{h}$ with its power being

3kw.

- The flow rates are controlled by adjusting the frequency convertor.
- The magnetic flow meter is installed in the vertical section of the rig which has a distance of $8D$ from the upper and lower bends. It covers the range of $0\sim 30\text{m}^3/\text{h}$ with an accuracy of at least 0.2%.
- The two pressure transmitters have a measuring range of 40kpa (400mbar) and accuracy of 40pa ($\pm 0.1\%$). Pressure transmitter 1 is installed 1m away from the bend to avoid bend effects and 1m prior to the swirl pipe to avoid swirl effects. Pressure transmitter 2 is mounted 4m downstream of the swirl pipe, where swirl effect should be fairly small.
- The hot film anemometer will be mounted in the positions downstream of the swirl pipe to measure mean wall shear stress and its fluctuation.
- The current (4-20mA) induced by the magnetic flow meter and the pressure transmitters are fed to a PC through a Squirrel Data Logger.



Schematic diagram of the hydraulic rig



Figure 8.3.1 Schematic diagram and layout of the experimental rig

8.4 Producing Swirl Pipe by Investment Casting

Stainless steel optimised swirl pipe was made for experimentation using an Investment Casting method. The Investment Casting is also known as the lost wax process. It is one of the oldest manufacturing processes by which complex shapes can be made with high accuracy. Connectors were designed for the two ends of the swirl pipe so that commercially available dairy clamps can be used to connect it with the transparent Perspex pipes. The drawings of the swirl pipe for investment casting are detailed in Appendix 8.1.

The process in developing the stainless steel swirl pipe is summarized as below:

- **Pattern production**

The process begins with production of one-piece heat-disposable patterns of swirl pipe. These patterns are made of wax adopting a 3D printing technique, which have the exact geometry of the required swirl pipe, but can be made slightly larger in order to compensate the volumetric shrinkage during the solidification of the stainless steel in the ceramic mould.

- **Pattern assembly**

The patterns are fastened onto runners which are attached to the pouring cup. The patterns, runners and pouring cups comprise the cluster or tree, which is used to produce the ceramic mould.

- **Producing ceramic shell mould**

In this process the entire cluster is dipped into ceramic slurry, drained, and then coated with ceramic sand. After drying, this process is repeated for seven or eight times until a self-supporting shell is formed.

- **Removing the wax**

The coated cluster is positioned in a high temperature furnace where the

wax pattern melts and runs out through the gates, runners and pouring cup. This leaves a ceramic shell containing the cavity of the desired casting shape of the swirl pipe.

- **Casting**

The ceramic shell moulds are fired to burn out the traces of pattern material (wax) and to preheat the moulds in preparation for casting. The hot moulds may be poured using static pressure of the molten metal heat or with assistance of vacuum, pressure and/or centrifugal force. This enables production of the trickiest details of the original wax pattern of the swirl pipe.

- **Cleaning**

After the poured moulds have cooled, the mould material is removed from the casting cluster by mechanical vibration, abrasive blasting and chemical cleaning. The individual castings are then removed from the cluster.

- **Machining and finishing**

The dairy clamp connectors of the casting swirl pipe are then polished by machining; the surface is treated with sandblasting.

Figure 8.4.1 demonstrates the technological process of manufacturing the optimised swirl pipe.

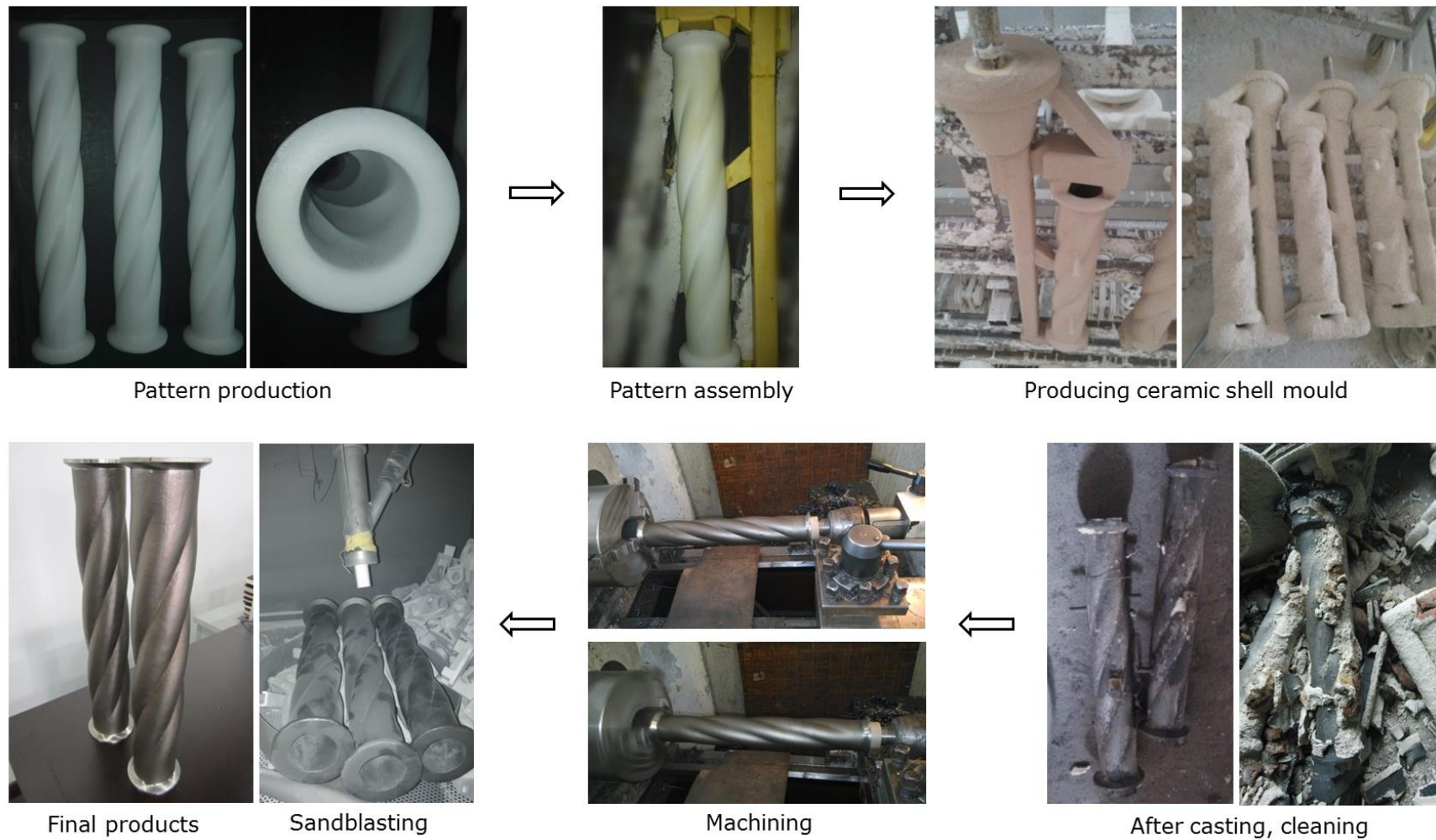


Figure 8.4.1 Demonstration of the investment casting process for optimised swirl pipe

8.5 Pressure Drop Validation

8.5.1 Pressure Drop Measurement

The normal procedure for measuring pressure drop is to measure the static pressure at the wall in the upstream and downstream pipe. This is complicated in swirl flows induced by the swirl pipe which:

- Leads to non-equilibrium pressure distribution in the cross-sectional flow planes downstream.
- Causes the static pressure at the wall to be higher than the cross-sectional average (KRISHNA, 2009).
- Gives rise to dynamic pressure that is stored in the swirling motion (KRISHNA, 2009).

In order to avoid the swirl effect on pressure measurement, the pressure tapping 1 was moved to 1m prior to the swirl pipe and pressure tapping 2 was positioned 4m downstream of the swirl pipe. A pair of pressure transmitters, as shown in Figure 8.5.1b, with a measuring range of 0-40kPa and accuracy of $\pm 0.1\%$ was used to measure the pressure drop between pressure tapping one and pressure tapping two ($L=5.4\text{m}$ including swirl pipe or control pipe). The flow rates were controlled by adjusting the frequency convertor which controls the rotating speed of the motor of the pump consequently the mass flow rate. Flow rates were monitored by a magnetic flow meter, as shown in Figure 8.5.1c, with an accuracy of 0.2%. The pressure transmitters and magnetic flow meter have been calibrated by the manufacturer (Endress+Hauser) before delivery.

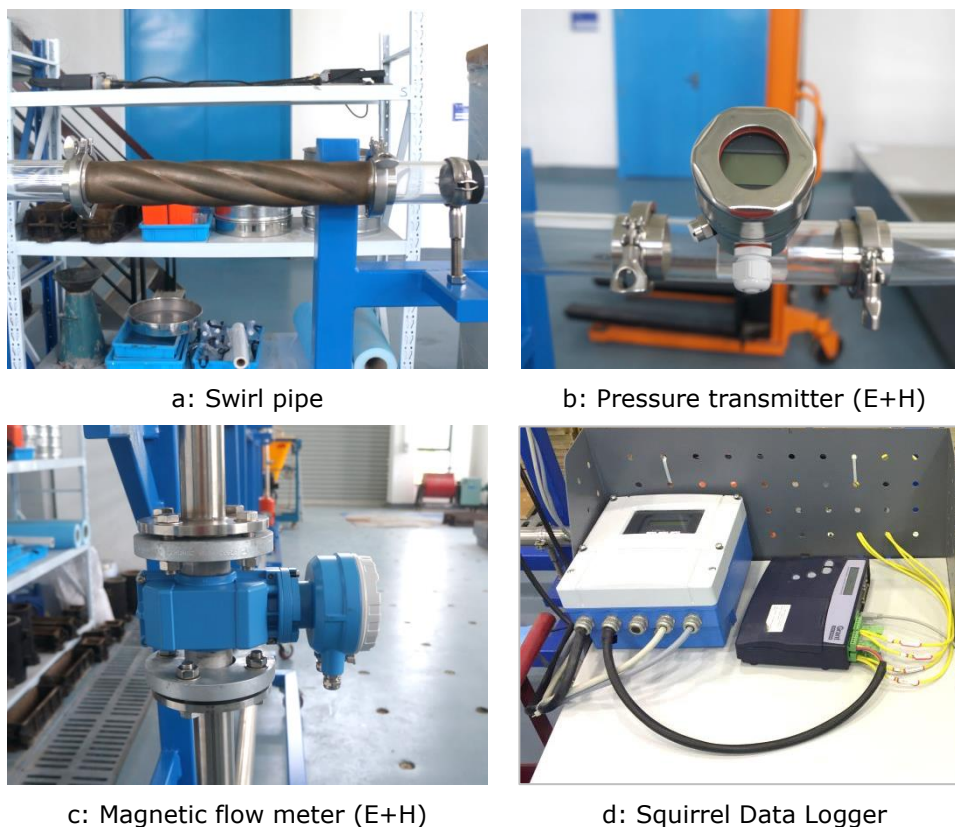


Figure 8.5.1 Swirl pipe, pressure transmitter, magnetic flow meter and squirrel data logger

The baseline velocities against which the pressure drop measurements were performed are listed in Table 8.5.1. The standard 4-20mA current induced by the pressure transmitters and the magnetic flow meter were fed to a PC with the help of a Squirrel Data Logger (Figure 8.5.1d) where the analog signals were converted into digital signals for recognition by the PC. The data logger has a sampling interval of 1s and readings are stored every logging interval. Therefore 60 readings of flow rate and static pressure values can be acquired per minute.

Table 8.5.1 Flow velocities at which pressure drop measurements were performed

Velocity (m/s)	Mass flow rate (m ³ /h)	Re
1.00	7.065	49761
1.25	8.831	62201
1.50	10.598	74641
1.75	12.364	87081
2.00	14.130	99521
2.25	15.896	111962
2.50	17.663	124402

The general measurement procedures were as below:

- 1) Install swirl pipe on the rig. Carry out zero point correction for the pressure transmitters if their initial readings were not zero. This is to correct the pressure resulting from the orientation of the device.
- 2) Turn on the pump; adjust frequency convertor while observing the mass flow rate monitor to obtain a required velocity, 1m/s ($7.065\text{m}^3/\text{h}$).
- 3) Wait for the flow rate reading to stabilize, log readings for pressure at pressure tapping 1 and 2, and the mass flow rate. The logging lasts for 5 minutes, therefore approximately 300 reading were collected for each sensor.
- 4) Adjust the frequency convertor to obtain a velocity of 1.25m/s ($8.831\text{m}^3/\text{h}$); repeat step 3) to log data.
- 5) Repeat step 4) up to a velocity of 2.5m/s. It was found at higher velocities that the de-aerator could not sufficiently remove bubbles, therefore velocities higher than 2.5m/s were not attempted.
- 6) Stop the pump; and reproduce another two sets of experiments by repeating step 1) to 5).

In order to calculate the pressure drop across the 400mm length swirl pipe only, pressure drops in cylindrical pipes were measured as well. A similar procedure was used as described above, however the swirl pipe was replaced by a 0.4m length transparent cylindrical Perspex control pipe.

8.5.2 Pressure Drop in Swirl Flow (1m cylindrical+0.4m swirl pipe+4m cylindrical)

At each velocity, the mean and standard deviation of the approximately 300 readings of flow velocity and pressure drop were calculated with the results for the three tests listed in Table 8.5.2.

Table 8.5.2 Pressure drop across 1m cylindrical+0.4m swirl pipe+4m cylindrical pipe for various velocities

Test 1				Test 2				Test 3			
Velocity (m/s)	S.D. of velocity	Pressure drop (Pascal)	S.D. of pressure drop	Velocity (m/s)	S.D. of velocity	Pressure drop (Pascal)	S.D. of pressure drop	Velocity (m/s)	S.D. of velocity	Pressure drop (Pascal)	S.D. of pressure drop
1.000	0.001	1422.937	6.134	1.000	0.001	1458.920	6.408	1.000	0.001	1457.393	8.568
1.250	0.001	2029.391	10.533	1.249	0.001	2066.987	9.868	1.251	0.001	2053.529	10.036
1.502	0.001	2731.939	9.949	1.501	0.001	2768.630	10.758	1.500	0.001	2745.751	11.002
1.750	0.002	3523.672	14.796	1.750	0.002	3565.523	15.138	1.751	0.002	3550.592	14.785
2.001	0.002	4427.042	20.071	1.999	0.002	4473.593	18.682	2.001	0.002	4459.634	20.973
2.246	0.010	5436.053	61.906	2.249	0.009	5498.100	57.868	2.252	0.008	5495.750	49.425
2.496	0.023	6594.215	158.099	2.501	0.023	6660.634	161.078	2.503	0.025	6664.360	168.218

Table 8.5.3 Mean experimental pressure drop in swirl flow and comparison to CFD

Velocity (m/s)	Experimental					RANS (Pascal)	LES (Pascal)	Error RANS to experimental %	Error LES to experimental %
	Positive error of Velocity	Negative error of Velocity	Pressure drop (Pascal)	Positive error of pressure drop	Negative error of pressure drop				
1.000	0.000	0.000	1446.417	12.504	23.480	1177.224	967.576	-18.61	-33.11
1.250	0.001	0.001	2049.969	17.018	20.578	1780.268		-13.16	
1.501	0.001	0.001	2748.773	19.856	16.835	2465.825	2110.99	-10.29	-23.20
1.750	0.000	0.000	3546.596	18.928	22.924	3259.197		-8.1	
2.000	0.001	0.001	4453.423	20.170	26.381	4139.821	3507.27	-7.04	-21.25
2.249	0.003	0.003	5476.634	21.466	40.581	5132.492		-6.28	
2.500	0.003	0.004	6639.736	24.623	45.521	6208.421	5371.91	-6.5	-19.09

The pressure drops between tappings 1 and 2 are plotted against flow velocities for the three tests are shown in Figure 8.5.2. The differences of measured pressure drop at all velocities are within 2.46% throughout all three tests indicating good reproducibility and reliability of the experimental data. It is clear from Figure 8.5.2 and Table 8.5.2, the standard deviation of the measured velocity and pressure drop increases with increasing velocity, suggesting greater fluctuation of the flow variables in flows with higher velocities.

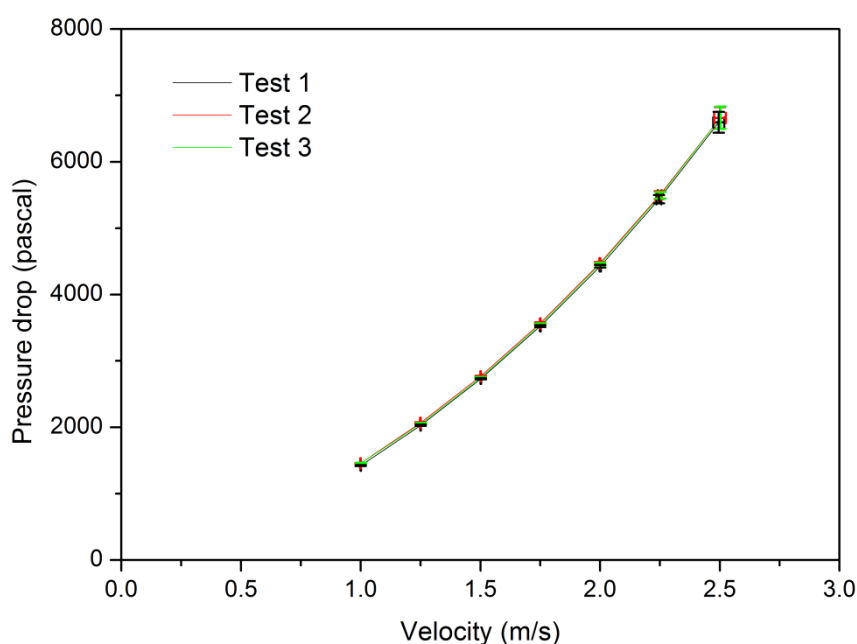


Figure 8.5.2 Pressure drop versus flow velocity for 1m cylindrical+0.4m swirl pipe+4m cylindrical pipe

The mean value of the three tests in terms of measured flow velocities and pressure drop caused by flow passing through the swirl pipe and cylindrical pipes were calculated and presented in Table 8.5.3 with their maximum positive and negative errors from the mean being included. The corresponding pressure drops across the same duration within the RANS and LES model were extracted and included in Table 8.5.3 as well, with the pressure drops extracted at exact values of flow velocity of 1, 1.25, 1.5, 1.75, 2, 2.25 and 2.5m/s.

It should be borne in mind that during experimentation it was difficult to attain the exact flow velocities of 1, 1.25, 1.5, 1.75, 2, 2.25 and 2.5m/s and direct

comparison of these experimental values with CFD results may introduce additional error associated with the difference in flow velocities. Previous researcher attempted to estimate the experimental pressure drop at the above exact velocities by fitting a quadratic polynomial to the experimental data points (Ariyaratne, 2005). However it was found in Table 8.5.3 that the mean velocities attained in the experimentation were sufficiently close to the exact flow velocities intended. Therefore, those values were used to quantify the difference between the experimental results and the CFD results. The method of quadratic polynomial curve fitting was not used as it also introduces errors to the calculated values.

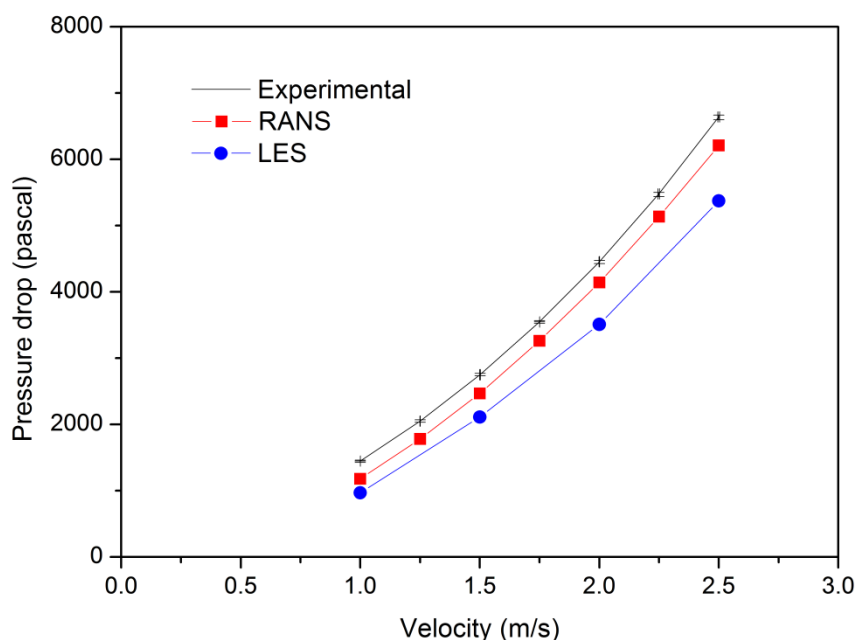


Figure 8.5.3 Comparison of the pressure drop in swirl flow obtained by experimentation and CFD

Figure 8.5.3 demonstrates the comparison of the experimental data with the RANS and LES simulation results. It is clear that pressure drop increases with increasing flow velocity for both experimental and CFD results. However, compared to the experimental data, the RANS and LES results were more conservative especially for the LES. The pressure drop predicted by RANS and LES are 6.5~18.6% lower and 19.1~33.1% lower respectively than the experimental value. The difference between the experimental and CFD values

may be due to the discrepancies between real flows and CFD model in that:

- Firstly, there are two types of pressure loss in the pipe system: 1) major loss due to friction in the pipe; 2) minor loss due to the components in the system (White, 2003). In the experimental rig, there are five connections (fittings) of cylindrical/cylindrical pipe or cylindrical/swirl pipe by dairy clamps between the two pressure transmitters. Crevices (see Figure 8.5.4a, 8.5.4b) were found in the interface of the connections which could cause localized disruption of the flow and thus give rise to minor pressure losses. The contribution of crevices on pressure drop may account for a larger proportion of the overall pressure drop in flows with lower velocities consequently amplifying the difference with the CFD results.
- Secondly, the internal surface roughness of the swirl pipe was estimated by the manufacturer to be $9 \times 10^{-6}\text{m}$; however measurements were carried out at the two ends of the swirl pipe (as they are accessible) where the surface was smooth as machining was applied (see Figure 8.5.4c). Inside the swirl pipe, the surface roughness is expected to be larger than $9 \times 10^{-6}\text{m}$. This should result in an additional pressure drop in the experimentation which was not included in the RANS model.
- Thirdly, in the RANS model, surface roughness was specified in the wall functions with the estimated value of the swirl pipe and cylindrical pipes. And the steady state simulation gave a prediction of time averaged pressure drop over a sufficiently long time. This should minimize the discrepancies between real flows and the RANS model giving better agreement. While in the near-wall treatment of the LES model, the internal pipe surface was treated as hydraulically smooth and the surface roughness cannot be specified. Uncertainty may be brought in because of the approximate representation of the wall boundaries. Moreover, the pressure drop in LES was the time averaged value over 2 seconds.

Prolonging the sampling time may increase the accuracy slightly; however it is not regarded to be cost-effective considering the massive time needed for computation.

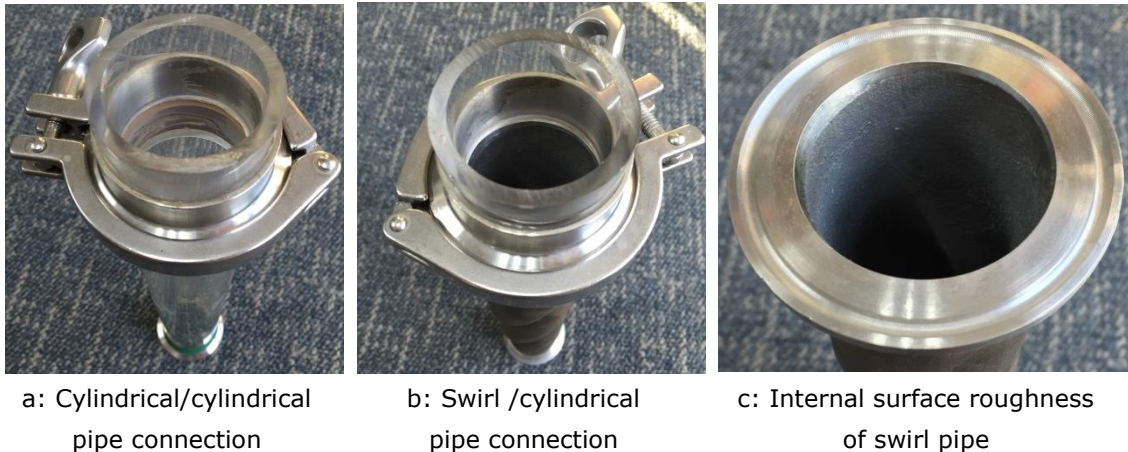


Figure 8.5.4 Crevices in the cylindrical/cylindrical and swirl/cylindrical connections; internal surface roughness of swirl pipe

8.5.3 Pressure Drop in Non-Swirl Flow (1m cylindrical+0.4m control pipe+4m cylindrical)

In this set of experiments the swirl pipe was replaced by a 0.4m cylindrical, transparent perspex control pipe with pressure drops between the two tappings measured for various flow velocities employing the same procedures mentioned previously. Three identical tests were performed and the results are shown in Table 8.5.4.

Table 8.5.4 Pressure drop across 1m cylindrical+0.4m control pipe+4m cylindrical pipe for various velocities

Test 1				Test 2				Test 3			
Velocity (m/s)	S.D. of velocity	Pressure drop (Pascal)	S.D. of pressure drop	Velocity (m/s)	S.D. of velocity	Pressure drop (Pascal)	S.D. of pressure drop	Velocity (m/s)	S.D. of velocity	Pressure drop (Pascal)	S.D. of pressure drop
1.000	0.003	1283.272	9.381	1.001	0.002	1335.212	8.640	1.001	0.001	1319.330	5.872
1.250	0.001	1829.188	8.902	1.250	0.001	1856.999	9.178	1.250	0.001	1853.928	8.780
1.504	0.003	2460.075	14.382	1.501	0.001	2479.067	11.221	1.499	0.001	2466.599	10.236
1.751	0.003	3177.938	16.171	1.751	0.002	3208.120	14.884	1.750	0.002	3184.954	14.392
2.011	0.013	4038.701	69.960	2.005	0.009	4045.800	49.118	2.000	0.002	4000.206	19.902
2.254	0.024	4935.189	184.879	2.247	0.024	4940.538	142.208	2.248	0.011	4907.284	61.617
2.485	0.036	5890.860	270.691	2.504	0.024	5969.367	173.307	2.497	0.026	5900.098	165.994

Table 8.5.5 Mean experimental pressure drop in cylindrical pipe flow and comparison to Darcy–Weisbach equation

Experimental						Darcy–Weisbach equation			
Velocity (m/s)	Positive error of velocity	Negative error of velocity	Pressure drop (Pascal)	Positive error of pressure drop	Negative error of pressure drop	Colebrook equation (Pascal)	Blasius Equation (Pascal)	Error Colebrook to experimental %	Error Blasius to experimental %
1.001	0.000	0.001	1312.605	22.608	29.333	1131.959	1141.895	-13.76	-13.01
1.250	0.000	0.000	1846.705	10.294	17.517	1684.463	1687.402	-8.79	-8.63
1.501	0.003	0.002	2468.581	10.487	8.505	2328.601	2321.592	-5.67	-5.95
1.751	0.000	0.000	3190.337	17.783	12.399	3070.438	3040.484	-3.76	-4.70
2.005	0.005	0.005	4028.236	17.565	28.030	3902.563	3840.861	-3.12	-4.65
2.250	0.004	0.003	4927.671	12.868	20.387	4830.028	4720.039	-1.98	-4.21
2.495	0.008	0.010	5920.108	49.258	29.248	5828.240	5675.723	-1.55	-4.13

The measured pressure drops in the cylindrical pipes (over 5.4m) for various velocities in the three tests are plotted in Figure 8.5.5. The differences in the measured pressure drop at all velocities are within 3.89% showing a good level of confidence in the experimental data. The mean pressure drops over the 5.4m cylindrical pipes calculated from the three tests are presented in Table 8.5.5 with their maximum positive and negative errors from the mean being included.

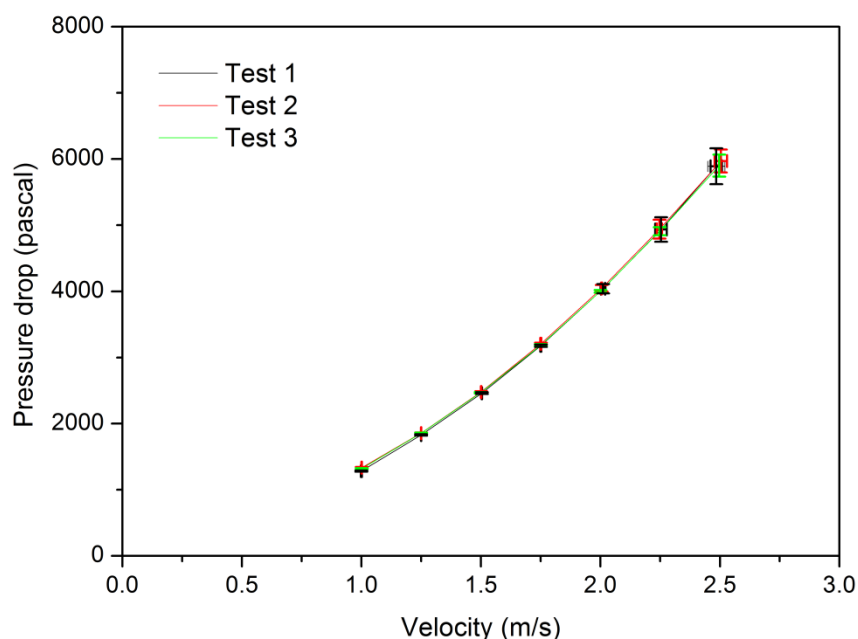


Figure 8.5.5 Pressure drop versus flow velocity for 1m cylindrical+0.4m control pipe+4m cylindrical pipe

Theoretical pressure drops can be calculated in straight cylindrical pipes through knowledge of the friction of the pipe and can be estimated according to the Darcy–Weisbach equation (Sleigh and Goodwill, 2008):

$$\Delta P = f_D \cdot \frac{L}{D} \cdot \frac{\rho V^2}{2} \quad (8.5.1)$$

Where

ΔP is the pressure loss due to friction

f_D is the Darcy friction factor which can be found from a Moody diagram or

by solving the Colebrook equation

L is the length of the pipe

D is the hydraulic diameter

V is the average velocity of the fluid flow

ρ is the density of the fluid

The friction factor f_D under different flow velocities can be obtained by solving the Colebrook equation or the Blasius equation $f_D = \frac{0.3164}{Re^{0.25}}$ which is valid for $Re = 3 \times 10^3 \sim 1 \times 10^5$. The theoretical pressure drops calculated employing the Colebrook and Blasius equation respectively are shown in Table 8.5.5.

Figure 8.5.6 depicts the variation of experimental and theoretical pressure drop with flow velocity. The experimental and calculated theoretical values showed good agreement and the experimental values are 1.6%-13.8% and 4.1%-13.0% higher than the theoretical value based on the Colebrook and Blasius equation respectively. The same argument in the last section also applies here in that crevices existed in the fittings between the two pressure tapping giving rise to minor pressure losses which cannot be covered by the theoretical equations.

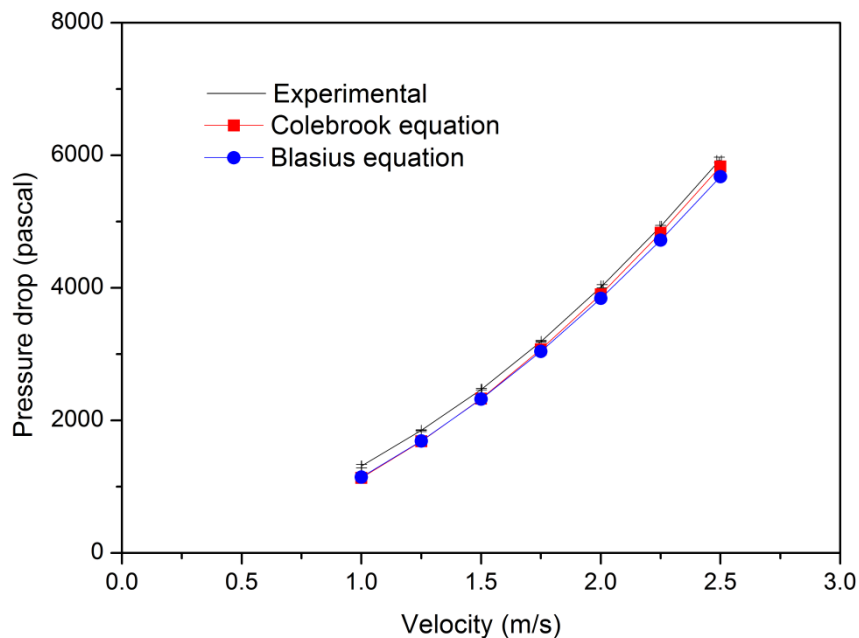


Figure 8.5.6 Comparison of the pressure drop in cylindrical pipe flow obtained by experimentation and the Darcy–Weisbach equation

8.5.4 Pressure Drop across Swirl Pipe Only

The pressure drop across the 400mm optimized swirl pipe was obtained by subtracting the pressure drop across the 1m and 4m cylindrical pipes (the blue sections shown in Figure 8.5.7b) with the control pipe in place from the overall pressure drop between the two pressure tapings with the swirl pipe in place (pressure drop over 1m cylindrical pipe + 0.4m swirl pipe + 4m cylindrical pipe as shown in Figure 8.5.7a). The subtraction is based on the assumption that the pressure losses occurred in the 1m cylindrical pipe and the 4m cylindrical pipe are the same with the swirl pipe or with the control pipe. It should be noted that the subtraction introduces further errors into the pressure drop across the swirl pipe only. A comparison of the experimental pressure drop across the swirl pipe only with the RANS and LES predictions is in Table 8.5.6. The pressure drop across swirl pipe only obtained by experimentation and CFD for various flow velocities is plotted in Figure 8.5.8.

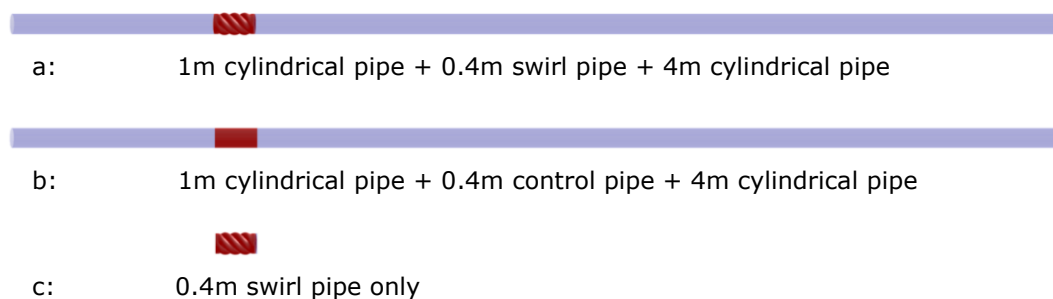


Figure 8.5.7 Demonstration of the calculation of pressure drop across the swirl pipe only by subtraction

Table 8.5.6 Comparison of the experimental pressure drop across the swirl pipe only with the RANS and LES results

Velocity (m/s)	Experimental					RANS (Pascal)	LES (Pascal)	Error RANS to experimental %	Error LES to experimental %
	Positive error of velocity	Negative error of velocity	Pressure drop (Pascal)	Positive error of pressure drop	Negative error of pressure drop				
1.000	0.000	0.001	231.042	35.112	52.813	166.130	146.39	-28.10	-36.64
1.250	0.001	0.001	340.057	27.312	38.095	260.622		-23.36	
1.500	0.004	0.003	463.050	30.343	25.340	364.918	329.44	-21.19	-28.85
1.750	0.000	0.000	592.580	36.711	35.323	490.904		-17.16	
2.000	0.006	0.006	723.575	37.735	54.411	629.512	566.56	-13.00	-21.70
2.250	0.007	0.006	913.977	34.334	60.968	799.068		-12.57	
2.500	0.011	0.014	1158.154	73.881	74.769	976.598	835.27	-15.68	-27.88

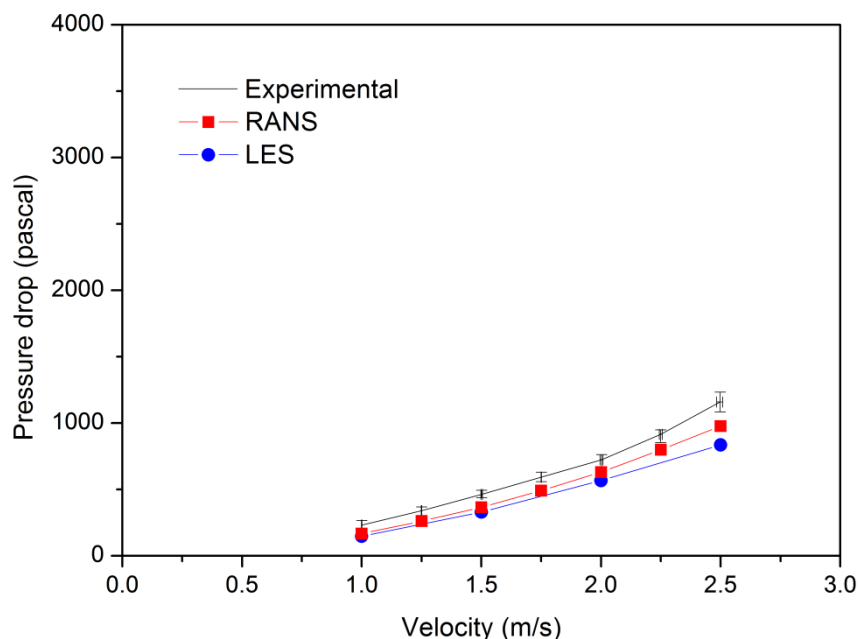


Figure 8.5.8 Pressure drop across swirl pipe only obtained by experimentation and CFD for various flow velocities

Figure 8.5.8 shows that the pressure drop across the swirl pipe only increases with increasing flow velocities for both experimental and RANS/LES results. However the experimental results are 15.7%-28.1% and 27.9%-36.6% larger than the values predicted by RANS and LES respectively. The arguments, presented in section 8.5.2 and 8.5.3, in terms of the causes of errors between experimentation and CFD apply to here as well. However additional error may be introduced associated with the assumption that the pressure losses in the 1m and 4m cylindrical pipes are the same in swirl or non-swirl flows. As suggested in the RANS and LES models the pressure losses in the cylindrical pipes just downstream of the swirl pipe are slightly greater than that without swirl. Therefore, the subtraction has counted the slightly increased pressure drop occurred in the 4m cylindrical pipe downstream of the swirl pipe into the pressure drop across the swirl pipe only, consequently increasing errors between experimentation and CFD.

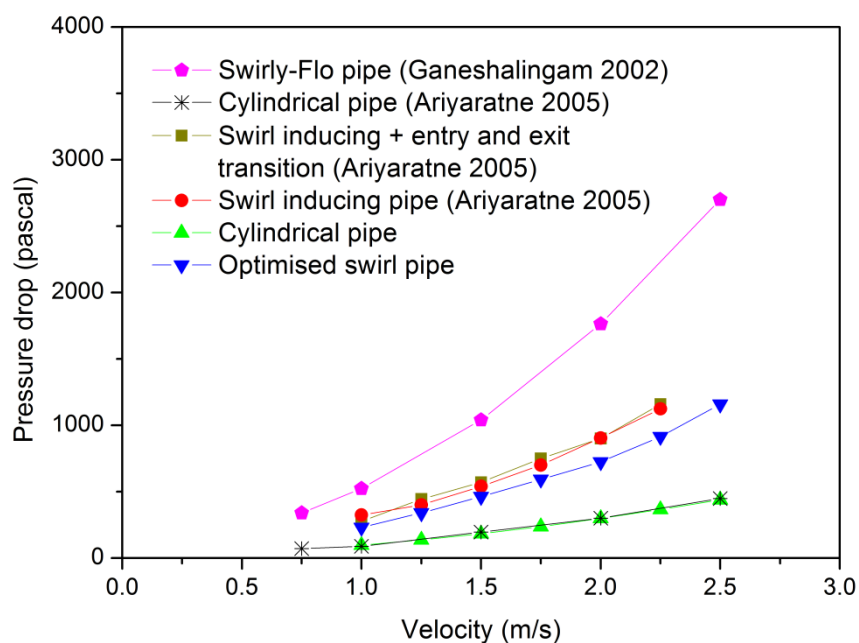


Figure 8.5.9 Comparison of Pressure Loss across optimised swirl pipe with previously used swirl pipes

Figure 8.5.9 shows a comparison of experimental pressure drops in water passing across the *Swirly-Flo* pipe (400mm length) measured by Ganeshalingam (2002), the swirl inducing pipe (400mm), the swirl inducing pipe + entry and exit transition (600mm) by Ariyaratne (2005), the optimised swirl pipe used in this study and the pressure drop across the cylindrical control pipe. It should be noted that it is not entirely appropriate to compare the measured pressure drop data for the various types of swirl pipes because:

- The *Swirly-Flo* pipe and the optimised swirl pipe used in this study were made of steel. However the swirl pipes Ariyaratne (2005) used were produced by rapid prototyping using plastics, which had a better surface finish. Therefore, the friction factors of the swirl pipes made of steel were greater than that of the plastic swirl pipes (surface roughness of optimised swirl pipe: $9 \times 10^{-6}\text{m}$ versus $2.09 \times 10^{-6}\text{m}$ for swirl inducing pipe).
- The cross-sectional area of the (three-lobed) *Swirly-Flo* pipe was smaller than that of the cylindrical pipe (Ariyaratne, 2005).

Despite the errors associated with the differences in materials and friction factors, it is clear that the three-lobed swirl pipe ($P:D=6:1$) caused significant pressure drop at high velocities. This is approximately 5 times larger than that in cylindrical pipe at the speed of 2.5m/s. The four-lobed swirl inducing pipe ($P:D=8:1$) proposed by Ganeshalingam (2002) caused approximately twice larger pressure drop than that in the cylindrical pipe at the velocity of 2.25m/s. With the inclusion of entry and exit transition pipe at the two ends of the swirl inducing pipe (600mm in total), the pressure drop caused by the sudden change from circular to lobed cross-section and vice versa were eliminated. However, due to the longer length, the pressure drop across it is close to the swirl inducing pipe.

The pressure drop across the optimised swirl pipe, which comprised an entry transition, half of the swirl inducing pipe (200mm in length) and an exit transition, is approximately 1.6 times larger than that in the cylindrical pipe. The CFD results in Chapter 5 have showed that this optimised swirl pipe (400mm in length) gave rise to slightly greater initial swirl intensity at its exit than the case of 600mm length swirl pipe. The experimental results have demonstrated that the optimised swirl pipe caused minimal pressure loss among all the designs. Therefore, this optimised swirl pipe should be the most cost-effective in swirl induction.

8.6 Wall Shear Stress Validation

8.6.1 Constant Temperature Anemometry (CTA)

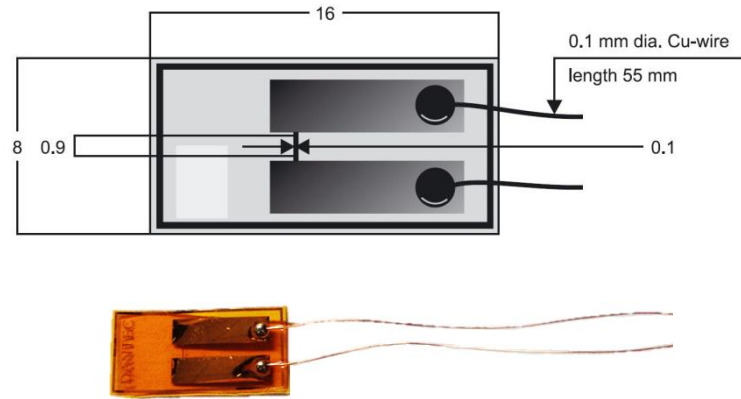
The wall shear stress in swirl flows were measured employing a Constant Temperature Anemometry (CTA) which is an analog instrument designed for the

measurement of temperature, shear stress, velocity and velocity fluctuations in, e.g., jets, boundary layers, and transitional flows.

The CTA measurement principle is based on the cooling of the small sensor placed in the flow. The temperature (resistance) of the sensor is kept constant by an advanced feedback control loop (servo-loop) that contains an electronic bridge circuit. In this way, the anemometer produces a continuous voltage that is proportional to the instantaneous flow velocity.

For the measurement of wall shear stress, a fast response Constant Temperature Anemometer (CTA) system comprising a Glue-on hot-film probe and a MiniCTA 54T42 produced by DANTEC Measurement Technology was used. The Glue-on hot film probe is a special version of the flush-mounting probe where the sensor is deposited on a 50 μm thick polyimide foil carrying quartz coating. The hot film is so thin that it is submerged in the viscous region of the boundary layer. The nickel sensor is $0.1 \times 0.9\text{mm}$ and connected to gold-plated lead areas. The copper wires soldered to the leads constitute the electrical connection between the probe cable and the probe. The dimension of the Glue-on probe is shown in Figure 8.6.1a. The MiniCTA version 54T42 as shown in Figure 8.6.1b is a single channel anemometer that can be used with many of Dantec's wire and film probes. The MiniCTA is mounted in a small box equipped with BNC connectors (one for the probe cable and one for the output voltage) and one input connector for a 12 VDC power adapter. The voltage output can be fed to a PC via a NI A/D board.

The hot-film probe is working on the principle that the heat transfer from a sufficiently small heated surface depends only on the flow characteristics in the viscous region of the boundary layer. By similarity between the heat and the gradient transport of momentum, the amount of the heat transfer into the fluid gives a measure of the wall shear stress (Berca, 2007).



a: Glue-on hot-film probe 55R47S



b: MiniCTA 54T42

Figure 8.6.1 Glue-on hot-film probe and MiniCTA 54T42

When the hot-film probe glued onto the internal pipe wall is fed with a current the voltage required to maintain a constant temperature at the hot-film probe is related to the gradient of the near wall velocity and hence the wall shear stress or friction velocity (Hanratty and Campbell, 1983, Sumer et al., 1993).

The relationship between the voltage (E_a) and the wall shear stress (τ_w) is given by:

$$E_a^2 = A + B\tau_w^{1/3} \quad (8.6.1)$$

where τ_w is the wall shear stress. E_a is the voltage required to maintain the preset temperature. The voltage is provided by the MiniCTA 54T42 which

guarantees that the overheat ratio of the sensor is maintained. A and B are constants that have to be found by probe calibration.

8.6.2 Calibration of the Hot-Film Probe

In order to perform measurements covering more points downstream of the swirl pipe, the hot film sensor was fixed, using Loctite 495 glue, to the internal surface of a removable cylindrical pipe section that has a length of 200mm with the longitudinal direction of the hot film being perpendicular to the direction of the flow. The removable section can be positioned at different locations downstream of the swirl pipe through dairy clamps. At each location (circumference), 5 measurement points were covered by the sensor at top, +45°, middle, -45° and bottom by rotating the removable section by 45° clockwise each time. The installation of the sensors is illustrated in Figure 8.6.2.

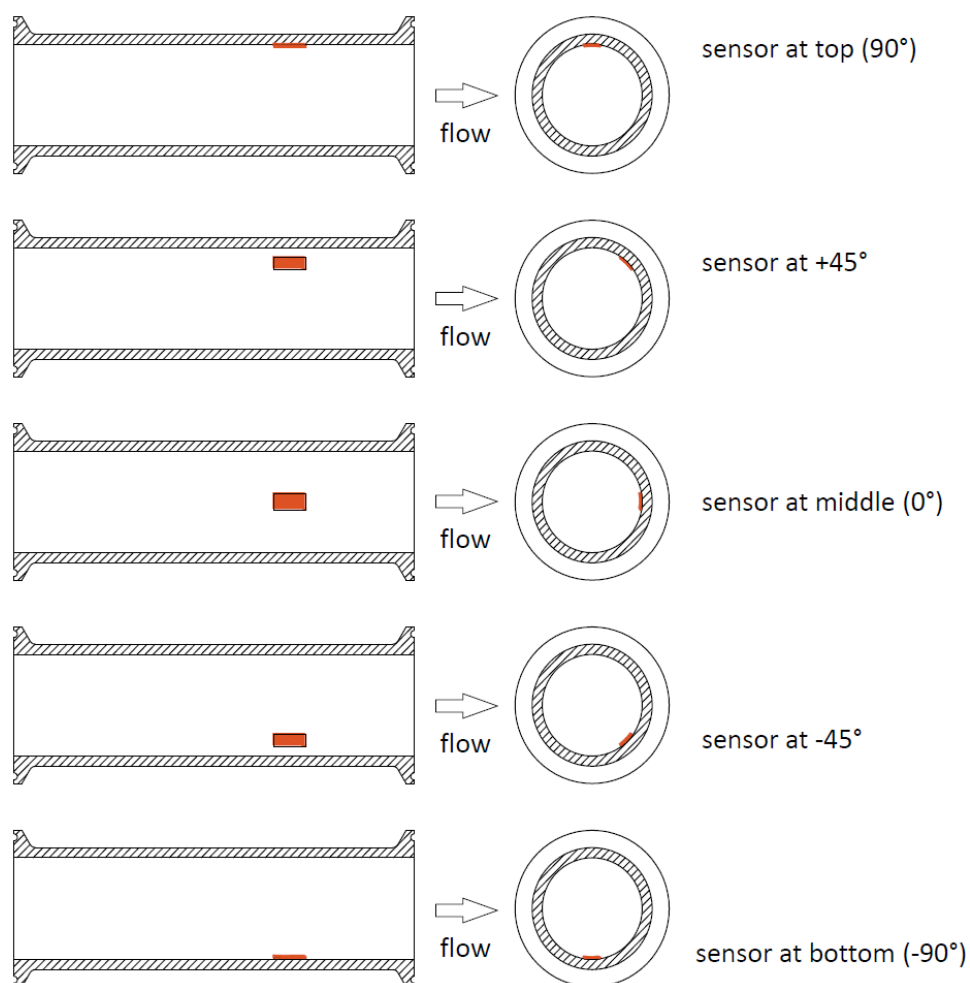


Figure 8.6.2 Allocation of the hot-film sensor at the five points on the circumference

At each of the five points along the circumference, sensor calibration was carried out in situ to determine the correlation of the output voltage induced by the hot-film resistance with the wall shear stress. The calibration can be performed in cylindrical pipe flows where the wall shear stress is directly proportional to the streamwise pressure gradient by (Su et al., 2010):

$$\tau_w = \frac{\nabla P d}{4L} \quad (8.6.2)$$

Where

ΔP = pressure loss due to friction in pipe,

d = pipe diameter,

L = length of pipe corresponding to pressure loss

At each of the five points, the sensor calibration was performed by measuring the pressure drops between the two pressure transmitters and the corresponding voltage outputs induced by the MiniCTA at a series of flow velocities. The general procedure was as below:

- 1) The MiniCTA was set up so that the hot-film sensor had an overheat ratio of 0.12. At this overheat ratio, the sensor was maintained at a temperature of 60 °C which is the maximum recommended operating temperature in water conditions.
- 2) Turned on the magnetic flow meter and the two pressure transmitters which had a distance of 4.7m between them. The hot film sensor was positioned in between the two pressure transmitters.
- 3) Started the pump and obtained flow velocities of 0.75m/s by adjusting the inverter.
- 4) Waited for the velocity to stabilise and then turned on the power of the MiniCTA to heat the hot film sensor. Constantly checking the voltage output from the MiniCTA until it was relatively stable.
- 5) Logged readings for the two pressure transmitters (which gave pressure drop across the 4.7m cylindrical pipe) and the mass flow rate using a Squirrel Data Logger.
- 6) Meanwhile, collected voltage readings at a sampling frequency of 1000Hz for 10s employing the MiniCTA Software v4.20. Repeated the collection another 4 times to get a mean value of voltage from the five collections of data.
- 7) Recorded the water temperature for measurement at this velocity using a thermometer.
- 8) Powered off the MiniCTA. Adjusted the inverter to obtain a flow velocity of 1m/s. Repeated steps 4), 5), 6) and 7) to log readings of pressure drop,

flow velocity and voltage output.

- 9) Repeated step 8) another 6 times so as to cover measurements at flow velocities of 1.25, 1.5, 1.75, 2, 2.25 and 2.5m/s.

The above measurement procedure is summarized in the following flow chart.

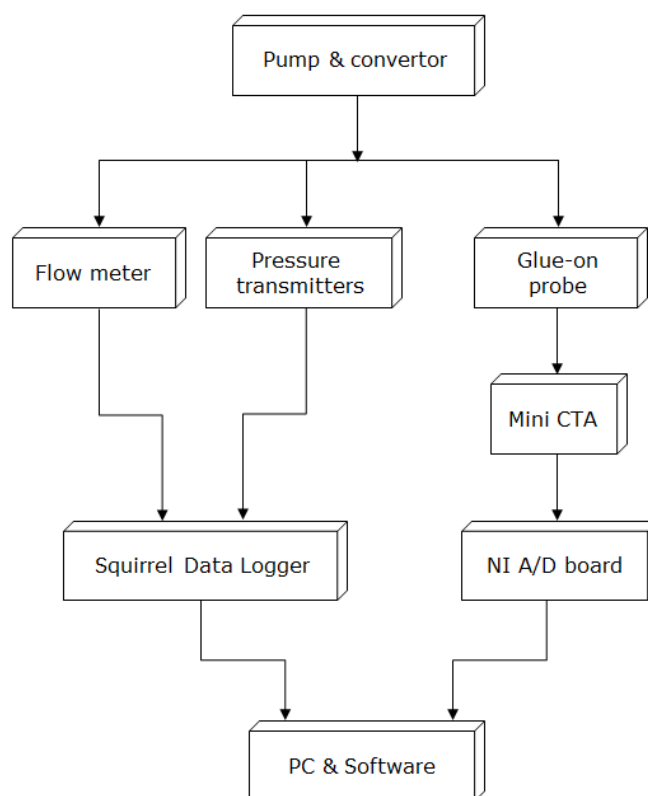


Figure 8.6.3 Measurement flow chart for sensor calibration

One of the factors influencing the heat transfer between the heated sensor and the water is the temperature difference between the water and the hot-film sensor. Since the hot film's temperature is kept constant, to avoid this influence, constant water temperature should be maintained during the course of the calibration. In the case of an unavoidable temperature change, a temperature correction is required. The temperature correction for CTA voltage can be calculated from (Jørgensen, 2002):

$$E_{corr} = \left(\frac{T_w - T_0}{T_w - T_a} \right)^{0.5} \cdot E_a \quad (8.6.3)$$

where

E_{corr} = corrected voltage

E_a = acquired voltage

T_w = sensor hot temperature (60°C)

T_0 = ambient reference temperature related to the last acquisition

T_a = ambient temperature during acquisition

It was found that there were slight temperature increases in the flows with higher velocities, partially because the hydraulic rig is a semi-closed loop. The E_a acquired at those velocities were corrected before being used for calibration.

The calculated wall shear stress in cylindrical pipe flows using equation 8.6.2, the E_a^2 , $\tau_w^{1/3}$ and so on for sensor calibration is presented in Appendix 8.2. Figure 8.6.4~8.6.8 shows the curve fitting of the data of wall shear stresses and bridge voltages obtained in the conditions of sensor at top, +45°, middle, -45° and bottom respectively.

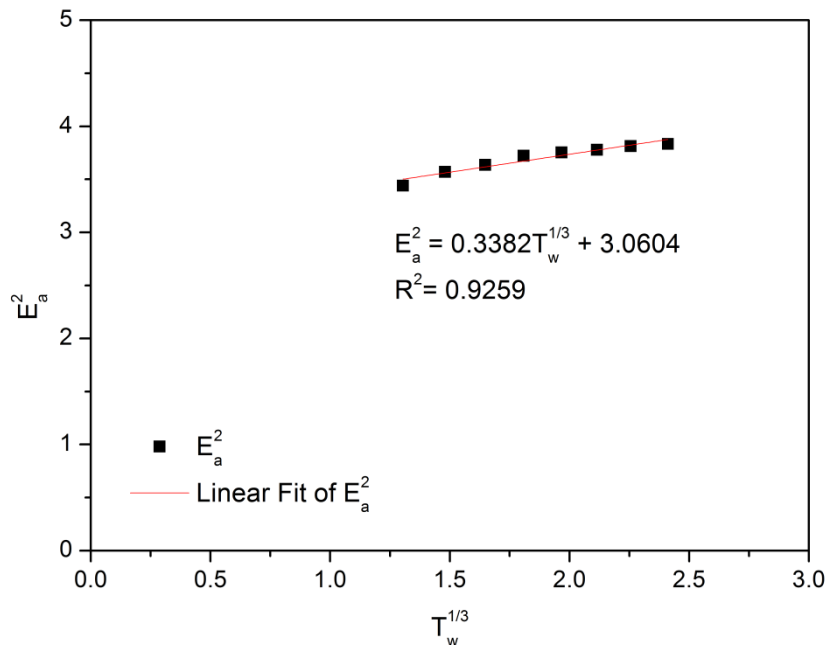


Figure 8.6.4 Calibration of hot-film sensor (sensor at top)

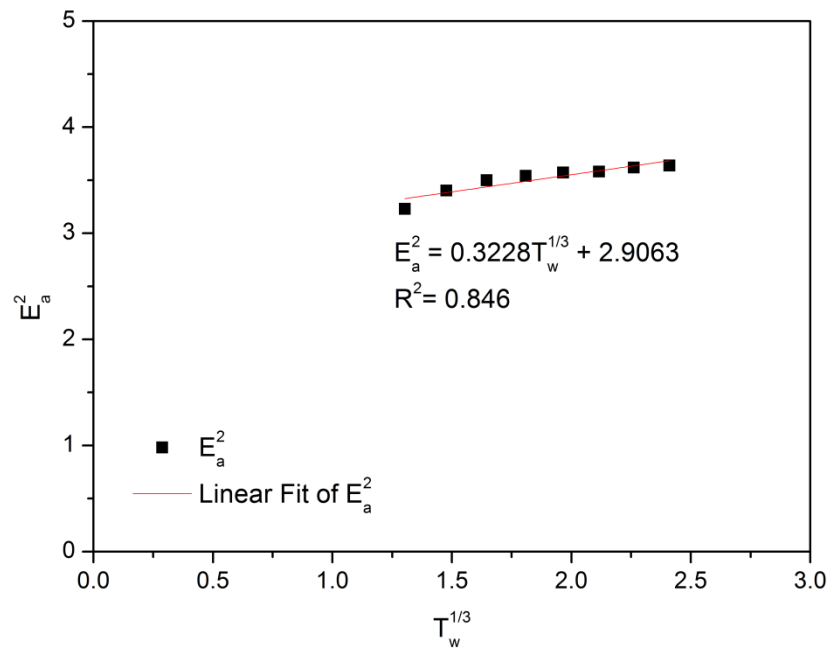


Figure 8.6.5 Calibration of hot-film sensor (sensor at +45°)

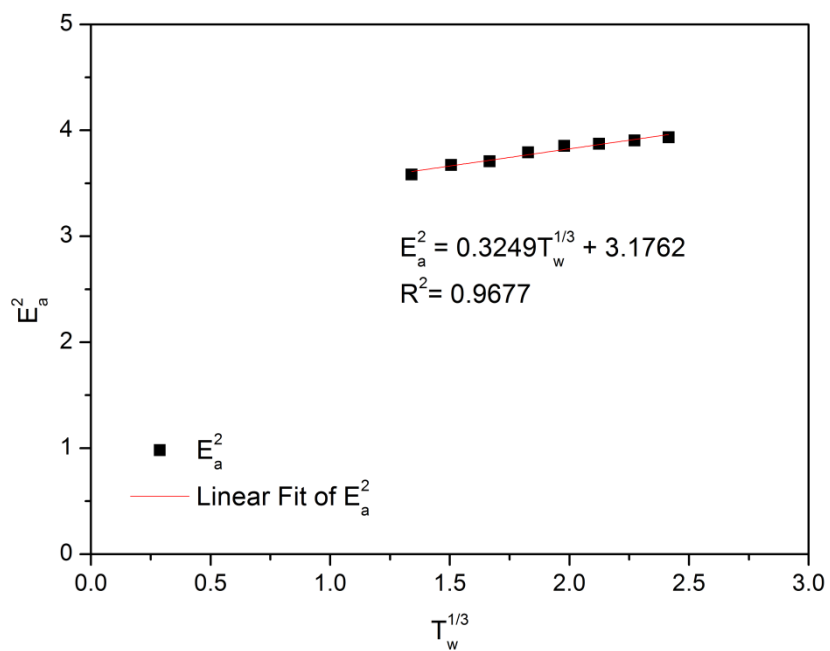


Figure 8.6.6 Calibration of hot-film sensor (sensor at middle)

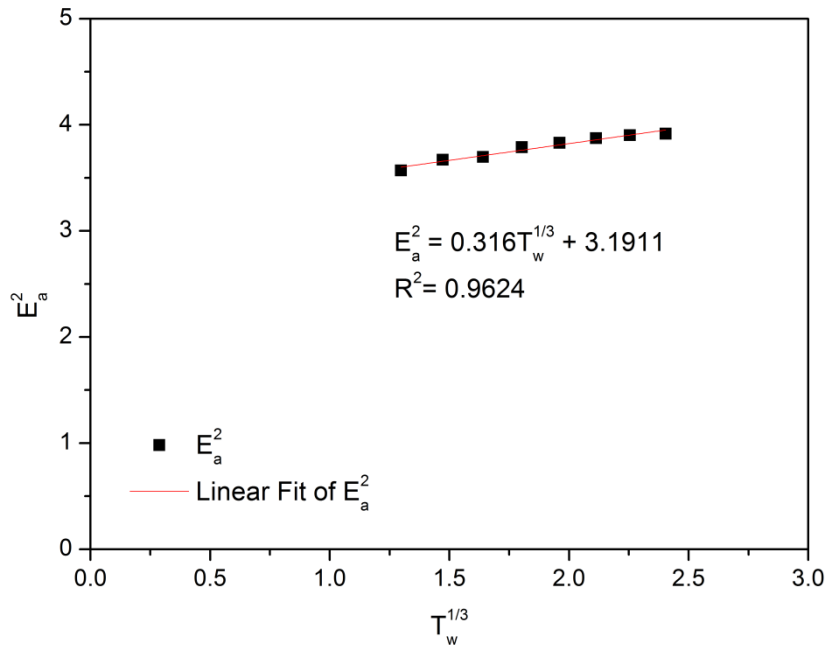


Figure 8.6.7 Calibration of hot-film sensor (sensor at -45°)

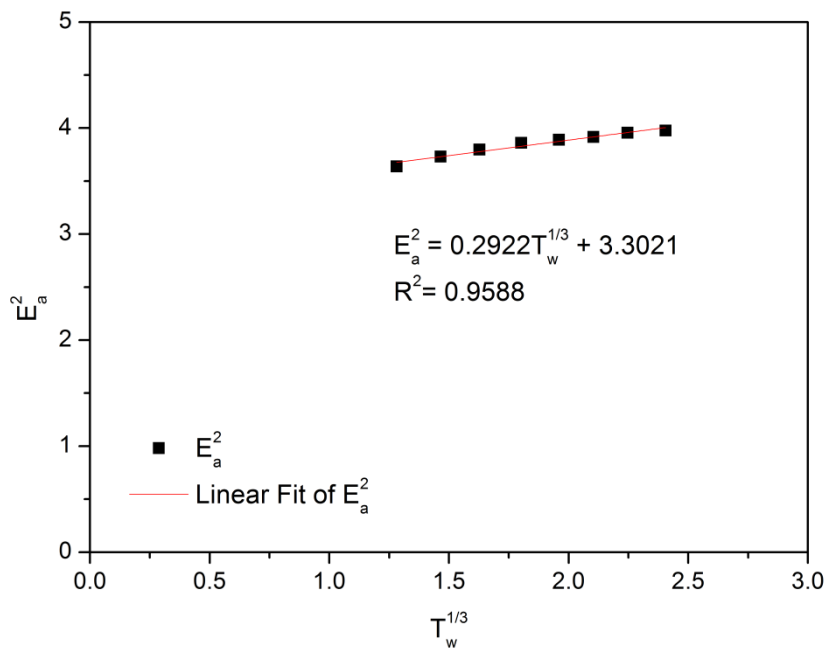


Figure 8.6.8 Calibration of hot-film sensor (sensor at bottom)

8.6.3 Measurements of Mean Wall Shear Stress in Swirl Flows

In swirl flows, wall shear stress measurements were performed at 10 circumferences starting at 0.13m downstream of swirl pipe and then 0.53m, 1.13m, 1.63m, 2.13m, 2.63m, 3.13m, 3.63m, 4.13m and 4.63m downstream of the swirl pipe. At each circumference, the sensor was positioned at the five

points in the order indicated in Figure 8.6.9. At each point, voltage acquisition was performed at velocities of 1m/s, 1.25m/s, 1.5m/s, 1.75m/s, 2m/s, 2.25m/s and 2.5m/s. At each flow velocity, voltage readings were sampled at a sampling frequency of 1000Hz for 10s, which was repeated for another 4 times to get a mean value. Therefore, a total number of 1750 mean voltage readings were obtained which resulted in 350 mean wall shear stress values at the circumferences covering a range of locations and flow velocities. The measurement procedure is shown in Figure 8.6.9.

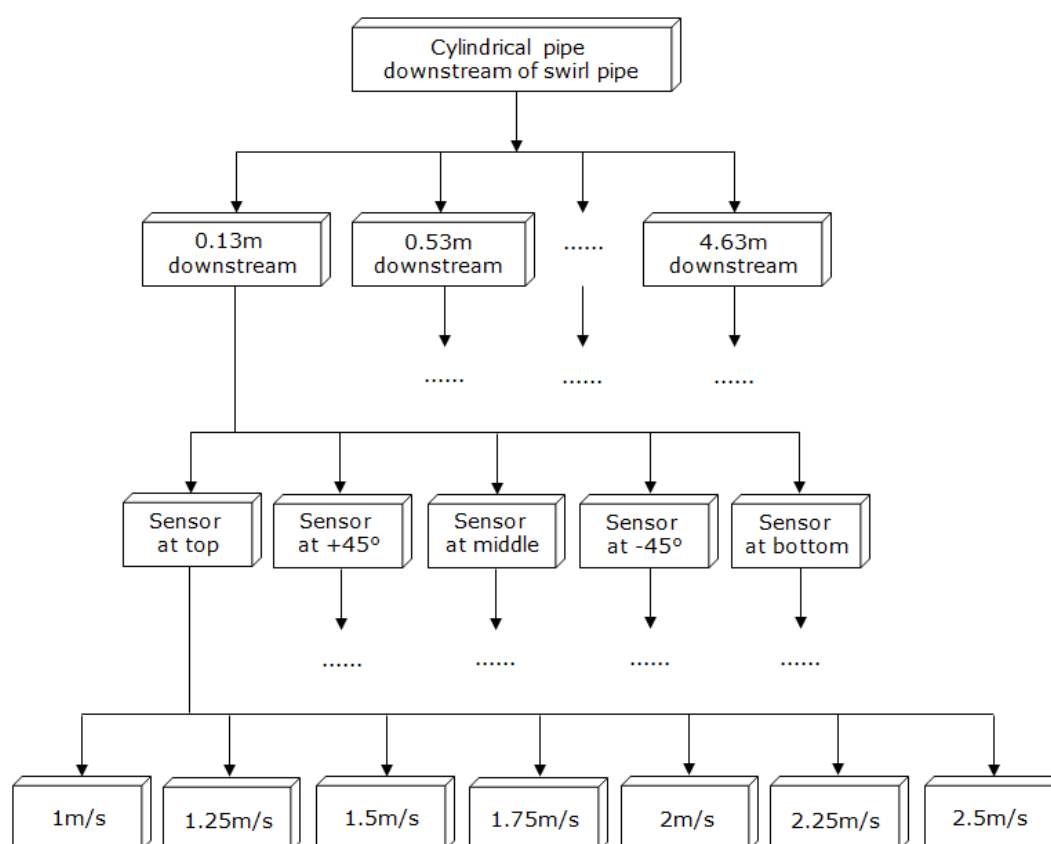


Figure 8.6.9 Measurement procedure for wall shear stress

At each point, the bridge voltage outputs obtained at each flow velocity were averaged over the five samplings. The mean voltages were then corrected in terms of water temperature difference between the calibration in cylindrical pipe flows and the data acquisition in swirl flows using equation 8.6.3. The corrected voltages were then converted into wall shear stresses using the calibration curves obtained in section 8.6.2. The conversion was performed in a way that

the voltage collected in the points of sensor at the top, +45°, middle, -45° and bottom in swirl flows were converted employing the calibration curves obtained in the corresponding conditions of sensor at the top, +45°, middle, -45° and bottom respectively, thus the calibration can be regarded as in situ.

The mean wall shear stress at circumferences downstream of the swirl pipe for various flow velocities is shown in Figure 8.6.10. Figure 8.6.11 shows the mean wall shear stress in cylindrical pipe flows at the same flow velocities calculated from equation 8.6.2. The detailed experimental results shown in the two figures are referred to Table 8.6.1.

It is clear from the two figures that the wall shear stresses increase with increasing flow velocities in conditions of both the cylindrical pipe flows and the swirl flows. However, for the same flow velocity, there is a clear increase of wall shear stress downstream of the swirl pipe which decreases gradually with increasing downstream distance as the swirl effect decays. The maximum and minimum increases of wall shear stress downstream of the swirl pipe, compared to the wall shear stress in the cylindrical pipe flows with various velocities, are calculated in Table 8.6.1. It demonstrates a considerable wall shear stress increase (91% for 2.5m/s flow velocity~279% for 1m/s flow velocity) at the circumference 0.13m downstream of the swirl pipe; and 15%~105% (2.5m/s~1m/s) increase of wall shear stress is guaranteed within 4.6m downstream of the swirl pipe. This at least 15%~105% increase in the wall shear stress could be important in improving Clean-In-Place efficiency in a closed processing system.

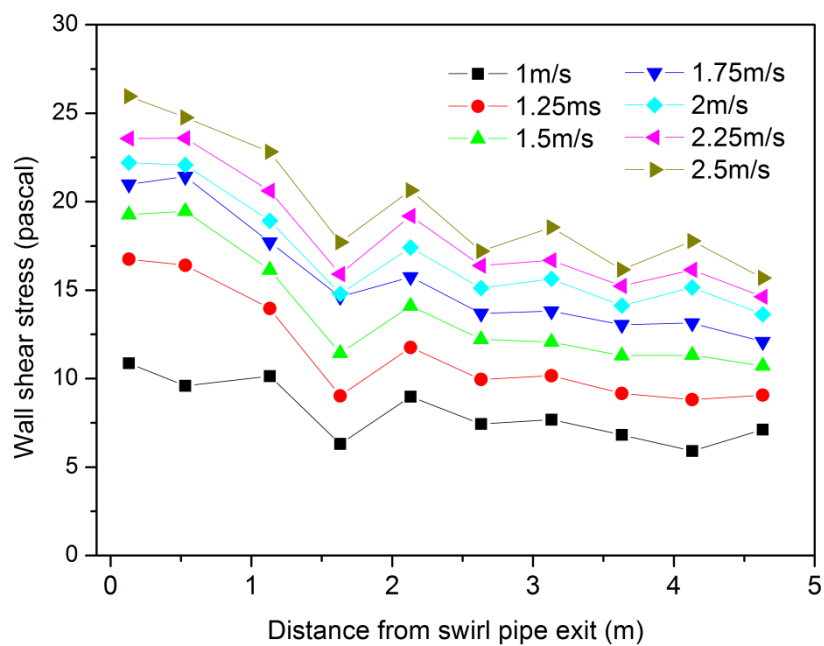


Figure 8.6.10 Mean wall shear stress downstream of swirl pipe for various flow velocities

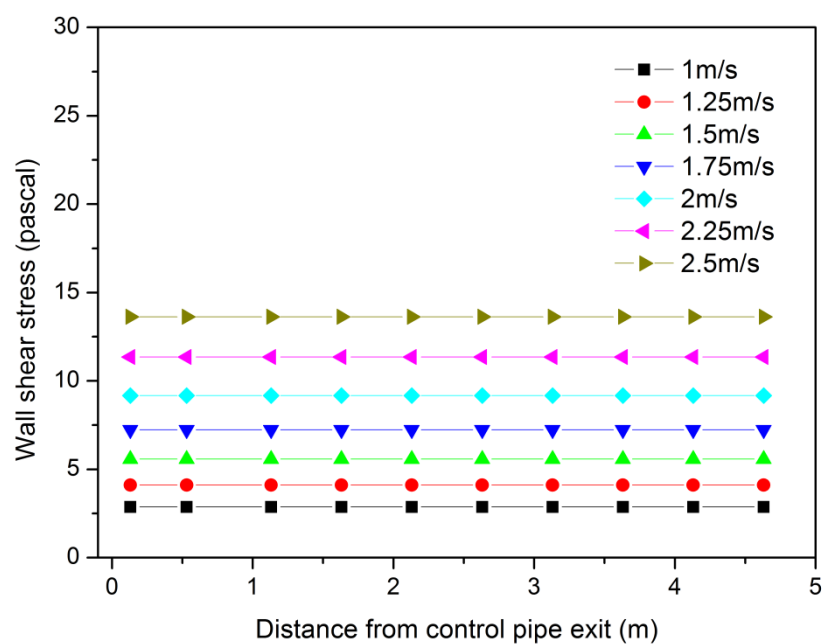


Figure 8.6.11 Mean wall shear stress downstream of control pipe for various flow velocities

Table 8.6.1 Mean wall shear stress downstream of swirl pipe and control pipe for various flow velocities

Location Velocity (m/s)	Wall shear stress in swirl flows (pascal)										WSS in cylindrical pipe flows (pascal)	Max. increase (%)	Min. increase (%)
	0.13m down- stream	0.53m down- stream	1.13m down- stream	1.63m down- stream	2.13m down- stream	2.63m down- stream	3.13m down- stream	3.63m down- stream	4.13m down- stream	4.63m down- stream			
1	10.873	9.593	10.138	6.309	8.984	7.434	7.679	6.823	5.906	7.124	2.872	278.59	105.64
1.25	16.748	16.411	13.965	9.026	11.761	9.953	10.166	9.165	8.814	9.073	4.112	307.30	114.35
1.5	19.275	19.461	16.145	11.444	14.106	12.225	12.072	11.296	11.331	10.723	5.577	248.95	92.27
1.75	20.985	21.422	17.720	14.630	15.755	13.690	13.817	13.044	13.144	12.094	7.234	196.13	67.18
2	22.206	22.078	18.922	14.790	17.411	15.122	15.634	14.130	15.152	13.632	9.169	142.19	48.67
2.25	23.570	23.590	20.612	15.905	19.188	16.388	16.688	15.233	16.149	14.629	11.349	107.86	28.90
2.5	25.964	24.757	22.815	17.708	20.638	17.205	18.552	16.161	17.778	15.686	13.623	90.59	15.14

Table 8.6.2 Comparison of mean wall shear stress in swirl flows obtained by experimentation and CFD models

Distance downstream (m)	WSS	2.5m/s flow velocity				2m/s flow velocity				1.5m/s flow velocity				1m/s flow velocity			
		LES (Pa)	Error LES to experimental (%)	RANS (Pa)	Error RANS to experimental (%)	LES (Pa)	Error LES to experimental (%)	RANS (Pa)	Error RANS to experimental (%)	LES (Pa)	Error LES to experimental (%)	RANS (Pa)	Error RANS to experimental (%)	LES (Pa)	Error LES to experimental (%)	RANS (Pa)	Error RANS to experimental (%)
0.13		23.77	-8.4	15.69	-39.6	16.01	-27.9	10.46	-52.9	8.98	-53.4	6.17	-68.0	3.93	-63.8	2.76	-74.6
0.53		19.00	-23.3	14.47	-41.6	12.72	-42.4	9.74	-55.9	6.88	-64.7	5.82	-70.1	2.92	-69.5	2.66	-72.3
1.13		15.49	-32.1	13.36	-41.4	9.59	-49.3	8.89	-53.0	5.36	-66.8	5.30	-67.2	2.47	-75.7	2.56	-74.7
1.63		13.89	-21.6	13.10	-26.0	8.46	-42.8	8.74	-40.9	4.78	-58.2	5.22	-54.4	2.28	-63.8	2.56	-59.5
2.13		12.45	-39.7	13.05	-36.8	7.92	-54.5	8.73	-49.9	4.35	-69.2	5.22	-63.0	2.14	-76.1	2.54	-71.7
2.63		12.00	-30.2	12.98	-24.5	7.75	-48.7	8.70	-42.5	3.97	-67.5	5.21	-57.4	1.99	-73.2	2.54	-65.9
3.13		11.67	-37.1	12.92	-30.4	7.44	-52.4	8.67	-44.5	3.89	-67.8	5.19	-57.0	2.00	-74.0	2.53	-67.0
3.63		11.58	-28.4	12.89	-20.2	7.35	-48.0	8.65	-38.8	3.81	-66.2	5.18	-54.1	1.92	-71.8	2.53	-62.9
4.13		11.52	-35.2	12.88	-27.6	7.29	-51.9	8.65	-42.9	3.76	-66.8	5.18	-54.3	1.95	-67.0	2.53	-57.1
4.63		11.20	-28.6	12.87	-17.9	7.07	-48.1	8.64	-36.6	3.54	-67.0	5.18	-51.7	1.95	-72.6	2.53	-64.5

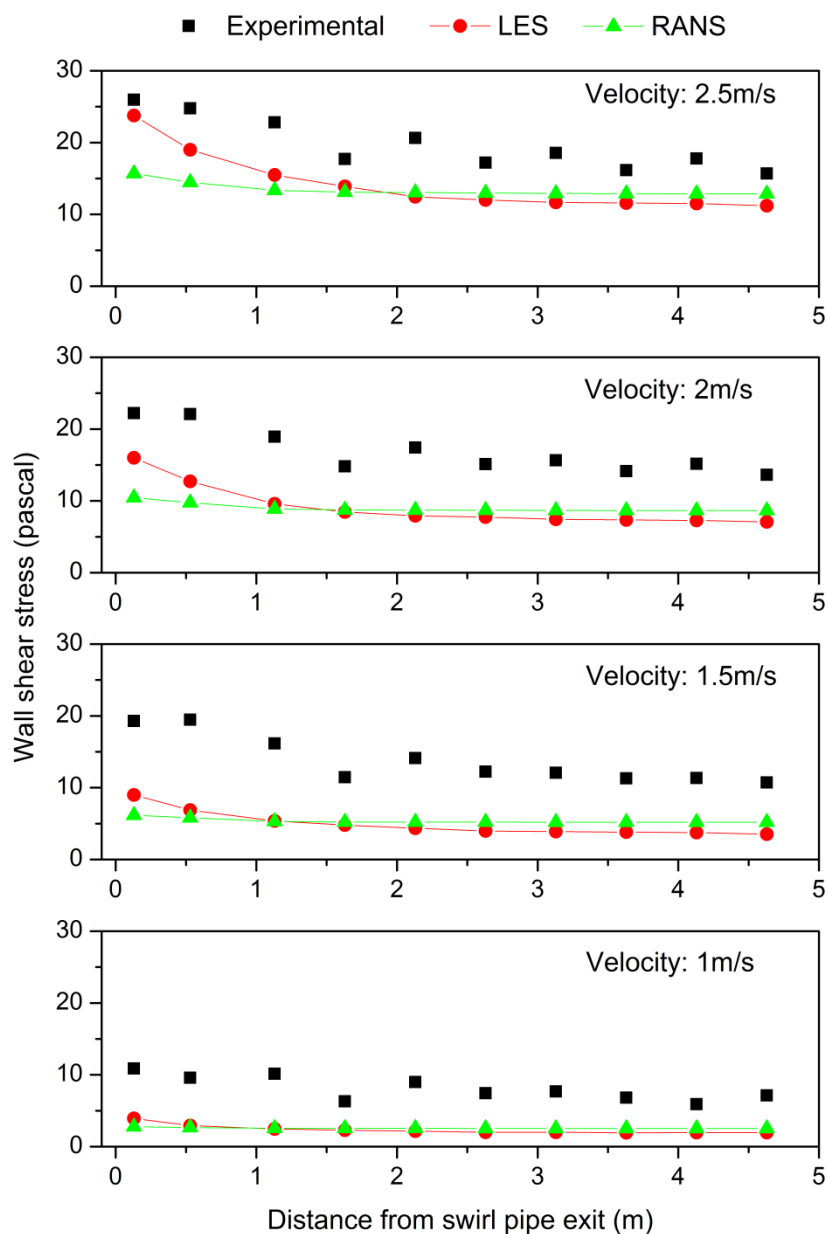


Figure 8.6.12 Comparison of mean wall shear stress downstream of swirl pipe obtained by experimentation and CFD models

The wall shear stress measured in swirl flows were compared to the RANS and LES models where data are available. The comparison is shown in Table 8.6.2 and Figure 8.6.12. Compared with the CFD results, the experimental measurements tend to overestimate the wall shear stress in swirl flows especially in the conditions of lower velocities and at circumferences further downstream of the swirl pipe. A detailed differences in percentage between experimental and CFD results are referred in Table 8.6.2. Despite the

differences (8%-76% lower for LES and 13%-75% lower for RANS), the experimentation confirms the tendency shown in the CFD models that swirl pipe induces a clear increase in the mean wall shear stress downstream which prevails for a downstream duration proportional to the flow velocity. Within the duration, the swirl pipe could be expected to improve the CIP efficiency in a closed processing system.

Hereafter discuss sources that may contribute to the experimental errors. They are:

- Errors associated with calibration

The calibration of the hot-film probe was performed in cylindrical pipe flows where the wall shear stress can be calculated from the pressure drop due to friction of the pipe between the two pressure transmitters. As was discussed in section 8.5.2 the measured pressure drop accounted for the minor loss due to the components in the system, such as the connections (fittings) of cylindrical/cylindrical pipe between the two pressure transmitters, therefore the overall pressure drop measured was larger than the pressure drop due to friction of the pipe. This overestimated pressure drop, when applied to calibration, contributes to an overestimation of the wall shear stress in swirl flows. From Table 8.5.5, the error associated with pressure drop measurement was greater in flows with lower velocities, resulting stronger overestimation of wall shear stress in swirl flows with lower velocities.

In addition, the difference between the fitting of the straight line and the points of $(\tau_w^{1/3}, E_a^2)$ on the graph (curve fitting errors), which is within 2%-10%, contributes to the errors associated with calibration.

- The angle made by the hot-film probe with the flow

The maximum heat dissipation between the probe and the water takes

place when the longitudinal direction of the hot film is perpendicular to the direction of the flow (Berca, 2007), which means the maximum voltage value at the output of the CTA. This requirement was met in cylindrical pipe flows during the probe calibration as the Glue-on probe was fixed onto the internal surface of the removable section by Loctite 495 glue with the longitudinal direction of the hot film being perpendicular to the pipe axis. However, in swirl flows the direction of the flow in the near wall region is not perpendicular to the cross-flow planes as shown in Figure 8.6.13, thus the angle made between the longitudinal direction of the sensor and the flow direction in the measurement points is less than 90° (approximately 70°). This is especially true in the duration just downstream of the swirl pipe where swirl prevails. Due to this, the wall shear stress just downstream of the swirl pipe was underestimated. Therefore, the rate of decrease of the experimental wall shear stress downstream of the swirl pipe is not as steep as the CFD prediction, especially the LES.

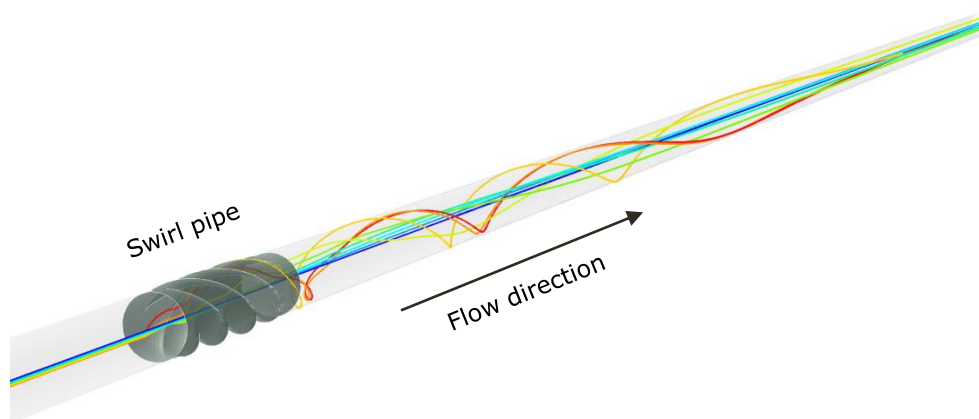


Figure 8.6.13 Flow direction in the near wall region of swirl flow

- Influence of change of the probe-water temperature

Another influence over the measurements of the wall shear stress is given by the variation in the water temperature due to, firstly the change in the ambient environment as no air conditioning was equipped in the laboratory, and secondly the rig being a semi-closed loop so that the

water temperature tended to increase slightly in flows with higher velocities. Since the hot-film's temperature is kept constant, the heat transfer by convection between probe and water changes with water temperature. The error associated with water temperature variation was minimized by carrying out temperature correction against the CTA voltage output.

- Wall effects

The hot-film probe was attached to the internal surface of the pipe and some amount of the measured heat of the probe is conducted to the wall. The conduction of the heat to the pipe wall is minimized by using the insulating polyimide foil. If not, the wall shear stress will be overestimated.

- Contamination of the hot-film probe

Another parameter taken into account is the contamination of the hot-film probe with the water impurities. Contaminants may adhere to the sensor and reduce the heat transfer resulting in a downward drift in the calibration (Jørgensen, 2002). To avoid this, cleaning of the probe was done at regular intervals using lens cleaning paper.

Despite the factors influencing the measurements with the hot-film probe, which were unavoidable due to the defects of the experimental apparatus and the complexity when applied in swirl flows, the experimental results has demonstrated the applicability of hot-film anemometer applied in wall shear stress measurement in swirl flows.

8.6.4 Fluctuation of Wall Shear Stress in Swirl Flows

The instantaneous wall shear stress at each measurement points can be calculated through the instantaneous voltage signals from the MiniCTA. The temporal wall shear stress over 1 second at the position 0.53m downstream of

swirl pipe with the condition of sensor at top and the flow velocity of 1, 1.5 and 2m/s are demonstrated in Figure 8.6.14. It was observed that the wall shear stress varies erratically about its mean value with time, with the fluctuation amplitude growing slightly with increasing flow velocities.

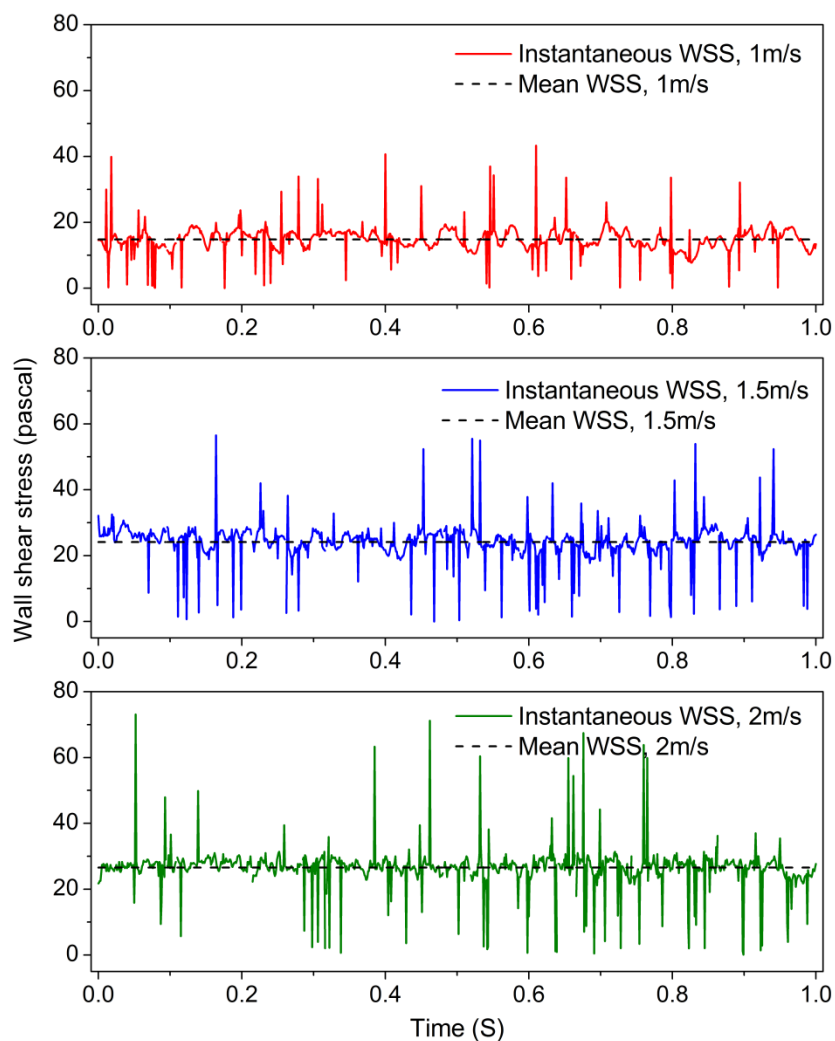


Figure 8.6.14 Examples of wall shear stress fluctuation downstream of swirl pipe measured by hot-film probe

The normalized fluctuation rate of the wall shear stress can be calculated from equation 7.4.1. However, as has been described in section 8.6.3 at each measurements point voltage was sampled at a frequency of 1000Hz for 10s, repeated 5 times. With the coverage of 5 points at each of the 10 circumferences and the 7 flow velocities under which measurements were performed, this resulted in a total number of 17,500,000 voltage values needed

to be calculated into wall shear stress. This becomes computationally costly and unaffordable.

The MiniCTA Software v4.20 is capable of performing calculations of the statistic derivatives of the raw data: mean, standard deviation, and turbulent intensity. Where the turbulence intensity, I , is defined as the ratio of the root-mean-square of the velocity fluctuations u' , to the mean flow velocity U . Therefore:

$$I = \frac{u'}{U} = \frac{\left[\frac{1}{N-1} \sum_{i=1}^N (u_i - U)^2 \right]^{1/2}}{U} = \left[\frac{1}{N-1} \sum_{i=1}^N \left(\frac{u_i}{U} - 1 \right)^2 \right]^{1/2} \quad (8.6.4)$$

Where $\frac{u_i}{U}$ is the normalized velocity. Equation 8.6.4 has the same form as equation 7.4.1 that is used for calculating the normalized fluctuation rate of wall shear stress. The turbulence intensity calculated from the raw data in the MiniCTA software is actually the normalized fluctuation rate of the instantaneous voltage signals. Since the same calibration curves were used in converting voltages at various circumferences into wall shear stresses, the normalized fluctuation rate of the wall shear stress should be proportional to turbulence intensity of the instantaneous bridge voltage. It is therefore decided to describe the unsteady behaviour of the normalized wall shear stress using the normalized fluctuation rate of the bridge voltage signals, which should demonstrate consistent variation trend of the wall shear stress fluctuation rate downstream of the swirl pipe.

Figure 8.6.15 and 8.6.16 illustrate the variation of the mean normalized voltage fluctuation rates (averaged from the five points at each circumference) downstream of the swirl and control pipes for various flow velocities. A clearer comparison of the normalized fluctuation rate of voltage signals under swirl flow and non-swirl flow conditions for various velocities is exhibited in Figure 8.6.17.

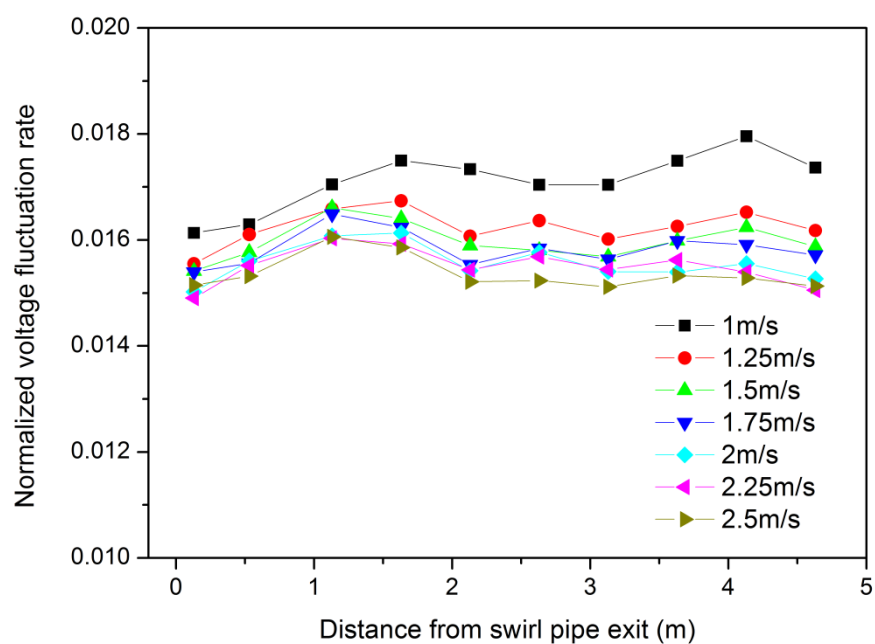


Figure 8.6.15 Normalized voltage fluctuation rates downstream of swirl pipe for various flow velocities

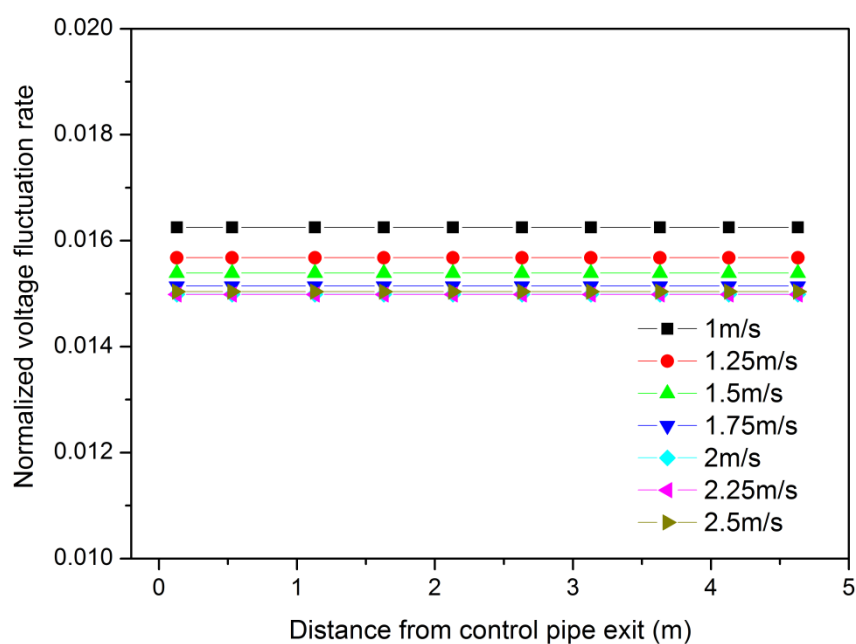


Figure 8.6.16 Normalized voltage fluctuation rates downstream of control pipe for various flow velocities

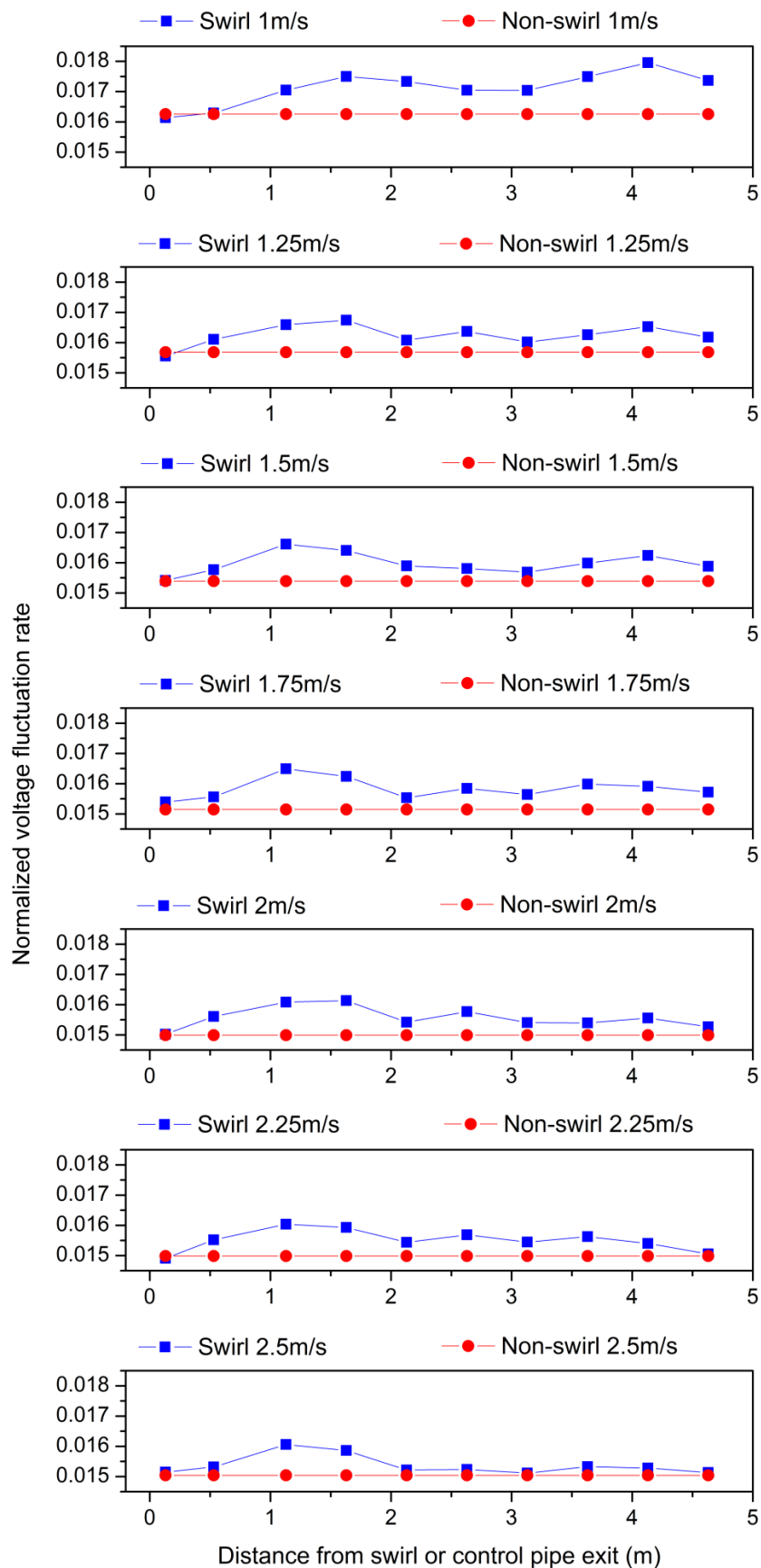


Figure 8.6.17 Comparison of the normalized fluctuation rate of voltage signals under swirl flow and non-swirl flow conditions

Figure 8.6.15~17 suggest that firstly swirl pipe induces a stronger fluctuation rate in the wall shear stress downstream than the non-swirl flow conditions. This is expected as swirl flow, which contains a tangential velocity component, is always accompanied by an increase in velocity fluctuations. Just downstream of the swirl pipe, the fluctuation rate is relatively low (might be stabilized by the stronger swirl just downstream of the swirl pipe) which increases with increasing downstream distance and reaches a maximum where possibly the vortex cores interact and dissipate. Afterward, the greater fluctuation rate induced prevails along the circular pipe experiencing ups and downs. The variation trend in the wall shear stress fluctuation suggested from Figure 8.6.15 shows good consistency with the LES predictions illustrated in Figure 7.4.18~22.

In fully developed cylindrical pipe flows, the turbulence intensity at the core can be estimated from the below formula derived from empirical correlation (ANSYS, 2011b):

$$I = \frac{u'}{U} = 0.16(Re_{d_h})^{-1/8} \quad (8.6.5)$$

Where Re_{d_h} is the Reynolds number based on the pipe hydraulic diameter d_h .

This formula was used to estimate the turbulence intensity on the inlet boundary conditions for the CFD model. It can be found from Table 6.2.1 that the turbulence intensity decreases slightly with increasing Reynolds number of the flow. A consistent trend can be found in Figure 8.6.15 and 8.6.16 with the turbulence intensity reducing slightly with increasing flow velocity in both swirl and non-swirl conditions.

It should be noted that a decreasing turbulent intensity does not mean that the flow becomes less turbulent. It just means that the root-mean-square of the

velocity fluctuations u' divided by the mean flow velocity U decreases. In fluid dynamics, the root-mean-square of the velocity fluctuations u' expresses the average magnitude of the velocity fluctuations. It links to the turbulence kinetic energy k by $u' = \left(\frac{2}{3}k\right)^{1/2}$ with k being the mean kinetic energy per unit mass associated with eddies in turbulent flow (H.K.Versteeg and W.Malalasekera, 2010). Actually both the velocity fluctuation and the mean velocity increase with increasing flow velocity, but the mean velocity increases even more, therefore turbulence intensity decreases. The turbulence intensity helps to indicate the variation of wall shear stress fluctuation rate downstream of swirl pipe under a fixed flow velocity by eliminating the level difference of the mean wall shear stress downstream of the swirl pipe.

It was also observed that, for the conditions of 2, 2.25 and 2.5m/s flow velocities, the fluctuation rate, once reaching a maximum value, experiences a clear decreasing trend. This may due to the inadequate efficiency of the De-aerator which cannot sufficiently remove bubbles at higher flow velocities. It has been suggested that the introduction of bubbles into the flow suppresses the overall fluctuation of the wall shear stress in the pipe flow (Su et al., 2010). In a fully closed processing system with no bubbles, the fluctuation rate of the wall shear stress at the internal pipe surface may be stronger.

The variation of normalized wall shear stress fluctuation rate, presented in the form of normalized fluctuation rate of voltage signals, has demonstrated that further downstream where the increase in the wall shear stress fades, the wall shear stress maintains a stronger fluctuation rate than in the non-swirl flow, which should contribute to the enhancement of CIP procedures over that duration in a closed processing system.

8.7 Conclusions

This chapter presented the experimental validation of the simulation results. The concepts of error/uncertainty and verification/validation were introduced. Efforts have been made to minimize the errors and uncertainties of the CFD models were summarized. The layout and specification of the hydraulic rig for validating the CFD results were described as were the processes of developing the stainless steel optimised swirl pipe using investment casting.

The measurement procedures employed to validate the pressure drop across the optimised swirl pipe using a pair of pressure transmitters were described and the possible reasons to the differences between experimental and CFD results were discussed. The following results have been obtained:

- The experimental pressure drops across the optimised swirl pipe in flows with various velocities are found to be 15.7%-28.1% and 27.9%-36.6% larger than the values predicted by RANS and LES respectively.
- The pressure drop across the optimised swirl pipe is approximately 1.6 times larger than that measured in cylindrical pipe flow.
- The optimised swirl pipe causes minimal pressure loss from all the various swirl pipe designs, which should be most cost-effective in swirl induction.

The wall shear stresses in swirl flows were measured by a Glue-on hot film sensor and a MiniCTA. The working principle of the measurement apparatus, the calibration procedures performed in cylindrical pipe flows and the measurements in swirl flows were detailed. The sources that may contribute to the experimental errors using hot-film sensor in swirl flows were discussed in terms of the sensor calibration, angle made by the hot-film probe with flow, influence of the change of the water temperature, etc. Despite the experimental

errors, the following findings can be noted:

- The experimental results confirm the CFD simulation that, without increasing flow velocity, the swirl pipe induces a clear increase in the mean wall shear stress downstream which decreases gradually with increasing downstream distance.
- The hot-film sensor tends to overestimate the mean wall shear stress downstream of the swirl pipe comparing to CFD with the RANS and LES predictions being 8%-76% and 13%-75% lower than the experimental results for various flow velocities.
- The normalized wall shear stress fluctuation rate, presented in the form of a normalized fluctuation rate of voltage signals, is greater downstream of the swirl pipe than in the conditions of non-swirl flows indicating stronger kinetic energy of the swirling flows. The variation of the normalized fluctuation rate is in consistent with that obtained in the LES model.
- The wall shear stress measurement demonstrates that, with the increase of the mean wall shear stress just downstream of the swirl pipe and the prevailing of greater wall shear stress fluctuation rate further downstream of swirl pipe where the increase of wall shear stress fades away, the swirl pipe should enhance the CIP procedures over a considerable downstream distance, at least within the measurement scope of the experimentation (4.6m), in a closed processing system.

It can be concluded that the experimentation has validated to a large extent the CFD models in that the swirl pipe should improve the cleaning efficiency of CIP procedures in closed processing systems.

CHAPTER 9: CONCLUSIONS AND FUTURE WORK

9.1 Conclusions

This thesis intended to address the fundamentals of improving the cleaning efficiency of CIP procedures in closed processing systems by locally introducing an intensified hydrodynamic force from swirl flow induced by an optimised swirl pipe without increasing the overall operating flow velocities. The investigation, carried out employing CFD and experimentation, covered further optimisation of the 4-lobed swirl pipe, RANS and LES simulation of the swirl flows induced by the optimised swirl pipe, and experimental validation of the numerical results. The following conclusions can be drawn from the investigation:

9.1.1 Further Optimisation of the 4-Lobed Swirl Pipe

- The further optimized 400mm length swirl pipe, which has a shorter length of swirl inducing pipe than previous research suggested, resulted in slightly greater initial swirl intensity at its exit at the expense of less pressure loss than the 600mm length swirl pipe.
- A shorter length of 200mm swirl inducing pipe used in conjunction with an entry and exit transition pipe was proven to be optimal in swirl induction.

9.1.2 RANS-Based Simulation of Swirl Flows

- The initial swirl intensity downstream of the swirl pipe was found to be proportional to the flow velocity. The swirl flows were observed to decay exponentially with distance downstream of the swirl pipe and inversely to the Reynolds number of the flow.
- Swirl pipe imposes a tangential wall shear stress within itself which

directs to downstream. A close positive correlation of swirl intensity and the tangential wall shear stress was identified which confirmed that the presence and variation of tangential wall shear stress is closely dependent on swirl intensity.

- The wall shear stress downstream of the swirl pipe was not evenly distributed but followed the pattern of the swirl pipe resulting in a wave-like circumferential distribution.
- Swirl pipe locally increased mean wall shear stress downstream of it, with the increased value and effective distance more pronounced for a flow with a larger Reynolds number.

9.1.3 Large Eddy Simulation of Swirl Flows

- The LES identified four vortex core regions forming inside the lobes of the swirl pipe which precess spirally about the circular pipe axis for some distance and then dissipate. The RANS failed to predict the vortex core regions within the swirl flows.
- The instantaneous tangential velocity, swirl intensity and wall shear stress were observed fluctuating about the time averaged value with a greater fluctuation level were detected in cross-flow planes that are further downstream of the swirl pipe where the swirl effect is less dominant. The fluctuation also increased with increasing flow velocities.
- The spiral pattern of the wall shear stress increases downstream of the swirl pipe which was due to the flow between the rotating vortex core centres and the wall being squeezed, producing a considerable increase in tangential velocity which then gave rise to a tangential wall shear stress.
- The calculation of a normalized wall shear stress fluctuation rate showed that, further downstream of the swirl pipe where the swirl effect and the increase of the mean wall shear stress is less dominant, the flow

experiences a high level of turbulence, resulting in a high fluctuation rate in the wall shear stress.

9.1.4 Experimental Validation

- The experimental pressure drops across the optimised swirl pipe were in good agreement with the RANS and LES predictions. The optimised swirl pipe gave the lowest pressure loss of all the swirl induction pipes tested experimentally.
- The wall shear stress measurements employing a hot-film anemometer validated the CFD models in that the swirl pipe induces a clear increase in both the mean and fluctuation rate of the wall shear stress downstream with the prevailing distance being proportional to the Reynolds number of the flow.
- The experimentation confirmed the CFD prediction that, with the ability to promote intensified hydrodynamic impact on the internal pipe surface, the swirl pipe should enhance the CIP procedures in closed processing systems over a considerable downstream distance dependent on the Reynolds number of the flow.

9.2 Contribution to Knowledge

This thesis contributes to the knowledge in that:

- A comprehensive literature survey of experimental and computational works were carried out in terms of cleaning of closed processing systems, swirl flow modelling and measurements, and equations and terms used by previous researchers.
- A further optimised 4-lobed swirl pipe has been identified and proven to be optimal in inducing swirl in pipes in comparison to previously used swirl induction pipes.

- A positive correlation between the tangential wall shear stress and the swirl intensity of swirl flows has been recognized in the CFD models, which explained why a swirl pipe exerts greater wall shear stress downstream than a circular pipe.
- An insight into the instability of the swirl flows have been given by the LES indicating intensified fluctuation of tangential velocity, swirl intensity and the wall shear stress in swirl flows.
- Rotating vortex cores have been identified within the swirl flows using LES which explains the formation of the spiral pattern of the wall shear stress distribution downstream of the swirl pipe.
- The increase in the mean wall shear stress and its fluctuation rate downstream of the swirl pipe was investigated numerically and experimentally under various flow velocities.
- The fundamentals of CIP improvement in closed processing systems employing an optimised swirl pipe have been addressed. A better understanding of hydrodynamics of swirl flows applied in CIP procedures has been gained especially in the boundary layer where cleaning takes place.

9.3 Further Work

This section gives recommendations for future research in order to further advance the present research.

9.3.1 CFD Modelling

- In the 3D time-dependent LES model of the present research, a Hybrid RANS-LES approach was used in the near-wall regions as it avoids the use of a very fine mesh in the near-wall region which results in substantially increased computational cost that is not affordable for the current personal workstation. The application of a wall resolved LES with

a fine mesh in the near-wall regions should be attempted which may provide improved predictions.

- With the rise of computing power, possibilities of a multiphase large eddy simulation should be examined. The numerical calculation of the particle-water flow can be performed using either an Euler-Euler or an Euler-Lagrange approach with the inclusion of forces such as forces between water and particle, inter-particles etc. The particles should be positioned initially only on the internal pipe walls with the adhesion force between the particles and the wall being specified so that the behaviour of the particles can be observed once the shear stress from the swirl flow is applied. However, such adhesion force model is not available in the FLUENT code and is yet to be developed. Moreover, even if such a model is available, the multiphase LES can be highly computationally expensive and prohibitive for industrial flows.
- So far, the optimisation criterion for swirl induction pipes has been the swirl effectiveness, which is based on the ratio of the swirl intensity produced to the pressure loss. As has been identified in the CFD models the swirl intensity and the tangential wall shear stress is positively correlated. Therefore, a swirl pipe that is optimal in swirl induction should also be optimal in increasing the overall wall shear stress of the swirl flow. However, in some cases, a higher cost of pressure loss may be acceptable to obtain greater wall shear stress. An optimisation criterion that emphasises more on the swirl intensity and less on the pressure loss may be more applicable in some conditions. Numerical optimisation of the swirl pipe based on this criterion is suggested.
- The beneficial effects of swirl pipe have been proven in the cleaning of straight circular pipes. Its potential in the cleaning of more complex geometries such as contractions, expansions, up-stands and bends has not been investigated yet.

9.3.2 Experimental Work

- Previous researchers have used Particle Image Velocimetry (PIV) with a single CCD (Charge Couple Device) camera to measure the flow field of swirl flows. However their attempts in measuring the tangential velocity component were not successful or satisfactory. The application of a stereo PIV which measures three velocity components in a plane (2D3C) using two CCD cameras may facilitate the measurement of tangential velocity, swirl intensity and the decay of the swirl flow.
- Glue-on hot film probe has been used for wall shear stress measurements in this study. The probe was calibrated in cylindrical pipe flows with the longitudinal direction of the hot film being perpendicular to the direction of the flow as maximum heat dissipation between the probe and the water takes place in this condition. However in swirl flows, the flow direction and the longitudinal direction of the hot film cannot be arranged entirely perpendicular to each other as the Glue-on probe once fixed on the pipe surface cannot be adjusted, thus resulting in the underestimation of the measured wall shear stress. This experimental error may be minimized by using a flush-mounted hot film probe which may allow the control of the angle made by the flush-mounted probe by designing a support so that it can be rotated by 5° or 10° each time. A correlation of the voltage outputs and the angles of the flush-mounted probe can be found which can be used to correct the wall shear stress measurements.
- Though the hydrodynamic advantages of the swirl pipe have been proven numerically and experimentally. Its performance in real cleaning practice has not been examined. The cleanability of the swirl flow induced by the swirl pipe can be assessed using an EHEDG (European Hygienic Equipment Design Group) test method (Jensen and Friis, 2004). The degree of cleanliness can be related to the removal of a soured milk soil

containing bacterial spores and can be assessed by evaluating the number of remaining spores after cleaning using the turbulent swirl flow.

REFERENCE

AIAA 1998. Guide for the Verification and Validation of Computational Fluid Dynamics Simulations. *AIAA Guide G-077-1998*. Reston, VA: American Institute of Aeronautics and Astronautics.

AIYEJINA, A., CHAKRABARTI, D. P., PILGRIM, A. & SASTRY, M. K. S. 2011. Wax formation in oil pipelines: A critical review. *International Journal of Multiphase Flow*, 37, 671-694.

ALGIFRI, A. H., BHARDWAJ, R. K. & RAO, Y. V. N. 1988. Turbulence measurements in decaying swirl flow in a pipe. *Applied Scientific Research*, 45, 233-250.

ANSYS. 2011a. *ANSYS FLUENT 14.0 Theory Guide* [Online]. Canonsburg, PA, USA. Available:
<http://148.204.81.206/Ansys/150/ANSYS%20Fluent%20Theory%20Guide.pdf>
 [Accessed 2012.03.05].

ANSYS. 2011b. *ANSYS FLUENT 14.0 User's Guide* [Online]. Canonsburg, PA, USA. Available:
<http://148.204.81.206/Ansys/150/ANSYS%20Fluent%20Users%20Guide.pdf>
 [Accessed 2012.03.01].

ANSYS. 2013a. *ANSYS CFD-Post Users Guide* [Online]. Canonsburg, PA, USA. Available: <http://orange.engr.ucdavis.edu/Documentation12.1/121/CFX/xpost.pdf>
 [Accessed 2012.03.15].

ANSYS. 2013b. *ANSYS Fluent Getting Started Guide* [Online]. Canonsburg, PA, USA. Available:
<https://uiuc-cse.github.io/me498cm-fa15/lessons/fluent/refs/ANSYS%20Fluent%20Getting%20Started%20Guide.pdf> [Accessed 2012.03.09].

ANSYS. 2013c. *ANSYS Fluent Meshing Users Guide* [Online]. Canonsburg, PA, USA. Available:
<http://148.204.81.206/Ansys/150/ANSYS%20Fluent%20Meshing%20Users%20Guide.pdf> [Accessed 2012.03.09].

ANSYS. 2013d. *ANSYS ICEM CFD Tutorial Manual* [Online]. Canonsburg, PA, USA. Available:
<http://www.petrodanesh.ir/Virtual%20Education/Mechanics/ICEM-CFD/PTEC-ICEM%20CFD%2014.5%20Tutorial%20Files.pdf> [Accessed 2012.03.12].

ARIYARATNE, C. 2005. *DESIGN AND OPTIMISATION OF SWIRL PIPES AND TRANSITION GEOMETRIES FOR SLURRY TRANSPORT*. PhD Thesis, University of

Nottingham.

BAKER, D. W. & SAYRE, C. L. 1974. Decay of Swirling Turbulent Flow of Incompressible Fluids in Long Pipes. In: DOWDELL, R. (ed.) *Flow: its measurement and control in science and industry*. Pittsburgh: Instrument Society of America, 301-312.

BAKKER, A. 2002. *Boundary Layers and separation* [Online]. Available: www.bakker.org/dartmouth06/engs150/11-bl.pdf [Accessed 2012.03.15].

BALI, T. 1998. Modelling of heat transfer and fluid flow for decaying swirl flow in a circular pipe. *International Communications in Heat and Mass Transfer*, 25, 349-358.

BARI, S. & VEALE, D. 2012. Improvement of BIB packaging product filling valve CIP performance and efficiency. *Food and Bioproducts Processing*, 90, 849-857.

BÉNÉZECH, T., FAILLE, C. & LÉCRIGNY-NOLF, S. (eds.) 1998. *Removal of Bacillus spores from closed equipment surfaces under cleaning-in-place conditions*, Cambridge: Jesus College.

BÉNÉZECH, T., LELIÈVRE, C., MEMBRÉ, J. M., VIET, A.-F. & FAILLE, C. 2002. A new test method for in-place cleanability of food processing equipment. *Journal of Food Engineering*, 54, 7-15.

BERCA, E.-L. 2007. *INSTRUMENTATION DEVELOPMENT FOR WALL SHEAR STRESS APPLICATIONS IN 3D COMPLEX FLOWS*. PhD Thesis, ÉCOLE POLYTECHNIQUE FÉDÉRALE DE LAUSANNE.

BERGMAN, B. O. & TRÄGÅRDH, C. 1990. An approach to study and model the hydrodynamic cleaning effect. *Journal of Food Process Engineering*, 13, 135-154.

BERTHE, A., KONDERMANN, D., CHRISTENSEN, C., GOUBERGRITS, L., GARBE, C., AFFELD, K. & KERTZSCHER, U. 2009. Three-dimensional, three-component wall-PIV. *Experiments in Fluids*, 48, 983-997.

BHASKARAN, R. & COLLINS, L. 2003. *Introduction to CFD Basics* [Online]. Available: <https://instruct1.cit.cornell.edu/courses/fluent/cfd/intro.pdf> [Accessed 2012.04.09].

BIRD, M. R. & FRYER, P. J. 1991. An experimental study of the cleaning of surfaces fouled by whey proteins. *Trans IChemE, Food Bioprod Proc*, 69C, 13-21.

BOUAINOUCHE, M., BOURABAA, N. & DESMET, B. 1997. Numerical study of the wall shear stress produced by the impingement of a plane turbulent jet on a plate. *Int J Numer Meth H*, 7(6), 548-564.

- CHANGANI, S. D., BELMAR-BEINY, M. T. & FRYER, P. J. 1997. Engineering and chemical factors associated with fouling and cleaning in milk processing. *Experimental Thermal and Fluid Science*, 14, 392-406.
- CHARLES, M. E., CHEH, C. H.-S. & CHU, L. H.-L. 1971. The flow of "settling" slurries in tubes with internal spiral ribs. *The Canadian Journal of Chemical Engineering*, 49, 737-741.
- CHEN, H. C. & PATEL, V. C. 1988. Near Wall turbulence models for complex flows including separation. *AIAA Journal*, 26(6), 641-648.
- CHEN, Z. 2011. *Wall Modeling for Implicit Large-Eddy Simulation*. PhD Thesis, Technische Universität München.
- CHORIN, A. J. 1968. Numerical Solution of the Navier-Stokes Equations. *Mathematics of Computation*, 22, 745-762.
- COGHLAN, A. 1996. Slime City. *New Scientist*, 15 (2045), 32-36.
- CONWAY, S., CARAENI, D. & FUCHS, L. 2000. Large eddy simulation of the flow through the blades of a swirl generator. *International Journal of Heat and Fluid Flow*, 21, 664-673.
- DAY, M. A. 2004. The no-slip condition of fluid dynamics. *Erkenntnis* 33, 285-296.
- DÉCAVÉ, E., DEMILLY, M., FOURCADE, B., BRUCKER, F., BOULANGÉ, L. & BRECHET, Y. 2005. Biological cell detachment kinetics from an inert substrate. *Philosophical Magazine*, 85: 3173.
- DEV, S. R. S., DEMIRCI, A., GRAVES, R. E. & PURI, V. M. 2014. Optimization and modeling of an electrolyzed oxidizing water based Clean-In-Place technique for farm milking systems using a pilot-scale milking system. *Journal of Food Engineering*, 135, 1-10.
- DOUGLAS, J. F., GASORIEK, J. M., SWAFFIELD, J. A. & JACK, L. B. 2006. *Fluid Mechanics (5th Edition)*, PEARSON Prentice Hall.
- DREESEN, P. 2003. *Biofilm: The Key to Understanding and Controlling Bacterial Growth in Automated Animal Drinking Water Systems* [Online]. Available: <http://www.edstrom.com/file.aspx?DocumentId=21> [Accessed 2012.03.06].
- DUDDRIDGE, J. E., KENT, C. A. & LAWS, J. F. 1982. Effect of surface shear stress on the attachment of *Pseudomonas fluorescens* to stainless steel under defined flow conditions. *Biotechnol Bioengng*, 24, 153-164.
- DURBIN, P. A. 2002. A perspective on recent developments in RANS modeling. In: FUEYO, W. R. (ed.) *Engineering Turbulence Modelling and Experiments* 5. Oxford:

Elsevier Science Ltd, 3-16.

EHEDG 1992. A method for assessing the in-place cleanability of food processing equipment. *Trends in Food Science & Technology*, 3, 325–328.

EHEDG 2004. EHEDG Guidelines: Hygienic Equipment Design Criteria. In: FLENNER, S. (ed.). European Hygienic Engineering and Design Group.

ELEVERS, K. T., PETERS, A. C. & GRIFFITH, C. J. 1999. Development of biofilms and control of biofilm in the food industry In: WIMPENNY, J., GILBERT, P., WALKER, J., BRADING, M. & BAYSTON, R. (eds.) *Biofilms: The good, the bad, the ugly* (pp. 139-145). UK: Bioline, 139-145.

FAILLE, C., LEBRET, V., GAVINI, F. & MAINGONNAT, J. F. 1997. Injury and lethality of heat treatment of *Bacillus cereus* spores suspended in buffer and poultry meat. *Journal of Food Protection*, 60, 544–547.

FOCKE, W., ZACHARIADES, J. & OLIVIER, I. 1985. The effect of corrugation inclination angle on the thermodynamic performance of plate heat exchangers. *International Journal of Heat and Mass Transfer*, 28, 1469-1479.

FOKEER, S. 2006. *An Investigation of Geometrically Induced Swirl Applied to Lean Phase Pneumatic Flows*. PhD Thesis, University of Nottingham.

FOKEER, S., LOWNDES, I. S. & HARGREAVES, D. M. 2010. Numerical modelling of swirl flow induced by a three-lobed helical pipe. *Chemical Engineering and Processing: Process Intensification*, 49, 536-546.

FOWLER, H. W. & MCKAY, A. J. 1980. The measurement of microbial adhesion. In: BERKELEY, R. C. W., LYNCH, J. M., MELLING, J., RUTTER, P. R. & VINCENT, B. (eds.) *Microbial Adhesion to Surfaces*. Chichester: Ellis Horwood Limited, 143–161

FRIIS, A. & JENSEN, B. B. B. 2002. Prediction of Hygiene in Food Processing Equipment Using Flow Modelling. *Food and Bioproducts Processing*, 80, 281-285.

FROUD, D., O'DOHERTY, T. & SYRED, N. 1995. Phase averaging of the precessing vortex core in a swirl burner under piloted and premixed combustion conditions. *Combustion and Flame*, 100, 407-412.

GALLOT-LAVALLÉE, T., M. LALANDE, M. & CORRIEU, G. 1984. Cleaning kinetics modeling of holding tubes fouled during milk pasteurization. *Journal of Food Process Engineering*, 7, 123-142.

GANESHALINGAM, J. 2002. *Swirl Induction for Improved Solid-Liquid Flow in Pipes*. PhD Thesis, University of Nottingham.

GEORGE, D. D. 2007. *Effects of 4-lobe swirl-inducing pipe on pressure drop*. Master

Thesis, University of Nottingham.

GERMANO, M., PIOMELLI, U., MOIN, P. & CABOT, W. H. 1996. *Dynamic Subgrid-Scale Eddy Viscosity Model*, Stanford, CA, Center for Turbulence Research.

GIJSEN, F. J. H., GOIJAERTS, A. M., VOSSE, F. N. V. D. & JANSSEN, J. D. 1997. A new method to determine wall shear stress distribution. *Journal of Rheology*, 41(5), 995-1006.

GILLHAM, C. R., FRYER, P. J., HASTING, A. P. M. & WILSON, D. I. 1999. Cleaning-in-Place of Whey Protein Fouling Deposits. *Food and Bioproducts Processing*, 77, 127-136.

GRABHOFF, A. 1992. Hygienic design: The basis for computer controlled automation. *Food and Bioproducts Processing, Transactions of The Institution of Chemical Engineers Part C*, 70, 69-77.

GRABHOFF, A. 1997. Cleaning of heat treatment equipment. In: FEDERATION, I. D. (ed.) *Fouling and Cleaning of Heat Treatment Equipment*. Brussels: International Dairy Federation, 32-44.

GROBE, S. & SCHRÖDER, W. 2008. Dynamic wall-shear stress measurements in turbulent pipe flow using the micro-pillar sensor MPS3. *International Journal of Heat and Fluid Flow*, 29, 830-840.

GUILLEMOT, G., LORTHOIS, S., SCHMITZ, P. & MERCIER-BONIN, M. 2007. Evaluating the Adhesion Force Between *Saccharomyces Cerevisiae* Yeast Cells and Polystyrene From Shear-Flow Induced Detachment Experiments. *Chemical Engineering Research and Design*, 85, 800-807.

GUPTA, A., LILLEY, D. G. & SYRED, N. 1984. Swirl Flow. *Energy and Engineering Sciences Series*. Tunbridge Wells: Abacus Press, 475.

H.K.VERSTEEG & W.MALALASEKERA 2010. *An Introduction To Computational Fluid Dynamics: The Finite Volume Method Second Edition*, England, Prentice Hall.

HALL, J. E. 1998. Computational fluid dynamics: A tool for hygienic design. In: WILSON, D. I., FRYER, P. J. & HASTING, A. P. M. (eds.) *Fouling and cleaning in food processing*. Cambridge: Jesus College, 144-151.

HALSEY, D. M. 1987. Flowmeters in Swirling Flows. *Journal of Physics E: Scientific Instruments*, 20, 1036-1040.

HANRATTY, T. J. & CAMPBELL, J. A. 1983. Measurement of wall shear stress. In: GOLDSTEIN, R. J. (ed.) *Fluid mechanics measurements*. Washington, DC: Hemisphere Corporation, 559-615.

- HARITONIDIS, J. H. 1989. The Measurement of Wall Shear Stress. *In: GAD-EL-HAK, M. (ed.) Advances in Fluid Mechanics Measurements*. Springer-Verlag, 229-261.
- HEYWOOD, N. I. & ALDERMAN, N. J. 2003. Developments in Slurry Pipeline Technologies. *Chem. Engng. Progress*, April, 36-43.
- HOWARD, G. W. 1939. Effects of Rifling on Four-Inch Pipe Transporting Solids. *Transactions of the American Society of Civil Engineers*, 106, 135-147.
- HUANG, Y. & YANG, V. 2009. Dynamics and stability of lean-premixed swirl-stabilized combustion. *Progress in Energy and Combustion Science*, 35, 293-364.
- HUBBE, M. A. 1984. Theory of detachment of colloidal particles from flat surfaces exposed to flow. *Colloids and Surfaces* 12, 151-178.
- HUSMARKA, U., FAILLEB, C., RÖNNER, U. & BENEZECH, T. 1999. Bacillus spores and moulding with TTC agar: A useful method for the assessment of food processing equipment cleanability. *Biofouling*, 14, 15-24.
- HWANG, Y. K. & WOO, N. S. 2007. Wall Shear Stress in the Helical Annular Flow with Rotating Inner Cylinder. *DIFFUSION AND DEFECT DATA PART B SOLID STATE PHENOMENA*, 120, 261-266.
- ITO, S., OGAWA, O. & KURODA, C. 1980. Turbulent Swirling Flow in a Circular Pipe. *JOURNAL OF CHEMICAL ENGINEERING OF JAPAN*, 13, 6-10.
- JENSEN, B. B. B. & FRIIS, A. 2004. Critical wall shear stress for the EHEDG test method. *Chemical Engineering and Processing: Process Intensification*, 43, 831-840.
- JENSEN, B. B. B. & FRIIS, A. 2005. Predicting the cleanability of mix-proof valves by use of wall shear stress. *Journal of Food Process Engineering*, 28, 89-106.
- JENSEN, B. B. B., FRIIS, A., BÉNÉZÉCH, T., LEGENTILHOMME, P. & LELIÈVRE, C. 2005. Local Wall Shear Stress Variations Predicted by Computational Fluid Dynamics for Hygienic Design. *Food and Bioproducts Processing*, 83, 53-60.
- JENSEN, B. B. B., STENBY, M. & NIELSEN, D. F. 2007. Improving the cleaning effect by changing average velocity. *Trends in Food Science & Technology*, 18, S58-S63.
- JONES, T. F. 1997. Pipe Design for Improved Particle Distribution and Reduced Wear. ECSC Final Report 7220-EA/841.
- JONES, T. F. & GANESHALINGAM, J. 2002. Towards optimal swirl-inducing pipe. 15th *International Symposium on Hydrotransport*. Banff, Canada: BHR Group.
- JØRGENSEN, F. E. 2002. *How to measure turbulence with hotwire anemometers*

- [Online]. DANTEC DYNAMICS. Available: <http://www.dantecdynamics.com/Admin/Public/DWSDownload.aspx?File=files%2ffiler%2fsupport%2fand%2fdownload%2fresearch%2fand%2feducation%2fpracticalguide.pdf> [Accessed April 5th 2013].
- K-PATENTS. 2013. *EHEDG method for assessing the in-place cleanability of food processing equipment* [Online]. EHEDG. Available: http://www.kpatents.com/assets/files/downloads/tcn_1-00-02_ehedg_test.pdf [Accessed 2015.01.12].
- KAWAI, S. & LARSSON, J. 2010. A dynamic wall model for large-eddy simulation of high Reynolds number compressible flows. *CTR Annual Research Briefs*, 25-37.
- KIM, S.-E. & CHOUDHURY, D. 1995. A Near-Wall Treatment Using Wall Functions Sensitized to Pressure Gradient. In *ASME FED Vol. 217, Separated and Complex Flows*. ASME.
- KITOH, O. 1991. Experimental study of turbulent swirling flow in a straight pipe. *Journal of Fluid Mechanics*, 225, 445-479.
- KOBAYASHI, T. & YODA, M. 1987. Modified k- ϵ model for turbulent swirling flow in a straight pipe. *JSME International Journal, Series 2: Fluids Engineering, Heat Transfer, Power Combustion, Thermophysical Properties* 259, 66-71.
- KRISHNA, M. S. R. V. 2009. *Investigation of Swirl Flows Applied to the Oil and Gas Industry*. Master's thesis, Texas A&M University.
- LAUGA, E., BRENNER, M. P. & STONE, H. A. 2005. Microfluidics: The No-Slip Boundary Condition. In: EDITORS J. FOSS, C. T., A. YARIN, SPRINGER (ed.) *Handbook of Experimental Fluid Dynamics*. New-York.
- LAUNDER, B. E. & SPALDING, D. B. 1972. *Lectures in Mathematical Models of Turbulence*, London, England, Academic Press Inc.
- LAUNDER, B. E. & SPALDING, D. B. 1974. The numerical computation of turbulent flows. *Computer Methods in Applied Mechanics and Engineering*, 3, 269-289.
- LELIEVELD, H. L. M., MOSTERT, M. A., HOLAH, J. & WHITE, B. 2003. *Hygiene in Food Processing*, Cambridge, UK, Woodhead Publishing.
- LELIÈVRE, C., ANTONINI, G., FAILLE, C. & BÉNÉZECH, T. 2002a. Cleaning-in-Place Modelling of Cleaning Kinetics of Pipes Soiled by Bacillus Spores Assuming a Process Combining Removal and Deposition. *Food and Bioproducts Processing*, 80, 305-311.
- LELIÈVRE, C., LEGENTILHOMME, P., CÉCILE GAUCHERB, LEGRANDB, J., FAILLEA, C.

- & BÉNÉZECHA, T. 2002. Cleaning in place: effect of local wall shear stress variation on bacterial removal from stainless steel equipment. *Chemical Engineering Science*, 57, 1287-1297.
- LI, G., HALL, P., MILES, N. & WU, T. 2015. Optimization of a Four-Lobed Swirl Pipe for Clean-In-Place Procedures. *ICCE 2015 : International Conference on Clean Energy*. San Francisco, USA: World Academy of Science, Engineering and Technology.
- LI, H. & TOMITA, Y. 1994. Characteristics of Swirling Flow in a Circular Pipe. *Journal of Fluids Engineering*, 116, 373-373.
- LILLY, D. K. 1967. The Representation of Small-Scale Turbulence in Numerical Simulation Experiments. In: GOLDSTINE, H. H., ed. *Proceedings of the IBM Scientific Computing Symposium on Environmental Sciences*, 1967 Yorktown Heights, New York. International Business Machines Corporation (IBM), 195-210.
- LORTHOIS, S., SCHMITZ, P. & ANGLES-CANO, E. 2001. Experimental Study of Fibrin/Fibrin-Specific Molecular Interactions Using a Sphere/Plane Adhesion Model. *JOURNAL OF COLLOID AND INTERFACE SCIENCE*, 241, 52-62.
- MATIC, M. 2010. *Importance of Beer Line Cleaning* [Online]. Available: <http://www.micromatic.com/draft-keg-beer-edu/importance-beer-line-cleaning-aid-72.html> [Accessed 2012.03.06].
- MIKULČIĆ, H., VUJANOVIĆ, M., ASHHAB, M. D. S. & DUIĆ, N. 2014. Large eddy simulation of a two-phase reacting swirl flow inside a cement cyclone. *Energy*, 75, 89-96.
- MONFORT, D., BENHAMADOUCHE, S. & SAGAUT, P. 2010. Meshless approach for wall treatment in Large-Eddy Simulation. *Computer Methods in Applied Mechanics and Engineering*, 199, 881-889.
- NAJAFI, A. F., MOUSAVIAN, S. M. & AMINI, K. 2011. Numerical investigations on swirl intensity decay rate for turbulent swirling flow in a fixed pipe. *International Journal of Mechanical Sciences*, 53, 801-811.
- NAJAFI, A. F., SAIDI, M. H., SADEGHIPOUR, M. S. & SOUHAR, M. 2005. Numerical analysis of turbulent swirling decay pipe flow. *International Commission In Heat and Mass Transfer*, 32. Elsevier Publisher 627-638.
- NEJAD, A. S., VANKA, S. P., FAVALORO, S. C., SAMIMY, M. & LANGENFELD, C. 1989. Application of laser velocimetry for characterization of confined swirling flow. *Journal of Engineering for Gas Turbines and Power*, 111, 36-45.
- NESBITT, B. 2000. *Guide to European Pumps and Pumping. European Guide Series (REP)*, Europe, John Wiley and Sons Ltd.

- NGUYEN, T. D., WELLS, J. C. & NGUYEN, C. V. 2010. Wall shear stress measurement of near-wall flow over inclined and curved boundaries by stereo interfacial particle image velocimetry. *International Journal of Heat and Fluid Flow*, 31, 442-449.
- O'DOHERTY, T. & GARDNER, R. 2005. Turbulent Length Scales in an Isothermal Swirling Flow. *The 8th Symposium on Fluid Control, Measurement and Visualization*. Japan.
- OBERKAMPF, W. L. & TRUCANO, T. G. 2002. Verification and validation in computational fluid dynamics. *Progress in Aerospace Sciences*, 38, 209-272.
- PARCHEN, R. R. & STEENBERGEN, W. J. 1998. An Experimental and Numerical Study of Turbulent Swirling Pipe Flows. *Fluids Eng*, 120(1), 54-61.
- PATHOGENCOMBAT. 2011. *Factors affecting fouling and cleanability of closed food contact surface* [Online]. EU Integrated Project PathogenCombat. Available: <http://www.pathogencombat.com/Publications/~media/Adtomic/Unique%20Achievements/Leaflets/Factors%20affecting%20fouling%20and%20cleanability%20of%20closed%20food%20contact%20surface.ashx> [Accessed 2012.03.08].
- PAULSSON, B. O. & TRÄGÅRDH, C. 1989. Removal of soil particles in wall boundary layer flows-The hydrodynamic effect. In: M. G. KESSLER, K. WELCHNER & LUND, D. B., eds. *Fouling and cleaning in food processing*, June, 1989 1989 prien.
- PAZ, C., SUÁREZ, E., CONCHEIRO, M. & PORTEIRO, J. 2013. Experimental study of soot particle fouling on ribbed plates: Applicability of the critical local wall shear stress criterion. *Experimental Thermal and Fluid Science*, 44, 364-373.
- PAZ, C., SUÁREZ, E., EIRÍS, A. & PORTEIRO, J. 2012. Experimental evaluation of the critical local wall shear stress around cylindrical probes fouled by diesel exhaust gases. *Experimental Thermal and Fluid Science*, 38, 85-93.
- PIOMELLI, U. 1999. Large eddy simulation achievements and challenges. *Progress in Aerospace Science*, 35, 335-362.
- POWELL, M. S. & SLATER, N. K. H. 1982. Removal rates of bacterial cells from glass surfaces by fluid shear. *Biotechnol Bioengng*, 24, 2527-2537.
- RAO, A. R. & KUMAR, B. 2007. *Friction Factor for Turbulent Pipe Flow* [Online]. Department of Civil Engineering, IISc, Bangalore-560012, India. Available: <http://eprints.iisc.ernet.in/id/eprint/9587> [Accessed 1 Dec. 2014].
- RAYLOR, B. 1998. *Pipe design for improved particle distribution and improved wear*. PhD Thesis, University of Nottingham.
- READER-HARRIS, M. J. 1994. The decay of swirl in a pipe. *International Journal of Heat and Fluid Flow*, 15 212-217.

RICHARDSON, P. S., GEORGE, R. M. & THORN, R. D. 2000. Application of computational fluid dynamics simulation to the modelling of cleanability of food processing equipment. *Food & Drink 2000 Processing Solutions for Innovative Products*. Rugby, UK: Institution of Chemical Engineers, 64-66.

ROBINSON, A. W. 1921. *Delivery pipe for hydraulic dredging machine*. US patent application.

ROCKLAGE-MARLIANI, G., SCHMIDTS, M. & VASANTA RAM, V. 2003. Three-Dimensional Laser-Doppler Velocimeter Measurements in Swirling Turbulent Pipe Flow. *Flow, Turbulence and Combustion*, 70, 43-67.

ROCKLAGE-MARLIANI G., S. M. A. R. V. I. V. 2003. Three-dimensional Laser-Doppler Velocimeter Measurements in Swirling Turbulent Pipe Flow. *Flow Turbulence and Combustion*, 70, 43-67.

RODE, S., MIDOUX, N., LATI:, M. A., S., A. & SAATDJIAN, E. 1994. Hydrodynamic of liquid flows in packed beds:An experimental study using of electrochemical shear rate sensors. *Chemical Engineering Science*, 49, 889-900.

RUDOLPH, I., REYER, M. & NITSCHKE, W. 2009. A WALL SHEAR STRESS MEASUREMENT TECHNIQUE USING THE THERMAL WAKES OF SMALL HEATED SPOTS. *Proceedings of The Institution of Mechanical Engineers Part G-journal of Aerospace Engineering*, 683-690.

SCHRIEK, W., SMITH, L. G., HAAS, D. B. & HUSBAND, W. H. W. 1974. The Potential of Helically Ribbed Pipes for Solids Transport. *Canadian Mining and Metallurgical Bulletin*. Canadian Institute of Mining and Metallurgy, 84-91.

SELVAM, R. P. & GOVINDASWAMY, S. 2001. *AEROELASTIC ANALYSIS OF BRIDGE GIRDER SECTION USING COMPUTER MODELING* [Online]. University of Arkansas. Available: <http://ntl.bts.gov/lib/11000/11100/11186/1095.pdf> [Accessed 2014.05.14].

SENOO, Y. & NAGATA, T. 1972. Swirl flow in long pipes with different roughness. *Bulletin of the JSME*, 15, 1514-1521.

SHARMA, M. M., CHAMOUN, H., SARMA, D. S. H. S. R. & SCHECHTER, R. S. 1991. Factors Controlling the Hydrodynamic Detachment of Particles from Surfaces. *Journal of Colloid and Interface Science*, 149, 121-134.

SHARMA, M. M., CHAMOUN, H., & SITA RAMA SARMA, D. S. H. 1991. Factors controlling the hydrodynamic detachment of particles from surfaces. *Journal of Colloid interface Science*, 28(3), 121-134.

SHAW, C. T. 1992. *Using Computational Fluid Dynamics*, New York, Prentice Hall.

- SHEPLAK, M., CATTAFESTA, L. & NISHIDA, T. 2004. MEMS Shear Stress Sensors: Promise and Progress. *24th AIAA Aerodynamic Measurement Technology and Ground Testing Conference*. Portland, OR.
- SHIH, T.-H., LIOU, W. W., SHABBIR, A., YANG, Z. & ZHU, J. 1995. A New $k-\epsilon$ Eddy-Viscosity Model for High Reynolds Number Turbulent Flows. *Computers & Fluids*, 24, 227–238.
- SHUR, M. L., SPALART, P. R., STRELETS, M. K. & TRAVIN, A. K. 2008. A hybrid RANS-LES approach with delayed-DES and wall-modelled LES capabilities. *International Journal of Heat and Fluid Flow*, 29, 1638–1649.
- SINGH, V. P. & CHARLES, M. E. 1976. The flow of sand/water slurries in horizontal pipes with internal spiral ribs — effect of rib height. *The Canadian Journal of Chemical Engineering*, 54, 249–254.
- SLEIGH, A. & GOODWILL, I. 2008. *An Introduction to Fluid Mechanics* [Online]. Available: www.efm.leeds.ac.uk/CIVE/FluidsLevel1 [Accessed 2012.03.06].
- SMAGORINSKY, J. 1963. General Circulation Experiments with the Primitive Equations. *Monthly Weather Review*, 91, 99–164.
- SMITS, A. J. & LIM, T. T. 2000. *Flow visualisation: techniques and examples*, Imperial College Press.
- SPALL, R. E. & ASHBY, B. M. 2010. A Numerical Study of Vortex Breakdown in Turbulent Swirling Flows. *Journal of Fluids Engineering*, 122, 179–183.
- SPANNER, E. F. 1940. *Improvements in tubular heat exchanger apparatus*. GB patent application.
- SPEZIALE, C. G., S. SARKAR & B. GATSKI, T. 1991. Modelling the Pressure-Strain Correlation of Turbulence: An Invariant Dynamical Systems Approach. *J. Fluid Mech*, 227, 245–272.
- SPEZIALE, C. G., YOUNIS, B. A. & BERGER, S. A. A. 2000. Analysis and modelling of turbulent flow in an axially rotating pipe. *Journal of Fluid Mechanics*, 407, 1–26.
- SPIROFLO, I. 2010. *spiroflo and biofilms* [Online]. Littleton, USA. Available: http://www.spiroflo.com/media/spiroflo_and_biofilms_brochure.pdf [Accessed 2012.03.09].
- STEENBERGEN, W. & VOSKAMP, J. 1998. The rate of decay of swirl in turbulent pipe flow. *Flow measurement and instrumentation*, 9, 67–78.
- SU, Y., ZHANG, M., ZHU, X., HU, Q. & GENG, Y. 2010. Measurements of wall shear stress in horizontal air–water bubbly flows. *Flow measurement and instrumentation*,

21, 373-381.

SUMER, B. M., ARNSKOV, M. M., CHRISTIANSEN, N. & 2, F. E. J. 1993. Two-component hot-film probe for measurements of wall shear stress. *Experiments in Fluids*, 15, 380-384.

SYRED, N. 2006. A review of oscillation mechanisms and the role of the precessing vortex core (PVC) in swirl combustion systems. *Progress in Energy and Combustion Science*, 32, 93-161.

TEMPLETON, J. A., MOIN, P. & WANG, M. 2006. *WALL MODELS FOR LARGE-EDDY SIMULATION BASED ON OPTIMAL CONTROL THEORY* [Online]. California: Flow Physics and Computation Division, Department of Mechanical Engineering, Stanford University. Available: <http://web.stanford.edu/group/fpc/Publications/TF/templeton.pdf> [Accessed 2014.10.03].

TIMOSHENKO & STEPHEN, P. 1983. *History of Strength of Materials*, Dover Publications

TONKIN, R. J. J. 2004. *Swirling pipeflow of non-Newtonian and particle-laden fluids*. PhD Thesis, University of Nottingham.

VAZE, M. J. & BANERJEE, J. 2012. Estimation of Wall Shear Stress in Two-Phase Flow Using Hot Film Anemometry 2012 *International Conference on Fluid Dynamics and Thermodynamics Technologies (FDTT 2012)*. Singapore.

VERSTEEG, H. K. & MALALASEKERA, W. 1995. *An Introduction to computational fluid dynamics The finite volume method*, Longman House, Burnt Mill, Harlow, Longman Scientific & Technical.

VIGUERAS-ZUÑIGA, M. O., VALERA-MEDINA, A. & SYRED, N. 2012. Studies of the Precessing Vortex Core in Swirling Flows. *Journal of Applied Research and Technology*, 10, 755-765.

VISSER, J. 1970. Measurement of the force of adhesion between submicron carbon-black particles and a cellulose film in aqueous solution. *Journal of Colloid interface Science*, 34(1), 26-31.

VISSER, J. 1976. Adhesion of colloidal Particles. In: MATIJEVIC, E. (ed.) *Surface and Colloid Science*. New York: Wiley, 3-84.

VISSER, J. 1995. PARTICLE ADHESION AND REMOVAL: A REVIEW. *Particle Science and Technology*, 13, 169-196.

WEGNER, B., MALTSEV, A., SCHNEIDER, C., SADIKI, A., DREIZLER, A. & JANICKA, J. 2004. Assessment of unsteady RANS in predicting swirl flow instability based on LES

- and experiments. *International Journal of Heat and Fluid Flow*, 25, 528-536.
- WHITE, F. 2003. Fluid Mechanics. In: HOLMAN, J. P. & LLOYD, J. (eds.) *Fourth Edition*. Mc Graw-Hill Publishing Co. .
- WILCOX, D. C. 1998. *Turbulence Modelling for CFD (2nd Edition)*, La Canada CA, D C W Industries.
- WINTER, K. G. 1977. An Outline of the Techniques Available for the Measurement of Skin Friction in Turbulent Boundary Layers. *Progress in the Aeronautical Sciences*, 18, 1-57.
- WOLFE, S. E. 1967. *Method and apparatus for transporting slurries*. US patent application.
- WOLFSHTEIN, M. 1969. The Velocity and Temperature Distribution of One-Dimensional Flow with Turbulence Augmentation and Pressure Gradient. *International Journal of Heat and Mass Transfer*, 12, 301-318.
- WOOD, R. J. K., JONES, T. F., MILES, N. J. & GANESHALINGAM, J. 2001. Upstream swirl-induction for reduction of erosion damage from slurries in pipeline bends. *Wear*, 250 (2001), 770-778.
- YANG, Y. & KÆR, S. K. 2012. Comparison of Reynolds Averaged Navier-Stokes Based Simulation and Large-eddy Simulation for One Isothermal Swirling Flow. *Journal of Thermal Science*, 21, 154-161.
- YIANTSIOS, S. G. & KARABELAS, A. J. 1995. Detachment of Spherical Microparticles Adhering on Flat Surfaces by Hydrodynamic Forces. *JOURNAL OF COLLOID AND INTERFACE SCIENCE*, 176, 74-85.
- YUILLE, N. 1927. *Dredger Pipeline*. US patent application.
- ZHU, H., LIN, Y., ZENG, D., ZHOU, Y. & XIE, J. 2012. Simulation analysis of flow field and shear stress distribution in internal upset transition zone of drill pipe. *Engineering Failure Analysis*, 21, 67-77.
- ZOETEWIJ, M., DONCK, J. V. D. & VERSLUIS, R. 2008. *Particle removal in linear shear flow: model prediction and experimental validation* [Online]. The Netherlands: TNO Science and Industry. Available: <http://www.mstconf.com/UMaine%20Presentations/Particle11zoetewijarticle.pdf> [Accessed 2012.03.02].

APPENDICES

Appendix 2.1 Mechanism of Particle Detachment in Flow

The model presented here is proposed by Lorthois et al. (2001) to estimate the net adhesion force of fibrin-coated spherical latex beads on fibrin-coated flat surface. The model was used later by Guillemot et al. (2007) to evaluate the adhesion force between *Saccharomyces cerevisiae* yeast cells and polystyrene.

In this model, it is assumed the presence of specific bonds between particles and surfaces defines the contact area (contact radii a); and the roughness of polystyrene is small compared to the characteristic thickness (l) of the protein meshwork binding the particle to the flat surface.

The particles on a surface experience several forces. These forces can be related to the particle itself, or being induced by the flow field at the location of the particle (Zoeteweij et al., 2008). The relevant forces acting on a particle are shown schematically in Figure A2.1.1 (Guillemot et al., 2007).

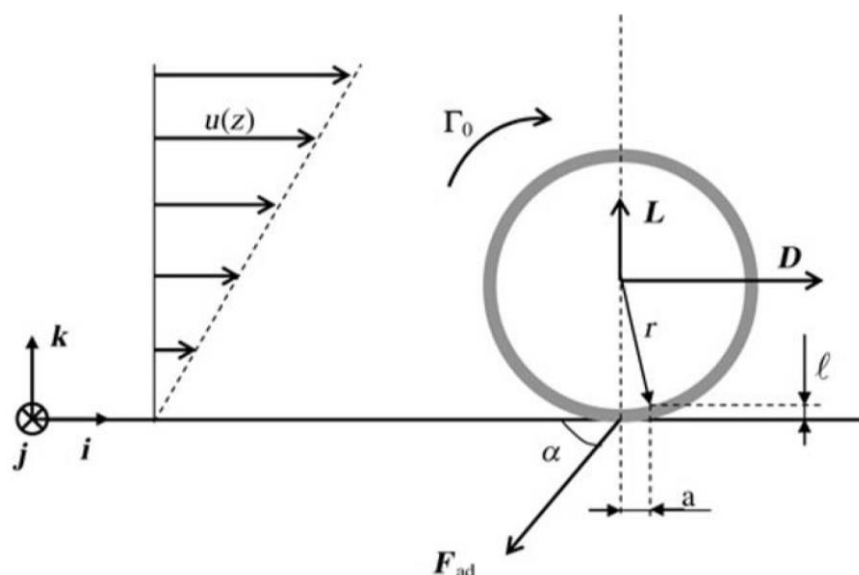


Figure A2.1.1 Schematic diagram of a particle adhering to a flat surface and definition of hydrodynamic forces, torque and adhesion force exerted over the particle (after Guillemot et al. ,2007)

Where D : drag force; L : lift force; Γ_0 : torque at sphere centre; F_{ad} : adhesion force; r : particle radii; a : contact area radii; ℓ : characteristic thickness of the protein meshwork binding the particle to the polymeric plate; α : the angle which defines the direction of deformation of the material constituting the sticking layer.

Adhesion Force

The gravity force and the Van der Waals force are directly related to the particle, and not affected by the flow. They are the adhesion force attach the particles on the equipment surface (Zoeteweij et al., 2008).

The gravity force is given by:

$$F_G = m \cdot g = \rho \cdot V \cdot g \quad \text{A2.1.1}$$

Where:

F_G =gravity force

m = particle mass

V =particle volume

g = the gravitational acceleration

The second contribution is the Van der Waals force, which is for a spherical particle given by:

$$F_V = \frac{A_H \cdot d}{12z_0^2} \left(1 + \frac{2a^2}{z_0 \cdot d} \right)$$

A2.1.2

Where:

A_H = material dependent Hamaker constant

d = particle diameter

z_0 = particle-to-surface distance (usually assumed to be $z_0=0.4$ nm)

a = contact area radius of the particle, as shown in Figure A2.1.1

For most metals and glass particles, the gravity becomes important for particle diameters larger than 1.0 mm. For plastic materials, this transition occurs at 10 mm. For smaller particles, the gravity interaction (proportional to d^3) can be neglected, and the Van der Waals force (proportional to d) is the most relevant interaction. Electrostatic and capillary forces are not taken into account in here.

Removal Force

The surrounding fluid exerts pressure forces and viscous forces on an object. The components of the resultant force acting on the object immersed in the fluid are the drag force and the lift force (Bakker, 2002).

Cleaning flow will exert forces on the particles, which can be classified in lift and drag force. Near the surface, a boundary layer will be present in the flow. In this boundary layer, there is a gradient in the stream-wise velocity. Close to the wall the velocities are small, a linear velocity profile is assumed in the boundary layer.

The velocity gradient results in a lift force F_L acting perpendicular to the stream-wise direction, pointing towards the region with higher velocities. Since the particles are in the boundary layer of the flow, these particle will experience a lift force F_L expressed by (Zoetewij et al., 2008):

$$F_L = 1.615 \cdot \eta \cdot d^2 \left(\frac{\rho}{\eta} \frac{\partial u}{\partial y} \right)^{1/2} U_p$$

A2.1.3

Where:

$\partial u / \partial y$ = gradient in y-direction of the velocity profile $u(y)$, the term must be evaluated at the centre of the particle, at $y=d/2$

p = location of particle whose flow velocity is U_p

d = particle diameter

η = fluid viscosity

The drag force represents the force that is exerted on a particle by a flow in stream-wise direction. The drag force is given by:

$$F_D = \frac{1}{2} \rho U^2 \cdot C_D \cdot A$$

A2.1.4

Where:

ρ = fluid density

U = characteristic fluid velocity at the position of the particle ($=U_p$)

C_D = drag coefficient

A = effective area of the particle perpendicular to the flow direction

For small particles (particle Reynolds number in the Stokes range $10^{-4} < Re_p < 2$), the value of the drag coefficient C_D is given by:

$$C_D = 1.7009 \cdot f = 1.7009 \frac{24}{Re_p}$$

A2.1.5

The term $f = 24/Re_p$ represents the friction on a spherical particle falling in a static fluid column. The pre-factor 1.7009 corrects for the effect of the wall, which changes the flow pattern around the particle and thus the drag force.

Particle Motions

Based on the particle and flow properties, possible particle behaviours can be categorized in: complete removal by lift, sliding over the surface and rolling over the surface (Zoetewij et al., 2008).

The particle motion in flow is based on the force and the torque balance between the forces. When the lift force is larger than the adhesive force (Van der Waals force and the gravity force) $F_L \geq F_V + F_G$, particles will be lifted up from the surface.

In situations where the drag force is larger than the static friction force, the particle will start sliding over the surface. The static friction of a particle on a surface is expressed by the static friction factor μ . The minimum force needed to overcome static friction is $F_{friction} = \mu \sum F_{\perp}$. F_{\perp} are forces perpendicular to the surface. So for particle sliding, the inequality is $F_D \geq \mu(\overrightarrow{F_V} + \overrightarrow{F_G} + \overrightarrow{F_L}) = \mu(F_V + F_G - F_L)$ with lift force is in the opposite direction.

Particle rotation happens when:

$$M_D + F_D L_1 + F_L L_2 \geq (F_V + F_G) L_2$$

A2.1.6

Where:

L_1 = length of arm of torque for drag force, equals $d/2$ assuming that the contact radius is very small compared to the particle diameter d

L_2 = length of arm of torque for drag force, equals the contact radius a

M_D = moment of the surface stresses

Among the different motions (lift, sliding and rotation), particle rotation turns out to be the responsible mechanism of particle removal. The lift force is, in general, much smaller than the adhesion force. Some researchers define the critical hydrodynamic force as the fluid drag force acting on an attached particle required to initiate rolling (Sharma et al., 1991).

Visser (1976) suggested that the lift force contributes negligibly to the dislodging force acting on the particle. He considered the fluid drag as a tangential force contributing to the dislodging force, and expressed the tangential force in terms of shear stress acting on the wall. This gives:

$$F_H = 32R^2\tau_w \quad \text{A2.1.7}$$

Where R is the particle radius, he postulated that the removal of spherical particles from a flat surface is determined by the magnitude of the wall shear stress τ_w . He also postulated that the tangential force required for particle release is proportional to the adhesion force:

$$F_H = \gamma F_{ad} \quad \text{A2.1.8}$$

Where F_{ad} is the adhesion force, F_H is tangential force, γ is a proportionality constant that will depend on the particle release mechanism.

If the release mechanism is sliding, γ is the coefficient of friction.

If the release mechanism is rolling, the constant of proportionality has been evaluated by Hubbe (1984) by performing a torque balance and is given as :

$$F_{ad} \cdot a = 1.399 F_H \cdot R \quad A2.1.9$$

Where a is the radius of the contact area (see Figure A2.1.1). It is a function of particle material and size and surface forces acting between the particle and contact surface. It is demonstrated by Sharma's (1991) centrifuge experiments that the mechanism of detachment is rolling rather than sliding or lifting.

The equation theoretically provides a physical insight into how hydrodynamic force affects detachment from a surface and a method for estimating the hydrodynamic force required to release an attached particle. But it cannot be precise because surface roughness appears to play a key role in determining the release force (Sharma et al., 1991).

Relationship between Adhesion Force and Wall Shear Stress

It is necessary to demonstrate the relationship of adhesion force that binds particles to the pipe surface and the wall shear stress at detachment since wall shear stress is considered the governing factor for cleaning.

From Figure A2.1.1 (Guillemot et al., 2007), it is easy to have

$$r^2 = a^2 + (r - l)^2 \quad A2.1.10$$

Based on the simplification that l is negligible compared to r (Lorthois et al., 2001, Décavé et al., 2005), we have

$$a = \sqrt{2lr} \quad A2.1.11$$

Use the classical expression of hydrodynamic drag, torque at sphere centre, and lift in the ideal case of a laminar infinite linear shear flow over a single spherical particle in contact with an infinite plane at rest. And Adopt Newton's second law. The relationship of adhesion force and wall shear stress can be expressed in the follow equations.

$$\|F_{ad}\| \cos \alpha = 32.0 r^2 \tau_w \quad A2.1.12$$

$$\|F_{ad}\| \sin \alpha = 43.9 r^3 \tau_w \quad A2.1.13$$

α is the angle which defines the direction of deformation of the material constituting the sticking layer (see Figure A2.1.1).

Eliminating α between these two equations leads we have

$$\tau_w = \frac{\|F_{ad}\|}{r^2 \sqrt{1024 + 964(r/l)}} \quad A2.1.14$$

$$\|F_{ad}\| = \tau_w r^2 \sqrt{1024 + 964(r/l)} \quad A2.1.15$$

Equation 2.14 and 2.15 theoretically demonstrate a positive correlation between adhesion force of particle to equipment surface and fluid shear stress on the wall. It seems that if the adhesion force is determined, wall shear stress required to remove, for example half of the initially attached particles, can be calculated using

$$\|F_{ad}\| = \tau_{w50\%} r^2 \sqrt{1024 + 964(r/l)} \quad A2.1.16$$

However, adhesion force value between particle and pipe surface is influenced by many factors as discussed in section 2.1.3.2. Very few literatures report the

adhesion force value. And even the value reported can only reflect that specific experiment condition. It is not universally applicative. And direct measurement of the adhesion force value can be very complex.

An alternative approach to show the advantages of swirling flow with respect to non-swirling flow could be comparing the percentage of residual particles after cleaning using the two kind of flow in same temperature and flow rate. Or to compare the velocity required for the two kind of flow to achieve same cleanability. For theoretically a lower velocity is required to yield the same level of local wall shear stress compared with non-swirling flow.

According to the literature, a relationship of wall shear stress and cleaning efficiency was established experimentally and theoretically. So it is possible to use wall shear stress to investigate the potential of swirl pipe on cleaning in straight circular pipe.

Appendix 3.1 Spreadsheet for 4-Lobed Transition Pipe

Table A3.1 Spreadsheet for 4-Lobed Transition Pipe

$\gamma(deg)$	$\gamma(rad)$	f_l	f	$R(mm)$	$y(mm)$	$r(mm)$	$\beta(n=0.5)$	x/L	$Twist(t=1)$
45	0.7854	0	0.2854	25	0	25	0	0	0
46	0.8029	0.0243	0.3032	24.8809	0.6036	24.4578	0.1224	0.2275	20.4775
47	0.8203	0.0477	0.3215	24.7622	1.1816	23.9412	0.1731	0.2732	24.5840
48	0.8378	0.0704	0.3405	24.6437	1.7355	23.4486	0.2120	0.3046	27.4146
49	0.8552	0.0924	0.3601	24.5254	2.2668	22.9785	0.2448	0.3295	29.6567
50	0.8727	0.1138	0.3803	24.4074	2.7769	22.5296	0.2738	0.3506	31.5512
51	0.8901	0.1345	0.4010	24.2895	3.2670	22.1005	0.3000	0.3690	33.2137
52	0.9076	0.1547	0.4224	24.1718	3.7382	21.6902	0.3242	0.3857	34.7097
53	0.9250	0.1743	0.4444	24.0543	4.1917	21.2975	0.3468	0.4009	36.0803
54	0.9425	0.1934	0.4669	23.9368	4.6285	20.9216	0.3681	0.4150	37.3532
55	0.9599	0.2120	0.4901	23.8194	5.0493	20.5614	0.3883	0.4283	38.5480
56	0.9774	0.2302	0.5138	23.7020	5.4551	20.2161	0.4077	0.4409	39.6793
57	0.9948	0.2479	0.5381	23.5846	5.8467	19.8849	0.4262	0.4529	40.7584
58	1.0123	0.2653	0.5629	23.4672	6.2248	19.5672	0.4442	0.4644	41.7940
59	1.0297	0.2822	0.5883	23.3498	6.5901	19.2622	0.4615	0.4755	42.7934
60	1.0472	0.2989	0.6142	23.2323	6.9431	18.9692	0.4784	0.4863	43.7626
61	1.0647	0.3151	0.6406	23.1148	7.2846	18.6878	0.4949	0.4967	44.7066
62	1.0821	0.3311	0.6676	22.9971	7.6150	18.4172	0.5110	0.5070	45.6297
63	1.0996	0.3468	0.6950	22.8792	7.9348	18.1571	0.5268	0.5171	46.5359
64	1.1170	0.3622	0.7230	22.7612	8.2446	17.9070	0.5423	0.5270	47.4287
65	1.1345	0.3774	0.7514	22.6429	8.5449	17.6663	0.5577	0.5368	48.3112
66	1.1519	0.3923	0.7803	22.5245	8.8359	17.4346	0.5728	0.5465	49.1864
67	1.1694	0.4070	0.8097	22.4057	9.1181	17.2116	0.5878	0.5562	50.0573
68	1.1868	0.4214	0.8395	22.2867	9.3919	16.9969	0.6027	0.5659	50.9266
69	1.2043	0.4357	0.8697	22.1674	9.6577	16.7900	0.6175	0.5755	51.7972
70	1.2217	0.4497	0.9003	22.0478	9.9157	16.5908	0.6323	0.5852	52.6720
71	1.2392	0.4636	0.9314	21.9278	10.1663	16.3988	0.6471	0.5950	53.5539
72	1.2566	0.4773	0.9627	21.8074	10.4097	16.2138	0.6619	0.6050	54.4461
73	1.2741	0.4909	0.9945	21.6865	10.6463	16.0355	0.6768	0.6150	55.3520
74	1.2915	0.5043	1.0266	21.5653	10.8763	15.8636	0.6918	0.6253	56.2754
75	1.3090	0.5176	1.0590	21.4435	11.0999	15.6979	0.7069	0.6358	57.2205
76	1.3265	0.5308	1.0917	21.3213	11.3173	15.5381	0.7222	0.6466	58.1920
77	1.3439	0.5439	1.1247	21.1985	11.5289	15.3840	0.7377	0.6577	59.1955
78	1.3614	0.5568	1.1580	21.0752	11.7347	15.2355	0.7536	0.6693	60.2375
79	1.3788	0.5697	1.1915	20.9513	11.9350	15.0922	0.7698	0.6814	61.3258
80	1.3963	0.5824	1.2253	20.8268	12.1299	14.9541	0.7864	0.6941	62.4701
81	1.4137	0.5951	1.2592	20.7016	12.3197	14.8209	0.8034	0.7076	63.6824

Appendix 3.1

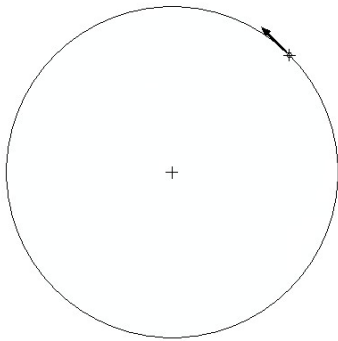
82	1.4312	0.6077	1.2934	20.5758	12.5044	14.6924	0.8211	0.7220	64.9778
83	1.4486	0.6203	1.3277	20.4493	12.6843	14.5686	0.8394	0.7375	66.3767
84	1.4661	0.6328	1.3621	20.3221	12.8594	14.4492	0.8585	0.7545	67.9065
85	1.4835	0.6452	1.3967	20.1941	13.0300	14.3340	0.8786	0.7734	69.6067
86	1.5010	0.6577	1.4314	20.0653	13.1960	14.2231	0.8997	0.7949	71.5371
87	1.5184	0.6700	1.4662	19.9357	13.3578	14.1161	0.9221	0.8200	73.7969
88	1.5359	0.6824	1.5010	19.8053	13.5153	14.0131	0.9461	0.8508	76.5763
89	1.5533	0.6948	1.5359	19.6740	13.6686	13.9138	0.9719	0.8928	80.3553
90	1.5708	0.7071	1.5708	19.5418	13.8180	13.8182	1.0000	1.0000	90.0000

Appendix 3.2 Spreadsheet for 4-Lobed Swirl Inducing Pipe

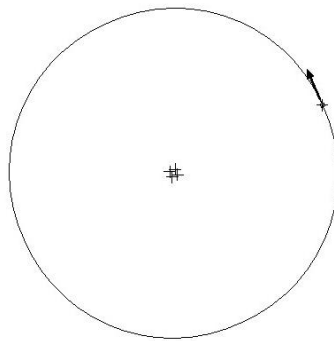
Table A3.2 Spreadsheet for 4-Lobed Swirl Inducing Pipe

<i>Sections</i>	$R_{cs} (mm)$	$r_f(mm)$	x/L	<i>Twist(deg) clockwise</i>
1	19.5418	13.8182	0	0
2	19.5418	13.8182	0.05	9
3	19.5418	13.8182	0.1	18
4	19.5418	13.8182	0.15	27
5	19.5418	13.8182	0.2	36
6	19.5418	13.8182	0.25	45
7	19.5418	13.8182	0.3	54
8	19.5418	13.8182	0.35	63
9	19.5418	13.8182	0.4	72
10	19.5418	13.8182	0.45	81
11	19.5418	13.8182	0.5	90
12	19.5418	13.8182	0.55	99
13	19.5418	13.8182	0.6	108
14	19.5418	13.8182	0.65	117
15	19.5418	13.8182	0.7	126
16	19.5418	13.8182	0.75	135
17	19.5418	13.8182	0.8	144
18	19.5418	13.8182	0.85	153
19	19.5418	13.8182	0.9	162
20	19.5418	13.8182	0.95	171
21	19.5418	13.8182	1	180

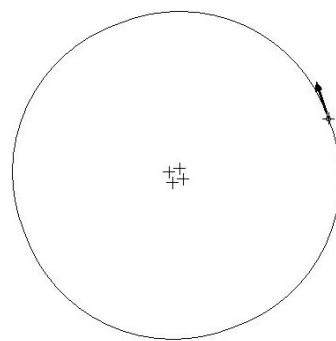
Appendix 3.3 Cross-section Development of the 4-Lobed Transition Pipe



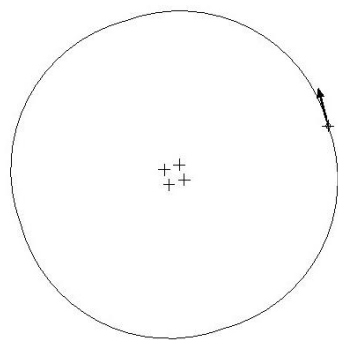
Section 1, $\gamma = 45^\circ$



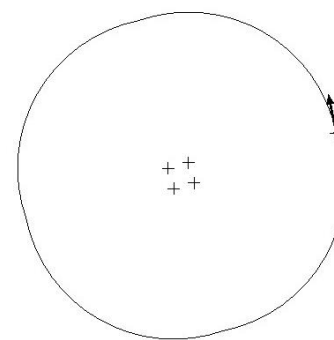
Section 2, $\gamma = 46^\circ$



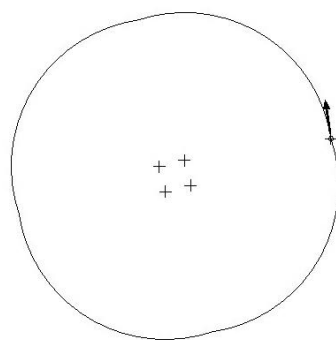
Section 3, $\gamma = 47^\circ$



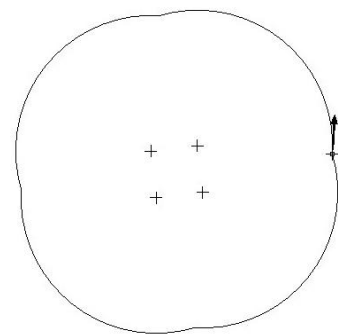
Section 4, $\gamma = 48^\circ$



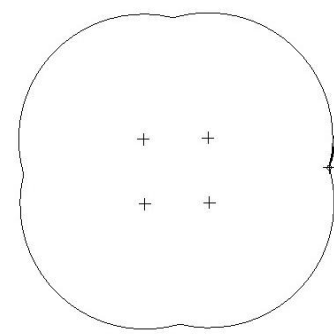
Section 5, $\gamma = 49^\circ$



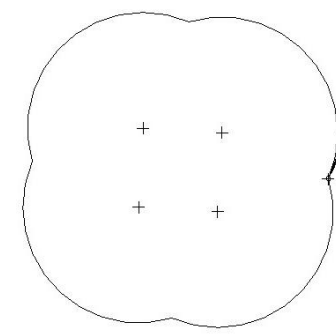
Section 6, $\gamma = 50^\circ$



Section 7, $\gamma = 55^\circ$



Section 8, $\gamma = 60^\circ$



Section 9, $\gamma = 65^\circ$

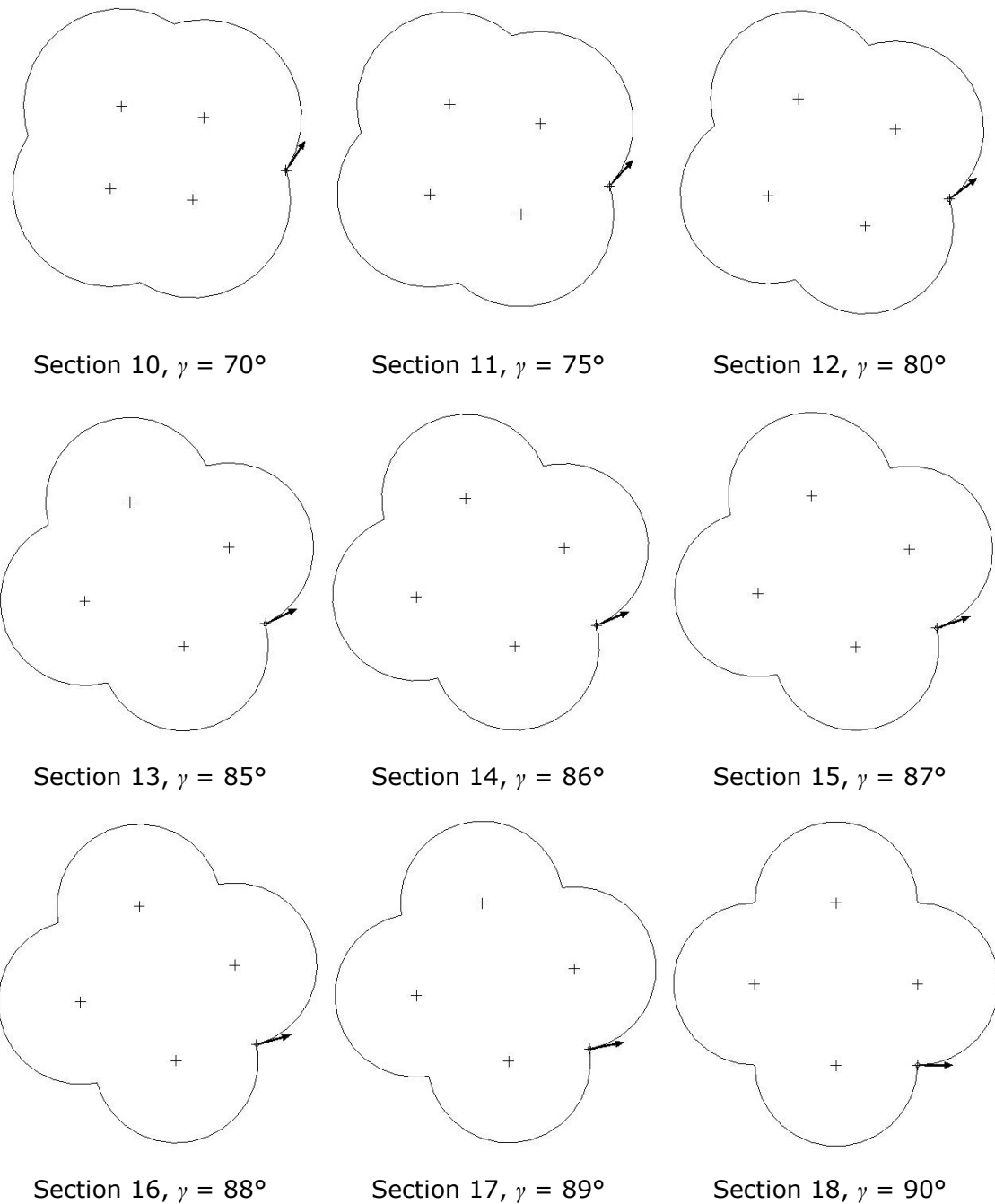


Figure A3. 1 18 Sections Used To Sweep and Blend Into the 4-Lobed Transition Pipe

The arrows represent the start points and the four points inside the sections indicate the centre of the lobes.

Appendix 5.1 Optimization of a Four-Lobed Swirl Pipe for Clean-In-Place Procedures

San Francisco USA Jun 07-08, 2015, 17 (6) Part VII

Optimization of a Four-Lobed Swirl Pipe for Clean-In-Place Procedures

Guozhen Li, Philip Hall, Nick Miles, Tao Wu

Abstract—This paper presents a numerical investigation of two horizontally mounted four-lobed swirl pipes in terms of swirl induction effectiveness into flows passing through them. The swirl flows induced by the two swirl pipes have the potential to improve the efficiency of Clean-In-Place procedures in a closed processing system by local intensification of hydrodynamic impact on the internal pipe surface. Pressure losses, swirl development within the two swirl pipe, swirl induction effectiveness, swirl decay and wall shear stress variation downstream of two swirl pipes are analyzed and compared. It was found that a shorter length of swirl inducing pipe used in joint with transition pipes is more effective in swirl induction than when a longer one is used, in that it has a less constraint to the induced swirl and results in slightly higher swirl intensity just downstream of it with the expense of a smaller pressure loss. The wall shear stress downstream of the shorter swirl pipe is also slightly larger than that downstream of the longer swirl pipe due to the slightly higher swirl intensity induced by the shorter swirl pipe. The advantage of the shorter swirl pipe in terms of swirl induction is more significant in flows with a larger Reynolds Number.

Keywords—swirl pipe, swirl effectiveness, CFD, wall shear stress, swirl intensity.

I. INTRODUCTION

Industries such as dairy, beverage, brewing, processed foods, pharmaceutical, and cosmetics rely heavily on Clean-In-Place (CIP) procedures to frequently clean their production lines. A CIP procedure is a method of cleaning the interior surfaces of pipes, vessels, process equipment and associated fittings, without disassembling them. The benefit to industries by using CIP is that the cleaning is faster, less labor intensive, more repeatable, and poses less chemical exposure risks to people. Efficient CIP is important to maintain good operation of the production line and more importantly to ensure the appropriate level of hygiene and thus the safety of the products [1], [2]. Efficient CIP will result not only in reduced downtime and costs for cleaning but also decreased environmental impact (in the disposal of spent chemicals) [3].

Guozhen Li is with the University of Nottingham Ningbo China, 199 Taikang East Road, Ningbo, 315100, China (e-mail: Guozhen.LI@nottingham.edu.cn).

Philip Hall is with the University of Nottingham Ningbo China, 199 Taikang East Road, Ningbo, 315100, China (Philip Hall is corresponding author, phone: +86(0)574 8818 0018; e-mail: Philip.Hall@nottingham.edu.cn).

Nick Miles is with the University of Nottingham Ningbo China, 199 Taikang East Road, Ningbo, 315100, China (e-mail: Nick.Miles@nottingham.edu.cn).

Tao Wu is with the University of Nottingham Ningbo China, 199 Taikang East Road, Ningbo, 315100, China (e-mail: Tao.Wu@nottingham.edu.cn).

CIP is usually performed by the circulation of formulated detergents which typically involves a warm water rinse, washing with alkaline and/or acidic solution, and a clear rinse with warm water to flush out residual cleaning agents [4]. Research established that the CIP efficiency depends on mainly four energy factors: the chemical action from detergents to dissolve soil in order to facilitate removal, the thermal energy - the cleaning temperature, the cleaning time, and the favorable mechanical energy (or hydrodynamic effect) to physically remove soil [2], [5]-[8]. An efficient combination of those factors varies depending on the type of soil and the severity of the fouling and a restriction in one factor may be compensated by increasing the effect of one or more of others [5]. Literature showed that, of the hydrodynamic factors, the wall shear stress, which is a measure of the mechanical action of fluid flow on a process surface, is considered the dominating factor for cleaning. The effective removal rate is significantly influenced by the wall shear stress applied during cleaning [1], [5], [9].

Lately we proposed a method to improve the CIP efficiency by introducing swirl motion into CIP flow which should intensify the hydrodynamic effect of cleaning fluid to physically remove the soil. We have numerically identified the potential of a geometrically induced swirl flow generated from flow passing through a four-lobed swirl pipe (600mm in length, 50mm in diameter) on improving the CIP efficiency by locally increasing the mean shear stress at the internal pipe surface without increasing the overall flow velocity [10]. The Computational Fluid Dynamics (CFD) model showed that the 600 length four-lobed swirl pipe imparted a tangential wall shear stress to the swirl flow downstream of it which is proportional to the swirl intensity of the swirl flow induced. As a result of the presence of tangential wall shear stress, the mean wall shear stress downstream of the swirl pipe was increased.

However, it was found that the pressure loss across the four-lobed swirl pipe is more significant than that of the circular pipes, which is due to the additional turbulence generated through the artificial roughness of the non-circular pipe cross-sections of the swirl pipe. This paper intends to further optimize the 600mm length four-lobed swirl pipe by shortening its length to 400mm. This should further decrease the extra pressure loss expended in inducing swirl into flow passing through the swirl pipe. A criterion based on the ratio of the swirl intensity produced to the pressure loss was used to calculate the swirl effectiveness of the two swirl pipes. The

pressure losses across the 600mm and 400mm swirl pipes, the swirl development within the two swirl pipes, their swirl effectiveness, swirl decay and wall shear stress variation downstream of two swirl pipes were analyzed and compared.

II. THE 600MM LENGTH AND 400MM LENGTH FOUR-LOBED SWIRL PIPES

Swirl flow is one of the well-recognized configurations of the flow in the industrial equipment and is accentuated for its various applications as well as its sophisticated scientific basis [11]. At the University of Nottingham, researches into method to generate swirl flow using helically formed pipes have been carried out for many years. Early emphasis concentrated on the physical effects of swirl section, later research was directed toward optimizing the swirl configuration, number of lobes, pitch to diameter ratio and so on. Ganesalingam[12] tested various cross-sections of pipe (3, 4, 5 and 6 lobed) and concluded that a 4-lobed cross-section was most effective at swirl generation. The evaluation criteria was the Swirl Effectiveness which was deemed to be the swirl intensity that could be induced for a given pressure drop. He recommended a P:D ratio of 8 and 400mm of length as optimal for the 4-lobed pipe. Pitch is the axial distance travelled by the each lobe as it rotates through 360 degrees (Singh, 1976), therefore a pitch to diameter (P:D) ratio of 8 indicates that the lobed cross-section rotates by 360 degrees (one swirl) in a length equivalent to 8 diameters. The swirl inducing pipe, as shown in Fig. 1, has an equivalent cross-sectional area to the circular pipe delivering fluid to the swirl pipe and the swirl pipe has an 'equivalent' diameter of 50mm.



Fig.1 Swirl inducing pipe, 400mm length, P:D=8

It was found that there were high entry and exit pressure losses across this swirl inducing pipe due to the sudden change in cross-section from lobed to circular and vice versa. Transition geometries prior to and after the swirl pipe were suggested to eliminate these pressure losses. This should further improve the applicability of the swirl inducing pipes. However the transition section would have to be short and effective. Otherwise it will increase overall pressure drop and, in the case of exit transition, may decrease swirl intensity.

Ariyaratne[13] designed and optimized a transition pipe for use as an entry and exit duct with the swirl inducing pipe. It was found that transition pipes either before or after the swirl inducing pipe reduced entry and exit pressure losses by providing a gradual transition from circular to lobed cross-section and vice versa. They also increased induced swirl and reduced swirl decay. As shown in Fig.2, the transition pipe's cross-section changes from circular to 4-lobed shape gradually. The area of the cross-sections is constant and equal to the swirl pipe's. The length of transition pipe is 100mm, and each lobe rotates by 90°.

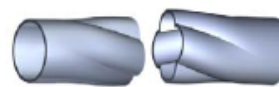


Fig.2 Entry and exit transition pipes, 100mm length

Based on the study of Ariyaratne, a swirl pipe configuration of 100mm transition pipe prior + 400mm swirl inducing pipe + 100 transition pipe after (as shown in Fig. 3) is deemed to be optimum, which is demonstrated in Fig. 3. However, in this configuration:

- The swirl pipe has the lobed cross-section rotated by 540° (one and a half swirl) instead of 360° (one swirl), which was used in the previous designs.
- The longer swirl pipe results in more pressure loss due to the increase in contact area and thus friction.
- When entry transition pipe was used in conjunction with swirl pipe, a higher tangential velocity was generated. However, the induced swirl appeared to be constrained by the swirl pipe inducing pipe geometry. A shorter length of swirl inducing pipe will therefore be required to generate an equivalent amount of swirl [13].

Ariyaratne[13] suggested that, with the inclusion of transitions, a shorter length of swirl inducing pipe than previously determined is optimum. Therefore we propose a swirl pipe configuration of 100mm transition pipe prior + 200mm swirl inducing pipe + 100 transition pipe after. This configuration has one swirl, shorter length, and is expected to be more cost effective in swirl induction.

We will numerically compare the two swirl pipe configuration in terms of pressure cost, swirl intensity, swirl effectiveness, swirl decay rate, and the shear stress of swirl flow acted on the pipe surface induced by them as we intend to apply the swirl pipe into pipe cleaning industries where the wall shear stress was reported to be the governing factor in the Clean-In-Place procedures [1].

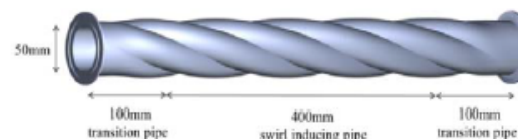


Fig.3 100+400+100 swirl pipe, 600mm length, one and a half swirl

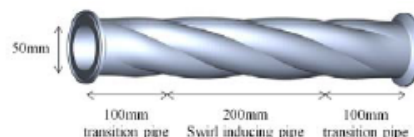


Fig.4 100+200+100 swirl pipe, 400mm length, one swirl

III. TERMS AND DEFINITIONS

This section introduces a number of terms and equations that will be used in this paper.

A. Swirl Effectiveness

Ganeshalingam [12] defined a Swirl Effectiveness parameter, based on the ratio of the swirl intensity produced to the pressure loss, and used it in all swirl effectiveness calculations. The effectiveness of swirl induction was deemed to be the swirl intensity that could be induced for a given pressure drop. This parameter is also used in this research for the comparison of the two swirl pipe configurations in terms of swirl effectiveness.

$$\text{Swirl Effectiveness} = \frac{\text{Swirl Intensity}}{\frac{\Delta P}{\frac{\rho \times u^2}{2}}} \quad (1)$$

Where ΔP is pressure drop, ρ is density, and u is flow velocity.

B. Swirl Intensity and Its Decay Rate

Swirl intensity or swirl number, S , is commonly used to quantify the degree or strength of a swirl within a pipe. This non-dimensional number is defined as the ratio of the angular momentum flux to the axial momentum flux, multiplied by the hydraulic radius [14]. A widely accepted expression of the swirl intensity is given by [15]:

$$S = \frac{\int_0^R u w r^2 dr}{R \int_0^R u^2 r dr} \quad (2)$$

Where w is the tangential velocity, m/s; u is the axial velocity, m/s; r is the radius at the point where tangential velocity is calculated, m; R is the pipe radius, m.

The decay process is quantified by expressing the swirl intensity S as a function of stream wise position x . In most references, the observed swirl intensities are fitted with exponential decay functions

$$S = S_0 e^{-\beta \frac{x}{D}} \quad (3)$$

Where β is the decay rate, S_0 is the initial swirl intensity and D is the pipe diameter. The swirl decay rate $\beta = a \times f'$, where a is the empirically or numerically determined coefficient, f' is the Moody friction factor.

C. Tangential Wall Shear Stress

The expression for tangential wall shear stress was derived by Kitoh by treatment of the Reynolds averaged angular momentum equation for incompressible, stationary and axially symmetric flow [14]. The equation later was used by Steenbergen and Voskamp [15] and Najafi et al. [11]. For a detailed introduction of tangential wall shear stress and the non-dimensional tangential wall shear stress please refer to [10]. Steenbergen and Voskamp concluded that the existence of tangential wall shear stress in the swirl flow causes reduction of fluid flow swirl intensity [15].

IV. NUMERICAL METHOD AND MODELS

A. Flow Domain

Configuration of the two modelled pipe flow systems for

use with FLUENT academic code [16] is shown in Fig. 5. The 2m straight circular pipes prior to the swirl pipes serve as development section to ensure the flow is fully developed before entering the swirl pipe. The 8m straight circular pipes downstream of the swirl pipes are the test section. The circular pipe has a diameter of 50mm; the swirl pipe has an equivalent diameter of 50mm and its cross-sectional areas are constant and equal to the circular pipe.

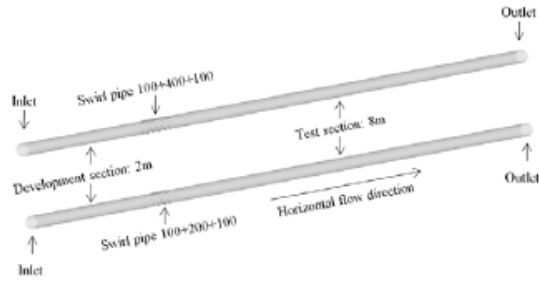


Fig.5 Configuration of simulation geometry

B. Meshing

Shear stress acting on the pipe wall is of interest in this study, and when an accurate prediction of stress in the boundary layer is required, the boundary layer meshes should consist of quads, hexes, or prisms, and the use of pyramid or tetrahedral cells immediately adjacent to the wall should be avoided [17]. ICEM CFD (ANSYS, USA) mesh generation software was used to mesh the computational domain with structured hexahedral cells. ICEM CFD uses a primarily top-down blocking approach to efficiently mesh complex models using all hexahedral cells without the need to subdivide the geometry. The blocking can be associated with topologically similar geometries. To make sure the blocks in accordance with swirl pipes are well fitted, the blocks are rotated by 45° by moving vertexes of the blocks. O-grid blocks are used to improve overall mesh quality. The cross sectional view of the circular, transition, swirl pipe meshes and the surface mesh of a swirl pipe section are demonstrated in Fig. 6(a-c).

Mesh adaption for Non-Equilibrium wall functions was carried out to make sure that the first point where the velocity is calculated is in the log-law region. To ensure that the errors associated with the size of mesh were minimized, a quick mesh independence test was carried out. The detailed process of mesh adaption for wall functions and mesh independence test are described in [10].

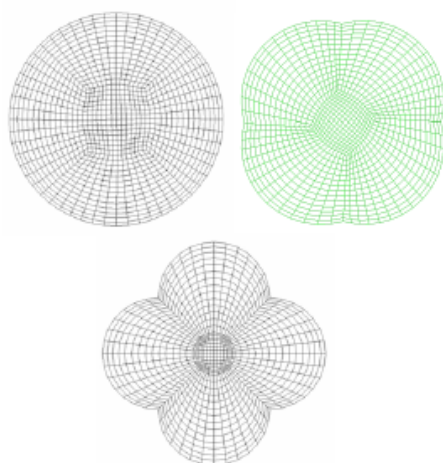


Fig.6a Cross sectional view of the circular, transition and swirl pipe meshes

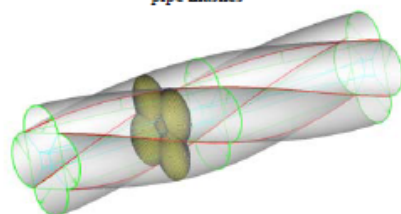


Fig.6b Association between blocks and geometry

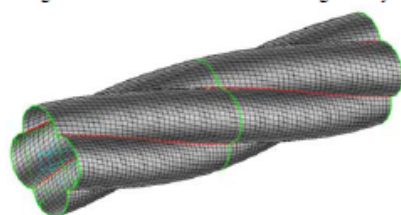


Fig.6c Surface mesh at the intersection of lobes

C. Numerical Model Description

The governing equations required to predict the flow patterns for the incompressible, single phase, turbulent, swirling flow in the straight and swirl pipe are termed the 'Navier-Stokes Equations'. They are the conservation of mass, momentum and energy. The conservation of energy was not used in the current simulation since heat transfer was not of interest in this investigation.

The flow being modeled is swirling and in such turbulent flows viscosity is typically anisotropic, so the most reliable turbulence model Reynolds Stress Model (RSM) was chosen [11], [18]. The RSM closes the Reynolds-averaged Navier-Stokes equations by solving transport equations for the Reynolds stresses, together with an equation for the

dissipation rate. This means that seven additional transport equations are required in 3D flows. Since the RSM accounts for the effects of streamline curvature, swirl, rotation, and rapid changes in strain rate in a more rigorous manner than one-equation and two-equation models, it has greater potential to give accurate predictions for complex flows [19]. The transport equations for the transport of the Reynolds Stresses are referred to [18] and [20].

D. Simulation Set-Up

Material:

Simulations were carried out with single-phase water, and the flow was assumed to be steady and isothermal. The water density and viscosity were specified as 998.2 kgm^{-3} and $1.003 \times 10^{-3} \text{ kgm}^{-1}\text{s}^{-1}$.

Boundary conditions:

At the inlet, a velocity inlet boundary condition was used. The turbulence was specified in terms of intensity and hydraulic diameter at both the inlet and outlet. The turbulence intensity is defined as the ratio of the root-mean-square of the velocity fluctuations to the mean velocity. It was calculated from [16]:

$$I = 0.16 \times (Re)^{-1/8}, \quad Re = (U \times D) / \mu \quad (4)$$

Where Re is the Reynolds number, U is the average velocity, ρ is the density, and μ is the viscosity. A series of simulations were carried out with inlet velocities being 1m/s, 2m/s and 3m/s.

A pressure outlet boundary condition was imposed at the outlet of the computational model. This boundary condition results in a better rate of convergence when backflow occurs during iteration.

The pipe walls were specified as being stationary and no slip walls to match the simulation conditions. Wall roughness was modelled by specifying the roughness height, K_s , as $1.5 \times 10^{-5} \text{ m}$. This value is so small that the walls can be considered to be hydraulically smooth. The Non-Equilibrium wall functions were applied in the near wall region.

Solver:

Pressure-based Segregated Solver was chosen for the steady state simulation. Absolute velocity formulation was used.

Solution methods:

The SIMPLE discretization technique was applied for the pressure-velocity coupling. A second order upwind scheme was employed for viscous terms.

Convergence Criterion:

The convergence criterion used for all cases was that the scaled residuals of x , y , z velocities, k , and ϵ , and Reynolds stresses have decreased by four orders of magnitude. The mass flow rate at the outlet was also monitored and the solution was deemed to have reached a steady state when this parameter achieved a constant value over a large number of iterations.

V. RESULTS AND DISCUSSIONS

A. Pressure Drop

The pressure loss across the lobed swirl pipe itself is greater than circular pipe due to the additional turbulence generated through artificial roughness of the non-circular pipe surfaces [12], [13]; the energy lost is partly converted into angular momentum of swirling flow. Fig. 7 demonstrates the pressure drop within the 600mm and 400mm length swirl pipes with the inlet velocities being 3m/s, 2m/s, and 1m/s respectively. From the Fig. 7, a larger inlet velocity causes larger pressure drop in both the 100+400+100 swirl pipe and the 100+200+100 swirl pipe. From Table I, For the three inlet velocities, the overall pressure drop caused by the 100+400+100 swirl pipe is larger than the 100+200+100 swirl pipe due to its larger contact area with fluid thus pipe friction and the differences in pressure drop are more obvious in flows with higher velocities.

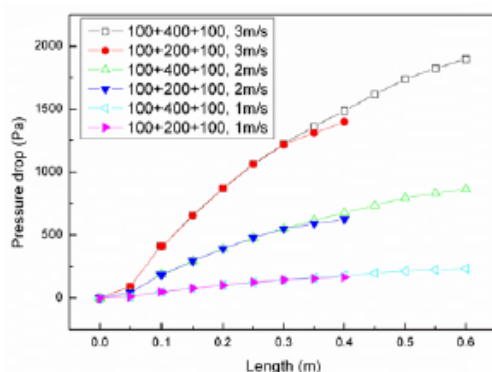


Fig.7 Pressure drop across the two swirl pipes in flows with various inlet velocities

TABLE I
COMPARISON OF THE TWO SWIRL PIPES ON PRESSURE DROP AND TANGENTIAL VELOCITY

Velocity (m/s)	Pressure drop (Pascal)		Final tangential velocity (m/s)	
	600mm swirl pipe	400mm swirl pipe	600mm swirl pipe	400mm swirl pipe
1	233.24	165.25	0.151	0.156
2	866.2	625.86	0.33	0.345
3	1894.99	1399.5	0.545	0.555

B. Swirl Development within Swirl Pipe

The swirl pipe adds a rotating momentum to the flow within itself and direct to the circular pipe downstream of it, turning the fluid clockwise in addition to the axial velocity along the pipe. The velocity component, which mainly affects the swirl flow field, is the tangential velocity component, which has a distribution dependent on the swirl generation mechanism [11]. Fig. 8 shows the development of tangential velocity within the 100+400+100 swirl pipe and 100+200+100 swirl pipe for the three inlet velocities of 3m/s, 2m/s and 1m/s. It is

clear that both the two swirl pipes induce larger tangential velocity in flows with higher velocities. For the three inlet velocities and for the 100+400+100 swirl pipe, a sharper tangential velocity increase is seen from the middle of the entry transition pipe (0.05m in the horizontal axis) and it reaches the highest value in the middle of the 400mm swirl inducing pipe (0.3m in the horizontal axis); the tangential velocity decreases slightly in the second half of the swirl inducing pipe indicating that it is acting as a constraint to the induced tangential velocity. While in the case of 100+200+100 swirl pipe, the whole 200mm swirl inducing pipe contributes to the tangential velocity development as it can be seen that the largest value appears at the joint of swirl inducing pipe to the exit transition pipe with this largest values are almost identical in the two swirl pipes. In both the two swirl pipes, exit transition pipe causes a decrease in tangential velocity. However, the final tangential velocity at the exit of the 100+200+100 swirl pipe is slightly larger than that of the 100+400+100 swirl pipe in flows with the three different inlet velocities.

Fig.9 shows the variation of swirl intensity within the two swirl pipes for the three velocities. Generally, in both the 100+400+100 and 100+200+100 swirl pipe, the first 0.3m length of the swirl pipes contribute to swirl induction with the swirl intensity value and its variation trend are almost identical. In the rest of the swirl pipes (0.3~0.6m for the 600mm swirl pipe and 0.3~0.4 for the 400mm swirl pipe), decrease in swirl intensity are observed in both the swirl pipes, however, the final swirl intensity downstream of 100+200+100 swirl pipe is slightly higher than that of the 100+400+100 swirl pipe. The detailed initial swirl intensity downstream of both the swirl pipes for the three velocities is listed in Table II.

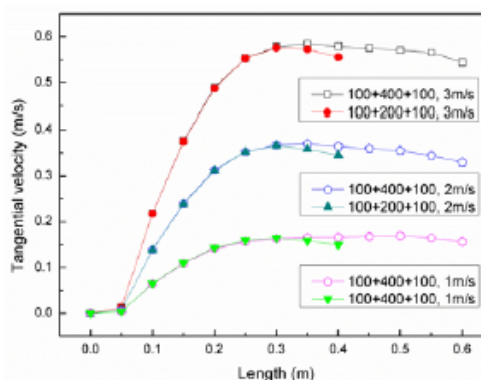


Fig.8 Tangential velocity distribution within the two swirl pipes for various inlet velocities

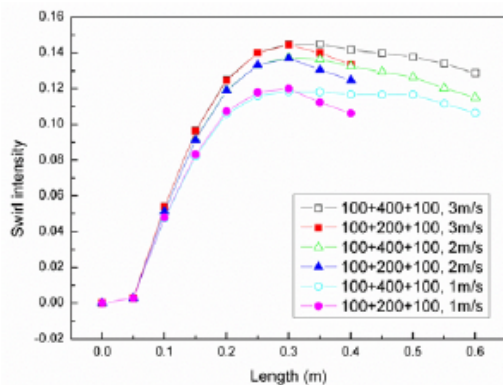


Fig.9 Swirl intensity distribution within the two swirl pipes for various inlet velocities

TABLE II
COMPARISON OF THE TWO SWIRL PIPES ON SWIRL INTENSITY
AND SWIRL EFFECTIVENESS

Velocity (m/s)	Final swirl intensity		Swirl effectiveness	
	600mm swirl pipe	400mm swirl pipe	600mm swirl pipe	400mm swirl pipe
1	0.106	0.106	0.228	0.321
2	0.115	0.125	0.265	0.398
3	0.129	0.133	0.305	0.428

C. Swirl Effectiveness

Fig. 10 shows the swirl effectiveness variation within the 100+400+100 and 100+200+100 swirl pipe with three different inlet velocities. In the entry transition pipe for all three conditions, there is a quick increase in swirl effectiveness. This is because the gradual transition from circular cross-section to the lobed geometry reduces frictional losses from the pipe walls thereby producing a more effective swirl induction in the expense of a smaller pressure drop. The quick increase in tangential velocity is further continued within the swirl inducing pipe that it is immediately adjacent to the entry transition pipe where the swirl effectiveness reaches its highest value in this duration (0.1~0.15m). Afterward, the increase in tangential velocity slows down till the tangential velocity reaches the maximum value in 0.3m in the horizontal axis as shown in Fig. 8. In this duration, swirl inducing pipe still contributes to swirl induction despite of the negative slope in swirl effectiveness. After the point of 0.3m, the second half of the swirl inducing pipe and the exit transition pipe of the 100+400+100 swirl pipe is restricting the tangential velocity that has been generated. However, only the exit transition pipe of the 100+200+100 swirl pipe is restricting the tangential velocity thus the overall swirl effectiveness of the 100+200+100 swirl pipe is larger than the 100+400+100 swirl pipe. It is also clear from Fig. 10 that swirl effectiveness of the two swirl pipe is larger in flows with higher velocities. A detailed swirl effectiveness value for the two swirl pipes in the three conditions is referred to Table II.

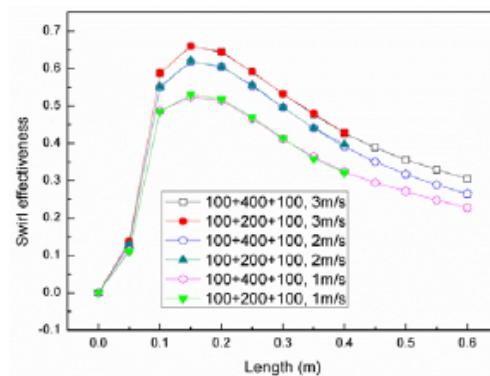


Fig.10 Swirl effectiveness variation within the two swirl pipes for various inlet velocities

D. Swirl Decay

The induced swirl flow decayed with increasing distance downstream the swirl pipe and reverted back to the upstream flow profile at different distances downstream according to the inlet velocities. The decay of swirl is caused by the transport of angular momentum to the pipe wall. Fig. 11 depicts the average tangential velocity distribution downstream of both the 100+400+100 swirl pipe and the 100+200+100 swirl pipe for inlet velocities of 3m/s, 2m/s and 1m/s. It is clear for both the two swirl pipes that tangential velocity decreases with increasing distance downstream and finally decreases to zero where the swirl effect fades away. It is also clear that the effectiveness of both the two swirl pipes is more prominent for flows with larger velocities. However, for the same inlet velocities, the initial tangential velocities downstream of 100+200+100 swirl pipe and along the circular pipe are slightly larger than that of when 100+400+100 swirl pipe is used, this is even true in flows with a larger velocity.

Fig. 12 presents the swirl intensity calculated at swirl pipe exit and planes downstream of the two swirl pipe exits. It is clear for both the two pipes that swirl intensity decreases with increasing distance downstream of the swirl pipe exit with larger swirl intensity observed both at the swirl pipe exit and downstream of it in flows with higher velocities (Reynolds number). The swirl decay rate is in good agreement with exponential trend with the decay rate of swirl flow induced by 100+400+100 swirl pipe in flows with inlet velocity of 3m/s, 2m/s and 1m/s being 0.0332, 0.0356, and 0.0398 while the decay rate for 100+200+100 swirl pipe are 0.0328, 0.0349 and 0.0398. It is clear that, for the inlet velocity of 2m/s and 3m/s, 100+200+100 swirl pipe has a superior swirl induction effect as it induces larger initial swirl intensity downstream and has a smaller swirl decay rate than when 100+400+100 swirl pipe is used. However, for the inlet velocity of 1m/s, the advantage of 100+200+100 swirl pipe is negligible.

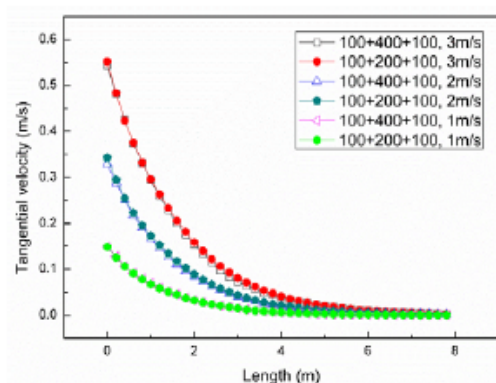


Fig. 11 Tangential velocity distribution downstream of the two swirl pipes for various inlet velocities

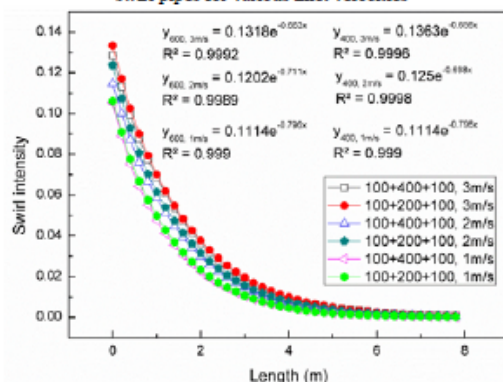


Fig. 12 Swirl intensity variation downstream of the two swirl pipes for various inlet velocities

E. Wall Shear Stress

The effects of the two swirl pipes on increasing shear stress at the pipe surface are also investigated and compared as we intend to apply this swirl pipe into Clean-In-Place procedures, in which the wall shear stress was reported to be the local tangential force acting on the soil on the surface and remove them [21].

The shear stress, for a Newtonian fluid, is defined by the normal velocity gradient at the wall as: $\tau_w = \mu \frac{\partial u}{\partial y}$, where μ is dynamic viscosity of the fluid, u is velocity of the fluid along the boundary and y is height above the boundary. For swirl flow, angular momentum is transported into the pipe wall, generating a sharp tangential velocity gradient in the wall. It is expected this tangential velocity gradient will induce tangential wall shear stress acting on the pipe surface in addition to the axial wall shear stress that is parallel to the straight circular pipe.

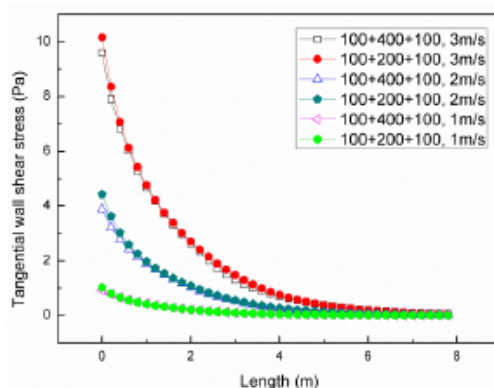


Fig. 13 Tangential wall shear stress distribution downstream of the two swirl pipes for various inlet velocities

From Fig. 13, it is clear that flow passing through both the two swirl pipes will generate tangential shear stress at the wall and direct to the downstream. The tangential shear stress will decay and finally fades away with a similar variation trend of tangential velocity as shown in Fig. 11, which suggests that tangential wall shear stress is closely associated with tangential velocity thus swirl intensity. It can be noticed that an increase of inlet velocity from 1 m/s to 3 m/s causes a sharp rise in tangential wall shear stress downstream of the two swirl pipes; this may suggest that the effect of the swirl pipe on tangential shear stress is more prominent in flows with a higher Reynolds number.

It is also clear from Fig. 13 that the initial tangential wall shear stress and the values downstream of the 100+200+100 swirl pipe are slightly larger than that of 100+400+100 swirl pipe and this is clearer in flows with larger inlet velocities.

Fig. 14 depicts the average non-dimensional tangential wall shear stress along the pipe downstream of the two swirl pipe exits for various inlet velocities. It shows that the trend of variation for non-dimensional tangential wall shear stress is similar to that of swirl intensity as shown in Fig. 12. This further indicates that the presence and variation of tangential wall shear stress is mainly dependent on swirl intensity. One again, the 100+200+100 swirl pipe is slightly better in increasing non-dimensional tangential wall shear stress than the 100+400+100 swirl pipe due to the relatively larger swirl intensity induced.

Fig. 15 presents the average axial wall shear stress downstream of the two swirl pipe exits for various inlet velocities. It shows that the two swirl pipes also has the effect of increasing axial wall shear stress downstream them but in a very slight way and lasts for a short distance compared with tangential wall shear stress. The effect of the swirl pipes on axial wall shear becomes less obvious with decreasing inlet velocity (Reynolds number). Their effect is almost negligible for flows with an inlet velocity of 1 m/s. with the same inlet velocities, 100+200+100 swirl pipe induces a slightly higher axial wall shear stress increase than that of 100+400+100

swirl pipe, however, its advantage stops being obvious in flows with lower velocities.

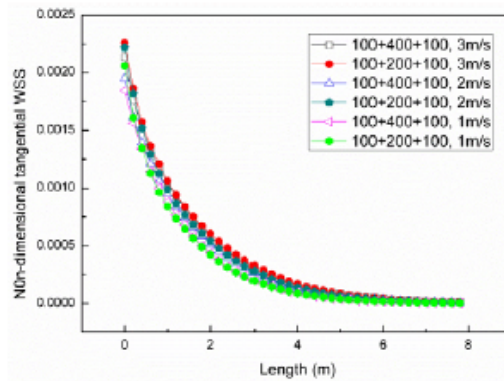


Fig.14 Non-dimensional tangential WSS distribution downstream of the two swirl pipes for various inlet velocities

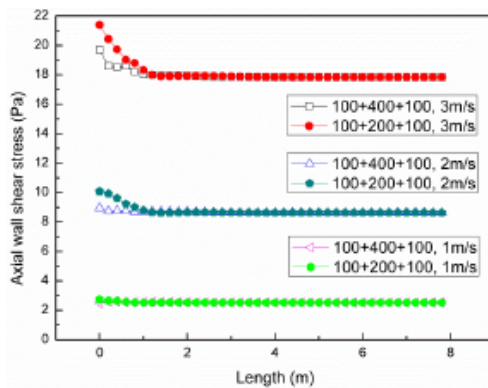


Fig.15 Axial wall shear stress distribution downstream of the two swirl pipes for various inlet velocities

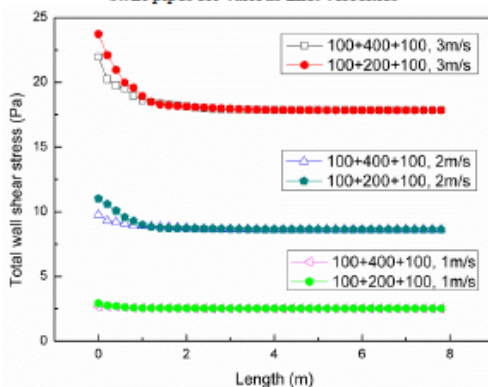


Fig.16 Total wall shear stress distribution downstream of the two swirl pipes for various inlet velocities

Fig. 16 shows the total wall shear stress downstream of the two swirl pipes, which is the combined action of the tangential and axial shear stress component acting on the pipe surface. It is clear that swirl pipes locally increases mean wall shear stress downstream of it, with the increased value and effective distance more remarkable for a faster inlet flow velocity (a large Reynolds number and large swirl intensity). For a flow velocity of 3m/s which is typically the velocity of cleaning fluid circulating in a Clean-In-Place procedure, 100+400+100 swirl pipe raises mean shear stress at the wall from 17.8 Pascal prior swirl pipe inlet to 22 Pascal (23.5% increase) just downstream of it. The wall shear stress decays in accordance with swirl intensity, and in the point 1m (20D) downstream swirl pipe exit the increase in wall shear stress is 5%. While the 100+200+100 swirl pipe rises wall shear stress from 17.8 Pascal before it to 23.7 Pascal (33.1% increase) downstream of it and maintains at least 5% increase in mean wall shear stress in the position 1.1m (22D) downstream of it. Therefore, it can be concluded that 100+200+100 swirl pipe is better in increasing and maintaining wall shear stress downstream it than that of 100+400+100 swirl pipe. The advantage of 100+200+100 swirl pipe on increasing total wall shear stress is more obvious in flows with larger velocities, which is typically the velocity used in the CIP procedures.

VI. CONCLUSIONS

In this study, the ability of two swirl pipes in terms of inducing swirl into flows passing through them have been numerically investigated and compared. The objective has been the prediction and comparisons of pressure drop and tangential velocity caused by the two swirl pipes, the swirl intensity and its decay law downstream of the two swirl pipes, the swirl effectiveness of the two swirl pipes and their effects on increasing the wall shear stress downstream of them. The following results have been obtained:

- The overall pressure drop caused by the 100+400+100 swirl pipe is larger than the 100+200+100 swirl pipe for the same inlet velocities and the pressure drop increases with increasing inlet velocities.
- For the 100+400+100 swirl pipe, the entry transition pipe and the first half of the swirl inducing pipe contribute to swirl development, the second half of swirl inducing pipe and the exit transition pipe act as a constraint to the induced swirl. While within the 100+200+100 swirl pipe, only the exit transition pipe constrains the induced swirl. The final tangential velocity and the swirl intensity just downstream of the 100+200+100 swirl pipe for various inlet velocities are slightly larger than that of 100+400+100 swirl pipe.
- The overall swirl induction effectiveness of the 100+200+100 swirl pipe is larger than that of the 100+400+100 swirl pipe.
- The induced tangential velocity, swirl intensity and the effective distances are slightly larger downstream of the 100+200+100 swirl pipe than when 100+400+100 swirl

pipe is used with its advantage is more true in flows with larger Reynolds Number.

- Swirl pipes impose a tangential wall shear stress within itself and direct to downstream with its value and variation trend being dependent on swirl intensity. The induced tangential wall shear stress after the 100+200+100 swirl pipe is slightly larger than when 100+400+100 swirl pipe is used due to the relatively larger swirl intensity.
- The axial and total wall shear stress are also slightly larger downstream of the 100+200+100 swirl pipe than that of the 100+400+100 swirl pipe with its advantage being more true in flows with a larger inlet velocity.
- The 100+200+100 swirl pipe is more cost-effective in swirl induction and is better in maintaining the wall shear stress increase downstream it than that of 100+400+100 swirl pipe.

From the simulation results, 100+200+100 swirl pipe induce slightly stronger swirl into flows passing through it and also lasts for slightly longer distance than that of 100+400+100 swirl pipe in the expense of a smaller pressure loss. It is also clear that the 100+200+100 swirl pipe is more cost effective in increasing wall shear stress downstream of it than when a 100+400+100 swirl pipe, thus it should results in better performance when applied in the Clean-In-Place procedures in the pipe cleaning system.

REFERENCES

- [1] Lelièvre, C., et al., Cleaning in place: effect of local wall shear stress variation on bacterial removal from stainless steel equipment. *Chemical Engineering Science*, 2002. 57: p. 1287-1297.
- [2] Jensen, B.B.B., et al., Local Wall Shear Stress Variations Predicted by Computational Fluid Dynamics for Hygienic Design. *Food and Bioprocess Processing*, 2005. 83(1): p. 53-60.
- [3] Gillham, C.R., et al., Cleaning-in-Place of Whey Protein Fouling Deposits. *Food and Bioprocess Processing*, 1999. 77(2): p. 127-136.
- [4] Dev, S.R.S., et al., Optimization and modeling of an electrolyzed oxidizing water based Clean-In-Place technique for farm milking systems using a pilot-scale milking system. *Journal of Food Engineering*, 2014. 135(0): p. 1-10.
- [5] PathogenCombat, E.I.P., Factors affecting fouling and cleanability of closed food contact surface. 2011.
- [6] Lelieveld, H.L.M., Mostert, M.A., Holah, J. and White, B., *Hygiene in Food Processing*. Vol. 1st edn. 2003, Woodhead, Cambridge, UK.
- [7] Changani, S.D., M.T. Belmar-Beiny, and P.J. Fryer, Engineering and chemical factors associated with fouling and cleaning in milk processing. *Experimental Thermal and Fluid Science*, 1997. 14: p. 392-406.
- [8] Sharma, M.M., et al., Factors Controlling the Hydrodynamic Detachment of Particles from Surfaces. *Journal of Colloid and Interface Science*, 1991. 149: p. 121-134.
- [9] Hwang, Y.K. and N.S. Woo, Wall Shear Stress in the Helical Annular Flow with Rotating Inner Cylinder. *DIFFUSION AND DEFECT DATA PART B SOLID STATE PHENOMENA*, 2007. 120: p. 261-266.
- [10] Li, G., et al., Improving the efficiency of 'Clean-In-Place' procedures using a four-lobed swirl pipe: A numerical investigation. *Computers & Fluids*, 2015. 108(0): p. 116-128.
- [11] Najafi, A.F., S.M. Mousavian, and K. Amini, Numerical investigations on swirl intensity decay rate for turbulent swirling flow in a fixed pipe. *International Journal of Mechanical Sciences*, 2011. 53(10): p. 801-811.
- [12] Ganesalingam, J., Swirl Induction for Improved Solid-Liquid Flow in Pipes. 2002, University of Nottingham.
- [13] Ariyaratne, C., DESIGN AND OPTIMISATION OF SWIRL PIPES AND TRANSITION GEOMETRIES FOR SLURRY TRANSPORT, in School of Chemical, Environmental and Mining Engineering. 2005, University of Nottingham.
- [14] Kiroh, O., Experimental study of turbulent swirling flow in a straight pipe. *Journal of Fluid Mechanics*, 1991. 225: p. 445-479.
- [15] Steenbergen, W. and J. Voskamp, The rate of decay of swirl in turbulent pipe flow. *Flow measurement and instrumentation*, 1998. 9: p. 67-78.
- [16] ANSYS, I., ANSYS FLUENT 14.0 User's Guide. 2011: Southpointe, Canonsburg, PA, USA.
- [17] Bakker, A., Boundary Layers and separation, in *Applied Computational Fluid Dynamics*. 2002.
- [18] Fokeer, S., I.S. Lowndes, and D.M. Hargreaves, Numerical modelling of swirl flow induced by a three-lobed helical pipe. *Chemical Engineering and Processing: Process Intensification*, 2010. 49(5): p. 536-546.
- [19] ANSYS, I., ANSYS FLUENT 14.0 Theory Guide. 2011: Southpointe, Canonsburg, PA, USA.
- [20] Speziale, C.G., S. Sarkar, and T. B.Gatski, Modelling the Pressure-Strain Correlation of Turbulence: An Invariant Dynamical Systems Approach. *J. Fluid Mech.*, 1991. 227: p. 245-272.
- [21] Jensen, B.B.B., M. Stenby, and D.F. Nielsen, Improving the cleaning effect by changing average velocity. *Trends in Food Science & Technology*, 2007. 18: p. S58-S63.

Appendix 8.1 Drawing of the Optimised Swirl Pipe for Investment Casting

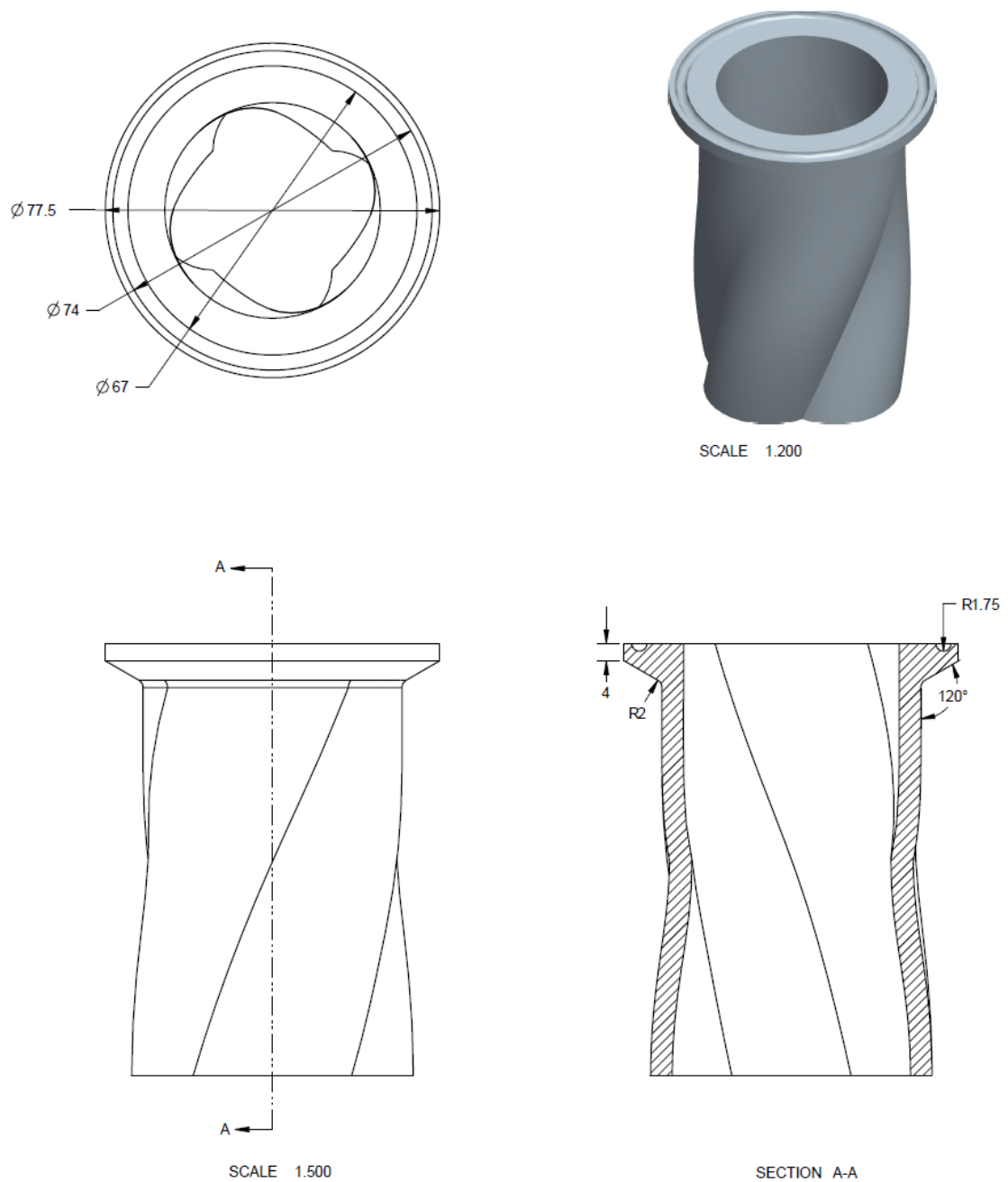


Figure A8.1.1 Drawing of the transition pipe and dairy clamp connector

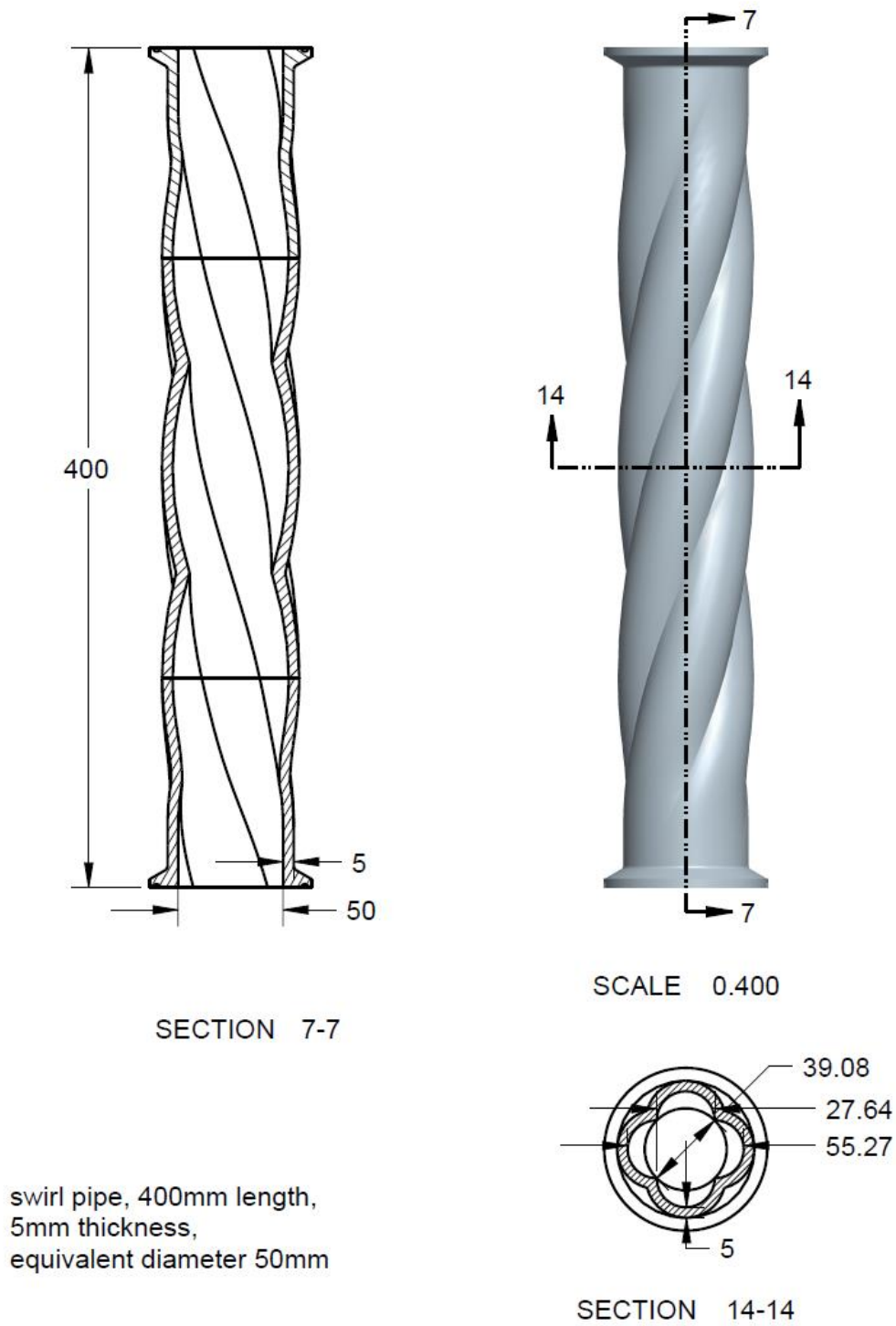


Figure A8.1.2 Drawing of the optimized swirl pipe

Appendix 8.2 Experimental and Calculated data for Calibrating the Tot-film Sensor

The experimental data of pressure and voltage and the calculated wall shear stress in cylindrical pipe flows, E_a^2 , $\tau_w^{1/3}$ for calibrating the hot-film sensor is shown in Table A8.2.1~A8.2.5 for conditions of sensor at top, +45°, middle, -45° and bottom respectively.

Table A8.2.1 Experimental and calculated data for calibrating the hot-film sensor (sensor at top)

T °C	Velocity m/s	E_a^2 corrected	E_{corr}	E_a mean	E_{a1}	E_{a2}	E_{a3}	E_{a4}	E_{a5}	Coefficient of error of E_{ai}	Pressure at 1 Pa	Pressure at 2 Pa	Pressure drop Pa	T_w Pa	$T_w^{1/3}$
21.5	0.750	3.441	1.85493	1.85493	1.85703	1.85559	1.85405	1.85354	1.85442	0.00075	2550.880	1717.476	833.404	2.217	1.304
21.5	1.001	3.571	1.88974	1.88974	1.88991	1.88966	1.89057	1.88925	1.88930	0.00028	3204.841	1986.657	1218.184	3.240	1.480
21.5	1.250	3.636	1.90687	1.90687	1.90776	1.90643	1.90642	1.90704	1.90670	0.00029	4161.576	2479.717	1681.859	4.473	1.648
21.5	1.498	3.723	1.92961	1.92961	1.93084	1.92975	1.92877	1.92938	1.92930	0.00040	5295.704	3072.169	2223.535	5.914	1.808
21.6	1.750	3.754	1.93759	1.93507	1.93579	1.93440	1.93568	1.93498	1.93451	0.00033	6600.375	3741.069	2859.306	7.605	1.966
21.7	1.999	3.779	1.94399	1.93894	1.93875	1.93946	1.93834	1.93909	1.93906	0.00022	8071.421	4518.331	3553.090	9.450	2.114
22	2.243	3.813	1.95267	1.93995	1.94084	1.94008	1.94030	1.93918	1.93933	0.00036	9697.876	5386.864	4311.012	11.465	2.255
22.2	2.513	3.834	1.95798	1.94010	1.94127	1.94004	1.94014	1.93916	1.93990	0.00039	11690.290	6419.580	5270.710	14.018	2.411

Table A8.2.2 Experimental and calculated data for calibrating the hot-film sensor (sensor at +45°)

T °C	Velocity m/s	E_a^2 corrected	E_{corr}	E_a mean	E_{a1}	E_{a2}	E_{a3}	E_{a4}	E_{a5}	Coefficient of error of E_{ai}	Pressure at 1 Pa	Pressure at 2 Pa	Pressure drop Pa	T_w Pa	$T_w^{1/3}$
22	0.750	3.230	1.79715	1.79715	1.79982	1.79881	1.79731	1.79497	1.79485	0.00124	2553.237	1722.477	830.760	2.209	1.302
22	1.000	3.403	1.84477	1.84477	1.84158	1.84482	1.84568	1.84549	1.84630	0.00101	3205.663	1994.875	1210.788	3.220	1.477
22	1.250	3.500	1.87094	1.87094	1.87059	1.87182	1.87100	1.87050	1.87079	0.00028	4153.367	2479.284	1674.083	4.452	1.645
22	1.502	3.541	1.88186	1.88186	1.88278	1.88206	1.88157	1.88090	1.88199	0.00037	5305.872	3080.607	2225.265	5.918	1.809
22	1.752	3.572	1.89002	1.89002	1.88959	1.89017	1.89009	1.89062	1.88962	0.00023	6612.401	3760.106	2852.295	7.586	1.965
22	1.999	3.582	1.89256	1.89256	1.89363	1.89297	1.89148	1.89324	1.89148	0.00054	8088.585	4529.332	3559.253	9.466	2.115
22.2	2.251	3.620	1.90260	1.89758	1.89846	1.89758	1.89774	1.89718	1.89696	0.00030	9772.334	5426.664	4345.670	11.558	2.261
22.5	2.500	3.639	1.90751	1.89492	1.89588	1.89574	1.89447	1.89378	1.89473	0.00047	11631.830	6369.208	5262.622	13.996	2.410

Table A8.2.3 Experimental and calculated data for calibrating the hot-film sensor (sensor at middle)

T °C	Velocity m/s	E_a^2 corrected	E_{corr}	E_a mean	E_{a1}	E_{a2}	E_{a3}	E_{a4}	E_{a5}	Coefficient of error of E_{ai}	Pressure at 1 Pa	Pressure at 2 Pa	Pressure drop Pa	T_w Pa	$T_w^{1/3}$
22.4	0.750	3.583	1.89301	1.89301	1.89491	1.89351	1.89187	1.89245	1.89228	0.00065	2550.862	1646.744	904.118	2.405	1.340
22.4	1.001	3.674	1.91689	1.91689	1.91821	1.91695	1.91574	1.91626	1.91729	0.00050	3205.000	1922.506	1282.494	3.411	1.505
22.4	1.249	3.708	1.92557	1.92557	1.92546	1.92636	1.92420	1.92575	1.92605	0.00043	4155.608	2416.235	1739.373	4.626	1.666
22.5	1.502	3.792	1.94736	1.94477	1.94409	1.94541	1.94595	1.94319	1.94519	0.00057	5291.444	2998.273	2293.171	6.099	1.827
22.5	1.749	3.853	1.96302	1.96040	1.96176	1.95933	1.95916	1.96068	1.96110	0.00058	6556.796	3645.681	2911.115	7.742	1.978
22.5	2.003	3.873	1.96805	1.96543	1.96647	1.96617	1.96466	1.96425	1.96561	0.00049	8047.410	4446.534	3600.876	9.577	2.124
22.7	2.251	3.905	1.97611	1.96821	1.96874	1.96875	1.96824	1.96765	1.96767	0.00028	9715.956	5307.707	4408.249	11.724	2.272
22.9	2.502	3.934	1.98354	1.97031	1.97047	1.97143	1.97016	1.97056	1.96892	0.00046	11589.850	6295.058	5294.792	14.082	2.415

Table A8.2.4 Experimental and calculated data for calibrating the hot-film sensor (sensor at -45°)

T °C	Velocity m/s	E_a^2 corrected	E_{corr}	E_a mean	E_{a1}	E_{a2}	E_{a3}	E_{a4}	E_{a5}	Coefficient of error of E_{ai}	Pressure at 1 Pa	Pressure at 2 Pa	Pressure drop Pa	T_w Pa	$T_w^{1/3}$
22.1	0.749	3.569	1.88926	1.88926	1.89172	1.88863	1.88698	1.88864	1.89031	0.00096	2589.182	1767.294	821.888	2.186	1.298
22.1	1.000	3.671	1.91608	1.91608	1.91594	1.91594	1.91603	1.91657	1.91592	0.00014	3244.629	2045.595	1199.034	3.189	1.472
22.1	1.250	3.697	1.92277	1.92277	1.92521	1.92406	1.92259	1.92174	1.92025	0.00101	4200.877	2542.147	1658.730	4.412	1.640
22.1	1.498	3.790	1.94671	1.94671	1.94713	1.94724	1.94684	1.94636	1.94601	0.00027	5327.060	3125.848	2201.212	5.854	1.802
22.2	1.753	3.831	1.95729	1.95471	1.95489	1.95471	1.95561	1.95388	1.95446	0.00032	6649.118	3816.713	2832.405	7.533	1.960
22.4	2.001	3.874	1.96825	1.96045	1.96013	1.96098	1.96004	1.96052	1.96058	0.00019	8131.750	4586.707	3545.043	9.428	2.113
22.5	2.238	3.902	1.97545	1.96500	1.96552	1.96531	1.96485	1.96456	1.96476	0.00020	9730.105	5423.617	4306.488	11.453	2.254
22.6	2.498	3.917	1.97902	1.96592	1.96535	1.96698	1.96576	1.96509	1.96642	0.00039	11690.910	6468.104	5222.806	13.890	2.404

Table A8.2.5 Experimental and calculated data for calibrating the hot-film sensor (sensor at bottom)

T °C	Velocity m/s	E_a^2 corrected	E_{corr}	E_a mean	E_{a1}	E_{a2}	E_{a3}	E_{a4}	E_{a5}	Coefficient of error of E_{ai}	Pressure at 1 Pa	Pressure at 2 Pa	Pressure drop Pa	T_w Pa	$T_w^{1/3}$
22.5	0.750	3.639	1.90761	1.90761	1.90456	1.90725	1.90782	1.91020	1.90820	0.00106	2545.863	1754.958	790.905	2.103	1.281
22.5	1.003	3.731	1.93168	1.93168	1.93168	1.93234	1.93307	1.93011	1.93118	0.00058	3206.430	2024.181	1182.249	3.144	1.465
22.5	1.250	3.797	1.94846	1.94846	1.94998	1.94670	1.94865	1.94897	1.94801	0.00063	4163.741	2544.002	1619.739	4.308	1.627
22.6	1.502	3.861	1.96496	1.96233	1.96295	1.96436	1.96153	1.96124	1.96160	0.00067	5307.829	3109.221	2198.608	5.847	1.802
22.6	1.754	3.890	1.97235	1.96972	1.97151	1.97114	1.96848	1.96850	1.96896	0.00075	6620.224	3792.948	2827.276	7.519	1.959
22.7	1.994	3.917	1.97917	1.97388	1.97273	1.97511	1.97321	1.97423	1.97413	0.00047	8052.990	4553.290	3499.700	9.308	2.104
22.9	2.236	3.956	1.98896	1.97832	1.97899	1.97837	1.97759	1.97816	1.97850	0.00026	9672.930	5412.948	4259.982	11.330	2.246
23	2.514	3.976	1.99403	1.98069	1.98192	1.98133	1.97985	1.98032	1.98003	0.00045	11686.510	6456.997	5229.513	13.908	2.405

